

University of Alberta

Characterization of Wear in a Laboratory-Scale Slurry Pipeline

by

Derek John Loewen

A thesis submitted to the Faculty of Graduate Studies and Research
in partial fulfillment of the requirements for the degree of

Master of Science

Mechanical Engineering

©Derek John Loewen

Fall 2013

Edmonton, Alberta

Permission is hereby granted to the University of Alberta Libraries to reproduce single copies of this thesis and to lend or sell such copies for private, scholarly or scientific research purposes only. Where the thesis is converted to, or otherwise made available in digital form, the University of Alberta will advise potential users of the thesis of these terms.

The author reserves all other publication and other rights in association with the copyright in the thesis and, except as herein before provided, neither the thesis nor any substantial portion thereof may be printed or otherwise reproduced in any material form whatsoever without the author's prior written permission.

Dedication

To my family

Abstract

Hydraulic transport is commonly employed in the mining industry to transport crushed ore to a processing facility. Dense slurry flows inflict heavy wear on pipes, leading to significant process downtime and loss of revenue. Several factors have been identified as key contributors to pipe wear. This work examines the effects of flow rate and solids concentration, and offers a formulation for developing a predictive slurry wear model. A modified flow model was developed and coupled with other wear models to describe wear within slurry pipes.

Preliminary model verification was conducted through experimental testing. Sliding-abrasion wear data was found to be an exponential function of velocity and a linear function of shear stress. The particle impingement wear model produced simulated wear profiles comparable to profiles observed on pipelines in service. The modified flow model has not been validated here, but preliminary results indicate possible improvements in accuracy over the SRC model.

Acknowledgments

This research could not have been completed without the assistance, guidance, and encouragement of numerous people. I would like to thank each of you for your contribution to the successful completion of this project.

I have received a great deal of valuable advice and assistance from various people at the University of Alberta. I gratefully acknowledge the help of the mechanical engineering staff, especially Rick Conrad for his electrical expertise, Andrew Campbell for being my “go-to man” for materials-related questions, Bernie Faulkner for sharing his wealth of knowledge on strain gauging, the IT group for their cheerful assistance with network and computer issues, Teresa Gray for patiently helping me with lab purchases, and the outstanding group of professors who not only taught my classes, but employed me as a TA. I owe a huge debt of thanks to several individuals who assisted me in my project work, namely Eric Penner for coaching me in using the LabWindows/CVI software development environment, Debjyoti Sen for his valuable assistance with the optical experiments and data pre-processing, and Derek Russell and Shantanu Diwakar for performing experimental runs in my stead while I was required to live off-campus. Thank you also to fellow graduate students for companionship, conversation, and occasionally a good coffee. Marc, Vivek, Amanda, Stephen, Jamie, Nicolas, Mona, Dan, and Andrew – it’s been a lot of fun getting to know you all.

Outside of school, I wish to thank the many people who I was privileged to have in my life during the course of my academic adventure. My warmest thanks go to my family for always being there for me, and for giving encouragement when I needed it. Thank you for understanding my academic workload, for cheerfully picking up the slack with household chores, and for being the most supportive bunch of people that a guy could ask for. I also would like to thank my former co-workers and friends at Millennium Place, Kinsmen Leisure Centre, and U of A Aquatics for their continued encouragement and interest in my progress. Of course, none of this would have been possible without the help of my Heavenly Father, who provided the ability, strength, and endurance I needed every day. All glory goes to Him.

Finally, from the bottom of my heart I would like to extend my sincerest thanks to my academic supervisors, Dr. Michael Lipsett and Dr. David Nobes. Your guidance, knowledge, and input were invaluable to the completion of this project. Thank you especially to Dr. Lipsett for your patience and encouragement, for taking a personal interest in my professional development, and for your ability to motivate me to go further than I thought possible. I have learned so much from both of you, and I am grateful to have had such an excellent team of advisors.

Table of Contents

1	Introduction.....	1
1.1	Oilsand Mining & Hydrotransport	1
1.2	Pipe Wear	2
1.3	Motivation and Objectives of the Thesis	2
2	Relevant Theory and Review of the Literature	4
2.1	Describing Solid-Liquid Slurry Flows in Pipes.....	4
2.1.1	Hydrotransport.....	5
2.1.2	Mechanics of Slurry Flow	6
2.1.3	The SRC Two-Layer Flow Model.....	8
2.1.4	Shear Interface Layer	14
2.2	Wear	17
2.2.1	Friction and Particle Lifting Forces	19
2.2.2	Slurry Pipe Wear Profiles in Service	20
2.2.3	Sliding Erosion	23
2.2.4	Solid Particle Erosion.....	24
2.2.5	Finnie’s Model for Erosive Wear by Solid Particles	25
2.2.6	Bitter’s Model for Erosive Wear by Solid Particles.....	27
2.2.7	Oka’s Model for Erosive Wear by Solid Particles	28
2.3	Pipe Stresses and Strains	29
2.3.1	Stress	29
2.3.2	Strain	31
3	Model Development.....	33
3.1	Introduction	33
3.2	Modified Flow Model.....	33
3.3	Shear Interface Layer Parameters	37

3.4	Sliding Erosion.....	42
3.5	Impingement.....	45
3.6	Model Verification and Validation	49
4	Experimental Methodology	51
4.1	Introduction	51
4.2	Principal Assumptions.....	51
4.3	Definition of Variables	52
4.4	Experimental Equipment	52
4.5	Instrumentation	57
4.5.1	Data Acquisition	57
4.5.2	Flow Rate and Density.....	59
4.5.3	Gauge Pressure	60
4.5.4	Temperature	61
4.5.5	Strain	61
4.6	Test Materials	64
4.7	Control Software.....	66
4.8	Experimental Procedure	70
4.8.1	Wear Testing	71
4.8.2	Optical Particle Tracking.....	73
5	System Calibration and Commissioning	77
5.1	Introduction	77
5.2	Calibration.....	77
5.2.1	Pressure sensors	77
5.2.2	Temperature Sensors	78
5.2.3	Coriolis Flow Meter	80
5.2.4	Strain Spool	81
5.2.5	Optical Equipment	87

5.3	Commissioning.....	87
5.3.1	Pressure Sensors	88
5.3.2	Temperature Sensors	89
5.3.3	Pipe Loop System	91
5.3.4	Wear Materials.....	91
5.3.5	Control Software	93
5.4	Equipment Issues	94
6	Experimental Results and Discussion	95
6.1	Wear Testing	95
6.2	Strain Testing	98
6.3	Optical Particle Tracking	102
7	Modeling and Simulation Results	124
7.1	Modified Two-Layer Flow Model Results	124
7.2	Impingement Wear Simulation Results	126
7.3	Sliding Abrasive Wear Modeling	134
8	Conclusions and Recommendations for Future Work.....	144
8.1	Conclusions	144
8.1.1	Experimental Apparatus Development.....	144
8.1.2	Summary of Experimental Results	146
8.1.3	Modeling of Slurry Flow and Pipe Wear.....	148
8.2	Recommendations for Future Work	150
	References.....	154
	Appendices	158
	Appendix A – Pipe Loop Software Code.....	159
	Appendix B – Impingement Wear Model Code	179
	Appendix C – Modified Two-Layer Model MathCAD Worksheet	183
	Appendix D – Modified Piping Drawings.....	192

Appendix E – Material Data Sheets.....	195
Appendix F – Pump Data Sheets	202
Appendix G – Sensor Data Sheets.....	204
Appendix H – High-Speed Camera Data Sheet	209
Appendix I – Sample Thermal Correction For Strain Readings	212
Appendix J – Experimental Equipment Issues.....	214
J.1 Pump	215
J.2 Coriolis Meter	218

List of Tables

Table 1 - Pressure transducer calibration constants	78
Table 2 - RTD calibration constants	79
Table 3 - Experimental run properties	95
Table 4 - Impingement wear simulation results	128
Table 5 - Flow conditions for simulation, phase 2	132
Table 6 - Simulation results, phase 2	132
Table 7 - Sensitivity analysis results	140
Table 8 - Experimental run properties	141
Table 9 - Predictive error of the model.....	142

Table of Figures

Figure 1 - Graphical representation of the SRC Two-Layer Model [Gillies et al., 1991]	9
Figure 2 - Concentration profile results [replotted from Pugh & Wilson, 1999]	15
Figure 3 - Velocity profile results [replotted from Schaan & Shook, 2000]	17
Figure 4 - Typical wear profiles in a straight, inclined oilsands hydrotransport line (data points are interpolated using splines) [replotted from Schaan et al., 2007]	21
Figure 5 - Typical wear profile occurring in coarse tailings lines (data points interpolated using splines) [replotted from Schaan et al., 2007]	22
Figure 6 - Schematic of modified two-layer model	35
Figure 7 - Cross-section geometry of the modified two-layer model	35
Figure 8 - Cross section view of a slurry pipe	43
Figure 9 - Schematic of particle impingement simulation	45
Figure 10 - Geometrical representation of a particle-wall collision	47
Figure 11 - Rendering of pipe loop, with key components labeled	53
Figure 12 - Pipe loop system overview	53
Figure 13 - Slurry pump with flush water line installed at the seal	54
Figure 14 - VFDs for mixer (left) and pump (center); network switch at bottom	54
Figure 15 - Mixing tank with electric mixer	55
Figure 16 - Waste tank, sieve box, and catch bin	56
Figure 17 - Removable test section with clear viewing tube and axial preload support rods	57
Figure 18 - DAQ with external power supply	58
Figure 19 - Coriolis meter with bundled 4-20mA outputs (pink)	59
Figure 20 - Pressure transducer	60
Figure 21 - RTD thermocouple	61
Figure 22 - Strain pool with eight rosettes spaced 25.7° apart	63
Figure 23 - A sample urethane-coated test specimen	65
Figure 24 - Software flow diagram	67

Figure 25 - Screenshot of control software	68
Figure 26 - Setup for optical particle-tracking experiments.....	75
Figure 27 - Pressure transducer calibration curves	78
Figure 28 - RTD calibration curves.....	80
Figure 29 - Change in strain readings with temperature.....	82
Figure 30 - Calibration results: axial strain	83
Figure 31 - Calibration results: circumferential strain	84
Figure 32 - Strain calibration: hoop strain	85
Figure 33 - Strain calibration: axial strain	86
Figure 34 - Optical calibration target	87
Figure 35 - Pressure readings for a water flow test	89
Figure 36 - Temperature differential across the pump	90
Figure 37 - Temperature differential at steady state	90
Figure 38 - Garnet sand particles prior to testing	92
Figure 39 - Garnet sand particles following 3.5 hrs of testing.....	92
Figure 40 - Wear specimen after testing	93
Figure 41 - Sample wear specimens after undergoing testing	96
Figure 42 - Rate of mass loss with respect to pump speed	97
Figure 43 - Measured mass flow rates at experimental pump speeds	97
Figure 44 - Hoop strain at 6.4vol% slurry concentration.....	99
Figure 45 - Axial strain at 6.4vol% slurry concentration.....	100
Figure 46 - Hoop strain at 13.5vol% slurry concentration.....	100
Figure 47 - Axial strain at 13.5vol% slurry concentration.....	101
Figure 48 - Optical results: 30 Hz pump speed.....	103
Figure 49 - Optical results: 40 Hz pump speed.....	103
Figure 50 - Optical results: 50 Hz pump speed.....	104
Figure 51 - Optical results: 60 Hz pump speed.....	104

Figure 52 - Raw image of garnet slurry flow.....	105
Figure 53 - Sample sharpened, inverted image.....	105
Figure 54 - Sample background to be subtracted from images	106
Figure 55 - Resolving velocity vectors	107
Figure 56 - Sample plot of time-averaged velocity vectors	107
Figure 57 - Axial velocity histogram, 30 Hz pump speed.....	109
Figure 58 - Vertical velocity histogram, 30 Hz pump speed	109
Figure 59 - Spatial distribution of particles, 30 Hz pump speed.....	110
Figure 60 - Particle count with height, 30 Hz pump speed	110
Figure 61 - Axial velocity distribution, 30 Hz pump speed	111
Figure 62 - Variation in axial velocity with height, 30 Hz pump speed	111
Figure 63 - Vertical velocity distribution, 30 Hz pump speed.....	112
Figure 64 - Variation in vertical velocity with height, 30 Hz pump speed	112
Figure 65 - Axial velocity histogram, 40 Hz pump speed.....	113
Figure 66 - Vertical velocity histogram, 40 Hz pump speed	113
Figure 67 - Spatial distribution of particles, 40 Hz pump speed.....	114
Figure 68 - Particle count with height, 40 Hz pump speed	114
Figure 69 - Axial velocity distribution, 40 Hz pump speed	115
Figure 70 - Variation in axial velocity with height, 40 Hz pump speed	115
Figure 71 - Vertical velocity with height, 40 Hz pump speed	116
Figure 72 - Variation in vertical velocity with height, 40 Hz pump speed	116
Figure 73 - Axial velocity histogram, 50 Hz pump speed.....	117
Figure 74 - Vertical velocity histogram, 50 Hz pump speed	117
Figure 75 - Spatial distribution of particles, 50 Hz pump speed.....	118
Figure 76 - Particle count with height, 50 Hz pump speed	118
Figure 77 - Axial velocity distribution, 50 Hz pump speed	119
Figure 78 - Variation of axial velocity with height, 50 Hz pump speed	119

Figure 79 - Vertical velocity distribution, 50 Hz pump speed.....	120
Figure 80 - Variation of vertical velocity with height, 50 Hz pump speed.....	120
Figure 81 - Comparison of layer-specific velocities	125
Figure 82 - Comparison of layer-specific cross-sectional areas.....	126
Figure 83 - Impingement wear rates predicted by Monte Carlo simulation	129
Figure 84 - Wear profiles observed in coarse tailings lines (points connected with splines) (replotted from Schaan et al., 2007)	130
Figure 85 - Simulated wear profile (10 second duration).....	130
Figure 86 - Simulated wear profile (60 second duration).....	131
Figure 87 - Simulated wear profile (120 second duration).....	131
Figure 88 - Simulated wear profile - condition set #1	133
Figure 89 - Simulated wear profile - condition set #2	133
Figure 90 - Simulated wear profile - condition set #3	134
Figure 91 - Wear rate with respect to velocity	135
Figure 92 - Wear rate with respect to shear stress	135
Figure 93 - Wear rate with respect to shear stress * velocity	136
Figure 94 - Wear rate with respect to shear stress * velocity * concentration.....	137
Figure 95 - Wear data corrected for threshold shear stress and concentration	139
Figure 96 - Predicted and actual wear rates.....	141
Figure 97 - Pump inlet/outlet pressure with respect to pump speed	216
Figure 98 - Mass flow data proving for the Coriolis meter	218
Figure 99 - Density at 60 Hz, 6.4vol% concentration (run #1)	219
Figure 100 - Density at 60 Hz, 6.4vol% concentration (run #1), filtered using 5th-order Butterworth lowpass filter (0.01 Hz)	220

Nomenclature

A : cross-sectional area of the pipe

A_1 : cross-sectional area of the upper slurry flow layer

A_2 : cross-sectional area of the lower slurry flow layer

A_s : cross-sectional area of the shear interface layer

C_1 : total solids fraction of the upper layer

C_2 : the difference between concentrations C_{lim} and C_1

C_c : volume fraction of contact-load solids, averaged over the whole pipe

C_D : coefficient of particle drag

C_f : volume fraction of fines

C_{lim} : total solids fraction of the lower layer

C_{max} : maximum allowable solids fraction, based on particle packing

C_r : *in situ* volume fraction of coarse particles

C_t : total *in-situ* volume fraction of solids

C_v : total delivered volume fraction of solids

C_w : total *in situ* weight fraction of solids

d : particle diameter

d^+ : dimensionless particle diameter

d' : value of particle diameter used during standardized testing

D : inner diameter of the pipe

D_{H1} : hydraulic diameter of the upper slurry flow layer

D_{H2} : hydraulic diameter of the lower slurry flow layer

D_{HS} : hydraulic diameter of the shear interface layer

\dot{D} : damage/erosion rate

E : Young's modulus of material

\dot{E}_k : rate of input kinetic energy of impacting particles

\dot{E}_{k0} : threshold rate of input kinetic energy required for damage to occur

E_1 : Young's modulus of particle material

E_2 : Young's modulus of impacted surface material

f_f : upper (fluid) friction factor

f_2 : lower (Fanning) friction factor

f_{12} : interfacial friction factor

f_{sl} : particle friction factor

F_s : shear force acting vertically on the pipe (function of axial location along pipe)

h_1 : maximum thickness of the upper layer

h_2 : maximum thickness of the lower layer

h_s : thickness of the shear interface layer

Hv: Vickers hardness number of the impinged material, in [GPa]

I : area moment of inertia

k_0 : empirically-derived constant (Oka model)

k_1 : empirically-derived constant (Oka model)

k_3 : empirically-derived constant (Oka model)

$\sum k$: total minor losses, based on pipe geometry such as entrances, exits, elbows, and tees. For the experimental test rig, this value is taken to be 5.5.

K : velocity at which the elastic limit of the impinged material is reached

L : length of pipe section

\dot{m} : slurry mass flow rate

M : bending moment induced by weight (function of axial location along pipe)

M_p : total mass of impinging particles

n : empirically-determined, material-specific power constant

p : plastic flow stress of the impacted material

P_1 : perimeter of the upper slurry flow layer

P_1 : perimeter of the lower slurry flow layer

P_1 : perimeter of the shear interface layer

P_i : internal pressure

P_o : external pressure

q_1 : empirically-derived constant (Oka model)

q_2 : empirically-derived constant (Oka model)

r : radial distance from pipe center

r_o : external pipe radius

r_i : internal pipe radius

R : average value of the pipe's outer and inner radii

Re_2 : Reynolds number for the lower slurry flow layer

s_1 : empirically-derived constant (Oka model)

s_2 : empirically-derived constant (Oka model)

S_1 : interfacial perimeter between the upper layer and the pipe wall

S_{12} : interfacial perimeter between the upper and lower layers

S_{1s} : interfacial perimeter between the upper layer and the shear interface layer

S_2 : interfacial perimeter between the lower layer and the pipe wall

S_{2s} : interfacial perimeter between the lower layer and the shear interface layer

S_s : interfacial perimeter between the shear interface layer and the pipe wall

SG: slurry specific gravity

t : pipe wall thickness

T : temperature in [$^{\circ}\text{C}$]

V : slurry velocity averaged over the entire pipe cross-section

V_0 : the velocity above which a slurry mixture begins to move with a stationary bed

V_1 : average velocity of the upper slurry flow layer

V_2 : average velocity of the lower slurry flow layer

V_b : the velocity above which the solid bed begins to flow

V_d : the minimum deposition velocity of a slurry mixture

V_h : the velocity above which a slurry mixture flows with a homogeneous solids distribution

V_p : particle impact velocity

V_p' : value of particle impact velocity used during standardized testing

w_0 : uniform weight load per unit length of pipe

W_D : deformation wear rate

W_{C1} : cutting wear rate for the case where parallel particle motion does not go to zero

W_{C2} : cutting wear rate for the case where parallel particle motion goes to zero

y : vertical distance measured from the lower surface of the shear interface layer.

y_n : vertical distance from the neutral axis of the pipe cross-section

α : half-angle which subtends the chord defining the upper boundary of the shear interface layer

β : half-angle which subtends the chord defining the upper boundary of the lower layer

γ : cutting wear factor

δ : thickness of viscous boundary layer

ϵ : absolute surface roughness, given to be $4.6 \cdot 10^{-5}$ m for steel pipes

ε : material strain

$\varepsilon_{thermal}$: material strain due to thermal expansion

ζ : multiplier for wall stress

η_s : coefficient of friction between the bed solids and the pipe wall

η_{s0} : maximum coefficient of friction between the bed solids and the pipe wall, taken to be 0.5

θ : angle of impingement from the normal

κ : amount of energy required to remove one unit of material by deformation, determined experimentally

λ : linear solids concentration

ν : Poisson's ratio

μ_1 : viscosity of the upper slurry flow layer

μ_2 : viscosity of the lower slurry flow layer

μ_l : calculated viscosity of the liquid phase, $\mu_l(T) = 0.00002414 \cdot 10^{\frac{2478}{(T-413.15)}}$

μ_m : viscosity of the slurry mixture

ν_1 : Poisson's ratio for the particle material

ν_2 : Poisson's ratio for the impacted surface material

ρ_1 : density of the upper slurry flow layer

ρ_{2f} : density of the lower slurry flow layer

ρ_s : density of the solid phase

ρ_L : density of the liquid phase

ρ_m : average density of the slurry mixture

ρ_p' : density of the impacting particle, adjusted for angularity

σ : material stress (subscript numbers designate directions)

σ_y : elastic load limit

τ : solid shear stress experienced in the pipe walls

τ_0 : shear stress required to initiate damage to the pipe wall

τ_1 : flow shear stress between the upper layer and the wall

τ_{12} : flow shear stress between the upper and lower flow layers

τ_{1s} : flow shear stress between the upper and shear interface layers

τ_2 : flow shear stress between the lower layer and the wall

τ_{2c} : Coulombic friction component of shear stress between the lower layer and the wall

τ_{2h} : hydraulic friction component of shear stress between the lower layer and the wall

τ_{2s} : flow shear stress between the lower and shear interface layers

φ : empirically-derived proportionality constant

ψ : depth of cut due to erosion by a single particle

1 Introduction

1.1 Oilsand Mining & Hydrotransport

Canada's primary source of unconventional oil is oilsand, a naturally occurring substance consisting chiefly of bitumen, water, silica sand, and clay [Evans, 2012]. It may be found in loose, sandy deposits or encased in sandstone-like formations. Oilsand is sought after solely for its bitumen content, bitumen being the chief feedstock for heavy oil upgraders [Oilsands Information Portal, 2012]. In the province of Alberta, oilsand deposits are found in the Athabasca, Cold Lake, and Peace River deposits. In the open-pit mining process, oilsand is mined with large shovels and loaded into haul trucks [Lipsett, 2009]. The trucks transfer the oilsand to an input crusher for ease of further transport, and crushed oilsand is mixed with water to form a slurry that is piped from the mines to an extraction plant. These slurries consist of particles ranging in size from micron-scale fines to chunks of up to 12 centimeters in diameter [Gysling, 2004]. To reduce the high viscosity of bitumen, heat is applied to the oilsand slurries. Air is also introduced into the slurry, usually on the order of 5% by volume [Lipsett, 2009]. Turbulent mixing causes bitumen droplets to bind with air bubbles, allowing them to float to the free surface and form a froth. Froth formation is an important step in the successful recovery of bitumen. Some operators may add sodium hydroxide to facilitate liberation of bitumen from the oil sand through surfactant action. Enroute to the extraction plant, the combined effects of turbulent mixing and elevated temperatures cause lumps to be broken up ("digested") and bitumen to be liberated from the oilsand matrix. The processes of lump digestion, bitumen liberation, and froth formation are collectively known as conditioning [Lipsett, 2009].

Once the slurry reaches the extraction plant, bitumen froth is extracted in settling vessels and floatation cells, commonly using a variation of the Clark Hot Water Process. Finally, the remaining water, fines, and solids are pumped out to tailings ponds, where the solids settle over time. Much of the water from these ponds is recycled back into the hydrotransport process; figures of 80-95% are common [Alberta Environment and Water]. Bitumen undergoes upgrading to produce a usable form of crude oil which may be further refined into petroleum products.

1.2 Pipe Wear

High slurry density is desirable for overall lower water usage, better conditioning, and higher production rates. To prevent deposition and eventual pipe blockage, oilsand slurry is typically pumped at elevated rates on the order of 4-5 m/s [Gysling, 2004]. This operating strategy necessitates high pump output head. The scouring action of the slurry solids results in accelerated wear rates to the pipes and pumps [Roco *et al.*, 1987].

Oilsand hydrotransport pipes wear by several mechanisms, listed below.

- At typical slurry bulk velocities, an estimated 40-55% of the solid particles settle to form a dense, moving bed supported by the lower pipe surface. The sliding action of the solids bed inflicts erosive damage.
- The remaining solids are suspended by turbulence and particle lift forces in the flow region above the dense bed. Turbulent eddies cause particles to impinge against the pipe wall, resulting in impact damage.
- Caustic additives may corrode internal pipe surfaces. It has been observed that the damage resulting from simultaneous chemical and mechanical wear processes is not necessarily additive in nature. In some cases the net damage is greater than the sum total of each acting individually. This is known as erosion-corrosion, and is well documented [Neville *et al.*, 2007], although the phenomenon itself is not fully understood.

In spite of ongoing research, pipeline wear continues to be a serious problem in hydrotransport applications. One estimate of losses due to wear was on the order of \$450 million annually for one oilsands producer [Mochinaga *et al.*, 2006].

1.3 Motivation and Objectives of the Thesis

If left unchecked, eventually aggressive wearing leads to pipe rupture. To avoid this scenario, oilsands producers employ conservative pipe maintenance schedules. Standard practice is to rotate a section of pipe after a specified number of service hours, and to replace it after an additional duration of service

[Schaan *et al.*, 2007]. This practice is not based on the actual wear life of the pipe, but on conservative (low) estimates. Pipe sections are replaced well before the end of their useful lives. Consequently, this maintenance strategy results in both material and financial waste.

To help reduce maintenance and material costs, a damage model is needed which will predict the lifetime of a length of pipe. Numerous flow parameters affect the wear life of a section of pipe, including bulk solids concentration, mass flow rate, particle size and angularity, carrier fluid alkalinity, and others. These factors are time-variant due to variability of feedstock and process conditions. To be successful, this model should make predictions based on constant and time-varying parameters. It also needs the ability to predict both magnitude and location of the accumulated damage. Such a model would allow a trained operator to make predictions of the pipe's remaining useful life, thereby improving maintenance scheduling. Extensive work has been done towards modeling slurry flow regimes, but comparatively little effort has been expended on predictive wear modeling. The objective of this thesis is to build a framework for such a predictive model. Specifically, the contributions of velocity and solids concentration to pipe wear are investigated, and formulations are developed to link wear rate with flow parameters. Finally, proof of concept methods are developed for observing and modeling mechanisms of damage.

2 Relevant Theory and Review of the Literature

This chapter is divided into three sections. The first describes the physics of slurry pipe flows, and presents a model commonly used in the oilsands industry for this purpose. The second section discusses mechanical wear processes resulting from sliding abrasion and particle impingement. Finally, the third section briefly discusses the stresses and resultant strains experienced by a length of pipe.

2.1 Describing Solid-Liquid Slurry Flows in Pipes

The physics of simple pipe flows involving only a single liquid phase (i.e. water) have been well documented and modeled since the 1800s. In comparison, only recently have the physics of multiphase flows been successfully modeled. Since the pioneering work in the 1950s of Durand & Condolios in France and Newitt in Britain [Abulnaga, 2002], much of the interest in these flows has been driven by the mining and pulp industries, and more recently by the oilsands industry.

Slurries may be classified as settling or non-settling [Gillies *et al.*, 1991]. These classifiers depend on several factors, including particle size and density, bulk solids concentration, and carrier fluid density and viscosity. Generally, with regards to aqueous slurries, the term “non-settling” refers to slurries containing elevated concentrations of fines [Gillies *et al.*, 1991, 2004]. Fines tend to resist settling and may be distributed more or less homogeneously over the cross-section of the slurry flow [Gillies *et al.*, 1991]. Larger particles will naturally settle out of suspension and come to rest at the lower pipe surface, unless acted on by a substantial lifting force. Durand (1952) defines fines to be those particles “of a diameter inferior to 20 or 30 microns.” The work of Gillies *et al.* (1991, 2000, 2004) and Wilson *et al.* (2009) applies a maximum fines diameter of 74 μm . Since the work of Gillies *et al.* has become an oilsands industry standard, the 74 μm restriction on fines diameter will be applied here for consistency.

Slurries may be further classified as either Newtonian or non-Newtonian. The term ‘Newtonian’ designates a fluid in which shear stress and strain are related linearly by a constant viscosity, independent of time or shear rate. Non-Newtonian fluids may exhibit varying degrees of dependence on shear rate

and/or time (i.e. viscosity is not constant) [Durand, 1952]. Slurries with non-Newtonian carrier fluids and/or high concentrations of fines may exhibit non-Newtonian behaviour [Gillies *et al.*, 2004]. In contrast, slurries with a Newtonian carrier fluid and somewhat coarser particles will normally exhibit Newtonian behaviour. Newtonian behaviour is commonly seen in tailings slurries, which consist of sand, water, and trace petroleum residuals. The presence of bitumen may cause dense oilsand slurries to act in a non-Newtonian fashion. The contribution of these viscous effects on pipe wear is a complete study in itself, and they are neglected here. In order to examine purely mechanical wear, aqueous slurries of coarse sand are used in this thesis work. This results in negligible concentrations of solid fines. These slurries are therefore classified as both settling and Newtonian.

2.1.1 Hydrotransport

Typically, a single oilsand process line may experience an hourly throughput of up to 10000 tons of oilsand ore [Schaan *et al.*, 2000]. To maximize production and minimize water usage, slurry density is maintained at elevated levels (1450-1600 kg/m³ [Gysling, 2004]) during hydrotransport. A typical oilsands operation may utilize more than 90 km of steel pipe [El-Sayed, 2010]. To accommodate the high flow rates, pipe diameters are usually on the order of 700-900 mm. For economic reasons, pipes are commonly constructed of welded carbon steel [Lipsett, 2009]. A hydrotransport system typically consists of three types of pipe section [Lipsett, 2009]:

- Straight sections up to 5 km in length
- Elbows
- Shorter “spools”

There exists a minimum deposition velocity for slurry flows, below which the solids begin to settle. Eventually, if unattended, solids will accumulate at the bottom of the pipe, the moving bed of solids will cease to flow, and pipe blockage will occur. Assuming a sand particle size distribution of 100-400 microns, the minimum deposition velocity is approximately 3 m/s. Oilsand hydrotransport flow velocity is typically well beyond that limit – up to 5.5 m/s [Schaan *et al.*, 2007] – resulting in flow with a dense moving bed and a turbulent fluid layer of water, bitumen, fines, and air bubbles. Small rocks may also be

present, which are typically not included in slurry calculations [Lipsett, 2009]. The slurry may also contain quantities of naturally-occurring calcium and magnesium salts, as well as significant amounts of sodium [Lipsett, 2009]. In the presence of the steel pipe, these may create electrochemical potentials, which contribute to corrosion.

2.1.2 Mechanics of Slurry Flow

Solid-liquid slurry flow in a horizontal pipe can be described under one of four distinct flow regimes, listed below [Abulnaga, 2002].

1. Flow with a stationary bed
2. Flow with a moving bed
3. Fully-suspended, heterogeneous flow
4. Fully-suspended, symmetric (pseudo-homogeneous) flow

In a horizontal slurry pipeline with contents at rest, solids settle completely to the lower surface of the pipe, and their submerged weight is completely supported by the normal reaction of the pipe wall [Roco *et al.*, 1987]. Shook *et al.* (1991) use the term 'contact load' to describe these solids. The introduction of an axial pressure gradient along the pipe creates shear stresses, which set the liquid phase into motion. Flow regime #1 occurs at low velocities. As the velocity of the liquid phase is increased, fluid momentum and viscous effects induce motion of the solid particles. Initially the surface particles move with a tumbling, sliding motion. As the surface particles slide and tumble over each other, a portion of their momentum is transferred to underlying particles through impacts and sliding friction. With sufficient velocity, the entire mass of solids begins to slide along the lower surface of the pipe. In this state (flow regime #2), there exists a velocity gradient between the upper and lower surfaces of the solids bed. The lowest velocities are naturally found near the lower pipe wall, where sliding friction retards the motion of the bed. Upper-region particles may be borne up into the fluid stream by turbulent diffusion and dispersion stresses [Roco *et al.*, 1987]. It is common for these particles to migrate upwards or downwards within the fluid layer, in a bouncing motion. This is known as 'saltation.' As particles become suspended in the flow, some of the submerged solids weight acting on the lower pipe wall is relieved [Roco *et al.*, 1987]. Shook *et al.* (1991) use the term 'suspended load' to refer to solids

borne up by the flow in this fashion. As velocity increases, so does the fraction of suspended solids. With sufficient velocity, all of the particles may be suspended in the flow, resulting in flow regime #3. At this point, however, the effect of particle weight is not completely overcome, and particles tend to be more heavily concentrated in the lower regions of the flow. At sufficiently elevated velocities the particles may become uniformly distributed across the flow, resulting in flow regime #4.

Several factors affect the velocity ranges over which these four flow regimes occur, the principal ones being particle density, particle size, and bulk solids concentration [Abulnaga, 2002]. In general, as velocity increases, a given slurry will advance more quickly through the flow regimes if it consists of any or all of the following:

- lower density particles
- smaller particles
- lower bulk solids concentration

Four standard velocities associated with the previously-mentioned flow regimes are defined below [Abulnaga, 2002]. These have been designated unique symbols to avoid confusion with other variables used here.

- V_0 : The velocity at or above which the flow exhibits a stationary solids bed formation. Some particles in the upper region of the solids bed may move with the fluid flow or experience saltation. The stationary bed effectively reduces the cross-sectional area of the pipe through which flow may occur. Due to this constricted flow, head losses (and consequently, energy consumption) are high in this regime. As velocity increases beyond V_0 and solids begin to be entrained in the flow, head losses begin to decrease.
- V_b : The velocity at or above which the slurry flows with a moving solids bed formation, with or without saltation. Head losses continue to decrease up to the point at which all solids are suspended by the flow.
- V_d : The velocity at or above which the saltating bed flow transitions into a fully-suspended flow with solids distributed heterogeneously. This velocity is also known as the deposition velocity. Beyond this point, head losses show a rapid increase.
- V_h : The velocity at or above which all solids are homogeneously distributed with respect to height above the lower pipe surface.

The most useful of these transitional velocities, especially from an industrial standpoint, is the deposition velocity V_d . Since it is the point at which head losses are generally at a minimum, it is considered to be the lower velocity limit for hydrotransport applications. Newitt *et al.* (1955) calculated this velocity as a simple linear function of the particle's terminal settling velocity [described in Abulnaga, 2002]. Durand *et al.* (1952) chose to use a variable known as the "Durand factor" for the coefficient of the terminal settling velocity. This approach has been refined by later researchers. Others, such as Wilson (1976), developed equations based on the particle drag coefficient [described in Abulnaga, 2002].

In the work of Schaan *et al.* (2000), aqueous slurries with 1 mm Bakelite particles were flowed through a pipe of 104.7 mm internal diameter. These experiments revealed that at velocities above approximately 3 m/s, the local solids concentration in the moving bed increased (to a point) with distance from the pipe wall.

2.1.3 The SRC Two-Layer Flow Model

In order to model multiphase flow at a large-scale level with some accuracy while still keeping the physics at a manageable level, assumptions must be made with some care. Several models have been used with varying degrees of success throughout the past decades. Wilson (1970) developed a two-layer model which defined slurry flow as being stratified into two distinct layers, each having its own velocity [described in Gillies *et al.*, 1991]. The lower layer consists of a moving bed of solids, while the upper layer consists only of carrier fluid. Suspended solids – as well as the turbulence which supports them – are essentially ignored. The submerged weight of bed-layer solids is assumed to be supported entirely by the wall.

In 1991, Gillies *et al.* presented an improved two-layer model, valid for mixtures of up to 30-35 vol% solids. This model – which has become known as the Saskatchewan Research Council (SRC) Model – utilizes a simplified analysis of the wall friction mechanisms, in which two important parameters arise: coefficient of particle-wall friction, and carrier fluid rheology (mainly due to the presence of fines, assumed to be particles of size 74 microns or less). Contrary to the original Wilson model, this model assumes a uniform concentration of solids across the

upper layer. Continued experimentation has led to modifications to the original model. The version described and used here is the one presented in Gillies *et al.* (2004) and Wilson *et al.* (2009).

Slurry flow in an equilibrium state is modeled by conceptually dividing it into two distinct layers. The lower layer is defined by a moving bed of contact-load solids, along with interstitial carrier fluid. The maximum solids concentration (due to packing) is assumed to be approximately 60 vol%. In practice, the concentration value of the lower layer is the value measured at a point located a distance of 15% of the pipe diameter above the lower pipe surface [Gillies *et al.*, 2004]. The geometrical concepts of the model are represented in Figure 1. Subscripts 1 and 2 denote quantities relating to the upper and lower layers, respectively. The upper layer consists of suspended-load solids distributed homogeneously through carrier fluid. The layers are separated by an interface of zero thickness and length S_{12} . In reality, this step change in velocity and concentration does not exist; transition is continuous. To simplify calculations, slip is assumed between the upper and lower layers. S_1 and S_2 denote pipe interfacial lengths of the upper and lower layers, respectively. The model assumes no gaseous phase, while in practice up to 5 vol% of an oilsands slurry mixture may be air, in order to promote the formation of bitumen froth [Lipsett, 2009]. The velocity and bulk solids concentration of each layer are distinct, and each quantity is assumed constant across the layer (i.e. no slip between solid and liquid phases). Due to the difference in velocity, the layers experience a shear stress at the interface. Bulk solids concentration in the lower and upper layers is represented symbolically by the variables C_2 and C_1 , respectively. Velocity in those layers is represented respectively by V_2 and V_1 .

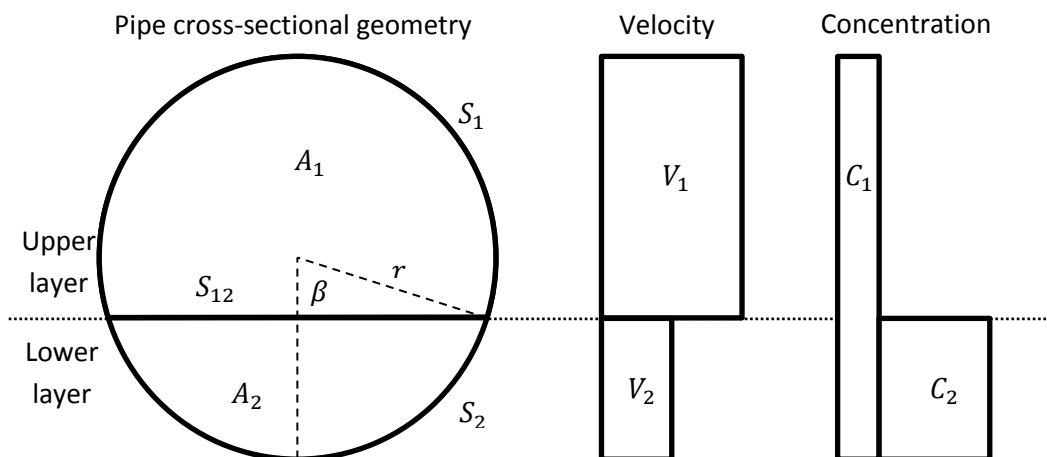


Figure 1 - Graphical representation of the SRC Two-Layer Model [Gillies *et al.*, 1991]

The equations for this model are provided below, with explanations to follow [Gillies *et al.*, 1991, 2000, 2004] [Wilson *et al.*, 2009].

The concentration of coarse solids is given by:

$$C_r = \frac{A_2(A_1C_1 + A_2C_2)}{A} = C_1 + C_c \quad (1)$$

The total concentration of coarse and fine solids is given by:

$$C_t = C_r + C_f \quad (2)$$

The solids concentration of the lower layer, including suspended and bed solids, is given by:

$$C_{\text{lim}} = C_1 + C_2 \quad (3)$$

The contact concentration is found from:

$$C_2A_2 = C_cA \quad (4)$$

Volume and mass continuity are defined by:

$$AV = A_1V_1 + A_2V_2 \quad (5)$$

$$C_vAV = C_1AV + C_2A_2V_2 + F_f \quad (6)$$

The following experimental derivations define the proportion of lower-layer solids and contact solids, respectively:

$$\frac{C_{\text{max}} - C_{\text{lim}}}{C_{\text{max}} - C_r} = 0.074 \left(\frac{V}{V_{\infty}} \right)^{0.44} (1 - C_r)^{0.189} \quad (7)$$

$$\frac{C_c}{C_r} = e^{-0.0097 \left[\left(\frac{V}{V_{\infty}} \right)^{0.864} \text{Re}^{0.193} \text{Fr}^{-0.292} \right]} \quad (8)$$

The experimental Reynolds and Froude numbers are defined as follows:

$$\text{Re} = \frac{DV\rho_m}{\mu_f(1 + 0.21\lambda^2)} \text{ or } 120000, \text{ whichever is less} \quad (9)$$

$$\text{Fr} = \frac{V}{\sqrt{gD(\text{SG} - 1)}} \text{ or } 3.0, \text{ whichever is less} \quad (10)$$

The following equations define the experimental parameters for dimensionless concentration and dimensionless particle diameter:

$$\lambda = \left[\left(\frac{C_{\max}}{C_r} \right)^{1/3} - 1 \right]^{-1} \quad (11)$$

$$d^+ = \frac{d\rho_f V \sqrt{\frac{f_f}{8}}}{\mu_f} \quad (12)$$

Two friction factors are defined to differentiate between slurry hydraulic friction and fluid hydraulic friction:

$$f_{sl} = \lambda^{1.25} \left(0.00005 + 0.00033e^{-0.10d^+} \right) \quad (13)$$

$$f_f = \frac{0.25}{\log_{10} \left[\frac{\varepsilon/D}{3.7} + \frac{5.74}{\text{Re}_f^{0.9}} \right]^2} \quad (14)$$

Boundary layer thickness and its effects on the coefficient of Coulombic friction are determined by:

$$\delta = \frac{5\mu_f}{\rho_f V \sqrt{\frac{f_f}{2}}} \quad (15)$$

$$\zeta = 2 \left(1 - \frac{\delta}{d} \right), 0.1 < \zeta < 1 \quad (16)$$

$$\eta_s = \eta_{s0} \zeta \quad (17)$$

The half-angle which subtends the lower layer is found iteratively from:

$$A_2 = \frac{1}{2} D^2 (\beta - \sin \beta \cos \beta) \quad (18)$$

The delivery rate of fines is found from:

$$F_f = C_f \frac{(1 - C_1)A_1V_1 + (1 - C_{\text{lim}})A_2V_2}{1 - C_r} \quad (19)$$

The hydraulic pressure gradient is found from the summation of forces acting on the upper and lower layers, respectively:

$$i\rho_L g = \frac{\tau_1 S_1 + \tau_{12} S_{12}}{A_1} \quad (20)$$

$$i\rho_L g = \frac{-\tau_{12} S_{12} + \tau_2 S_2 + F_2}{A_2} \quad (21)$$

The Coulombic friction force is found from:

$$F_2 = \frac{0.5\eta_s D^2 g C_2 (1 - C_{\text{lim}})(\rho_s - \rho_L)(\sin \beta - \beta \cos \beta)}{(1 - C_2)} \quad (22)$$

The hydraulic friction (shear) stresses per unit length of pipe are found from:

$$\tau_1 = \frac{V_1 |V_1|}{2} (f_1 \rho_1 + f_{sl} \rho_s) \quad (23)$$

$$\tau_2 = \frac{V_2 |V_2|}{2} (f_2 \rho_{2f} + f_{sl} \rho_s) \quad (24)$$

The interfacial shear stress per unit length of pipe is found from

$$\tau_{12} = 0.5 f_{12} (V_1 - V_2) |V_1 - V_2| \rho_1 \quad (25)$$

$$f_{12} = \frac{(1 + 2Y)}{\left[4 \log_{10} \left(\frac{D}{d_{12}} \right) + 3.36 \right]^2} \quad (26)$$

$$Y = \begin{cases} 5 + 1.86 \log_{10} \left(\frac{d_{12}}{D} \right) & \left(\frac{d_{12}}{D} \right) \geq 0.002 \\ 0 & \left(\frac{d_{12}}{D} \right) < 0.002 \end{cases} \quad (27)$$

The terminal settling velocity is determined by:

$$V_{\infty} = \sqrt{\frac{4gd_{50}(\rho_s - \rho_f)}{3C_D\rho_f}} \quad (28)$$

The Fanning friction factors f_1 and f_2 are calculated by the method of Churchill (1977), which is valid for both turbulent and laminar flows. The first step is to calculate the hydraulic diameter of each layer:

$$D_{H1} = \frac{4A_1}{S_1 + S_{12}} \quad (29)$$

$$D_{H2} = \frac{4A_2}{S_2 + S_{12}} \quad (30)$$

Next, the following parameters are calculated separately for each layer:

$$\text{Re} = \frac{\rho V D_H}{\mu} \quad (31)$$

$$A = \left\{ 2.457 \ln \left[\left(\frac{7}{\text{Re}} \right)^{0.9} + 0.27 \frac{\varepsilon}{D} \right]^{-1} \right\}^{16} \quad (32)$$

$$B = \left(\frac{37530}{\text{Re}} \right)^{16} \quad (33)$$

$$f = 2 \left[\left(\frac{8}{\text{Re}} \right)^{12} + (A + B)^{-1.5} \right]^{1/12} \quad (34)$$

The Two-Layer Model of Gillies *et al.* has been widely adapted as an industry standard by oilsands producers. Its conceptual simplicity, accuracy, and relative ease of application make it ideal for predicting flow parameters in a variety of conditions. It is widely used for predicting flow velocities and axial pressure gradient, both useful quantities from a flow control perspective. Where it falls short, however, is in its ability to model turbulent flow patterns which may lead to accelerated wear (discussed further in a later section).

2.1.4 Shear Interface Layer

As may be noted from the schematic in Figure 1, a key assumption of the SRC Two-Layer model is that both concentration and velocity experience a step change at a particular height above the lower pipe surface. At this location is a thin layer which will be referred to as the shear interface. The two-layer model assumes a zero thickness of the shear interface.

Wilson and his associates [Wilson 1987, 1988; Nnadi & Wilson 1992, 1995; Wilson & Pugh 1988, 1999] completed a large body of research on hydraulic sediment transport in open channels. Since much of the research concerned river flow, only stationary sediment beds were considered. Flows were analyzed using a dimensionless shear stress Y defined in Shields (1936). At bed shear stresses in excess of approximately 0.8, it was noted that bed formations such as dunes and ripples gave way to planar flow of solids at the surface of the bed. This layer of moving solids was termed the “shear layer.” The shear layer consists of carrier fluid and submerged solids. Initially [Wilson 1987] these solids were thought to be only contact-load solids. The depth of the shear zone varies and may be several grain diameters thick. Several key points to note are as follows:

- The concentration profile is essentially linear decreasing with height, with the loose-poured concentration at the bottom and zero at the top.
- The velocity profile is essentially linear increasing with height, and varies proportionally with the shear velocity of the stream.
- Depth of the layer varies proportionally with the bed shear stress.
- Turbulent motion is low due to damping by the solids gradient.
- The step interface described by the SRC Two-Layer model is located within the shear layer. Nnadi & Wilson (1995) place the step interface at half of the depth of the layer.

Nnadi & Wilson (1992) note that for low to moderate stream velocities, the layer may be assumed to have a constant shear stress profile. At elevated stream velocities, the shear layer becomes unstable and turbulent suspension increases, and the constant shear profile assumption is no longer valid. For this condition the authors developed a curvilinear spline equation to approximate the concentration profile across the shear layer, but Wilson (2005) holds to the use

of linear profiles, arguing that alternative profiles provide little additional accuracy (1987, 1988).

Research by Pugh & Wilson (1999) agrees that the shear layer may be several grain diameters thick. This may be seen below in Figure 2, which plots measured local solids concentration at normalized heights (y/D) above the lower pipe surface. Local concentration appears to be constant from $y/D = 0.0$ to $y/D = 0.2$ (stationary bed), changes quickly between $y/D = 0.2$ and $y/D = 0.65$ (shear layer), and is zero from $y/D = 0.65$ to $y/D = 1.0$ (upper layer). There is no step change in concentration here, contrary to the core assumption of the SRC Two-Layer model. Of note is the linearity of the concentration profile across the shear layer.

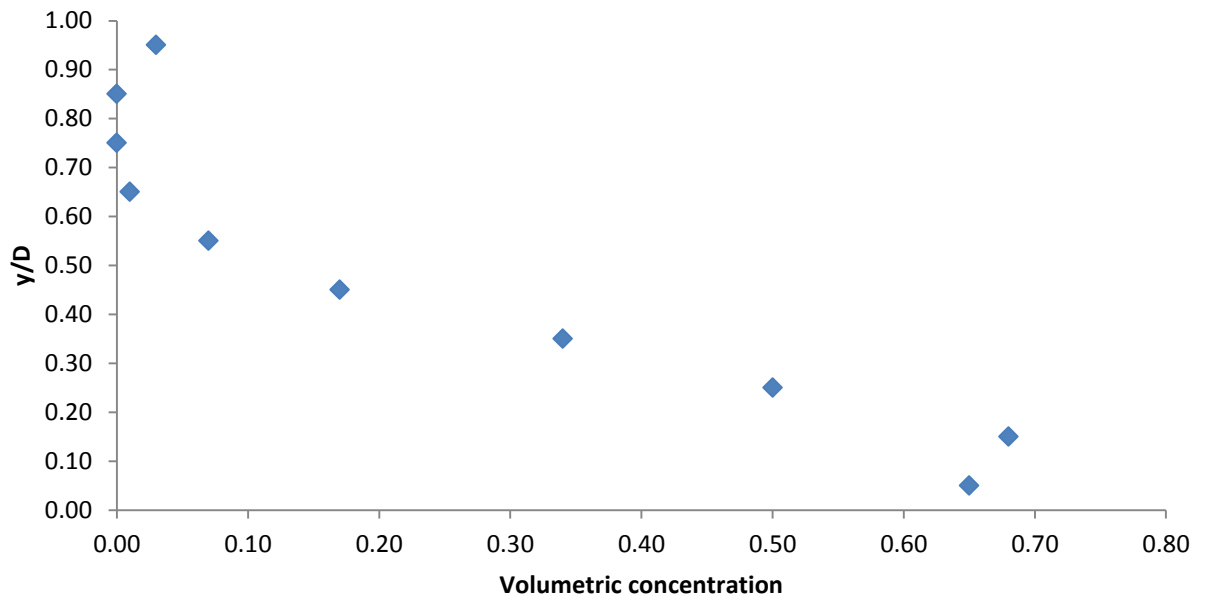


Figure 2 - Concentration profile results [replotted from Pugh & Wilson, 1999]

Shook *et al.* (1982) confirmed experimentally that when solids become suspended by turbulent eddies, their submerged weight is supported by the fluid. This sets up dispersive stresses within the fluid, resulting in an increased pressure gradient vertically across the pipe. The resultant pressure difference is equal to the pressure difference across an equal height of water, plus the submerged weight of the suspended solids.

Wilson & Pugh (1988) researched the effect of dispersive stresses on concentration profiles. They noted that in the shear zone, solids may be supported by both turbulent dispersion and solid-solid contact. Applying this concept mathematically, the authors developed a computer model to predict concentration profiles based on particle size. Cases of $d = 0.1$ mm, $d = 0.2$ mm, $d = 0.5$ mm, and $d > 1.0$ mm were plotted, and these were noted to be consistent with previously measured profiles. Of particular interest is that for all cases, the thickness of the shear layer remained constant under constant bed shear stress. The concentration profile, however, changed dramatically over the four cases. Larger particles (having high settling velocities) yielded shallow concentration profiles, while finer particles (with low settling velocities) yielded markedly steeper profiles.

Testing by Schaan & Shook (2000) used slurry flow without stationary bed conditions. Their results indicate that the velocity profile is linear in the shear zone (see Figure 3). The figure shows local velocity with respect to normalized height above the lower pipe surface (y/D). Results at mean velocities of 2.5 m/s and 4.5 m/s are displayed side by side for comparison. With minor exceptions, the velocity profile retains its shape over the experimental velocity range. The main point to note from this figure is that as y/D increases, the velocity change is approximately linear, both in the increasing and decreasing phases. As a side note, the velocity profile of the lower layer is somewhat steeper at a mean velocity of 4.5 m/s, which appears to confirm the previous discussion regarding an off-the-wall lifting force.

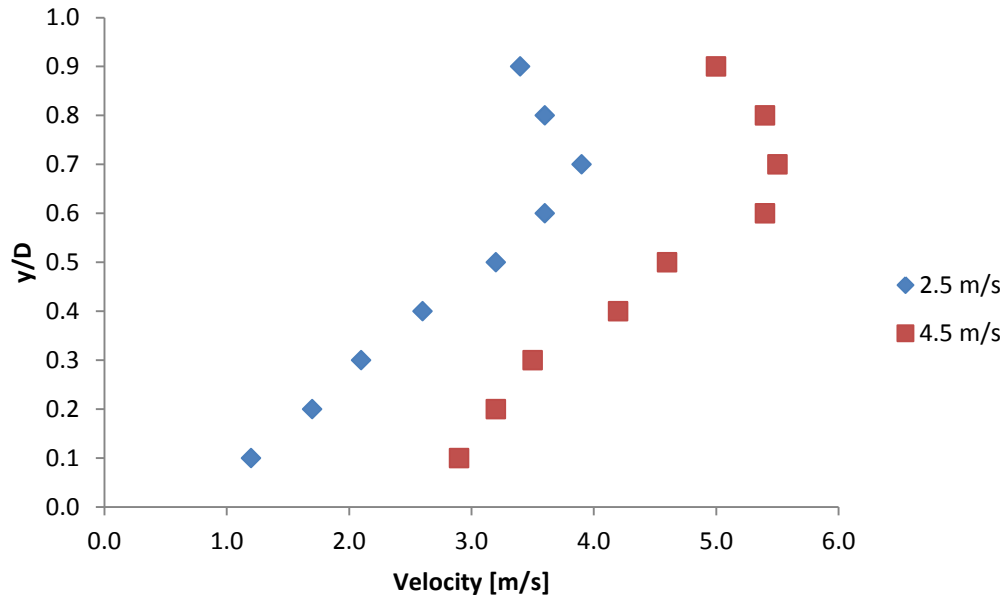


Figure 3 - Velocity profile results [replotted from Schaan & Shook, 2000]

In conclusion, experimental evidence points to the existence of a thick shear interface layer between the upper and lower slurry flow layers. The velocity and concentration profiles across the layer appear to vary in an approximately linear fashion with height. The depth of the layer varies proportionally to the shear velocity of the stream flow, and the upper velocity of the layer is a linear function of the bed shear stress. The step interface described in the SRC Two-Layer model lies within the shear layer. Nearly all of the available literature on the shear layer discusses it in the context of a stationary sediment bed. It is anticipated that this same shear layer – or a similar transitional layer – may also exist under slurry flow conditions other than stationary bed flow. One of the objectives of this thesis work is to determine whether such a layer exists under non-bed-flow conditions, and to characterize its concentration and velocity profiles.

2.2 Wear

Since the mechanism of slurry pipe wear is highly complex, wear in an industrial application (i.e. oilsands facility) is currently calculated as a linear function of usage time. This assumes solely equilibrium (fully-developed) flow conditions

and requires that limitations be placed on several flow parameters. As a result, these relations only serve as a rough guideline.

It is important to note that the Two-Layer model only describes large-scale flow mechanics and the resulting shear stresses. No information is given regarding wear processes acting on the pipe. This information must be obtained from external models. Several existing wear models are examined in this section to provide a framework for constructing a unified slurry pipe wear model.

Wear in slurry pipes is affected by the following factors [BHRA Fluid Engineering, 1980]:

- **Velocity.** Increased bulk velocity generally results in accelerated wear rates. This is due to higher impact velocities and increased rates of sliding abrasion. As shown later, this is also due to increased mass flux of particles, leading to higher rates of impact [Oka, 2004].
- **Concentration.** Up to a point, the probability of particle-wall impact increases with increasing solids concentration. Beyond that point, inter-particle impacts tend to reduce the probability of particle-wall impacts. Increased concentration also increases the weight of the moving solids bed, leading to accelerated wear due to sliding abrasion.
- **Slurry flow regime.** The flow regime (i.e. stationary bed flow, moving bed flow, heterogeneously suspended flow, and pseudo-homogeneously suspended flow) affects both particle dispersion and particle motion. This is especially true of moving bed flow and heterogeneously suspended flow conditions, as the concentration gradients result in higher wear rates near the bottom of the pipe. Note that because of slurry properties, “regime” is not simply defined by velocity or Reynolds number.
- **Impact angle.** Higher-angle particle-wall impacts (angles measured from the surface, 90° = normal) generally result in increased levels of plastic deformation wear, while cutting wear dominates at lower angles of impact. This is a key factor in solid particle erosion, and has been documented by several authors [Finnie, 1960] [Bitter, 1962] [Oka, 2004] [Kosel, 1992].
- **Particle size.** The size of a particle affects sliding-abrasive wear but not impact wear. Coarse particles tend to settle more quickly than fine

particles, resulting in a sliding bed formation. Fine particles (approximately 60 μm or smaller) cause little wear.

- **Particle density.** Dense particles settle quickly compared with those of lower density. Because of their higher settling velocity, denser particles are associated more with abrasive wear, and less with impact wear. The reverse is also true.
- **Particle angularity** (known as 'aspect ratio' in certain literature). In general, higher particle angularity allows for deeper surface penetration, leading to accelerated cutting wear rates.
- **Particle hardness.** A particle's hardness relative to that of the pipe wall is an indicator of its wearing ability, especially with regards to cutting wear. Harder particles experience lessened rates of degradation. Degraded (rounded) particles generally cannot wear as effectively against the pipe wall. This is also directly related to particle angularity.
- **Pipe material.** Harder materials are more susceptible to impact wear. Ductile materials are more susceptible to sliding abrasion (cutting) wear.
- **Pipe geometry.** Bends, tees, valves, reducers, and other locations involving a change in pipe geometry are all susceptible to elevated levels of wear. This is due to particle momentum as well as changes in particle dispersion, which can result in increased levels of particle-wall impacts.

2.2.1 Friction and Particle Lifting Forces

In the operations of a slurry pipeline, hydraulic gradient (friction or head losses per unit length) is a key parameter. Two components of head losses have been documented for slurry flow: Coulombic friction and hydraulic friction (Gillies *et al.*, 1991). Coulombic (velocity-independent) friction is produced by the sliding motion of solids along the pipe wall. This occurs predominantly in the solids bed region and may be ignored in the upper region where particles are fully suspended. Hydraulic (velocity-dependent) friction depends heavily on slurry viscosity and the square of velocity. This occurs in varying intensities across the entire inner pipe surface. Of the two forms of friction, only Coulombic friction is a contributor to pipe wear.

Schaan *et al.* (2000) noted that while slurry density exhibits a linear response to increases in particle concentration, friction with the pipe wall does not. The Coulombic component of friction responds in a markedly non-linear fashion.

Wilson *et al.* (2003) and Schaan *et al.* (2000) reported that a lifting force similar to the Magnus effect is produced by particles near the pipe walls. This lift force acts to repel particles from the walls, and its effects become more pronounced at higher velocities and on larger particles. This lift force is highly dependent on the velocity gradient across the pipe cross section (i.e. the shape of the velocity profile). It occurs in a viscous boundary layer at the pipe wall and is related to the thickness of that layer. As velocity increases, the thickness of the boundary layer increases, as does the effect of the lift force. At sufficiently high velocities, particles near the lower pipe surface appear to be repelled from the pipe walls, causing the hydraulic gradient to approach that of the carrier fluid alone.

Based on these results, it is expected that particle-wall (Coulombic) friction is high at low velocities where particles experience minimal lifting force. As velocity increases and the bed cross-section diminishes, Coulombic friction also diminishes. Conversely, hydraulic friction increases dramatically at elevated velocities. At the deposition velocity V_d , the sum of both forms of friction (i.e. total head losses) is at a minimum [Abulnaga, 2002].

2.2.2 Slurry Pipe Wear Profiles in Service

Schaan *et al.* (2007) obtained wear data from several locations at Syncrude's Aurora Mine as part of a pipe wear research work. A commercially available ultrasonic-B scanner was used to measure wall thicknesses at many locations around the pipe's circumference. This was repeated at several pipe locations, including hydrotransport lines and coarse tailings lines. Oilsand hydrotransport lines commonly exhibited a trough-like wear profile, with the highest wear rates occurring at a point 180° from the vertical. Typical wear rate profiles are given in Figure 4 below. These wear rate profiles were observed at different times at the same location on an inclined, straight hydrotransport line. It may be noted that wear rate itself appears to increase with time. The authors attribute this phenomenon to a change in grade of oilsand ore (from 11% to 12% bitumen by mass), which resulted in a decrease in suspended fines and an increase in particle size. Whether chemical effects played a role is unknown. However, the

authors note that the change in oilsand ore resulted in an order of magnitude increase in the contact load solids fraction C_c .

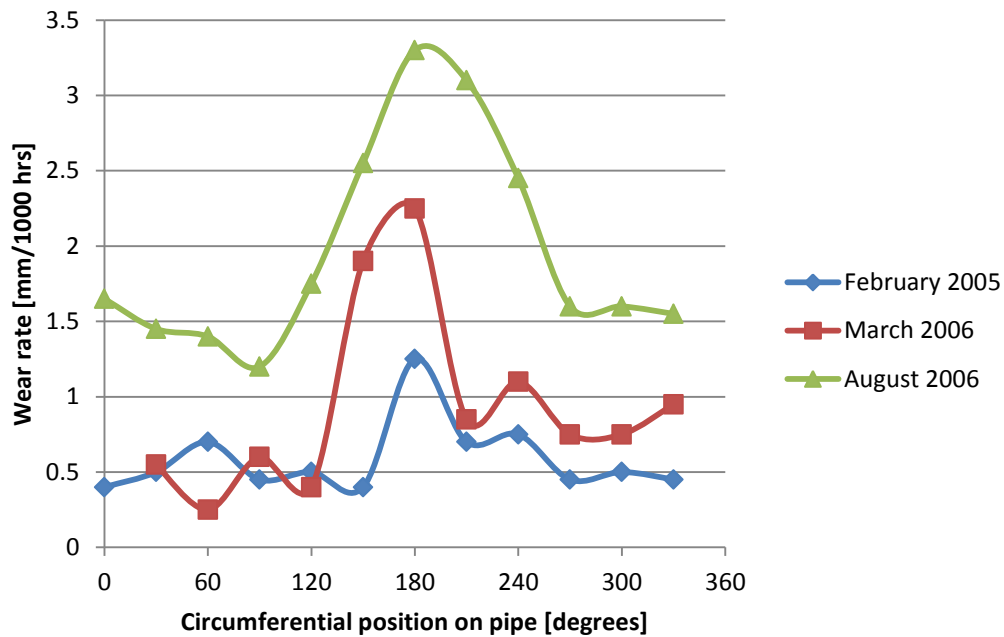
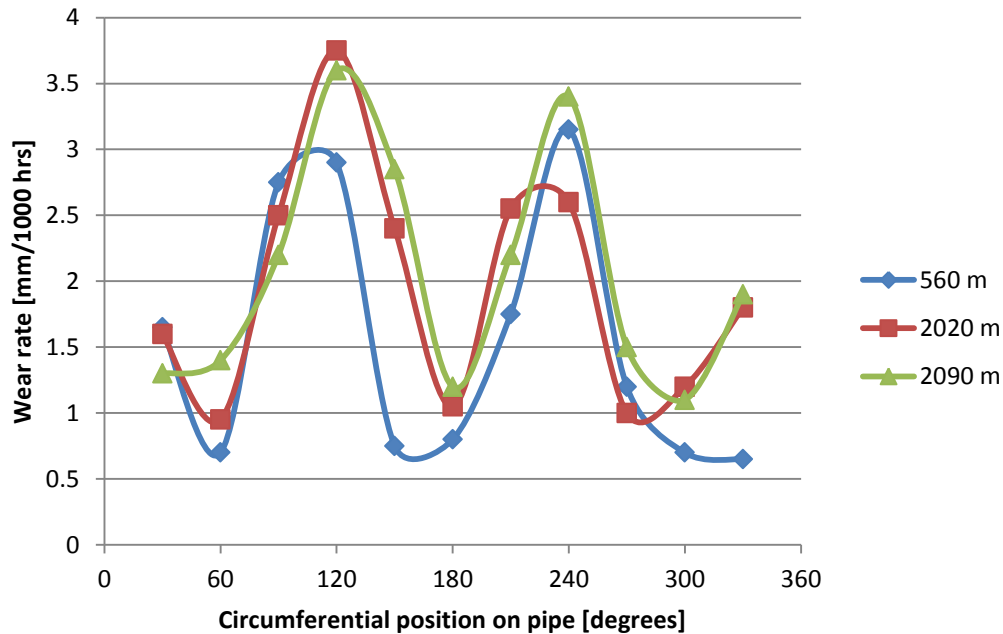


Figure 4 - Typical wear profiles in a straight, inclined oilsands hydrotransport line (data points are interpolated using splines) [replotted from Schaan *et al.*, 2007]

Schaan *et al.* also observed the wear profiles of coarse tailings pipes. It was discovered, as shown below in Figure 5, that the maximum wear consistently occurred at points on the pipe wall close to 120° and 240° from the vertical. In these cases, the velocity of the tailings slurry was given to be approximately 4 m/s. The authors attribute this unusual wear profile to the presence of a stationary solids bed in the pipe.



**Figure 5 - Typical wear profile occurring in coarse tailings lines (data points interpolated using splines)
[replotted from Schaan *et al.*, 2007]**

This research raises questions. How is maximum wear occurring at or below the top of a stationary bed formation? What secondary flows or other phenomena could be causing solids to wear against the pipe wall in these locations? Could this unusual wear profile be explained by the presence of a thick shear interface at the surface of the stationary bed?

It is postulated that the shear interface layer is responsible for the unusual wear patterns observed in the field. Assuming a completely stationary bed, a high bulk velocity would create a strong axial flow through the reduced cross-section area of the upper layer. In turn, this flow would entrain solid particles, inducing significant particle motion near the top of the bed due to turbulence and shear forces. Hence, a shear interface layer would be present, regardless of the stationary bed. Due to the strong particle flux in the shear interface, it is expected that impingement dominates the wear processes in this region. Minimal wear would occur at points beneath the bed, while maximum wear would occur at points at the surface of the bed. It is the intent of this thesis to explore this phenomenon in further depth.

2.2.3 Sliding Erosion

Roco *et al.* (1987) applied a numerical approach to modeling abrasive wear due to a sliding solids bed. This approach is based on a simple correlation of wear as a function of the energy interaction between particles and the pipe wall. The underlying assumption is that there exists a threshold energy point for the wall material, in excess of which wear may occur. This assumption has also been documented by other authors, including Bitter (1962) and Finnie (1960). Wear occurs due to the transmission of kinetic energy from particles to the pipe wall. Wear rate is described mathematically by the following relation:

$$\dot{D} = \varphi [\dot{E}_k - \dot{E}_{k0}] \quad (35)$$

This approach may be applied to impact, sliding abrasion, and random impact wear. In the work of El-Sayed *et al.* (2009), this method was adapted to describe sliding abrasive wear as a function of shear stress and velocity. The Roco equation was rearranged to describe damage rate (i.e. material loss) per unit area occurring over the arc S_2 , as follows:

$$\dot{D} = \varphi V [\tau_{avg} - \tau_0] \quad (36)$$

Note that the threshold kinetic energy has been effectively replaced by a threshold shear stress. This approach follows the assumption that abrasive wear in a slurry pipe is purely due to:

- Velocity of the lower layer (e.g. moving bed formation)
- Shear stresses due to Coulombic friction between moving particles and the pipe wall (impact wear is neglected)

This somewhat simplified approach assumes that system properties such as particle size or angularity are handled by the proportionality constant φ . The principal difficulty is that values of τ_0 and φ must be determined experimentally for each material. Another challenge is that local velocity in the region of the lower pipe wall is difficult to measure.

2.2.4 Solid Particle Erosion

In a fluid-solid system involving the motion of a bed, there exist two principal types of mechanical wear: deformation due to the cutting or plowing action of particles on the solid surface, and plastic deformation from repeated collisions, which results in a volume of material being removed from the solid surface [Bhushan, 2011]. These interactions between particles and the solid surface are known as erosion. The trajectory angle at which a particle strikes the surface is known as the angle of impingement. This angle is measured from the surface, relative to a vector normal to the surface. A particular material's response to erosive attack varies with its mechanical properties as well as the angle of impingement [Oka *et al.*, 2004]. For example, ductile steels tend to be more prone to wear from low-angle impingement, while brittle steels are more prone to wear from high-angle impingement. Finnie (1960) noted that the wear rate peaked at $\theta = 25^\circ$ for 1055 steel in the ferrite + pearlite condition, and at $\theta = 90^\circ$ for the same steel in the martensitic condition.

A sphere striking a flat surface at a high impingement angle under perfectly elastic conditions produces a crater-shaped deformation at the surface [Bitter, 1962]. The depth of this crater is a function of the kinetic energy of the impinging particle, as well as the elastic modulus of each material. In an ideal case, this kinetic energy is converted to potential energy in the form of deformation to the particle and the surface. In practice, some energy may be lost in the form of heat. Stresses are set up below the surface, the maximum occurring in the center of the crater, just below the surface at a distance of approximately half of the radius of the deformed region [Bitter, 1962]. If the impingement velocity is sufficiently low, the impact will be purely elastic and the material surface will undergo complete restoration immediately following the impact. If, however, the impact velocity is increased sufficiently, the maximum stress achieved will surpass the yield strength of the material, causing the surface to undergo a combination of both elastic and plastic deformation. Again, the elastic portion of the deformation will be restored following the impact; the plastic portion will not be restored.

Plastic deformation increases the elastic limit of the material through the process of strain hardening [Bitter, 1962]. Successive plastic deformations cause the surface material in the locality of the impacts to become increasingly more brittle. As strain hardening proceeds, the elastic limit eventually reaches the

strength of the material. At this point, if the material is strained further, it will fail, resulting in removal of a small amount of material in the locality of the impacts. Note that the material failure described above is different from fatigue damage due to cyclic elastic stresses.

At shallow impact angles, the particle impact results in a somewhat lessened elastic/plastic crater-type deformation, due to a decreased normal component of impact velocity [Bitter, 1962]. Instead, the impacting particle penetrates the surface and induces shear stresses in the surface material. If these shear stresses surpass the shear limit of the material, cutting of the surface occurs.

In practice, it is common to find both cratering-type deformation wear and cutting wear occurring simultaneously. At higher angles of impact, deformation will dominate. Conversely, at lower angles of impact, cutting will dominate.

It has been noted [Kosel, 1992] that solid particle erosion tends to follow a power-law relation of the form:

$$\dot{D} = \phi V_p^n \quad (37)$$

The constants ϕ and n in Equation 35 are empirically determined and reflect on the properties of the materials involved, as well as the conditions under which the erosion occurs. The value of n varies from material to material. n is commonly in the range of 2.0-2.5 for steels and 2.5-3.0 for ceramics, though values outside these ranges have also been observed [Kosel, 1992].

One issue with calculating impingement erosion is that particle velocity and direction are usually not those of the stream velocity [Finnie, 1960]. Particle velocity relative to the stream is difficult to determine. Within the stream, individual particles may move at widely varying velocities. For this reason, the influence of particle size is unclear.

2.2.5 Finnie's Model for Erosive Wear by Solid Particles

Finnie's wear formulation (1960), applied a mechanistic approach based on the motion equation of an individual particle. It is assumed that the vertical and horizontal components of the net force acting on the particle are constant with respect to each other. Particle rotation is assumed to be negligible during

cutting, and the depth and width of the cut are assumed to be constant. The volume of material (Q) removed by a single particle is given by:

$$Q = \begin{cases} \frac{mV_p^2}{p\psi K_F} \left(\sin 2\theta - \frac{6}{K_F} \sin^2 \theta \right) & \text{for } \tan \theta < \frac{K_F}{6} \\ \frac{mV_p^2}{p\psi K_F} \left(\frac{K_F \cos^2 \theta}{6} \right) & \text{for } \tan \theta \geq \frac{K_F}{6} \end{cases} \quad (38)$$

where

$$K_F = \frac{3C_D \rho_L}{4d\rho_s} \quad (39)$$

K_F is the ratio of vertical-to-horizontal forces acting on the particle

ψ is the ratio of contact depth to cut depth

p is the plastic flow stress reached in the material as it is cut by the particle

Both K_F and ψ are assumed to have a value of 2.

Finnie's model is a simple, elegant solution to describe a complex phenomenon. Part of its attractiveness lies in its ability to describe wear at varying impingement angles.

A drawback of Finnie's model is that it tends to underestimate wear at higher impact angles, and at 90° the wear drops to zero. It is noteworthy that much of the initial theory was developed using pneumatic "slurry" jets impacting at high speed (in the range of >30 m/s). At these speeds, particle rotation is low by comparison and therefore negligible. In industrial hydraulic slurries in pipes, particle rotation may be significant due to a number of factors, including velocity profiles across the pipe. During preliminary testing in this thesis work, rotation was observed consistently. The no-rotation assumption does not appear to be a good assumption for aqueous slurry applications, and the applicability of the model is questionable.

2.2.6 Bitter's Model for Erosive Wear by Solid Particles

Bitter's approach (1962) to modeling erosive wear utilizes the energy absorbed upon particle impact and released thereafter (i.e. kinetic energy losses of the particles during rebound). As in Finnie's work, high-speed pneumatic jets of particles were impinged upon target materials to build the model. The effects of particle size appear to be ignored. Wear is described as the sum total of deformation (W_D) and cutting (W_C) wear, each assumed to be acting independently of the other. Bitter's model introduces a constant K , defined as the threshold velocity above which plastic deformation will occur. Total wear rate may be expressed by the following equation:

$$\dot{D} = \begin{cases} W_D + W_{C1} & \text{for } \theta < \theta_0 \\ W_D + W_{C2} & \text{for } \theta \geq \theta_0 \end{cases} \quad (40)$$

where

$$W_D = \frac{M_p (V_p \sin \theta - K)^2}{2K} \quad (41)$$

$$W_{C1} = \frac{2M_p C (V_p \sin \theta - K)^2}{\sqrt{V_p \sin \theta}} \left[V_p \cos \theta - \frac{C (V_p \sin \theta - K)^2}{\sqrt{V_p \sin \theta}} \rho_p' \right] \quad (42)$$

$$W_{C2} = \frac{M_p [V_p^2 \cos^2 \theta - K_1 (V_p \sin \theta - K)^{3/2}]}{2\gamma} \quad (43)$$

$$C = \frac{0.288}{\sigma_y} \sqrt[4]{\frac{\rho_p'}{\sigma_y}} \quad (44)$$

$$K = \frac{\pi^2}{2\sqrt{10}} \sigma_y^{5/2} \left(\frac{1}{\rho_p'} \right)^{1/2} \left[\frac{1-\nu_1^2}{E_1} + \frac{1-\nu_2^2}{E_2} \right]^2 \quad (45)$$

$$K_1 = 0.82 \sigma_y^2 \sqrt[4]{\frac{\sigma_y}{\rho_p'}} \left[\frac{1-\nu_1^2}{E_1} + \frac{1-\nu_2^2}{E_2} \right]^2 \quad (46)$$

θ_0 is defined as "the impact angle at which the horizontal velocity of the particle has just become zero when the particle leaves the body."

The symbols κ and γ are deformation and cutting wear factors, respectively. This set of equations assumes a constant elastic load limit. Rather than deal with a changing elastic limit due to strain hardening, the value of σ_y is assumed to be the maximum elastic load limit for the particular material.

The chief drawback to Bitter's approach is the use of the deformation and cutting wear factors. These must be determined experimentally by measuring kinetic energy losses during individual particle collisions with the eroded material. In a hydraulic pipe setting, this approach is exceptionally difficult and impractical for this thesis work.

2.2.7 Oka's Model for Erosive Wear by Solid Particles

The wear model of Oka *et al.* (2005) takes a purely empirical approach, in contrast to the semi-mechanistic approach of Bitter (1962) and Finnie (1960). As in the previously discussed models, pneumatic slurry jets were used in the development of this model. Oka's model goes several steps beyond Bitter's model, taking into account the effects of particle size and the properties of the particle and wall materials. The model contains no reference to a threshold damage velocity. Input values of particle velocity and diameter are referenced against experimental values. Good use is made of the indentation behaviour of the wall, expressed in terms of the Vickers hardness number (Hv). The various constants have been tabulated for numerous materials. The equations are listed below:

$$E(\theta) = g(\theta)E_{90} \quad (47)$$

$$E_{90} = k_0(\text{Hv})^{k_1 b} \left(\frac{V}{V'} \right)^{k_2} \left(\frac{d}{d'} \right)^{k_3} \quad (48)$$

$$g(\theta) = (\sin \theta)^{n_1} (1 + \text{Hv}(1 - \sin \theta))^{n_2} \quad (49)$$

$$n_1 = s_1(\text{Hv})^{q_1} \quad (50)$$

$$n_2 = s_2(\text{Hv})^{q_2} \quad (51)$$

$$k_2 = 2.3(\text{Hv})^{0.038} \quad (52)$$

E_{90} is a measure of the erosive damage due to particle impact at an impingement angle of 90° , and $E(\theta)$ is the damage occurring from particle impact at an arbitrary angle from the normal. Both $E(\theta)$ and E_{90} are given in units of $[\text{mm}^3/\text{kg}]$ (volume of removed material per mass of impinging particles).

For a system of impinging sand particles, the following values were found [Bhushan, 2011]:

$$s_1 = 0.71, s_2 = 2.4, q_1 = 0.14, q_2 = -0.94, k_0 = 64, k_1 = -0.12, k_3 = 0.19$$

$$d' = 326 \text{ } [\mu\text{m}]$$

$$V' = 104 \text{ } [\text{m/s}]$$

This model is both practical and effective. It has been used in other research, including that of Bhushan (2011), which successfully used the model to predict wear rates across the inner surface of a cylindrical slurry mixing tank. It is an excellent candidate for a model to describe impingement wear within slurry pipes.

2.3 Pipe Stresses and Strains

2.3.1 Stress

In a slurry pipeline, pipe sections may undergo significant stresses. It is expected that the following stresses are present:

- **Shear stresses.** These result from friction between moving slurry and the pipe walls. These also arise within the pipe walls from the supported weight of the pipe and the slurry contained within it.
- **Pressure-related stresses.** These include circumferential, axial, and radial stresses which arise from elevated dynamic fluid pressures within the pipe.
- **Thermal stresses.** Thermal expansion may result in axial, radial, and circumferential stresses in the pipe wall.

- **Bending stresses.** These arise from the supported weight of the pipe and the slurry contained within it. They are most pronounced at the outer surface of the pipe, at an axial position midway between pipe supports.

Many of these stresses are dynamic in nature and may result in fatigue loading of the pipe members. Slurry flow-related shear stresses (acting axially along the pipe) have been mentioned earlier during the discussion of the two-layer flow model. Assuming a prismatic circular pipe, weight-induced shear stresses (acting both vertically and axially within the pipe walls) may be found from [Hibbeler, 2005]:

$$\tau = \frac{F_s}{\pi R^2 t} \sqrt{R^2 - y_n^2} \quad (53)$$

The shear force (due to weight) at any location z measured axially from one of the pipe supports may be determined from:

$$F_s(z) = \frac{w_0 L}{2} - w_0 z \quad (54)$$

Bending stresses in pipes act in the axial direction and may be described by:

$$\sigma_B = \frac{M y_n}{I} \quad (55)$$

For a section of pipe supported at both ends, the internal bending moment at any axial position z (referenced from one of the supports) along the pipe is given by:

$$M(z) = \frac{w_0 L}{2} z - \frac{w_0}{2} z^2 - \frac{w_0 L^2}{12} \quad (56)$$

For a pipe of constant cross-section, the area moment of inertia is given by [Hibbeler, 2005]:

$$I = \frac{\pi}{4} (r_o^4 - r_i^4) \quad (57)$$

When subjected to internal pressures – including static and dynamic pressures associated with slurry flow – pipe walls will experience stresses in all directions. The Lamé equations for describing axial, radial, and circumferential pressure-related stresses within cylindrical pipes are as follows, respectively [Budynas *et al.*, 2008]:

$$\sigma_z = \frac{r_i^2 P_i - r_o^2 P_o}{r_o^2 - r_i^2} \quad (58)$$

$$\sigma_r = \frac{r_i^2 P_i - r_o^2 P_o}{r_o^2 - r_i^2} - \frac{r_i^2 r_o^2 (P_i - P_o)}{r^2 (r_o^2 - r_i^2)} \quad (59)$$

$$\sigma_\theta = \frac{r_i^2 P_i - r_o^2 P_o}{r_o^2 - r_i^2} + \frac{r_i^2 r_o^2 (P_i - P_o)}{r^2 (r_o^2 - r_i^2)} \quad (60)$$

In this research, the stresses of primary concern are the shear stresses arising from friction between the pipe wall and the dense, flowing slurry. However, all of the stresses listed above may occur simultaneously. Individual stresses interact and produce large resultant stresses in the pipe material. When these are combined with events such as particle impingement, large resultant stresses may be created. The material yield stress may be quickly achieved, resulting in accelerated wear to the inner pipe surface.

2.3.2 Strain

While it is helpful to understand the stresses experienced by a section of pipe, it is difficult to measure stress directly. What can be measured are the material strains that result from these stresses. The ability to measure strains allows for observability of the process of interest – namely wall shear stress, in this case. One-dimensional strain is related to its corresponding stress by Hooke's Law:

$$\varepsilon = \frac{1}{E} \sigma + \varepsilon_{thermal} \quad (61)$$

In a three-dimensional scenario, combined stresses introduce some complexity. Strain components are calculated using this version of Hooke's Law (numerical subscripts denote orthogonal directions):

$$\varepsilon_1 = \frac{1}{E} [\sigma_1 - \nu(\sigma_2 + \sigma_3)] + \varepsilon_{thermal} \quad (62)$$

To calculate stresses from measured strains, Hooke's Law may be rearranged and written in the following form:

$$\sigma_1 = \frac{E}{1 + \nu} \left[\varepsilon_1 - \varepsilon_{thermal} + \frac{\varepsilon_1 + \varepsilon_2 + \varepsilon_3 - 3\varepsilon_{thermal}}{1 - 2\nu} \right] \quad (63)$$

Strain is commonly measured using strain gauges, and in some cases using optical techniques. One limitation of both methods in the scope of this work is that they measure strain over two-dimensional surfaces. Strains due to Coulombic friction stresses are present and strongest at the inner surface of a slurry pipe. In the interest of developing a relationship between the erosive wear and shear stresses experienced within slurry pipes, it would be valuable to be able to measure the resultant strains. Existing strain measurement techniques do not appear to be practical for measuring at the inner pipe surface. It is unknown whether shear strain has been successfully measured across a solid body, and if so, what proportion of the strain is transmitted through the body. It is a goal of this thesis work to investigate the possibility of applying existing strain measurement techniques to slurry pipes in an attempt to measure strains within the pipes.

3 Model Development

3.1 Introduction

When dealing with wear due to solid-liquid slurry flows through a pipe, numerous physical and chemical factors come into play. A mechanistic approach to predicting this type of wear is difficult; hence, an empirical approach must often be employed. Based on the flow and wear models discussed above, the development of a model is begun here to describe erosive wear on the inner surface of slurry pipes.

As a starting point, mechanical wear has been selected as the focus for this work. The extent to which slurry pipe wear occurs is based on a number of factors, including flow rate, bulk solids concentration, particle size distribution, and angularity of the sand particles. Both particle angularity and size distribution are difficult quantities to measure or control in an industrial setting with high throughput. For the purposes of this research, sand concentration and bulk flow rate have been identified as being the primary (and fully controllable) parameters of interest in determining mechanical wear rate.

Solid-liquid slurry flows may fall under one of four basic regimes: stationary bed flow, moving bed flow, heterogeneously-suspended flow, and pseudohomogeneously-suspended flow. Assuming that particle density and size remain constant, the governing factors in determining the flow regime are flow rate and solids concentration. As flow rate increases or concentration decreases, an increasing number of particles become suspended by turbulent fluid motion; the reverse is also true. Robust models have been formulated to describe the flows of settling slurries with a Newtonian carrier fluid through circular pipes. The intent of this work is to modify an existing slurry flow model in such a way that it may also be used to predict mechanical wear rates.

3.2 Modified Flow Model

As a starting point, the Improved Two-Layer model (“SRC model”) of Gillies *et al.* (1991) has been selected primarily for its widespread use in industry, as well as for its robustness and simplicity. It is valid for settling slurry mixtures up to 35%

concentration by volume, making it ideal for modeling hydrotransport. An idealized schematic is provided earlier in Figure 1.

In Chapter 2, it was discussed that Pugh *et al.* (1999) demonstrated the presence of a thick interface occurring between the upper and lower slurry flow layers. Across this “shear interface” layer, changes in solids concentration were shown to occur in a near-linear fashion, rather than the stepwise fashion described by the SRC model. Experimental results of Schaan *et al.* (2000) showed that the velocity distribution across the shear interface layer assumes a near-linear profile rather than a step change. Unusual pipe wear profiles, located in the region immediately above the stationary solids bed, were reported by Schaan *et al.* (2007). It is hypothesized by this author that these observations are all related, and that these wear phenomena are related to the properties of the shear interface layer. These properties are explored in some depth in this chapter.

The SRC Two-Layer model has been modified to encompass the findings of Schaan *et al.* (2000) and Pugh *et al.* (1999). The intent of this modification is to provide a base formulation which will allow the flow model to link to an empirical wear model through a probabilistic approach. Modifications are presented schematically in Figure 6 and Figure 7 below. Points to note include:

- The zero-thickness interface has been replaced by a thick interface of height h_s .
- Local solids concentration decreases with height across the interface.
- Local velocity increases with height across the interface.
- Half-angle α subtends the upper surface of the interface layer, while half-angle β subtends the lower surface of the interface layer.
- The boundary length between the upper layer and the interface layer is denoted by S_{1s} , while the boundary length between the interface layer and the lower layer is denoted by S_{2s} . S_s denotes the boundary length between the interface layer and the pipe wall.
- A_s , C_s , and V_s denote cross-sectional area, local solids concentration, and local velocity of the shear interface layer, respectively. Concentration and velocity are functions of height within the layer.

For the purpose of wear prediction, the wear mechanisms occurring in the lower layer and the shear layer are of principal concern. To be consistent with the work of Gillies *et al.* (2004), the volumetric solids concentration in the upper

layer is assigned a value C_1 , and the volumetric solids concentration of the lower layer is the variable quantity C_{lim} . The thickness of the shear layer (h_s) is determined in a later section of this chapter. The S variables refer to interfacial boundaries, denoted by heavy black lines in Figure 7.

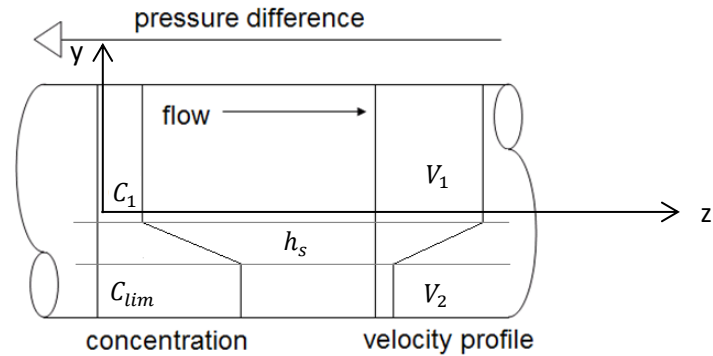


Figure 6 - Schematic of modified two-layer model

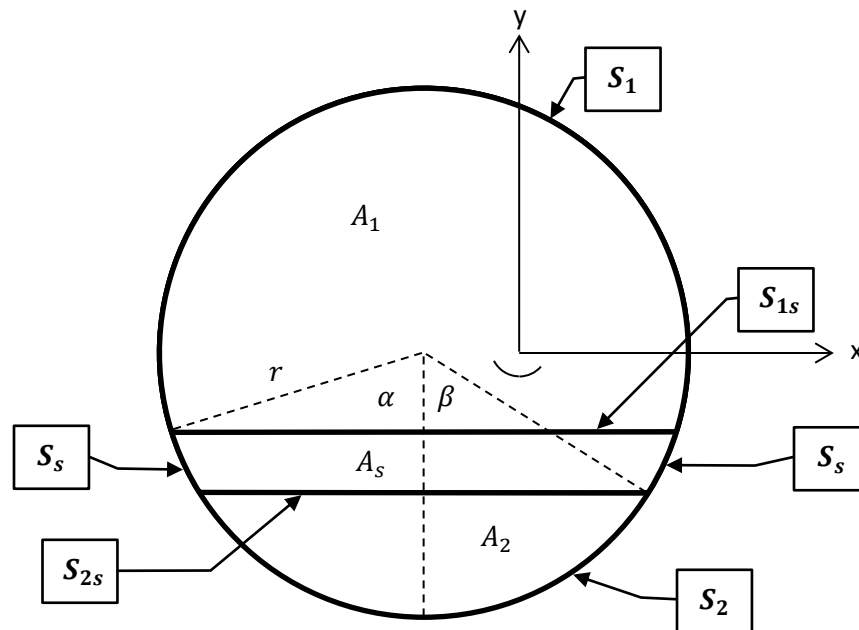


Figure 7 - Cross-section geometry of the modified two-layer model

In contrast to the step changes in velocity and particle concentration seen in the SRC model, this model assumes linear changes across the shear interface, in agreement with the results of Schaan *et al.* (2000) and Pugh *et al.* (1999). Local velocity and concentration are defined as linear functions of height within the shear layer, as shown below:

$$V_s(y) = V_2 + \frac{y}{h_s}(V_1 - V_2) \quad (64)$$

$$C_s(y) = C_{\text{lim}} + \frac{y}{h_s}(C_1 - C_{\text{lim}}) = C_{\text{lim}} - C_2 \frac{y}{h_s} \quad (65)$$

Using the two-layer model requires use of a Cartesian coordinate system, especially when defining layer thicknesses. However, since the frame of reference is a circular pipe, a cylindrical coordinate system is helpful for defining particle motion. The cylindrical coordinates are defined using normal ($\hat{\mathbf{n}}$), tangential ($\hat{\mathbf{t}}$), and axial ($\hat{\mathbf{z}}$) components. Here, bold-faced variables are vectors. Carets (^) denote unit vectors, over-bars (̄) denote 'mean' variables, and tildes (~) denote 'variance' variables. The velocities represented in this model are considered to be layer-averaged velocities (or chord-averaged, in the case of the shear interface layer). Average local velocity is represented by the vector $\bar{\mathbf{v}}$. The direction of this vector is always axial.

This representation is incomplete for typical industrial slurry flows, many of which experience elevated levels of turbulence. It is not known whether existing turbulence models would lend themselves well to describing slurry flows, since most have been developed for describing single-phase flows. This model is concerned with the large-scale process of slurry wear, rather than the small-scale physics of fluid flows and particle motion, eddy viscosity, or turbulent energy. The turbulent motion experienced within a slurry flow is essentially a series of random events. A Gaussian probability distribution is viewed as an appropriate representation, as it lends itself well to describing many natural random phenomena. Thus, turbulent velocity is modeled stochastically as a randomly-distributed, Gaussian vector $\tilde{\mathbf{v}}$ with mean = 0 and standard deviation to be determined experimentally. Based on an understanding of general slurry flows, the magnitude of the turbulence vector is a function of both bulk solids concentration and bulk flow rate. Both the magnitude and direction of this vector are defined to be random in three dimensions. In a cylindrical coordinate system, the turbulence vector may be represented by

$$\tilde{\mathbf{v}} = \tilde{v}_n \hat{\mathbf{n}} + \tilde{v}_t \hat{\mathbf{t}} + \tilde{v}_z \hat{\mathbf{z}} \quad (66)$$

The resultant total velocity may then be represented by the vector sum:

$$\mathbf{v} = \bar{\mathbf{v}} + \tilde{\mathbf{v}} = (\bar{v}_z + \tilde{v}_z) \hat{\mathbf{z}} + \tilde{v}_n \hat{\mathbf{n}} + \tilde{v}_t \hat{\mathbf{t}} \quad (67)$$

For the purposes of this model, it is assumed that the intensity of the turbulence in the upper layer remains constant across the thickness of the layer. As indicated by Wilson (1988), a concentration gradient will likely result in turbulent damping near the lower surface of the shear layer. It is expected that the magnitude of the turbulence vector in the shear layer will increase linearly with height, reflected in the following equation ('s' denotes shear layer, '1' denotes upper layer):

$$\tilde{\mathbf{v}}_s(y) = \frac{y}{h_s} \tilde{\mathbf{v}}_1 \quad (68)$$

Turbulence in the lower layer is assumed to be zero and is ignored, even though this is likely not the case. Based on the SRC Two-Layer model, the lower-layer solids are assumed to slide as a single unit over the pipe surface, and therefore lower-layer wear occurs exclusively due to sliding erosion. Any particle impingement which may occur in the lower layer is of no concern here, and knowledge of the turbulence levels of the lower layer would be of little help.

Since solids concentration is low in the upper layer, impingement by upper-layer particles is also assumed to be zero and is ignored. This assumption is justified by realizing that the majority of wear observed in the field occurs over the lower pipe surface.

3.3 Shear Interface Layer Parameters

It is difficult to calculate pipe wear (especially wear due to impingement) unless the shear interface layer is further defined. The parameter of primary interest is the layer thickness. Wilson (1976) modeled slurry flow as two layers separated by an interface of varying thickness [reported in Abulnaga, 2002]. This thickness was related to the interfacial shear stress [Gillies *et al.*, 2000]. Pugh & Wilson (1999) reported that the thickness of this layer was up to several grain layers thick. In the interest of defining the model equations, this section develops a method for determining the thickness of the shear interface layer. To provide maximum agreement with the well-developed modeling of Gillies *et al.*, the SRC model was solved, and its parameters were used to calculate the modified model parameters.

The first step is to define model behaviour in each flow regime:

- **Stationary bed.** In this regime, the shear interface lies above the stationary bed. As bulk velocity increases, solids migrate upwards from the bed into the shear interface layer. This transfer of solids drives a linear decrease in the cross-sectional area of the stationary bed, as well as a non-linear increase in the cross-sectional area of the shear layer. The cross-sectional area of the upper layer adjusts correspondingly.
- **Moving bed.** In this regime, the cross-sectional area of the bed layer continues to decrease linearly with bulk velocity. Solids migrate from the bed layer to the shear interface layer, causing the shear interface to swell in size. This continues until the bed layer is depleted of solids. Two special cases may occur:
 - If overall concentration is sufficiently high, the upper layer may disappear before the bed layer. To model this case mathematically, the upper layer is modeled as a layer of zero cross-sectional area. However, as the lower layer continues to be depleted of solids, the shear interface is unable to expand further unless the upper-layer concentration value is increased, since the lower-layer concentration cannot increase beyond C_{lim} . This continues until the shear interface layer expands to cover the entire flow cross section.
 - If overall concentration is sufficiently low, the bed layer may disappear before the upper layer. Similar to the previous case, the bed layer is modeled as having zero cross-sectional area, yet maintains a concentration value. To allow the shear interface to continue to expand, the bed-layer concentration must decrease. As before, this continues until the shear interface layer expands to cover the entire flow cross section.
- **Fully-suspended, non-homogeneous.** In this regime, the shear interface layer has expanded to cover the entire flow cross section. Both the upper layer and the bed layer are modeled as having zero cross-sectional area, yet maintaining a 'concentration' value. As bulk velocity increases, solids continue to migrate upwards, resulting in an increase in upper-level concentration and a corresponding decrease in lower-level concentration. At the same time, velocity increases more rapidly in the lower region than in the upper region. This continues until the solids concentration and velocity are uniform across the entire flow cross-section.

- **Fully-suspended, homogeneous.** In this regime, the solids concentration and velocity are uniform across the entire flow cross-section.

The following assumptions are made in order to define model behaviour:

- For the velocity range $V < V_b$ (moving bed flow), solids migrate from the bed to the shear interface layer. In the spirit of Wilson's shear-layer research [Wilson 1987, 1988, 2005; Nnadi & Wilson 1992, 1995; Wilson & Pugh 1988, 1999] this "solids pickup function" is defined as having a proportional relationship with average velocity.
- For the velocity range $V_b < V < V_u$ (heterogeneous, fully-suspended flow), the following changes occur in a linear fashion:
 - Lower-layer solids concentration decreases towards C_r
 - Upper-layer solids concentration increases towards C_r
 - Lower-layer velocity is interpolated between V_1 and V
 - Upper-layer velocity is interpolated between V_2 and V
- For the velocity range $V \geq V_u$ (pseudo-homogeneous flow)
 - Velocity for all layers is equal to the average velocity V
 - Solids concentration for all layers is equal to C_r
 - Lower-layer cross-sectional area = 0
 - Upper-layer cross-sectional area = 0

The next step is to model the behaviour of the lower flow layer as its velocity increases. As stationary bed flow transitions toward fully-suspended flow, the cross-sectional area of the lower layer gradually shrinks to zero. This behaviour is modeled in a linear fashion. To reflect this change, the lower area was redefined as follows:

$$A_2' = A \frac{C_c}{C_2} \left[1 - \frac{V}{V_d} \right] \quad (69)$$

The value of V_d is calculated from the following equation, given in [Abulnaga, 2002]:

$$V_d = F_L \sqrt{2gD_i \left(\frac{\rho_s}{\rho_L} - 1 \right)} \quad (70)$$

The half-angle β' is calculated from Equation 18. The maximum thickness of the lower layer is given by:

$$h_2' = r(1 - \cos \beta') \quad (71)$$

Limiting local concentrations and local velocities of the upper and lower layers are defined over a range of bulk velocities. These are given from the following equations:

$$V_l = \begin{cases} V_2 & V < V_d \\ V_2 + (V - V_2) \left(\frac{V - V_d}{V_h - V_d} \right) & V_d \leq V < V_h \\ V & V \geq V_h \end{cases} \quad (72)$$

$$V_u = \begin{cases} V_1 & V < V_d \\ V_1 + (V - V_1) \left(\frac{V - V_d}{V_h - V_d} \right) & V_d \leq V < V_h \\ V & V \geq V_h \end{cases} \quad (73)$$

$$C_l = \begin{cases} C_{\text{lim}} & V < V_d \\ C_{\text{lim}} + (C_r - C_{\text{lim}}) \left(\frac{V - V_d}{V_h - V_d} \right) & V_d \leq V < V_h \\ C_r & V \geq V_h \end{cases} \quad (74)$$

$$C_u = \begin{cases} C_1 & V < V_d \\ C_1 + (C_r - C_1) \left(\frac{V - V_d}{V_h - V_d} \right) & V_d \leq V < V_h \\ C_r & V \geq V_h \end{cases} \quad (75)$$

The height of the shear layer may be determined. Again, as flow transitions from a moving bed to a fully-suspended flow, it is expected that the shear layer gradually expands until its area is that of the pipe cross-section itself. The following steps are used:

1. Determine the reduction in cross-sectional area in the lower layer ΔA_2 .
2. Determine the mass flux of solids through ΔA_2 (Δm_s) and – maintaining continuity – use this value to calculate the increase in area of the shear interface layer.

The equations associated with these steps are listed below, and are solved simultaneously:

$$\Delta m_s = \begin{cases} 2 \int_{h_2'}^{h_2'+h_s} \left[V_l + \frac{y-h_2'}{h_s} (V_u - V_l) \right] \left[C_u + C_l \left(1 - \frac{y-h_2'}{h_s} \right) \right] \sqrt{r_i^2 - (r_i - y)^2} dy & V < V_h \\ \frac{1}{4} \pi h_s^2 V C_r & V \geq V_h \end{cases} \quad (76)$$

$$A_s = \int_{h_2'}^{h_2'+h_s} \sqrt{r_i^2 - (r_i - y)^2} dy \quad (77)$$

$$C_r A V = \Delta m_s + V_l A_2' C_l + V_u A_1' C_u \quad (78)$$

$$A = A_1' + A_s + A_2' \quad (79)$$

Once Δm_s , A_s , A_1' , and h_s are determined, the remaining model equations may be solved.

The half-angle α – which subtends the shear layer – may be determined:

$$\alpha = \cos^{-1} \left(\cos \beta' - \frac{h_s}{r_i} \right) \quad (80)$$

Interfacial lengths may be determined:

$$S_1 = 2r(\pi - \alpha) \quad (81)$$

$$S_{1s} = 2r \sin \alpha \quad (82)$$

$$S_s = r(\alpha - \beta') \quad (83)$$

$$S_{2s} = 2r \sin \beta' \quad (84)$$

$$S_2 = 2r\beta' \quad (85)$$

The force balance equations may be re-written to include the shear interface layer:

$$i\rho_L g = \frac{\tau_2 S_2 - \tau_{2s} S_{2s}}{A_2} \quad (86)$$

$$i\rho_L g = \frac{\tau_1 S_1 + \tau_{1s} S_{1s}}{A_1} \quad (87)$$

$$i\rho_L g = \frac{\tau_{2s}S_{2s} - \tau_{1s}S_{1s} + 2\tau_s S_s}{A_s} \quad (88)$$

The average velocity of the shear interface layer may be obtained by integrating across the area of the layer:

$$V_s = \frac{2}{A_s} \int_{h_2'}^{h_2'+h_s} \left[V_l + \frac{y-h_2'}{h_s} (V_u - V_l) \right] \sqrt{r_i^2 - (r_i - y)^2} dy \quad (89)$$

At this point, an attempt to define the interfacial shear stresses is hindered by a lack of supporting observations. However, based on SRC Two-Layer model equations, a reasonable estimate may be as follows:

$$\tau_{1s} = \frac{1}{2} f_{12} (V_1 - V_s) |V_1 - V_s| \rho_1 \quad (90)$$

$$\tau_{2s} = \frac{1}{2} f_{12} (V_s - V_2) |V_s - V_2| \rho_2 \quad (91)$$

If desired, the following parameters may also be calculated:

$$\text{Re}_s = \frac{\rho_s V_s D_{Hs}}{\mu_s} \quad (92)$$

$$D_{Hs} = \frac{4A_s}{S_{1s} + S_{2s} + 2S_s} \quad (93)$$

ρ_s and μ_s are determined by simply averaging between the respective values of the upper and lower layers.

Due to the difficulty of solving several of the above equations simultaneously, the model was solved using MathCAD Prime 2.0, and the complete worksheet is provided in the Appendix.

3.4 Sliding Erosion

Damage rate over the arc S_2 is assumed to be exclusively due to sliding erosion. The method described below is applied to empirically model the wear caused by friction between the moving slurry bed and the pipe wall. A schematic of a slurry pipe cross-section is given below for reference (the shear interface layer is

ignored for the moment). The variable y' represents the local depth of the solids bed at an arbitrary angle θ . The angle θ is measured counter-clockwise from a vertical line extending to the lower surface of the pipe.

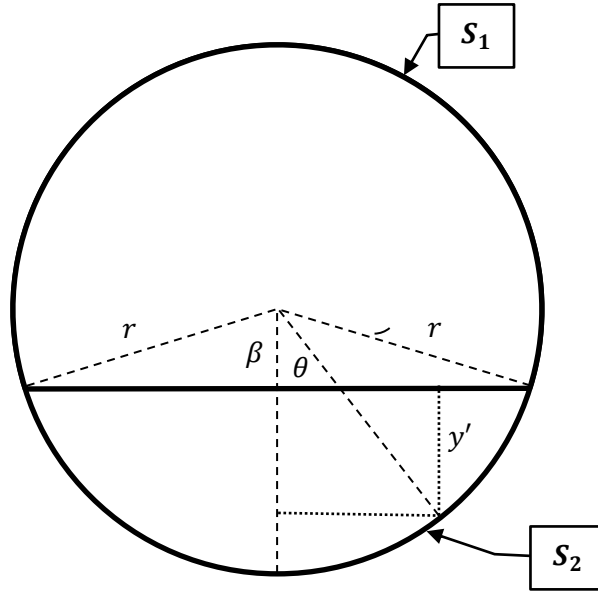


Figure 8 - Cross section view of a slurry pipe

In this research, velocity and shear stress values are calculated from the modified two-layer model. The method of Roco *et al.* (1987), as adapted by El-Sayed *et al.* (2009), is applied here to describe erosive wear on the pipe surface in contact with sliding bed solids. The following derivations are found in Lipsett (2012), and have been modified slightly to agree with the SRC model:

$$\dot{D} = \phi V_2 [\tau_{avg} - \tau_0] \quad (94)$$

where

$$\tau_{avg} = \frac{F_f}{D\beta} \quad (95)$$

First, define the effective density of the lower layer to be consistent with the SRC model:

$$\rho_{eff} = \frac{C_2(1 - C_{lim})}{1 - C_2} (\rho_s - \rho_f) \quad (96)$$

The pressure on the lower-layer pipe wall, due to the supported weight of submerged solids is given by:

$$P_\theta = \rho_{eff} g y' \quad (97)$$

where

$$y' = r(\cos \theta - \cos \beta) \quad (98)$$

Now define the shear stress (due to friction) at an angle θ on the pipe wall to be

$$\tau(\theta) = \eta_s P_\theta \quad (99)$$

Then the differential friction force per unit length is given by

$$dF_f = \tau(\theta) r d\theta = \eta_s \rho_{eff} g r^2 (\cos \theta - \cos \beta) d\theta \quad (100)$$

Integrating from $-\beta$ to $+\beta$ gives

$$F_f = \int_{-\beta}^{\beta} \eta_s \rho_{eff} g r^2 (\cos \theta - \cos \beta) d\theta \quad (101)$$

$$F_f = \left(\eta_s \rho_{eff} g r^2 \sin \theta \right)_{-\beta}^{\beta} - \left(\eta_s \rho_{eff} g r^2 \theta \cos \beta \right)_{-\beta}^{\beta} \quad (102)$$

$$F_f = 2\eta_s \rho_{eff} g r^2 \sin \beta - 2\eta_s \rho_{eff} g r^2 \beta \cos \beta \quad (103)$$

$$F_f = \frac{1}{2} \eta_s \rho_{eff} g D^2 (\sin \beta - \beta \cos \beta) \quad (104)$$

$$F_f = \frac{1}{2} \eta_s g D^2 \frac{C_2(1-C_{lim})}{1-C_2} (\rho_s - \rho_f) (\sin \beta - \beta \cos \beta) \quad (105)$$

The reader will note that Equation 105 is identical to Equation 22, defined in Chapter 2. Applying Equations 105 and 95 in Equation 94 yields the sliding-abrasive damage rate equation:

$$\dot{D} = \varphi V_2 \left[\frac{\eta_s D g C_2 (1 - C_{lim})}{2\beta(1 - C_2)} (\rho_s - \rho_f) (\sin \beta - \beta \cos \beta) - \tau_0 \right] \quad (106)$$

Equation 106 may be integrated with respect to time to obtain the total sliding-abrasive wear incurred upon a unit length of pipe by a moving bed of solids, over an arbitrary duration Δt :

$$D(t) = \varphi V_2 \Delta t \left[\frac{\eta_s D g C_2 (1 - C_{lim})}{2\beta(1 - C_2)} (\rho_s - \rho_f) (\sin \beta - \beta \cos \beta) - \tau_0 \right] \quad (107)$$

Parameters φ and τ_0 are material-specific and must be determined experimentally.

3.5 Impingement

In order to predict impingement damage rate to the pipe surface, it is necessary to determine the probability that a given particle will strike the pipe wall. This may be done as follows. For any given particle within the shear interface layer, define d to be the distance between the particle and the pipe wall, projected along the particle's current trajectory. Then the probability of damage to the wall within a given time step Δt is given by

$$P(\text{collision}) = P(\tilde{v}_n > 0) P\left(d \leq \frac{v}{\Delta t}\right)$$

$$P(\text{damage}) = P(\tilde{v}_n > v_0) P(\text{collision})$$

where v_0 is the magnitude of a threshold normal velocity required to incur damage to the pipe wall. This threshold velocity is given by K in Bitter's model (1962).

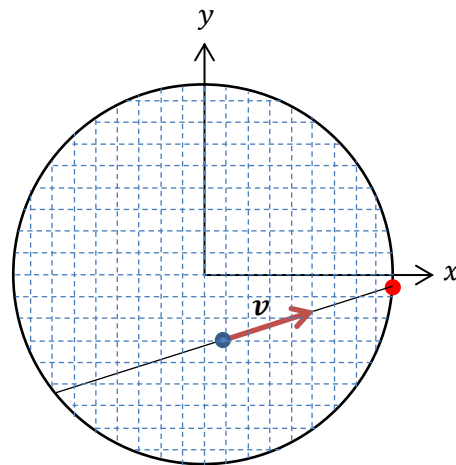


Figure 9 - Schematic of particle impingement simulation

Once the probability of damage has been established, the damage per unit length may be calculated by integrating a damage function along the upper arc of the pipe. Using the Oka *et al.* damage model, the damage per unit length – due only to impingement – may be represented by the following equation:

$$D = P(\text{damage}) \int_0^t \int_S E(\theta) \dot{m} dS dt \quad (108)$$

The impingement angle θ may be determined from

$$\theta = \tan^{-1} \frac{\tilde{v}_n}{\sqrt{\tilde{v}_t^2 + (\bar{v}_z + \tilde{v}_z)^2}} \quad (109)$$

Damage accumulation is calculated by means of a Monte Carlo-style simulation. A script was written in Matlab to simulate the impingement wear (full code provided in the Appendix).

The pipe cross-section is discretized into a grid, similar to that shown above in Figure 9, with each grid unit having dimensions of 1 mm x 1 mm. The pipe cross section is divided into layers with thicknesses calculated using a given bulk velocity. These values, as well as the velocities and concentrations are determined by solving the modified two-layer model.

Iterating vertically across the pipe cross section, each cell is assigned values of axial velocity, turbulent intensity (in three dimensions), and solids concentration. These values are calculated with respect to the properties of each layer, as well as location within the layer.

Turbulent velocity variables within the shear interface zone are defined as normal distributions with a mean of zero and a standard deviation equal to the previously calculated intensity values (varying with respect to height). For the present, turbulent intensity (standard deviation) is assumed to be identical in three dimensions at a given point.

Rather than deal with particles *per se*, the solids concentration value of each cell is assumed to represent an equivalent volume fraction of particles. However, the term “particle” is used here to denote an individual grid unit containing a set concentration of solids.

Impingement wear is calculated over a given time step; a rather simplified approach is used here. A graphical representation of the steps taken is given below in Figure 10. Each particle within the shear interface is evaluated to

determine whether – given its speed and direction – it will strike the pipe wall within the allotted time step. Particle trajectories are assumed to be perfectly straight, and particle-particle interactions have been purposely neglected here.

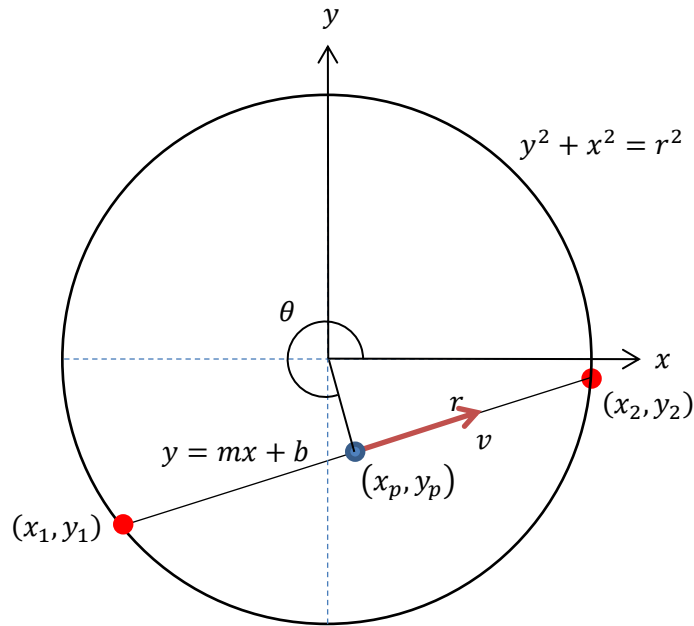


Figure 10 - Geometrical representation of a particle-wall collision

To determine whether a collision will occur, it is advantageous to work in a Cartesian coordinate frame. Normal and tangential (with respect to the pipe wall) components of each particle's velocity are converted to Cartesian x - y velocities by

$$v_x = v_n \cos \theta + v_t \sin \theta \quad (110)$$

$$v_y = v_n \sin \theta + v_t \cos \theta \quad (111)$$

where θ is the angle which determines the particle's location in a circular coordinate system. From these x - y velocities, the slope and intercept of the linear equation representing the particle's trajectory are calculated from

$$m = \tan^{-1} \left(\frac{v_y}{v_x} \right) \quad (112)$$

$$b = y_p - mx_p \quad (113)$$

The pipe wall is represented by the equation for a circle centered at the origin:

$$x^2 + y^2 = r^2 \quad (114)$$

Next, the point of impact is determined by solving for the points where the line intercepts the circle using the quadratic equation

$$x = \frac{-mb \pm \sqrt{m^2 r^2 + r^2 - b^2}}{1 + m^2} \quad (115)$$

Using the equation of the line, two corresponding values of y are determined from the x values. From the x and y components of the particle's velocity, the correct coordinate pair may be determined. Projected trajectory distance is calculated between the particle and the point of impact. If this distance is less than or equal to the distance that the particle will travel in the given time step, a collision is said to occur.

If it is determined that the particle will strike the pipe wall, then Bitter's method (1962) is applied. The normal component of velocity is analyzed to determine whether it exceeds a minimum threshold velocity required for damage to occur. If the threshold is exceeded, then damage is said to occur.

Once damage has been determined to occur from a given particle's interaction with the pipe wall, then the Oka *et al.* (2004) equations are applied to determine the quantity of material removal which will result from this impact. The Oka *et al.* equations return a value in cubic millimeters of material removal per kilogram of impacting solids. The mass flux of impacting solids is determined from the volumetric solids concentration of the respective particle, as well as the density of the solids.

The impingement calculations are repeated over multiple time steps, each time step being 1 second in duration. Particle velocities are re-randomized prior to each iteration. The accumulated damage is averaged over the total time duration to obtain a wear rate.

3.6 Model Verification and Validation

In order to provide any value, the models require validation. The sliding erosive wear model may be effectively validated by conducting tests on wear specimens. Slurry flow through a hydrotransport pipeline may be simulated in a laboratory pipe loop. The empirical constant φ may be determined by measuring mass loss over a specific time. At lower volumetric concentrations of sand and/or at higher flow rates, the moving bed tends to assume a pulsating flow pattern. Measuring V_2 , τ_2 , and the angle β is difficult even under the best of conditions. These values will be obtained from the modified two-layer flow model.

The impingement wear model may prove to be more difficult to validate. In order to create flow conditions similar to those described in Schaan *et al.* (2007), it is important to use higher sand concentrations and lower flow rates. Quantification may again be measured via mass loss over a specific time, but impingement angles and velocities require a more intricate measuring process. Optical particle tracking will be used to verify assumptions and to quantify model parameters, as both particle speed and direction may be measured using this technique. However, in order to actually observe and measure the impinging particle motion, higher flow rates and lower volumetric concentrations of sand are desirable. Hence, rather than physically measure impingement wear in a laboratory apparatus, it will be more feasible to use optical measurements to complete the impingement model, and then to compare the model predictions with conditions which have been observed in the field (such as those presented by Schaan *et al.*).

In conclusion, the knowledge gaps which are of interest to this research are summarized below:

- It is hypothesized that the sliding-abrasive wear occurring at the lower pipe surface may be a linear function of both velocity and shear stress. This linear relationship is defined by the material-specific threshold shear stress τ_0 and proportionality constant φ , both of which are to be determined through testing. These parameters should be linked back to the volumetric solids concentration and bulk velocity of the slurry flow.
- The modified two-layer slurry flow model is in a theoretical stage and must be proven. Essential parameters of the model – especially those relating to layer geometry and turbulent particle motion – must be verified through measurement.

- Impingement wear has been described here by a numerical simulation. This simulation model requires testing and verification; observations from the field serve as a good benchmark for comparison. Again, the model predictions should be linked to the volumetric solids concentration and bulk velocity of the slurry flow.

4 Experimental Methodology

4.1 Introduction

This chapter describes the experimental apparatus, equipment, and materials used to validate the wear models described earlier. The experimental variables, equipment, and test materials are described in detail. The original test plan required some unforeseen changes; these are discussed here as well. Finally, the development of the experiment control software is presented.

4.2 Principal Assumptions

In order to gain further understanding of slurry wear processes and the individual contributions made by the bulk concentration and mass flow rate, it is necessary to remove some of the complicating factors. It is advantageous to reduce the number of unknowns to those quantities which are easily measured and/or controlled onsite. It is also useful to examine the effects of as few parameters as possible in order to more fully understand their individual contributions. Additional complexity may be introduced later, once the principal parameters are better understood.

Two-phase aqueous sand slurries are used in this research, in order to eliminate challenging issues such as non-Newtonian effects, bitumen-related wall roughness effects, and flow effects arising from entrained air bubbles. This also allows the focus to remain on mechanical wear, without being concerned with the compounding effects of corrosive and erosive-corrosive wear. Silica sand makes a convenient slurry solid phase, since it is commonly found in nature, it is a common solid constituent of oilsand, and it is an economic option.

It may be deduced from the literature survey that mechanical slurry wear is governed primarily by three quantities: mass flow rate, bulk solids concentration, and particle size. Both mass flow rate and bulk solids concentration are directly controllable on an industrial site, within process constraints. Particle size is nearly impossible to control in an industrial setting such as an oilsand mine, as attested by the wide range of particle sizes found within hydrotransport lines.

The effects of particle size are not included in this study, and average particle size is kept constant.

4.3 Definition of Variables

Bulk velocity and concentration are the primary variables in this study. Other variables are kept constant, or else measured but not controlled. The variables of interest to this study are summarized below.

- **Controlled variables:** Particle density, particle size, fluid properties, pipe diameter, wear specimen properties
- **Manipulated variables:** pump speed, bulk concentration
- **Responding variables:** mass flow rate, process temperature, pressure drop, mass loss, pipe wall shear strain, particle velocity, thickness of shear interface layer

From the variables listed above, other useful quantities may be calculated; these are listed below.

- Mixture viscosity: $\mu_m = \mu_l(1 + 2.5C_w + 10C_w^2 + 0.0019e^{20C_w})$ [Gillies *et al.*, 2000]
- Mixture density: $\rho_m = \frac{100}{\frac{C_w}{\rho_s} + \frac{100-C_w}{\rho_l}}$ [Abulnaga, 2002]
- Average velocity: $V = \frac{4\dot{m}}{\rho_m \pi D^2}$
- Mixture Reynolds number: $Re_m = \frac{\rho_m V D}{\mu_m}$ [Abulnaga, 2002]

4.4 Experimental Equipment

The setup of the experimental equipment is shown below in Figure 12 and Figure 11. All testing in this research was completed using a laboratory-scale slurry pipeline loop. Initial slurry loop design was completed by colleagues Victor Jaimes and Suheil El-Sayed [El-Sayed, 2010], and was further developed and commissioned by this author. It is constructed of 12 m of 2 inch, schedule 40 plain steel pipe which has been painted black. An additional 5.5 m of 3 inch rubber suction hose is mounted to the pump inlet. All pipe sections and valves

are connected via bolted flanges. The primary components of the loop are described below.

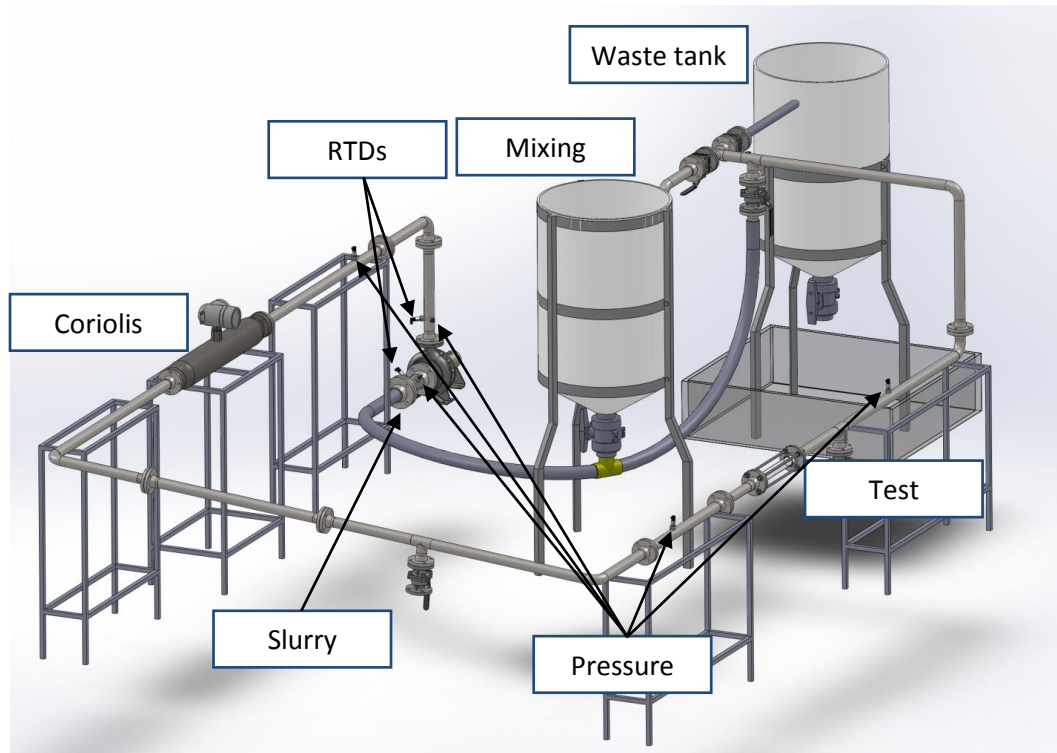


Figure 11 - Rendering of pipe loop, with key components labeled

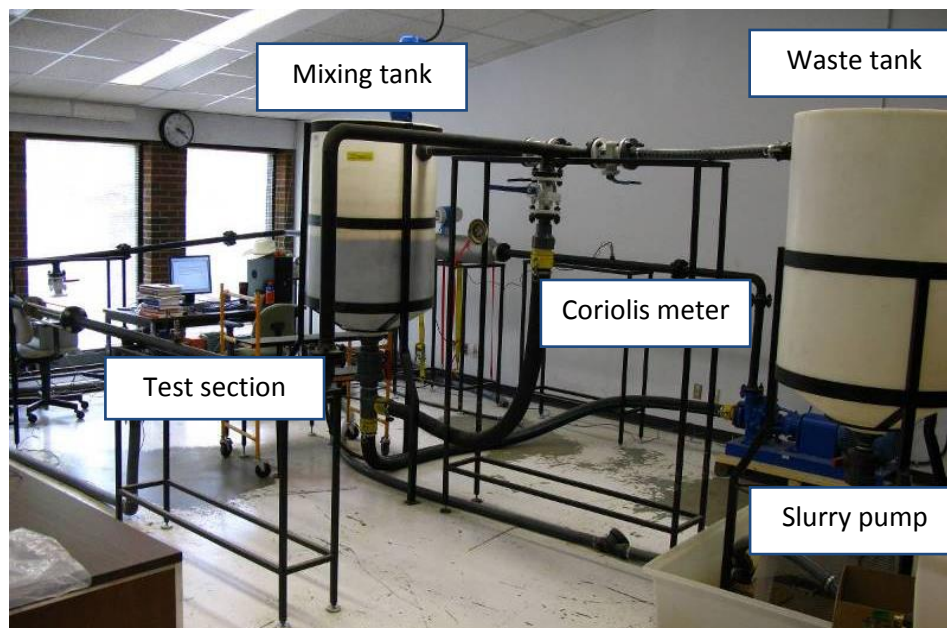


Figure 12 - Pipe loop system overview

The loop is powered by a 7.5 W Hayward Gordon XR2(7) TORUS slurry pump (Figure 13). It is designed for handling severe abrasives and features a recessed impeller design, a three inch inlet, and a two inch outlet. A domestic water line has been routed through the mechanical seal chamber to provide flushing, lubrication, and cooling during run time. The flush flow is controlled manually by means of a gate valve. By design, it is normal for some flush water to seep past the mechanical seal into the volute. Thus, when the mix tank bypass line is in use (creating a closed loop system), pressure in the pipe loop may be raised by increasing the flow rate of flush water. Pump control is achieved by means of a Lenze ACTech 0-60 Hz variable-frequency drive (VFD) unit (Figure 14).

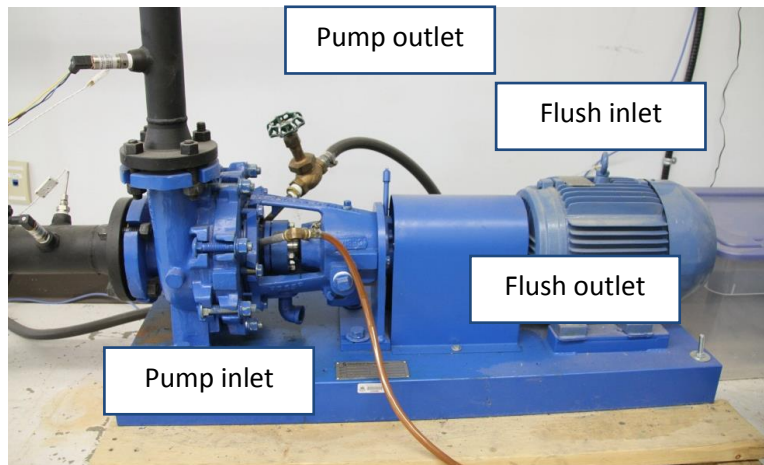


Figure 13 - Slurry pump with flush water line installed at the seal



Figure 14 - VFDs for mixer (left) and pump (center); network switch at bottom

An electric mixer (Figure 15) is used to control the uniformity of the slurry mixtures, especially when pumping slurry through the mixing tank. It features a three-blade mixing propeller mounted to an elongated drive shaft. Control is provided by a 0-60 Hz Leeson Speedmaster2 VFD (Figure 14).

A polyethylene mixing tank (Figure 16) is attached to the pipe loop, to provide a convenient location for adding fresh water and sand to the system. The electric mixer is mounted to the side of the tank, which requires the tank to be open at the top. The slurry return line entrance has been located such that inflow will always enter below the water level, to prevent fluid loss from excessive splashing. The tank is also equipped with a 3-inch outlet line which feeds directly into the pump supply line. Both the supply and return lines may be opened or closed by means of quarter-turn ball valves. Depending on the operator's valve settings, flow may run directly through the mixing tank (open loop system), or be diverted through a bypass line (closed loop system).



Figure 15 - Mixing tank with electric mixer

Both VFDs may be adjusted manually or controlled remotely by means of SMVector Ethernet control modules. These modules are mounted to the VFDs and are connected to a D-Link DSS-5+ network switch (Figure 14). The network switch, in turn, is connected directly to the data acquisition workstation.

A second plastic tank is attached to the pipe loop, to be used as part of a waste separation system (Figure 16). Flow may be diverted into the tank by means of a set of quarter-turn ball valves. The tank itself is equipped with a three-inch drain valve, which empties into a large wastewater catch bin. Inside the catch bin is a sieve box for separating sand from water. A 0.5 hp submersible pump is mounted into the catch bin, to drain water through a check valve into the building waste line.



Figure 16 - Waste tank, sieve box, and catch bin

A modular testing section was installed inline with the pipe (Figure 17). It consists of two slip-on steel flanges supported by four 24-inch threaded rods. Test pieces may be fitted into the flanges and tightened in place with nuts. Each flange features two o-rings to prevent fluid leakage. Each test piece is 19 ¼ inches in length with a 2 ¼ inch outer diameter. Test pieces currently include specially-fabricated specimens for measuring wear, as well as an instrumented

strain spool. When not testing, an optically clear viewing tube may be substituted for a test piece.



Figure 17 - Removable test section with clear viewing tube and axial preload support rods

Finally, a Windows XP-based desktop computer has been designated as a data acquisition workstation. This workstation runs on an AMD Athlon 64 X2 3800+ processor with 1 GB of available RAM. The data acquisition software itself is discussed in a later section of this chapter.

4.5 Instrumentation

4.5.1 Data Acquisition

All sensors have been wired into a National Instruments compact data acquisition unit (DAQ), model NI cDAQ-9178 (Figure 18). The DAQ is connected via USB interface to a data acquisition computer. The DAQ contains four signal-conditioning modules, listed below:

- NI-9208 (16 \pm 21.5 mA analogue current channels @ 500 S/s, 24-bit resolution)
- NI-9217 (4 channels for 3- or 4-wire 100 Ω RTDs @ 400 S/s, 24-bit resolution)
- NI-9236 x 2 (each with 8 quarter-bridge channels for 350 Ω strain gauges @ 10 kS/s/ch, 24-bit resolution)

All mounting and wiring was completed by this author.



Figure 18 - DAQ with external power supply

When selecting data sampling rates, the nature of the experiment was considered carefully in order to balance speed and accuracy. Once steady state flow conditions are achieved, the data of interest (pressure, temperature, and flow rate) do not fluctuate rapidly. To reflect this, a “slow” sampling rate of 50 Hz per channel was selected. Data collected at 50 Hz may then be processed to provide one-second average values. Over a lengthy experimental run, this prevents data logs from becoming unnecessarily large, while still preserving sufficient accuracy.

Since the sensors were to be operated in the presence of rotating machinery, shielded cable connections were utilized as much as possible to protect the data integrity. To protect the sensitive electronics from atmospheric contaminants, the DAQ and all supporting hardware were mounted inside a dust-proof enclosure. An external 12 V power supply was installed to provide power to several of the sensors, and a fuse was mounted in series to prevent potential damage in the case of a power surge.

4.5.2 Flow Rate and Density

An Endress+Hauser Proline Promass 83i Coriolis meter (Figure 19) has been installed in line with the pipe loop. Coriolis meters operate on the principle that a mass moving in a transverse fashion across a rotating reference frame is subjected to crosswise (Coriolis) forces. This model utilizes a single tube design, which has been factory balanced in order to avoid signal noise due to pipeline vibrations. Its primary function is to measure mass flow (flow rate and/or cumulative flow), but it is also useful for measuring many other flow parameters. Three 4-20 mA current outputs are available; the operator may decide which quantities are measured through these outputs. Currently mass flow rate, density, and process temperature have been selected as the outputs. The three outputs are wired into the DAQ using twisted wire pairs to mitigate electromagnetic interference known as “crosstalk.” The individual wire pairs were wired into the DAQ through the NI-9208 module. The 4-20 mA current readings from each output correspond to the following values:

- **Mass flow rate:** 0-10 kg/s
- **Temperature:** 0-100°C
- **Density:** 500-1500 kg/m³



Figure 19 - Coriolis meter with bundled 4-20mA outputs (pink)

4.5.3 Gauge Pressure

Pressure measurements – specifically pressure drop – are useful for analyzing pipe flow (i.e. restrictions due to settling, fluctuations near the pump outlet). Five American Sensor pressure transducers (model AST4000P00002B4E1000) have been mounted at various points along the pipe loop (Figure 20). These sensors measure gauge pressure at their respective locations. These are rugged, two-wire sensors with a 4-20 mA current output and a corresponding response range of 0-200 kPa (0-25 psi). The sensors are protected from damage at up to twice the rated operating pressure range, with a rated burst pressure of five times the rated operating range. Pressure transducers are threaded into ½-inch NPT sockets which have been welded to the pipe. Two are located immediately upstream and downstream of the pump, while the remaining three are placed at arbitrary locations along the piping. The sensors are wired into the NI-9208 DAQ module using shielded wire.



Figure 20 - Pressure transducer

4.5.4 Temperature

Temperature is used in calculations of the viscosity and density of the carrier fluid. It may also be a useful indicator of the energy losses/gains of the system. Thermal effects on wear are not included in this study, with the exceptions of thermal effects on water viscosity and density, and thermal strain.

Two Aircom RTD 3-wire thermocouples (model RT4GPBS3364T2MCXLT) are mounted on the pipe wall (Figure 21) immediately upstream and downstream of the pump. These measure process temperature, as well as temperature rise across the pump. As with the pressure gauges, they are threaded into $\frac{1}{2}$ -inch NPT sockets which have been welded to the pipe. Two spare RTDs are used to measure ambient room temperature. The RTDs measure a nominal 100Ω resistance at 0°C , with a rated linear response of $2.597\text{ }^{\circ}\text{C}/\Omega$ ($0.385\text{ }\Omega/^{\circ}\text{C}$). They are wired into the DAQ via the NI-9217 module.



Figure 21 - RTD thermocouple

Note that the Coriolis meter is also capable of measuring process temperature; however, those measurements are taken only for reference.

4.5.5 Strain

The principal investigation of this research is in attempting to model pipe wear as a function of bulk concentration and mass flow rate. However, there was also some interest in discovering whether the internal shear stresses induced by

slurry flow could be detected at the external pipe surface. If this were possible, these measurements could be used to provide some indication of wear rate.

Strain is commonly measured using strain gauges, and sometimes using optical measurement techniques. Advantages of strain gauges include the ability to measure strains on the order of 0.000001 (“microstrain”) in the vicinity of the gauge, low cost, and ready availability. The chief advantage of optical methods is the ability to measure strains over a large area, allowing creation of a “strain map.” In order to provide high resolution, complex systems of optics and lighting are required and only small areas may be measured.

At the outset, digital image correlation was considered as a possible technique for measuring strains at the pipe walls. However, the strains experienced by the pipe wall proved to be too minute for the imaging system to resolve.

It was hypothesized that, given a pipe wall of sufficient thinness and of a sufficiently elastic material, a portion of the internal strains would transmit to the external surface. To test this hypothesis, an instrumented strain spool was designed and built to fit into the removable test section of the pipe loop. One of the design requirements for this spool was that it be responsive to stress without rupturing. To reflect this, acrylic was selected for the tube material (schedule 40, 2 inch nominal diameter), and a portion of the tube wall was thinned to approximately 1 mm to allow for greater strain sensitivity with low risk of destroying the tube. Strain gauges were mounted to the lower half of the circumference to reflect the expectation that shear strains would be highest in this region. To allow observation of the strain distribution, eight 90° rosettes were mounted over the lower surface of the tube, spaced 25.7° apart. The strain rosettes are mounted such that they are capable of reporting strain in both axial and circumferential directions. The completed strain spool is shown below in Figure 22.



Figure 22 - Strain spool with eight rosettes spaced 25.7° apart

Signal processing was accomplished using NI-9236 data acquisition modules. These are quarter-bridge modules, and there is no built-in temperature compensation. Instead, temperature compensation is achieved during post-processing of the data, by calculating the material expansion and the change in gauge output with respect to temperature. The reason for using a quarter-bridge configuration, rather than a half- or whole-bridge configuration (both of which provide built-in temperature compensation), is because of the number of gauges used in this spool. The data modules provided 16 quarter-bridge slots, which coincided with the number of gauges mounted to the spool. A half-bridge configuration would have required twice as many input slots. The strain values are 'zeroed out' in the software (assuming linearity of strain) prior to taking readings. The strain spool may be installed in the test section of the pipe loop.

Equation 63 may be used to determine the pipe stresses from the strain readings. The only issue is that it requires all three strains to be known – which is not the case here. Strain in only two directions (axial and circumferential) is measured by the strain spool, but the third stress (radial direction) may be calculated using the appropriate Lamé equation. With some substitution and rearranging of the modified Hooke's Law given earlier, the third strain element may be calculated as follows:

$$\varepsilon_3 = \frac{\frac{1}{E}(1+\nu)(1-2\nu)\sigma_3 + \nu\varepsilon_1(1+2\nu) + \nu\varepsilon_2(1+2\nu) - 4\nu\varepsilon_{thermal}(1+\nu)}{1+3\nu-2\nu^2} \quad (116)$$

4.6 Test Materials

Silica sand is found abundantly in nature and is one of the primary solid components of oilsand. As noted from numerous literature sources, silica is also a common choice for slurry research. It was therefore selected as the solid phase for the test slurries. The choice of sand was SIL-4 industrial blasting sand which was readily available from SIL Industrial Minerals in Sherwood Park. This is a medium blasting sand of a 40-50 US mesh size (297-420 μm). To enable observation of the effect of bulk sand concentration, two semi-arbitrary values were selected: 5wt% and 10wt%.

PVC pipe lengths were initially selected to serve as wear test specimens. At the time of selection, it was not understood how extensive the wear rate would be. However, the PVC specimens were expected to display some visible signs of wear – such as scratching – even if that wear proved not to be extensive.

After two preliminary test runs, significant degradation of the silica sand particles was observed. High levels of silica fines were observed in the waste water. The pipe loop was not designed to constantly replenish itself with fresh sand. This resulted in sand particles becoming heavily degraded by flowing in contact with the rotating pump components, as well as the steel pipe walls. After over 65 hours of being subjected to slurry flow at the highest pump speed achievable, the PVC wear specimen showed no visible scratches or other signs of wear.

It was necessary to re-evaluate the choice of test materials. The following desired traits were set out for the slurry solid:

- easily obtainable
- low-cost
- strongly abrasive
- high hardness and angularity
- maintains abrasiveness

High hardness and angularity were required to produce accelerated wear rates in the specimens, with low particle degradation. Possible choices included steel grit, blasting slag, aluminum oxide grit, and garnet sand. All but the garnet sand were either prohibitively expensive or else lost their edge quickly by comparison. Garnet sand is readily available and is known to be an excellent abrasive. It is

used extensively in industry, especially for water-jet cutting applications, high-temperature fracking, and water filtration. Hence, garnet sand (with a manufacturer-supplied Mohs hardness value of 7.5-8.0) was the solid of choice. To further accelerate the wear rates on the test specimens, a coarse particle size of 8-12 grit (1.5 mm average diameter) was selected.

Some considerations for the wear specimen material were that it be readily available, require minimal processing, and be fairly rigid. For modularity, the wear specimens were required to be tubular in order to fit into the test section of the pipe loop. It was important that the material have low resistance to abrasive wear, to allow wearing to progress quickly. Several options were considered, including plastic, brass, aluminum, or a substrate coated with an epoxy-like material. In order to provide a readily abradable surface, 330 mL of Repro Light fast-cast urethane (from Freeman Manufacturing & Supply Co.) was applied evenly to the inner surfaces of the wear test specimens. This yielded a wall coating approximately 2.7 mm thick. The urethane requires a minimum gel time of 6-8 minutes, followed by a 1.5 - 2 hour demold time. In order to coat the inner surface evenly and provide a smooth finish, the specimens were capped on each end and turned for up to 2 hours on a lathe. Slight irregularities were observed in some of the specimens, but they were deemed to be of little significance. Repro Light is soft enough (Shore D hardness of 68) that a human fingernail may produce a visible scratch, and it was expected that garnet sand slurries would produce heavy visible erosion of the coating. A sample specimen is shown below in Figure 23.



Figure 23 - A sample urethane-coated test specimen

The expected outcome of flowing garnet sand slurry through urethane-coated pipe specimens was that measurable wear scars would be achieved in a relatively short period of time. This would allow for an increased number of runs to be realized in a reduced timeframe.

4.7 Control Software

Early in the research work, it became necessary to design and build a computer application which would serve two purposes: reading/recording data from the various sensors, and providing control for the pump and mixer. The National Instruments Labwindows/CVI coding environment was the tool of choice for this undertaking, as it is based on the C programming language and allows for fine control of program flow. Due to the intricacies of communicating with the DAQ and handling the motor control, this software application quickly evolved into an extensive project. A detailed explanation of the application-building process is beyond the scope of this document, but the main highlights are presented here. The complete set of code is provided in the Appendix, and a high-level diagram of the program flow is shown below in Figure 24.

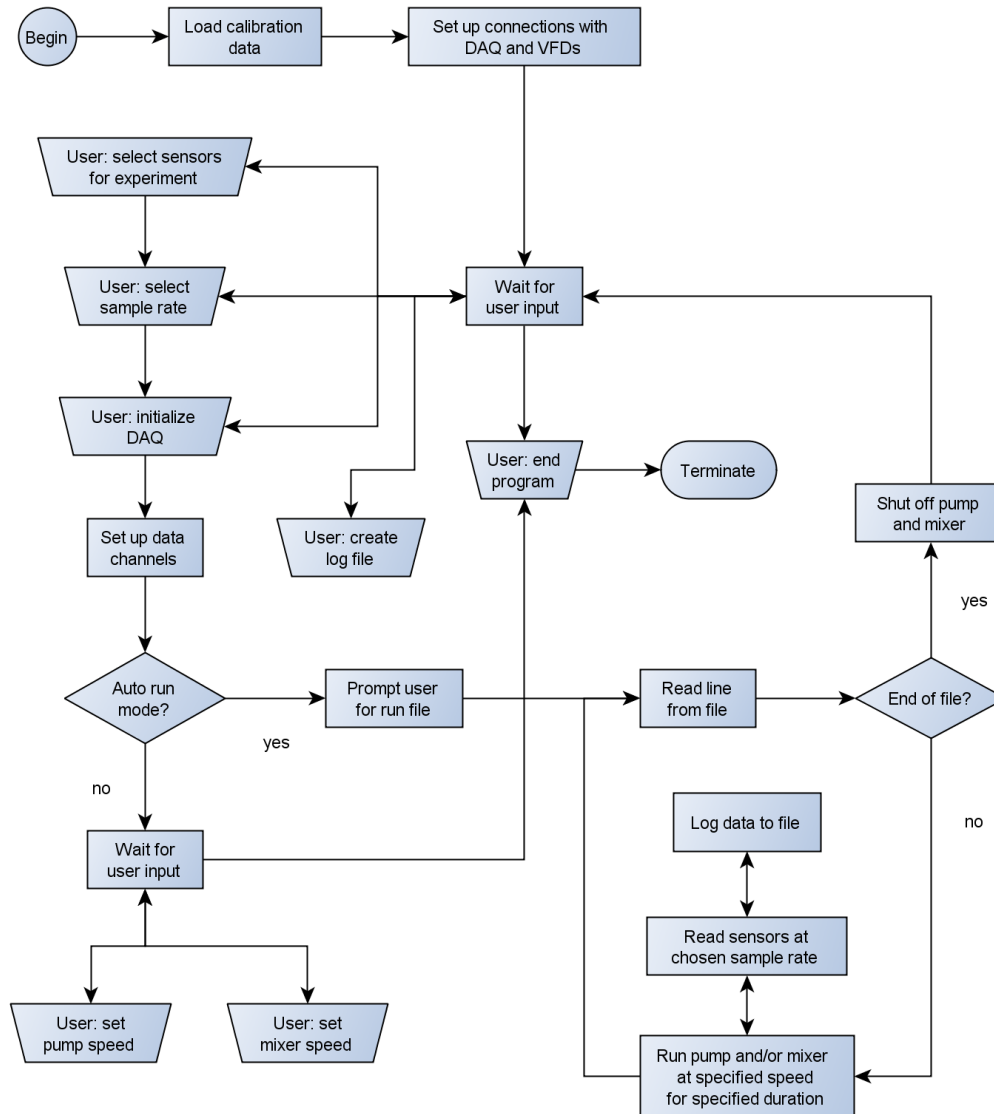


Figure 24 - Software flow diagram

The objective was to create an application that would feature robust functionality, a foolproof interface, stable device connections, and user-friendliness. After numerous tests and revisions, a finalized product was realized. A screenshot is shown below in Figure 25 and labeled elements are described in further depth below.

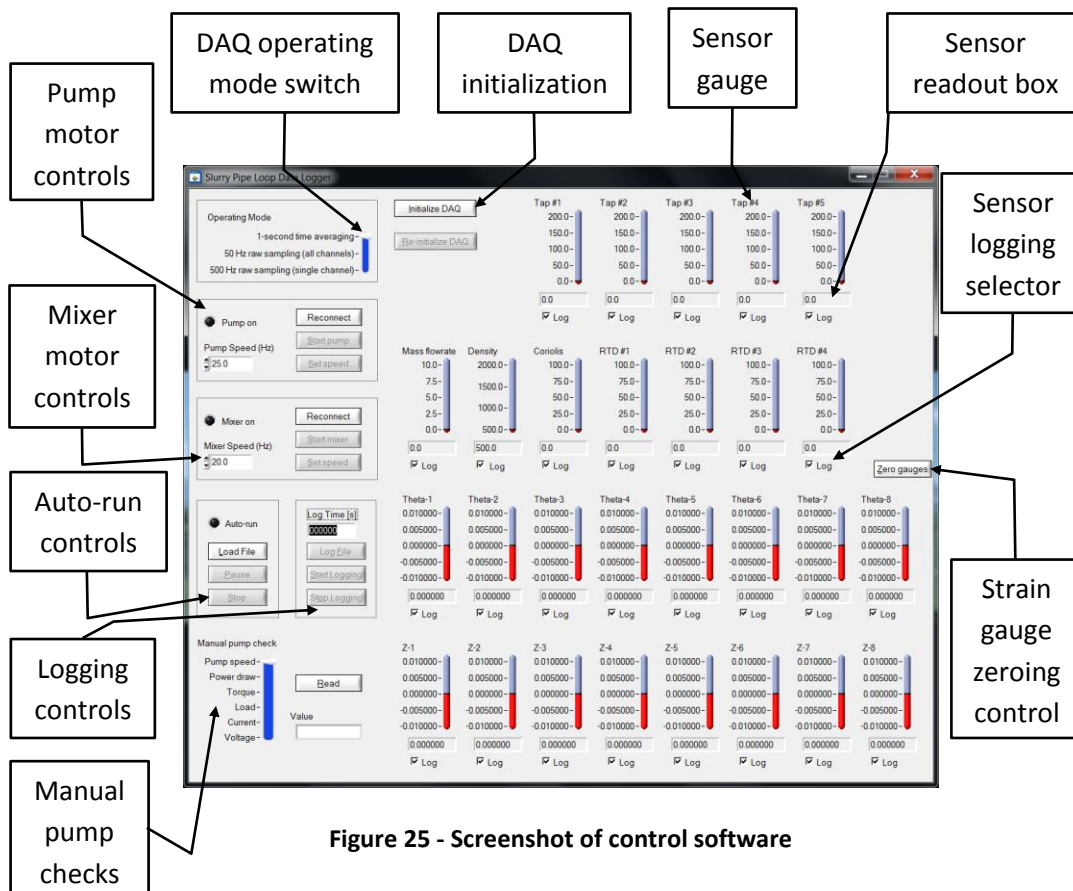


Figure 25 - Screenshot of control software

- DAQ operating mode switch.** This allows the user to select one of the three data acquisition modes displayed. The 9208 module only allows up to 500 Hz data rate, shared across all channels. As there are 8 channels feeding into that module, the default option is to read all sensor data at 50 Hz, and then average the values over 1-second increments. From preliminary testing, flow values tend to change slowly (if at all); hence, one-second data averaging is considered acceptable. If the user desires to observe any smaller-scale trends, there are options to read all data at 50 Hz without the averaging, or else to read from a single sensor at 500 Hz.
- Pump motor controls.** This sub-panel contains controls for starting and stopping the pump, setting the pump speed, and reconnecting to the controller in the case of a dropped connection. Both the pump and mixer motors are controlled by hypertext transfer protocol (HTTP) language over switched network connections. The Ethernet control modules act as web servers over the local network. Communication is accomplished in exactly the same fashion as a web browser would communicate with a web server over the Internet. The software transmits special strings of

characters which instruct the Ethernet module to make changes to the VFD's internal data registers. These registers correspond to a particular property or state of the device (many of which are read-only), such as speed, on/off, torque, load, and many others.

- **Mixer motor controls.** This control has the same functionality as the mixer control.
- **Auto-run controls.** This control allows the user to create “run” files, specifying speeds and time durations for either the pump or the mixer, or both. Once the run file is loaded, the software begins immediately and steps through the run file until its end, at which time the software shuts down the pump and mixer, and stops logging data.
- **Logging controls.** These controls allow the user to start/stop logging data to disk, and to specify the name of a text file which will contain both raw and calibrated data. The data buffer is logged every second, regardless of the DAQ settings.
- **Manual pump check controls.** Functionality has been provided to allow manual reads of the following pump parameters: speed, power draw, torque, load, voltage, and current. These parameters are accessed in the same fashion in which the pump and mixer are controlled – via HTTP communication between the control software and the VFDs. For VFD control, HTTP is robust and serves the purpose well. However, HTTP does not lend itself well to high-speed reads of pump parameters. The main issues are that each parameter must be read separately, and the time associated with a single read can be as long as 1-2 seconds. Consequently, each parameter may only be read approximately once every twelve seconds – i.e. the sample rate is 0.083 Hz. A sample rate of 0.083 Hz makes it difficult to observe the transient nature of power draw when pumping slurry. As a result, it was decided to leave these parameters as optional (i.e. their values would not be recorded along with DAQ data).
- **DAQ initialization.** Once the user has selected the desired DAQ settings and the sensors which are to be logged, the DAQ itself may be initialized. This control sets up all channels and their corresponding data structures. The DAQ communications are robust, but functionality has been included for resetting the DAQ in case of a dropped or interrupted connection.
- **Sensor gauges.** These displays show calibrated sensor data graphically in near real-time (updated every second).

- **Sensor readout boxes.** These displays show the same data as the sensor gauges, but in text format.
- **Sensor logging selection box.** These check boxes are used to tell the software which sensors to collect data from, both for display and for logging purposes.
- **Strain gauge zeroing control.** This button is used to zero out the strain gauges prior to an experiment. The gauges are all connected to quarter-bridge circuits, which means that there is no temperature correction built into the circuit. A change of a few degrees will result in large changes in strain.

Calibration constants for each instrument have been stored in the software. This allows raw sensor data to be corrected immediately after it is read from the DAQ. Both raw and corrected data are stored together in the log file.

4.8 Experimental Procedure

There are several desired outcomes for the experimental portion of this research. They are:

- To verify the assumption of linear concentration/velocity changes across the shear interface layer
- To obtain an empirical constant for the sliding-abrasive wear portion of the wear model (to aid in determining the rate of mass loss as a function of bulk concentration and bulk velocity)
- To examine the interactions between the pipe wall and sand particles in the shear interface layer (i.e. particle velocity and impact angle, to aid in determining the rate of impingement wear)
- To learn whether abrasion-induced shear stresses may be determined from measurements taken at the outer surface of the pipe wall

The experimental procedure consists of three distinct aspects: wear testing, optical particle tracking, and strain measurements. Strain measurements have been discussed earlier; the remaining testing is described in further detail below.

4.8.1 Wear Testing

Specially-constructed wear specimens are mounted in the removable test section of the laboratory pipe loop. Each specimen is subjected to slurry wear at varying flow rates and bulk solids concentrations over a set time duration. From preliminary tests, a test duration of three hours is sufficient to observe and quantify wear on the specimens.

For the purpose of these experiments, it is desirable to observe flow with a moving bed as well as fully suspended, non-symmetric flow, as those flow conditions are commonly found in industrial slurry pipelines. Using these flow conditions may increase the probability of being able to observe both abrasive wear and impingement wear. From preliminary tests, 30 Hz is an acceptable minimum speed for low-concentration slurries. However, to avoid settling and/or blockage near the vertical pipe sections during higher-concentration runs, the minimum has been adjusted to 40 Hz. 50 Hz and 60 Hz have been selected as the remaining speeds, mainly to provide sufficient difference in flow rates.

Mass loss is quantified by measuring the weight of each wear specimen before and after testing. In an industrial setting, material is pumped through the pipeline only once; in this experiment, the same material is circulated through the pipe loop repeatedly. This fact has some significance: the initial angularity of the sand particles decreases with time as the particles repeatedly impinge and/or abrade against the pipe walls, rotating pump components, and each other. From the literature, it is expected that this decreasing angularity results in a somewhat decreasing wear rate. It is also possible that as abrasion progresses in the wear specimens, the increasing presence of worn urethane fines may raise the viscosity and introduce some non-Newtonian behaviour in the slurry. This in turn may have a lessening effect on the wear rate. However, it would require extensive testing to identify the effects of particle angularity and material fines. This research is only concerned with the effects of bulk solids concentration and bulk flow rate, and so these secondary effects are ignored. It is assumed that the wear rate remains constant with time. This assumption is reflected in the practice of averaging the mass loss over the duration of the experiment.

From observations gained during preliminary runs, it is important to maintain a closed-loop (i.e. mixing tank not open to the atmosphere) pipe system, rather

than an open-loop system. The main reason for this is that this allows pump flush water to pressurize the mechanical seal, which in turn helps to suppress pump cavitation. From the pump curve, a maximum of approximately 13 feet NPSH (net positive suction head) is required for the experimental operating conditions. 13 feet NPSH is not possible to achieve under open-loop conditions with the available lab space. If the loop is closed, however, it is possible to raise the pipeline pressure to a point where cavitation is nearly eliminated. Closed-loop conditions have been achieved by isolating the mixing tank and opening the bypass line. The main problem with this arrangement is that it becomes difficult to remove any air bubbles from within the pipe. Another potential issue is that sand may not be evenly mixed into the carrier fluid at the onset of the experiments. Both of these issues may be resolved by running the slurry in open-loop conditions (i.e. slurry passes through the open mixing tank) for several minutes to allow any air to escape through the mixing tank, and also to allow sand to be mixed evenly through the carrier fluid. Once this initial stage has completed, the loop may be closed and the experiment may be commenced. To enhance sand mixing, the mixer is engaged while running in open-loop conditions. The final – and most important – issue arising from closing the loop is related to the solids concentration. During the setup of an experiment, the loop is filled with fresh water through the mixing tank. Since the underside of the mixing tank is located below the height of most of the piping, the level in the tank rises at the same time that the pipes are filling. Hence, the water level in the tank is used to indicate the volume of water in the entire system. When the loop is in the “open” state, the mixing tank acts as a large reservoir of fluid. As slurry is pumped through the mixing tank, sand is mixed with the reserve fluid, effectively diluting the bulk concentration. Obviously, if the mixing tank is isolated from the loop, the available fluid volume decreases significantly. The exact volume of the pipes themselves is unknown and must be estimated from the geometry of its components (or, in some cases, from CAD-based solid models). A calculated estimate of the volume of the closed pipe system is 62 L.

In order to help gain an understanding of any concentration-related effects, wear rates should be evaluated at several concentration values. City water is used for the carrier fluid. Two concentration values have been arbitrarily chosen: 5wt% and 10wt%. These values correspond with 300 L of water mixed with 15.8 kg and 33.3 kg of sand, respectively. Note that if the mixing tank is isolated from the pipe loop, these quantities of sand correspond to bulk concentration values of 21.5wt% and 38.4wt%, respectively.

4.8.2 Optical Particle Tracking

In the interest of building a usable slurry wear model, it is imperative to confirm the existence of the shear interface layer, and to gain understanding of its physical characteristics. To aid in these goals, an optical technique known as particle tracking velocimetry (PTV) is employed to track the flow of individual sand particles within the slurry flows.

During optical experiments, the variables of interest are:

- Controlled: bulk solids concentration, particle density, particle size distribution, carrier fluid properties
- Manipulated: pump speed
- Responding: bulk flow rate, particle velocity, particle distribution

PTV is an optical fluid velocity measurement technique which involves the use of one or more digital cameras to track the displacement of particles within the test fluid. Typically, a particle-tracking experiment involves the following elements:

- A test fluid. Most often, the fluid in question follows complex flow patterns.
- Tracking particles. These are generally small particles with a density which is near to that of the test fluid. This allows the particles to more closely follow the flow of the fluid, without themselves influencing the fluid flows. It is also desirable that the particles be optically reflective to enhance contrast. High contrast is necessary for the particles to stand out from the fluid background. Generally speaking, it is desirable to use low concentrations of tracking particles, as this allows for easier particle tracking.
- An illumination source. This is a requirement in most cases, as it can be difficult to obtain sufficient contrast without external lighting. Several methods of lighting exist, including strobe lighting, back-lighting (in the case of shadowgraphy), or a laser. The choice of light source depends primarily on the stated objective of the experiment. For instance, a laser light sheet may be used to illuminate a thin planar slice of a complex flow field, while strobes and back lights illuminate the entire flow field.
- A digital imaging device. Care must be taken in selecting the imaging device. These range from commercial, feature-rich digital SLR cameras to stripped-down, high-performance digital cameras. Experimental

properties such as field of view, resolution, depth of field, frame rate, shutter speed, spectral range, and flow velocity are all important factors to keep in mind when selecting the imaging device. One or more cameras may be employed, depending on the nature of the flows and the information one wishes to obtain (i.e. two-dimensional or three-dimensional motion).

In the design of this optical experiment, it was important to keep the following points in mind:

- There must be as little deviation from natural flow patterns as possible. Hence, it is necessary to utilize a clear viewing section, the interior surfaces of which are flush with adjacent pipe surfaces.
- In this case, the objective was not to determine fluid flow patterns, but to track the motion of slurry particles. Hence, sand particles serve as the tracking particles in this case. Given the nature of settling slurry flows, it would be extremely difficult to track additional particles. Garnet particles are very dense with respect to water (average specific gravity of 4.0, or approximately 3980 kg/m^3) and tend to quickly settle out of the flow to form an optically opaque moving bed formation at the lower pipe surface. Above the bed (shear interface layer), particles may still be strongly concentrated, and individual particles may be difficult to resolve in this region. Hence, bulk concentration must be kept reasonably low to enhance particle resolution.
- Strong optical contrast must be maintained in order for the particles to be detected during post-processing. In this case, constant back-lighting was used rather than front-illumination, as it creates high-contrast particle shadows against a bright background.

The objective of these imaging experiments was to identify particle motion (speed and angle) above the moving bed formation. It was hoped that the concentration values of the wear tests could be reapplied to the particle imaging tests, but a preliminary test showed that the 5wt% value was too low for this application. The final result was that particle imaging was achieved at several flow rates, using a single concentration value.

The specifications for the camera are listed below, as given in the product literature:

- Camera: MotionPro (PCI) camera, manufactured by Redlake MASD

- Sensor: 1280 x 1024 pixel CMOS (variable active sensor area)
- Frame rate: 500 - 16000 fps, based on active sensor area
- Double-framing: no

The complete setup for this experiment is shown below in Figure 26.



Figure 26 - Setup for optical particle-tracking experiments

It is important to note that the combined natures of settling slurry flows and of these experiments only allow for observation of the vertical and axial components of particle velocities. The presence of the moving bed creates optical conditions in which it is impossible to resolve individual particles when viewed from above. Viewing from the side means that in the shear layer, the normal component of particle velocity will also be normal to the camera lens and therefore will not be observable. While this is unfortunate, it may be possible that the vertical and axial velocity components serve as indicators of the nature of the lateral velocity components.

Through the use of particle tracking, it is expected that the following will be observed:

- Particle distribution changing from a moving bed to a heterogeneous (suspended) distribution as pump speed increases
- Particle motion showing increasing randomness with height in the shear layer, and with increases in pump speed

- Particle velocity increasing with height in the shear layer

High-speed video was shot at 1500 frames per second, using an active sensor area of 1280x640 pixels. DaVis software was used to process the video frames to extract velocity data. Final data processing was accomplished in MATLAB. Image processing is discussed in a later section.

5 System Calibration and Commissioning

5.1 Introduction

Prior to conducting experiments, calibration of sensors and commissioning of equipment were completed to confirm that all was functioning as intended. It was essential to ensure the integrity of the data being reported by all sensors. This section details the procedures taken towards those objectives. Also discussed are any issues which arose, and the steps which were taken to deal with them.

5.2 Calibration

5.2.1 Pressure sensors

Pressure taps were calibrated using an Omega DPI610 high-accuracy pressure calibrator. The device itself had been factory calibrated and was rated for 0.025% accuracy. Each sensor was threaded into a brass fitting installed on the calibrator. A built-in plunger pump was used to raise the static air pressure within the device. The plunger raised the pressure in very large increments; fine adjustments were made using a threaded dial. During this process, each sensor was wired into the DAQ. The current output of each sensor was read into National Instruments Measurements and Instrumentation (NI-MAX) software. This data was saved along with corresponding input pressure values. In this fashion each sensor was calibrated over its rated range of 0-200 kPa, in increments of 10 kPa. Pressure calibration data is presented below in Table 1 and Figure 27. The response of each sensor is readily seen to be linear, which allows for easy computation of “true” values.

Table 1 - Pressure transducer calibration constants

	Slope (m)	Offset (b)	Correlation coefficient
Pressure 1	$1.246 \cdot 10^4$	-50.34	1.000
Pressure 2	$1.247 \cdot 10^4$	-50.89	1.000
Pressure 3	$1.244 \cdot 10^4$	-50.19	1.000
Pressure 4	$1.243 \cdot 10^4$	-50.03	1.000
Pressure 5	$1.243 \cdot 10^4$	-49.66	1.000

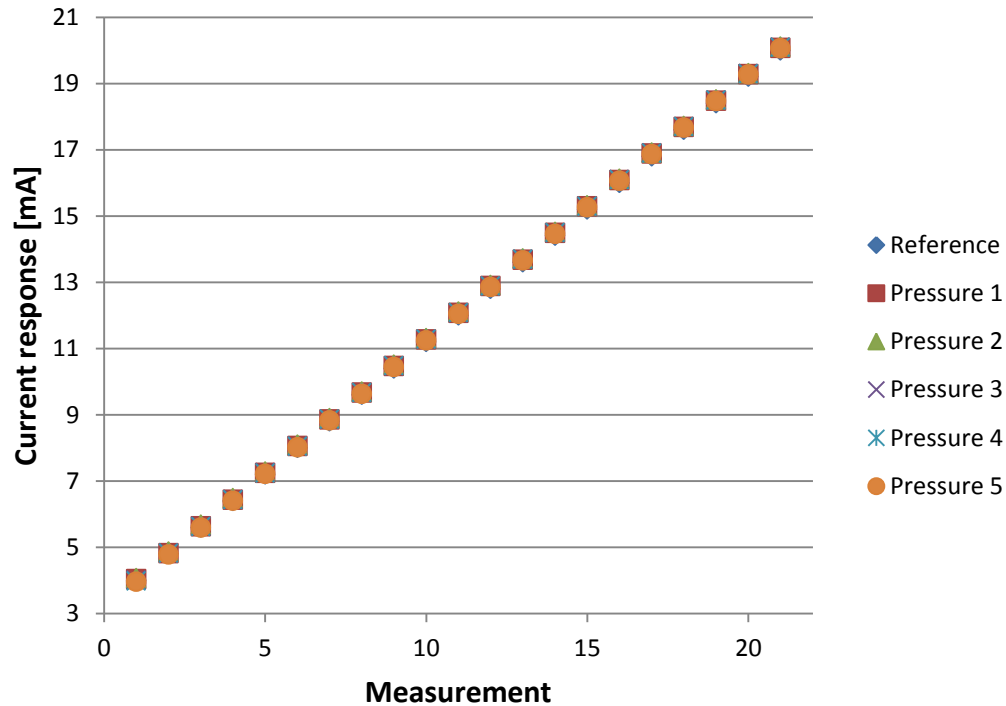


Figure 27 - Pressure transducer calibration curves

5.2.2 Temperature Sensors

RTD temperature sensors were calibrated using a factory-calibrated Cole-Parmer water bath with a built-in temperature control unit. The RTDs were suspended in the turbulent water bath, and their outputs were read into NI-MAX software. Fluid temperature was adjusted by manipulating the unit's set point. The response time of the control unit appeared to be high, as the fluid bath experienced significant temperature overshoot, especially at elevated set points. As the cooling function of the unit did not appear to be functioning correctly, fluid temperature stabilization required significant amounts of time. The

temperature of the fluid was allowed to stabilize before taking measurements, which were saved along with the sensor readings. Temperature was increased in 5°C increments. All four sensors were calibrated simultaneously, in order to better synchronize their calibrated outputs.

As mentioned, the cooling function of the water bath unit did not appear to be operational at the time of calibration. City water was chosen as the fluid medium, but since the calibration took place in summer, the lowest achievable temperature was just below 20°C, which severely limited the lower range of calibration. At the time of calibration, several preliminary tests had been conducted on the slurry pipe loop, and from these early results it was not expected that process temperatures would exceed 40°C. Therefore, that was the upper limit of calibration. Due to material changes in later tests, temperatures on the order of 57°C were observed during testing. In hindsight, an upper calibration limit of 60°C would have been preferable. However, it was known that these RTDs had been previously used by another student on an extensive research project, and had been successfully calibrated over a range of 10-90°C. He reported excellent linear response over the entire range [Evans, 2012]. With this knowledge it was felt that the RTD readings could be used with confidence. Calibration information for all four sensors is given below in Table 2 and Figure 28.

Table 2 - RTD calibration constants

	Slope (m)	Offset (b)	Correlation Coefficient
RTD 1	0.759	5.24	1.000
RTD 2	0.759	5.23	1.000
RTD 3	0.756	5.40	1.000
RTD 4	0.756	5.40	1.000

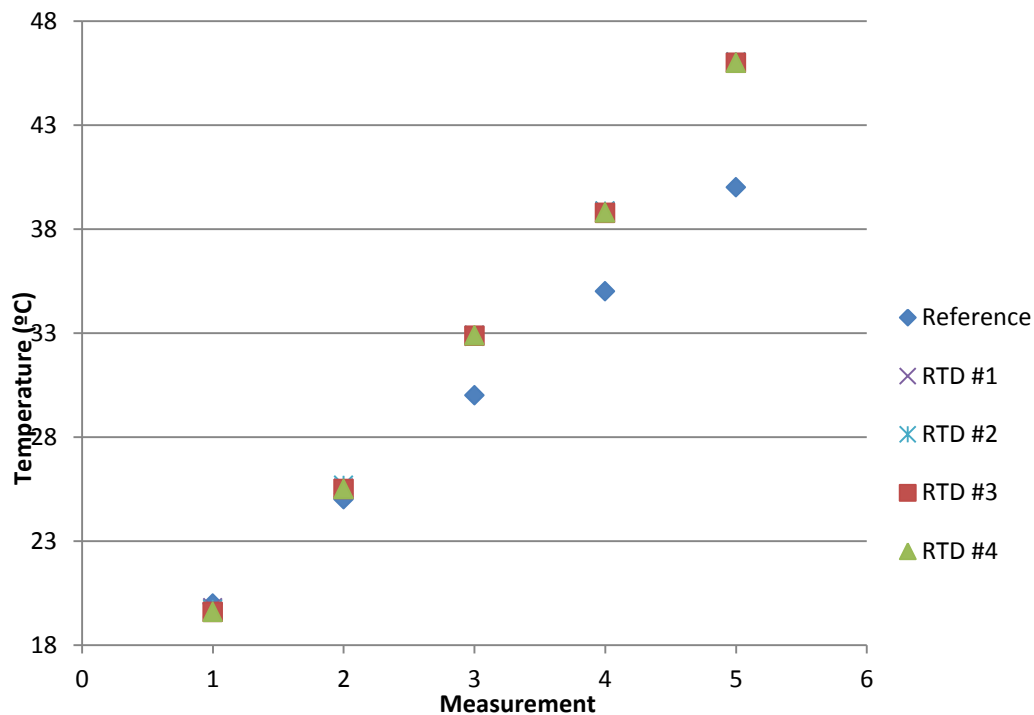


Figure 28 - RTD calibration curves

5.2.3 Coriolis Flow Meter

Prior to its installation in the slurry pipe loop, the Coriolis flow meter was known to have been factory-calibrated. It was decided that a simple check would be performed to ensure that the device was functioning within reasonable bounds. The data readings of primary importance are density and mass flow rate. Temperature may also be reported, but the primary sources of temperature data are the RTDs. The device's calculations of density and flow rate are independent of thermal measurements. Hence, the Coriolis meter's thermal measurements were not checked for accuracy.

Density was verified by filling the loop with water at 20°C and running it for several minutes while taking readings from the Coriolis meter. At that temperature, the density of water is 998 kg/m³, and the device gave steady readings of 996-997 kg/m³. This reading was deemed acceptable, since the device is rated for a maximum measured error of ±20 kg/m³. On later occasions, density measurements were taken while pumping sand slurry through the loop

at elevated speeds; these readings were also very close to the previously calculated density values.

5.2.4 Strain Spool

Eight 90° strain rosettes were mounted to an acrylic pipe spool whose walls were thinned to approximately 1 mm. The rosettes were wired to the DAQ by means of two NI-9236 quarter-bridge strain modules. Because of the manner in which the data acquisition software communicates with sensors, each DAQ initialization automatically causes the existing state of each strain gauge to be set as the new reference (“zero”) point, similar to the tare function on a weight scale. While this “zeroing” effect is useful as a means of removing sensor bias, there are still several factors which must be taken into account:

- **Material properties.** The substrate material is cast acrylic. The modulus of elasticity is given to be 2.8-3.3 GPa, the Poisson’s ratio is 0.37, and the shear modulus is 1.7 GPa [MATWEB, accessed April 6, 2013]. A modulus of elasticity value of 2.8 GPa was utilized in calculations, which gave good fit, as shown later.
- **Gauge factor.** This is the gain value which is used to translate gauge output into strain values. For the gauges in this project the value is given to be 2.17 (value supplied by the manufacturer on the back of the package).
- **Excitation voltage.** The voltage of the circuit to which the gauges are connected is an important factor in determining their output. The gauges are connected to a DAQ module with an excitation voltage given to be 3.3 V.
- **Linearity.** Gauges are designed such that their output responds linearly to strain. In practice this depends on several factors, including the surface preparation, adhesion, and soldering processes.
- **Temperature correction.** The strain output of the gauges is rated for a specific temperature. Above or below that value, the resistance of the gauges changes slightly. The strain gauges in this project are rated for 24.9°C. A function describing their output at varying temperatures (supplied by the manufacturer on the back of the package) is given to be $a_0 + a_1T + a_2T^2 + a_3T^3 + a_4T^4$, where

- $a_0 = -2.49 \cdot 10^1$
- $a_1 = 2.38 \cdot 10^0$
- $a_2 = -6.42 \cdot 10^{-2}$
- $a_3 = 3.77 \cdot 10^{-4}$
- $a_4 = -4.52 \cdot 10^{-7}$
- T is the temperature, given in degrees Celcius

Applying the manufacturer's correction equation, the impact of temperature on the strain readings over the applicable range of temperatures is shown below in Figure 29. Note that this applies only to the gauges themselves, not to the material to which they are mounted. Separate calculations must be completed to determine the thermal strain on the acrylic substrate.

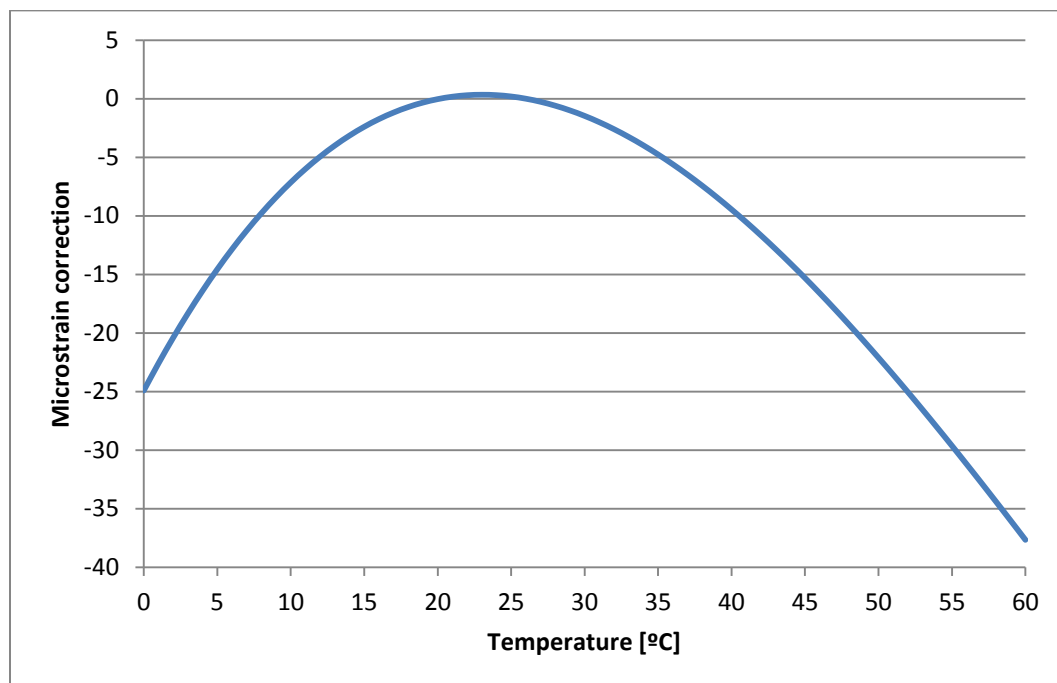


Figure 29 - Change in strain readings with temperature

To calibrate the strain spool, two tests were performed. The first involved applying an axial force of varying magnitude. This was accomplished by positioning the spool vertically on a solid surface, and resting a weight on the free end. Masses of 5, 10, and 15 kg were applied, and the strain gauge readings were recorded. The output is given below in Figure 30 and Figure 31.

The visibly nonlinear response is surprising. Another surprising result is the range of gauge responses at each applied force value. Some slight variance was anticipated, but such extreme variance is disconcerting. One possibility is that the spool may have been loaded slightly off-center. Slight shifts in the location of the weight's center of mass would induce bending stresses in the spool, which may explain the "hourglass" shape of the calibration curves. However, there is good probability that these results may be attributed to variations in tube wall thickness. Variations are normally present due to manufacturing tolerances. The tube wall was thinned down from the outside to enhance strain sensitivity; if any thickness variations were present, this would have intensified their effects, resulting in relatively large variations in wall thickness. If this is the case, it may be very difficult to gain useful information from the data obtained from the strain spool.

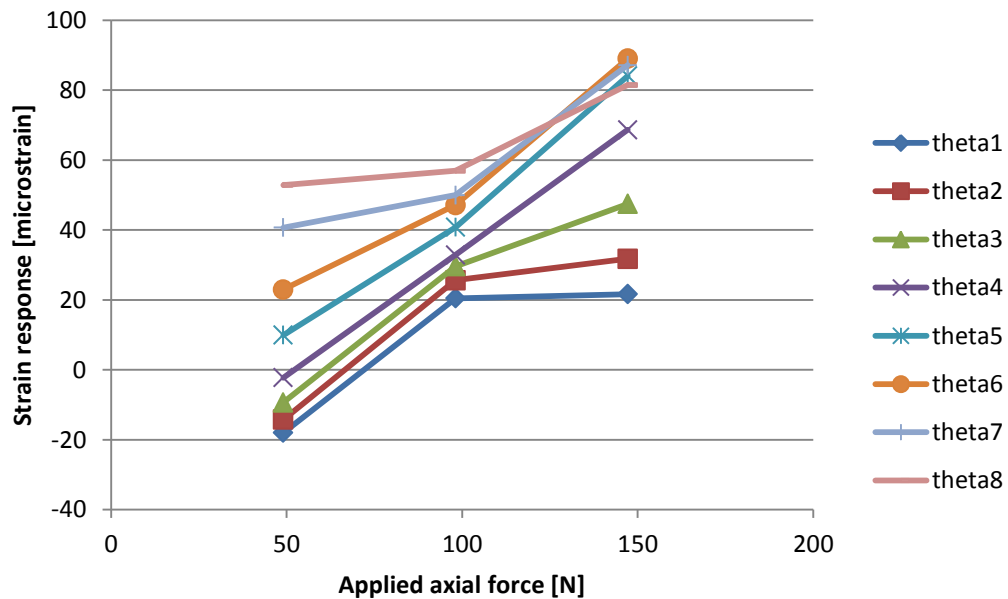


Figure 30 - Calibration results: axial strain

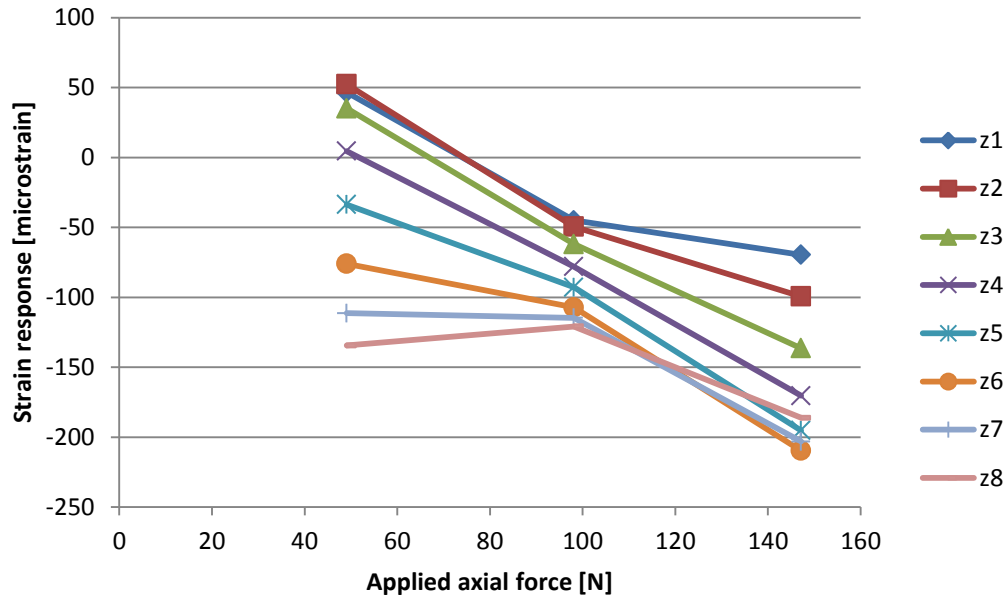


Figure 31 - Calibration results: circumferential strain

The second calibration test involved mounting the spool to the pipe rig and running clean water through it. The rate of flow was varied by adjusting the pump speed, and strain readings were recorded. These readings were compared with values calculated from the Lamé equations and Hooke's Law. Results are provided in Figure 32 and Figure 33. Flow-induced wall shear stresses were not included in the calculations. All strain values have been corrected both for thermal expansion of the material and for thermal gauge resistance effects. A sample calculation is provided in the Appendix.

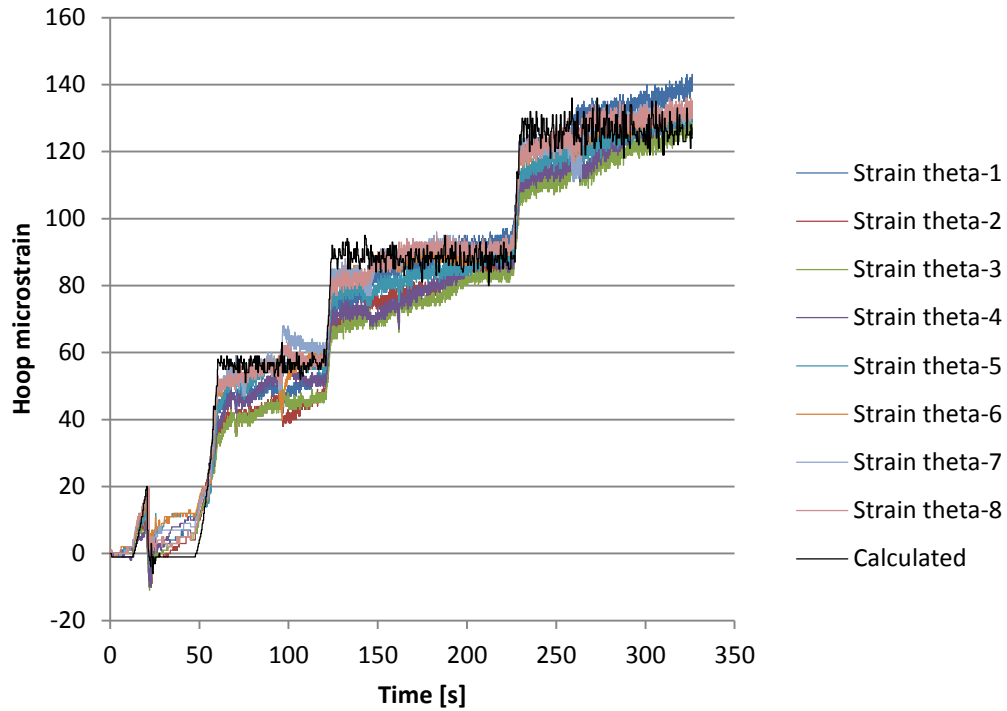


Figure 32 - Strain calibration: hoop strain

The hoop strains match calculated values loosely, but the strain response appears to have a transient nature. Strain readings creep steadily upwards while pump speed is held constant. One possible explanation is that the acrylic material is susceptible to viscoelastic creep deformation – a behaviour commonly associated with polymers. Acrylic is listed as having a creep modulus of 1.4-2.7 GPa (1 hr), or 1.0-1.8 GPa (1000 hrs) [MATWEB, accessed April 6, 2013]. Verification of creep behavior would require several minutes at each pump speed to observe whether the strain readings approach a steady-state value.

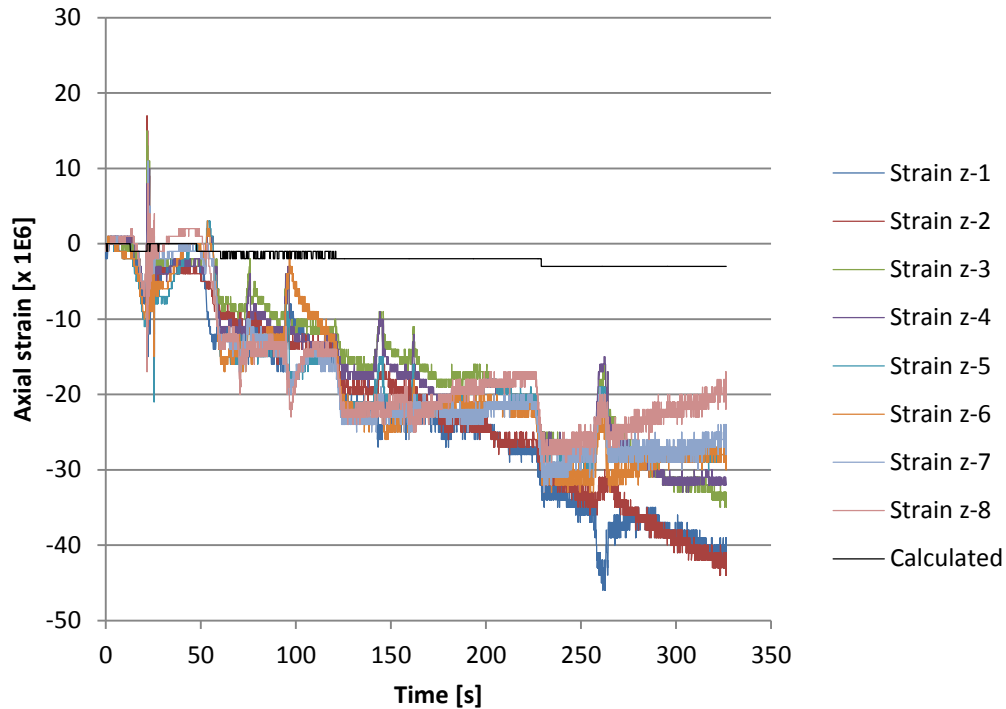


Figure 33 - Strain calibration: axial strain

While hoop strains showed minor deviations from calculated values, axial strains show significant deviation. Calculated axial strains were based entirely on pressure fluctuations – flow shear stresses were not accounted for. It is expected that these deviations correspond with shear strain at the tube wall, which is the very quantity which the strain spool was designed to measure. However, it is troubling to note the manner in which pressure disturbances cause certain gauges to read high and others to read low. This may be due to non-uniform axial clamping pressure on the spool, as well as non-uniform tube wall thickness. Either of these would result in non-uniform resistance to axial load. This would lead to bending of the spool under pressure, yielding gauge readings similar to those shown here. It is expected that this is a dominant source of potential error compared with the viscoelastic behaviour described earlier.

5.2.5 Optical Equipment

DaVis software was used to control the optical equipment and read out the images. In order to obtain valid data from the camera, however, it was necessary to calibrate it. In this case, calibration provides the software with a relationship between physical space and pixel space. This was accomplished by means of a calibration target wrapped around the pipe visualization section, shown below in Figure 34. The target was a sheet of paper printed with a standardized, high-contrast pattern of dots spaced at precise intervals. The camera was directed at the target, and target specifications were entered into the software. The software subsequently ran a self-calibration process, and the resulting calibration factor was 72:5 (pixels/mm), as reported by the software.

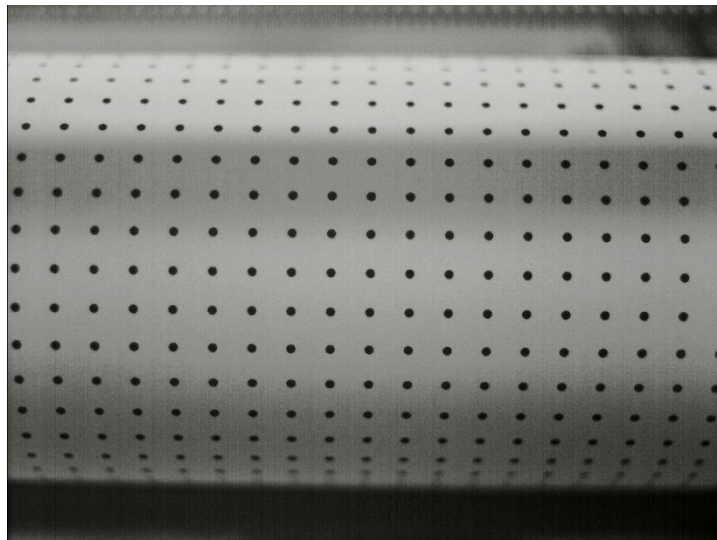


Figure 34 - Optical calibration target

5.3 Commissioning

Prior to the commencement of wear testing, preliminary test runs of the pipe loop were completed to commission it and its components. The functionality and reliability of the sensors, pump, and control software were of particular importance. The initial design of the entire loop had been completed by

previous students [El-Sayed, 2010], and its components had been assembled as per their specifications. At the beginning of this research, it had not yet been employed for testing. Thus it was important to test whether the loop's specifications were, in fact, appropriate for the intended use. This section details the steps which were taken to ensure the reliability of the equipment, as well as the integrity of the data which would be obtained from it.

5.3.1 Pressure Sensors

Functionality of the pressure transducers was checked to verify that they were the correct sensor for the intended experiments. A dense slurry mixture was pumped through the pipe loop at full speed, and pressure readings were observed using a pre-calibrated pressure transducer. To simulate a pipe blockage, the mixing tank return valve was briefly closed, then reopened. A large pressure spike was observed; however, pressure readings remained well below 200 kPa. During normal operation at full pump speed, pressures were below 100 kPa.

In order to measure the pressure drop across the entire pipe loop, five transducers were installed into the pipe rig. To allow pressure measurement immediately upstream and downstream of the pump, steel spools were designed and built to be mounted to the pump. A test run was completed on the pipe loop, and the pressure readings were recorded. The results are shown below in Figure 35. Pressure transducers are numbered in order of their position downstream from the pump.

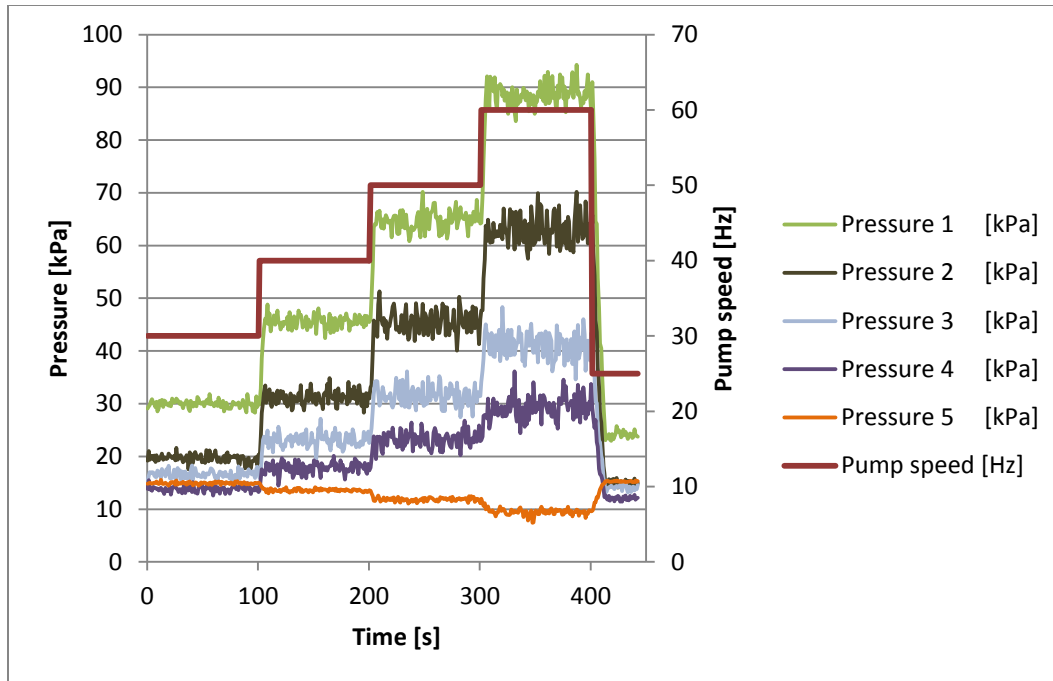


Figure 35 - Pressure readings for a water flow test

5.3.2 Temperature Sensors

The RTD temperature data was not deemed essential to the success of the wear experiments. However, this data was included to provide any additional insights into the wearing process. During strain testing, temperature data was useful for correcting the gauge readings. Every care was taken to ensure that these sensors reported accurately.

Tests were run to observe whether the temperature differential across the pump could be measured using the RTDs. Water was pumped through the loop at a pump speed of 25 Hz, and the results are shown below in Figure 36. A temperature differential may be clearly observed from the plot. It was later observed, however, that with time this differential diminishes and eventually vanishes as the system temperature reaches steady state. This is especially true at elevated pump speeds. This is shown below in Figure 37.

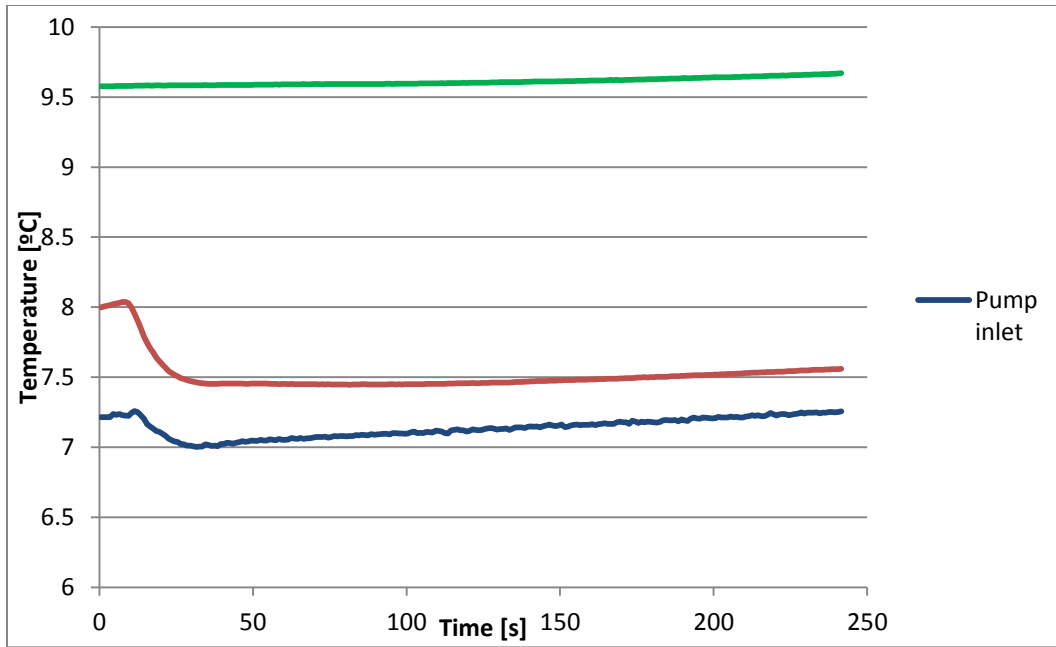


Figure 36 - Temperature differential across the pump

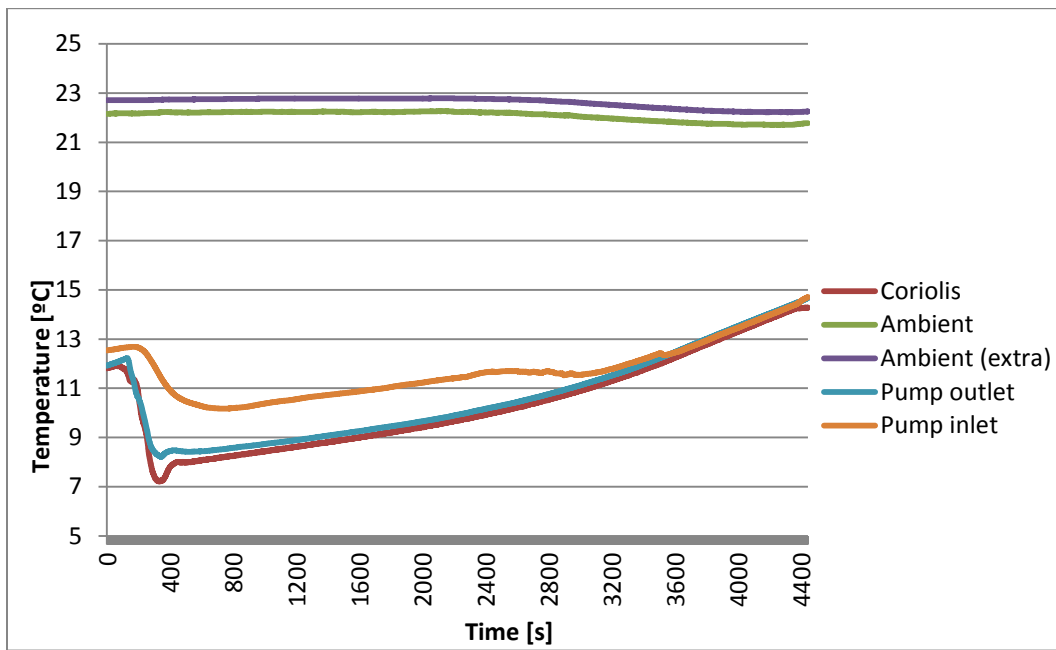


Figure 37 - Temperature differential at steady state

5.3.3 Pipe Loop System

During preliminary slurry testing, water levels in the mixing tank decreased noticeably over a day's time. This was attributed to both evaporation and splashing within the tank. Due to head losses, process water temperature often rose as high as 57°C during slurry runs. When the rig was operated in open-loop conditions (flow routed through the mixing tank), water evaporated quickly from the mixing tank, especially at warm ambient temperatures. Due to the original piping layout, slurry entered the mixing tank approximately 50-75 cm above the mixture level in the tank. Over an extended test run, large quantities of water and sand splashed out of the tank. These issues were a concern because lower water levels resulted in variability of test conditions and led to inconsistent test results.

Both issues were rectified by operating the rig in closed-loop conditions (flow routed around the mixing tank). In addition, piping was modified so that slurry returned to the mixing tank at a point below the mixture level. Drawings may be found in the appendix. If thermal wear effects are studied in the future, the installation of a chiller / heat exchanger system would be valuable for maintaining steady process temperatures.

5.3.4 Wear Materials

A slurry of #8-12 grit garnet sand was tested at 13.5% concentration by volume. After a 3.5 hr run, aggressive wearing was readily observed over the lower surface of the test specimen. As shown below in Figure 38 (before testing) and Figure 39 (following testing), light degradation of the particles was observed, yet many particles retained their aggressive edge.



Figure 38 - Garnet sand particles prior to testing



Figure 39 - Garnet sand particles following 3.5 hrs of testing

The wear specimen underwent testing as well. A 3.5-hour wear test of a urethane-coated specimen resulted in excellent visible scarring, as shown below in Figure 40.

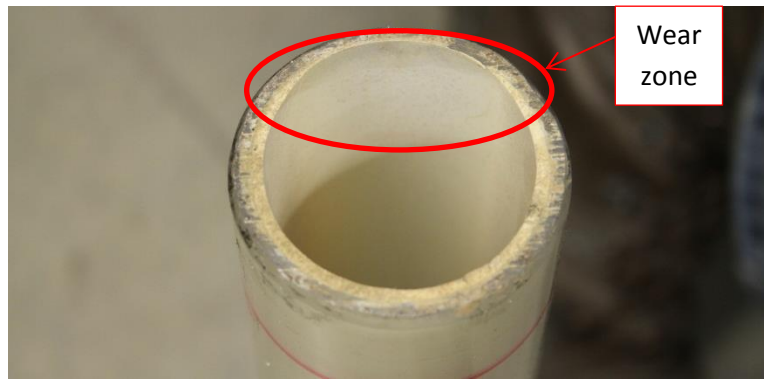


Figure 40 - Wear specimen after testing

5.3.5 Control Software

Special attention was given to ensuring that the control / data acquisition software functioned as intended, free of errors. Extensive testing was conducted on each of its functions, and several revisions were made before the software was deemed ready for use. It was important to ensure the following points:

- Software connects reliably with the DAQ
- Software connects reliably with the VFD controllers, and the integrity of the connection is maintained indefinitely
- All controls function flawlessly as intended
- Sensors faithfully return good data
- Data readings are presented on the screen in a format which is easy to read at a glance
- No data is lost in transition from the DAQ to the log file
- Auto-run (timer) features work consistently
- Any run-time errors are caught and dealt with gracefully
- All software procedures are executed as efficiently (especially with regards to memory and execution time) and effectively as possible

Specific problem areas were:

- Communication with the VFD controllers was problematic at times due to dropped connections and erratic behaviour. This was mainly due to:
 - HTTP connection time-outs
 - insufficient delay times between data transmissions

- attempting to utilize a single HTTP connection to communicate with both the pump and the mixer
- Software crashed when reading from all sensors, due to high memory usage and low available memory resources.

These issues were mostly corrected, although memory usage continued to be a problem when collecting data from all available sensors. To prevent errors from occurring, processes running in the background were kept to a minimum. There was also the possibility of a memory leak due to improper return of memory to the stack. Consequently, there was insufficient memory for consecutive experimental runs, and the software required a restart between runs.

5.4 Equipment Issues

During the commissioning process, several equipment issues arose. These are listed briefly below, and discussed in depth in the Appendix.

- Pump
 - The mechanical seal was damaged and required replacement
 - A flush-water system was required to cool and clean the mechanical seal during operation
 - The shaft required oil lubrication
 - Cavitation was noted during normal operation
- Coriolis meter
 - The device began to report consistently faulty data
 - Over the course of a 3-hour run, density values drifted significantly

6 Experimental Results and Discussion

This chapter presents the results of wear testing, strain testing, and optical particle tracking experiments. Data processing steps are documented, and brief discussions are provided regarding development of wear models.

6.1 Wear Testing

Twelve experimental runs were completed to determine wear rates under specific flow conditions. Two slurry concentration values were tested at three pump speeds, resulting in six experimental conditions. Each run was completed twice to assess repeatability. Experimental conditions are listed below in Table 3.

Table 3 - Experimental run properties

Trial	Concentration [vol%]	Pump speed [Hz]
1	6.4%	40
2	6.4%	40
3	6.4%	50
4	6.4%	50
5	6.4%	60
6	6.4%	60
7	13.5%	40
8	13.5%	40
9	13.5%	50
10	13.5%	50
11	13.5%	60
12	13.5%	60

A photo of two representative wear specimens is shown in Figure 41. The specimen at left was tested at a pump speed of 50 Hz and a slurry solids concentration of 6.4% by volume, while the one at right was tested at 50 Hz pump speed and 13.5% solids concentration by volume. In both specimens, the wear scarring (whiter region) is clearly visible. During testing, the specimens were oriented on the pipeline such that the wear scars occurred at the bottom

of the pipe. All specimens displayed the trough-like wear profile which Schaan *et al.* (2007) noted on oilsand hydrotransport lines. No impingement wear is visible at the edges of the sliding bed region. This apparent domination of sliding-abrasive wear may be attributed to the high specific gravity and coarse particle size of the garnet sand, both of which contribute to a high settling velocity. The results of Schaan *et al.* (2007) indicate that a stationary solids bed formation may be required in order to adequately observe impingement-dominated wear scarring.



Figure 41 - Sample wear specimens after undergoing testing

The mass of each wear specimen was measured on a scale before its respective test. The scale was capable of measuring with a resolution of 0.1 g. Each specimen's mass was measured three times in order to assess repeatability of measurements. Following the experiments, several days' time was allowed for the specimens to dry, to ensure that the final mass did not include any water. Specimens were weighed once again in the same manner as before. Assuming constant wear rates over the duration of the experiment, the mass difference was divided by the test time to obtain an average wear rate for that run. Average wear rate values are plotted below in Figure 42. Data is segregated by slurry concentration. Trend curves have been added as an aid in better understanding the data. Here, quadratic relations appear to provide better fit to the data than linear relations.

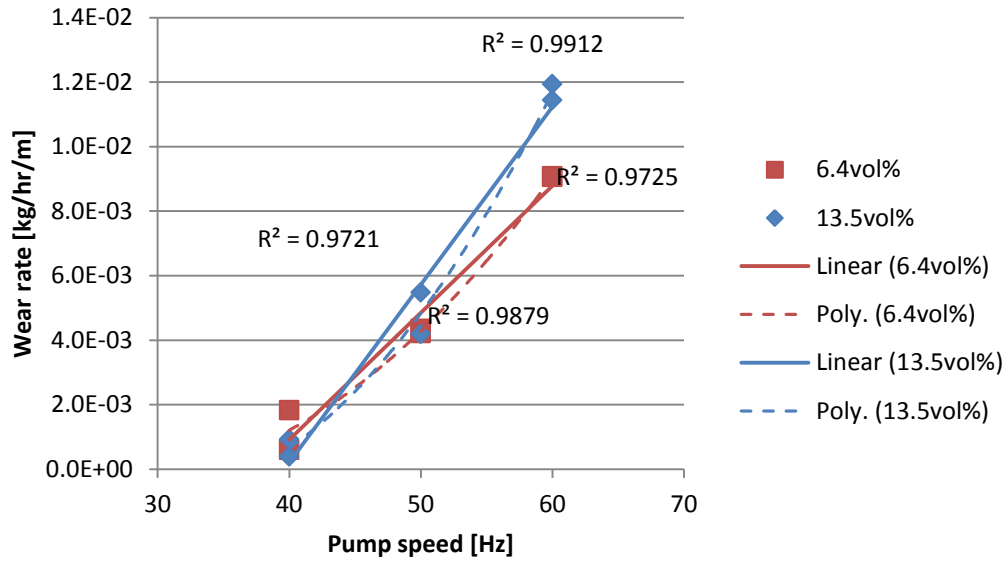


Figure 42 - Rate of mass loss with respect to pump speed

Under certain flow conditions, there appears to be significant spread in the data points. To gain insight into why this may be, recorded mass flow rates have been plotted in Figure 43 with respect to their corresponding pump speeds. Note the data spread at lower pump speeds.

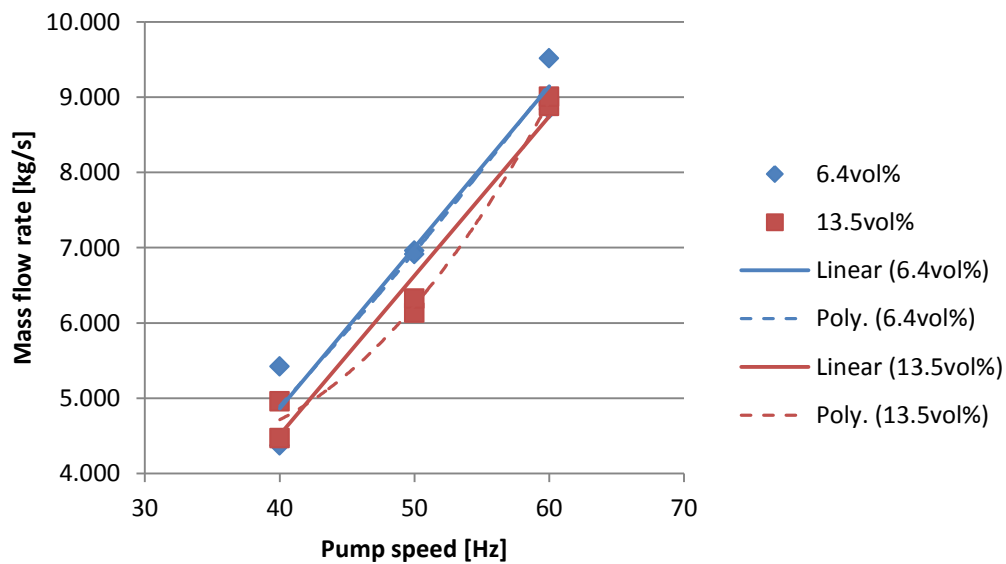


Figure 43 - Measured mass flow rates at experimental pump speeds

This data set shows significant spread at certain points, especially low pump speeds. It is not understood why this occurred, but one possibility is faulty data from the Coriolis meter. A short trial confirmed this: clean water returned a density value of 1040 kg/m^3 , while prior to the wear tests it had returned 995 kg/m^3 . This corresponds with an unacceptable error of 4.5%. Following each run, the rig was rinsed multiple times with clean water to remove any residual solids, but the density and mass flow readings remained high. It appears that the inertia of the Coriolis meter's sensitive tube may be compromised, resulting in skewed data.

6.2 Strain Testing

Strain testing was conducted to determine whether internal pipe wall shear stresses could be measured on the external surface. Test conditions were kept consistent with those used during wear tests.

Two tests were performed, using garnet sand concentrations of 6.4% and 13.5% by volume. The testing procedure for each concentration value ran as follows:

1. Zero out the strain gauges so that all gauges read the same when the system is at rest.
2. Run the pump at 40 Hz for two minutes to allow the flow to develop and stabilize.
3. Increase the pump speed to 50 Hz, then to 60 Hz, allowing the system to run for two minutes at each speed.
4. Shut off the pump and allow the system to return to rest.

Axial and circumferential strain readings for both tests are given below in Figure 44 through Figure 47. For all cases, the pressure-induced strains were calculated using the equations of Lamé and Hooke, as given below. Calculated values have been plotted in black, next to the actual strain readings. It is important to note that all strain readings have an initial value of zero. Consequently, the actual value is unknown. Relying on the linearity assumption, the initial values were replaced with the calculated value. Strain readings have been corrected both for thermal expansion of the acrylic tube material as well as any thermal resistance changes in the gauges. For reference, applicable stress and strain equations have been provided again below.

$$\sigma_z = \frac{r_i^2 P_i - r_o^2 P_o}{r_o^2 - r_i^2} \quad (117)$$

$$\sigma_r = \frac{r_i^2 P_i - r_o^2 P_o}{r_o^2 - r_i^2} - \frac{r_i^2 r_o^2 (P_i - P_o)}{r^2 (r_o^2 - r_i^2)} \quad (118)$$

$$\sigma_\theta = \frac{r_i^2 P_i - r_o^2 P_o}{r_o^2 - r_i^2} + \frac{r_i^2 r_o^2 (P_i - P_o)}{r^2 (r_o^2 - r_i^2)} \quad (119)$$

$$\varepsilon_1 = \frac{1}{E} [\sigma_1 - \nu(\sigma_2 + \sigma_3)] + \varepsilon_{thermal} \quad (120)$$

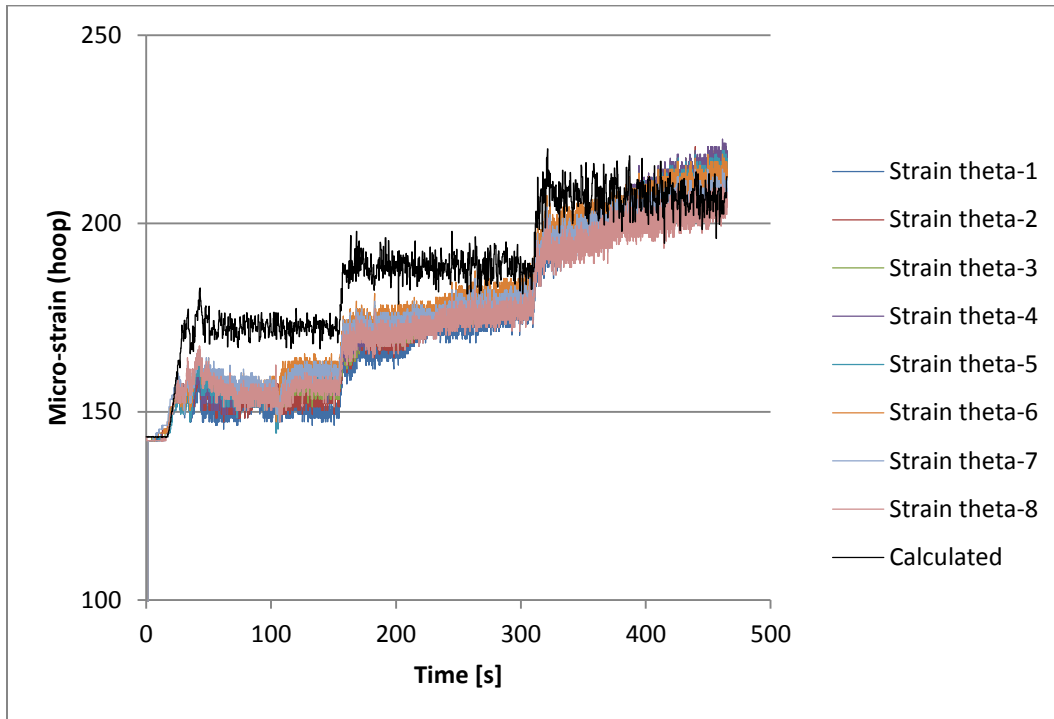


Figure 44 - Hoop strain at 6.4vol% slurry concentration

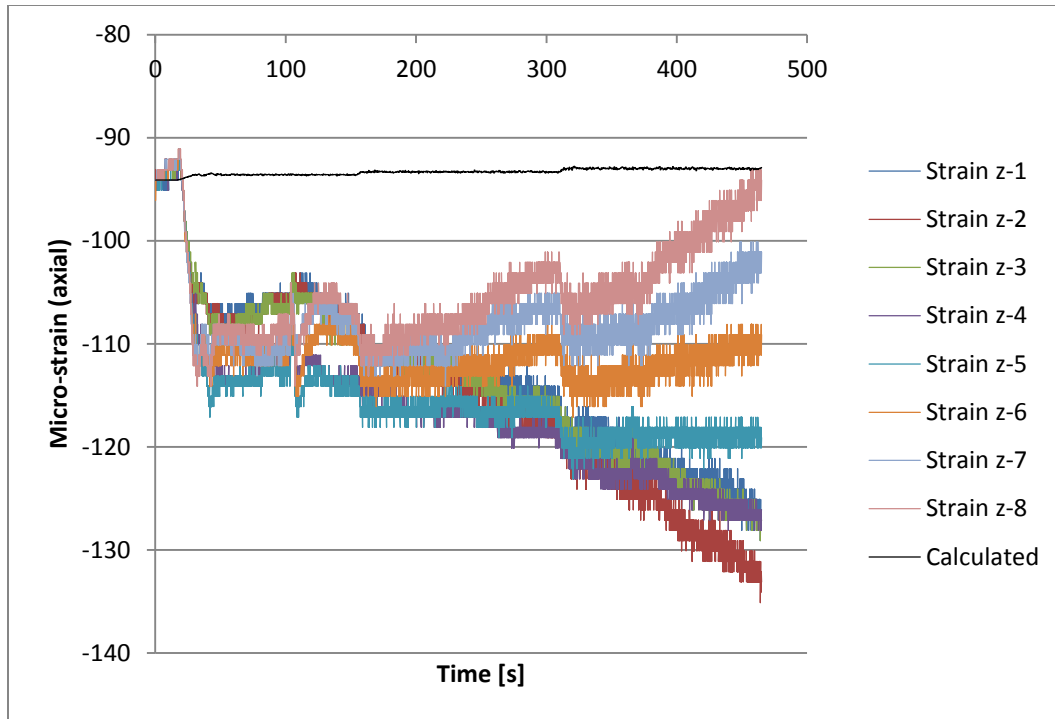


Figure 45 - Axial strain at 6.4vol% slurry concentration

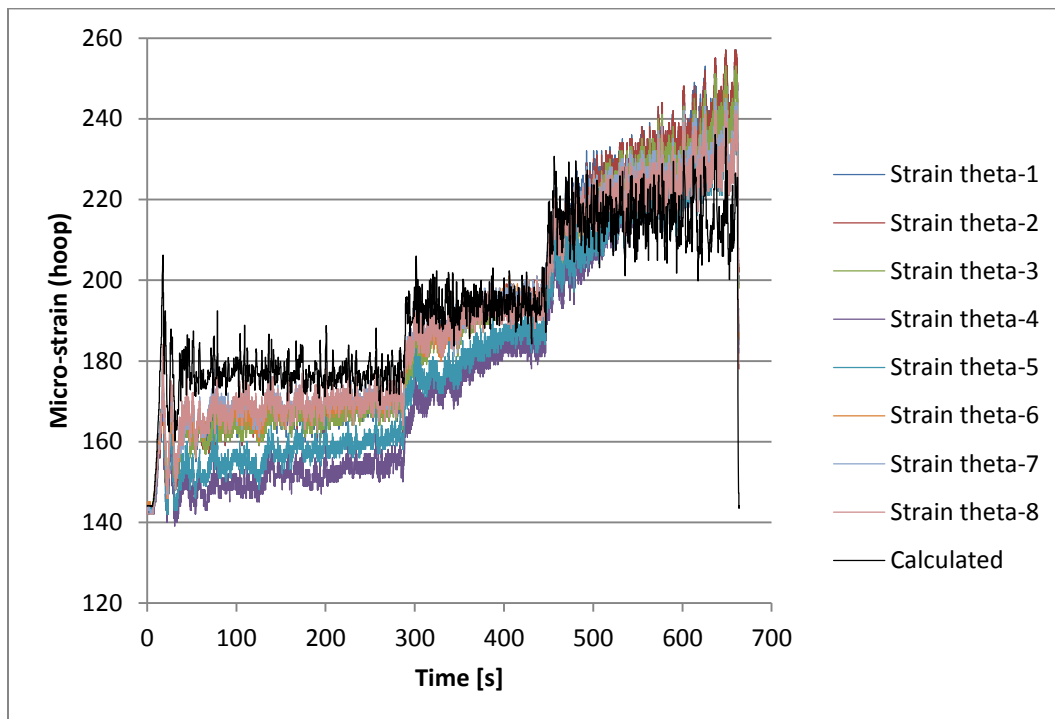


Figure 46 - Hoop strain at 13.5vol% slurry concentration

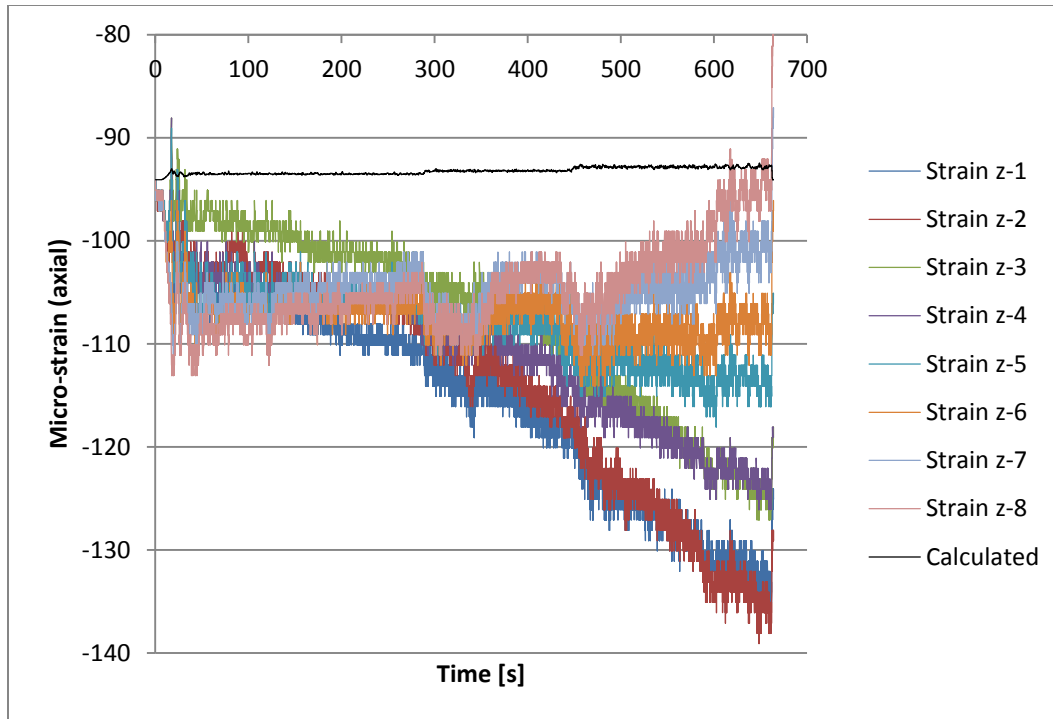


Figure 47 - Axial strain at 13.5vol% slurry concentration

There are several points to note regarding the strain readings:

- Circumferential strain readings roughly follow the calculated strain values, showing step increases with corresponding increases in flow rate. Of interest is the manner in which these readings creep steadily upward, well after the flow rate has stabilized. The reason for this behaviour is not known, but creep deformation is suspect. Under an applied stress, viscoelastic materials (especially polymers) respond in similar fashion to a spring-damper system, rather than a simple spring system. Hooke's law is inadequate for describing the strain response of creep-prone materials, and a viscous term must be included, of the form $\sigma = E\varepsilon + \eta \frac{d\varepsilon}{dt}$ [Plaseied *et al.*, 2009]. Solving this differential equation yields $\varepsilon(t) = \frac{\sigma_0}{E} \left(1 - e^{-tE/\eta}\right)$.
- Axial strain readings are slightly larger in magnitude than the predicted values. The reason for this is unknown. Here as with the circumferential readings, creep-style behaviour may be noted.
- Somewhat perplexing is the manner in which individual strain gauges respond to the stresses. Certain gauges appear to exhibit much higher sensitivity than others. There are several possible causes for this. A

gauge's sensitivity may be directly affected by the manner in which it is mounted to the substrate – e.g. amount of adhesive used in the mounting process, roughness of the substrate surface prior to adhesion, and overall integrity of adhesion between gauge and substrate. It is expected that this disparity may correspond with uneven clamping of the spool. Another likely cause is irregularities in the thickness of the tube walls. This can easily result from variations due to manufacturing tolerances, especially for castings and extruded components. Since the tube walls were thinned to allow for greater strain sensitivity, it is likely that certain gauges experienced elevated levels of strain due to reduced wall thickness in their respective vicinities. This would also provide an explanation for the slight observed differences in circumferential strain readings, as the three-dimensional stress-strain relation depends on circumferential as well as radial and axial stress components.

- It is noteworthy that the strains observed here are much higher than those due to Coulombic shear stress alone. The calculated pressure-induced axial stress is on the order of 1 MPa, while the calculated Coulombic shear stress is roughly 82 Pa. Hence, while the instrumented spool may be useful for measuring pipe stresses, it does not appear that it is able to resolve the relatively low Coulombic shear stress due to slurry bed flow.

A second set of strain tests was scheduled with the intent of checking for hysteresis effects, but unfortunately the instrumented spool fractured while being mounted in the test rig, such that it was rendered unusable. It appeared that this was due to the flange nuts being torqued excessively in an uneven fashion. This uneven axial load created stresses in the tube walls, which may have been amplified by any existing variations in wall thickness. A likely additional factor was the sudden step changes in wall thickness near the ends of the tube. These step changes create stress concentrations which may have amplified the material stresses by up to 1.5 times [Hibbeler, 2005].

6.3 Optical Particle Tracking

The final phase of investigation was a set of particle tracking velocimetry (PTV) experiments. At the time of this writing, documentation of the successful use of PTV to measure dense slurry flows has not been found in the literature. Thus,

the primary purpose of running these tests was to determine whether this technique would prove useful for observing slurry flow mechanics. The following objectives were set for the PTV experiments:

- Observation of the interactions between particles and the pipe wall.
- Confirmation of the behaviour predicted by the modified two-layer flow model.
- Verification of the height of the shear interface layer.
- Quantification of the turbulent motion of particles within the shear interface layer.

High-speed video (1500 frames/second, 1280x640 pixels) was recorded for pump speeds of 30, 40, 50, and 60 Hz. A solids concentration of 6.4% by volume was used for these runs. At higher concentrations, it would have been difficult to obtain any useful optical data. Still frames from each run are shown below. Note the manner in which blurring (due to particle speed) increases with speed. Also note that suspension of solids increases with speed, as expected. At 60 Hz, the solids are completely suspended, though asymmetrically with respect to the pipe axis.

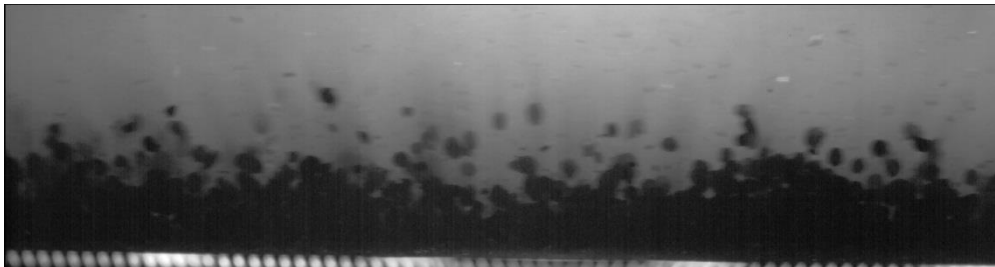


Figure 48 - Optical results: 30 Hz pump speed

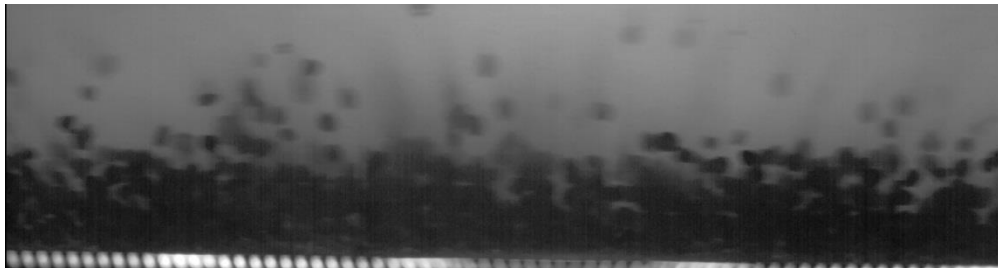


Figure 49 - Optical results: 40 Hz pump speed

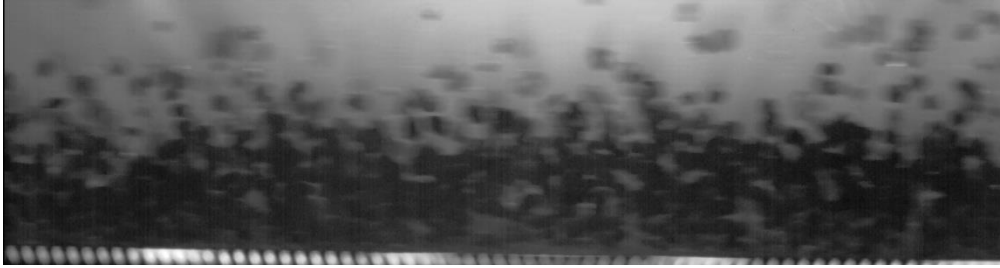


Figure 50 - Optical results: 50 Hz pump speed



Figure 51 - Optical results: 60 Hz pump speed

At both 30 and 40 Hz pump speeds, clear images were obtained in which suspended particles could be easily resolved. The 50 Hz case was more difficult to process, and the 60 Hz case was impossible to use at all, due to motion blurring of the particles. In all cases the bed region is optically very dense; consequently the software was unable to resolve individual particles in that region.

The videos for the 30, 40, and 50 Hz cases were processed to obtain velocity and location information for the suspended particles. The processing was completed as follows:

1. Raw video from the camera was imported into DaVis 8.0 software. For each data set, 1500 consecutive images were processed to obtain a time-averaged flow visualization.
2. To obtain flow vectors, consecutive images were paired to create double-frame images.

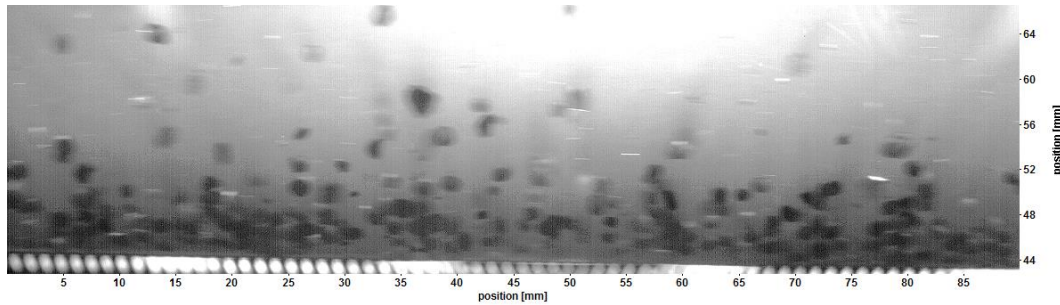


Figure 52 - Raw image of garnet slurry flow

3. Images were sharpened as necessary. Weak sharpening was applied to 50 Hz images, and moderate sharpening was applied to 30 and 40 Hz images. Images were inverted to allow for easier recognition of the particle shadows.

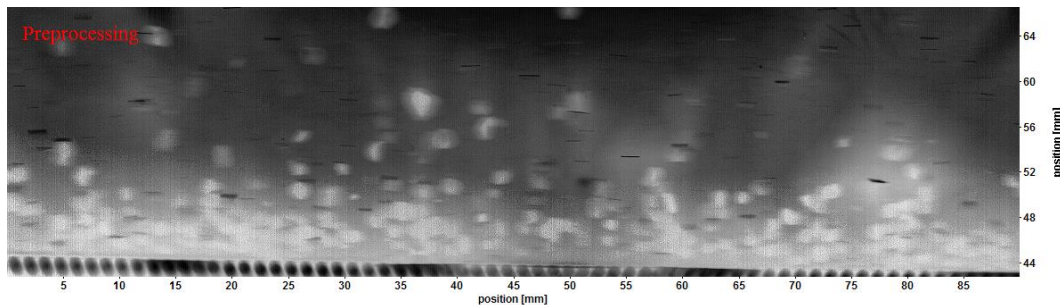


Figure 53 - Sample sharpened, inverted image

4. The particles were isolated from the background to remove background noise and to maximize particle contrast. First, a background was created using a “strict sliding maximum” filter with a kernel size of 35 pixels (approximately 2.5 mm in real space), to ensure that the background was created without any particles. The background was then subtracted from the images.

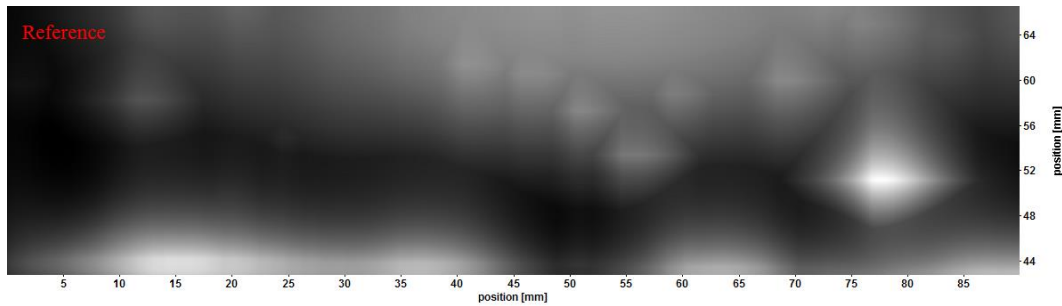


Figure 54 - Sample background to be subtracted from images

5. Particle recognition was accomplished through segmentation based on intensity threshold. A pixel was considered to be a part of the particle if it is brighter than the darkest pixel by 50%. Empirically-determined lower and upper intensity thresholds of 40% and 60% were used in determining particle sizes.
6. Each double-framed image in the video was analyzed to determine the displacement of particles between the two frames. A particle on the second frame was searched based on its position on the first frame. Two passes were made in order to reduce the chance of false pairing. In the first pass, an interrogation window of 10 mm (width) x 2 mm (height) was employed. For a successful match, a particle's diameter was allowed to deviate by a maximum of 30% between the two frames. This is known as the "partner particle selection criteria." For the second pass, the interrogation window size was reduced by a factor of 0.4. A particle filter was applied to ensure that the algorithm caught correct particles. The range of acceptable particle areas was set to a minimum of 4 mm² (to avoid picking up air bubbles) and a maximum of 16 mm². The velocity vectors were obtained for the entire set of images and overlaid on a single image. Each vector represents a time-averaged velocity vector for a particular location in space.

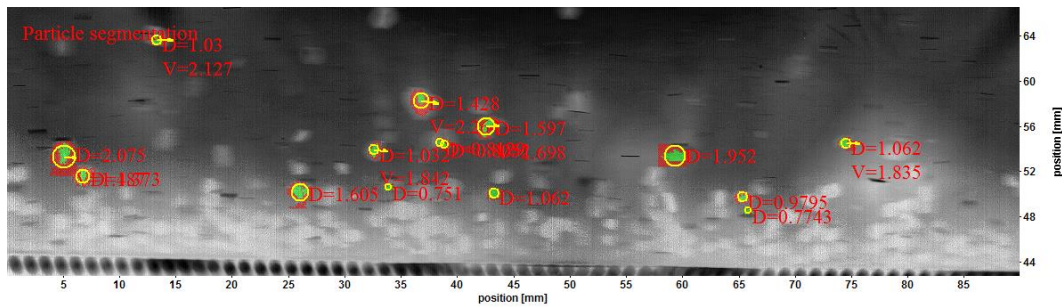


Figure 55 - Resolving velocity vectors

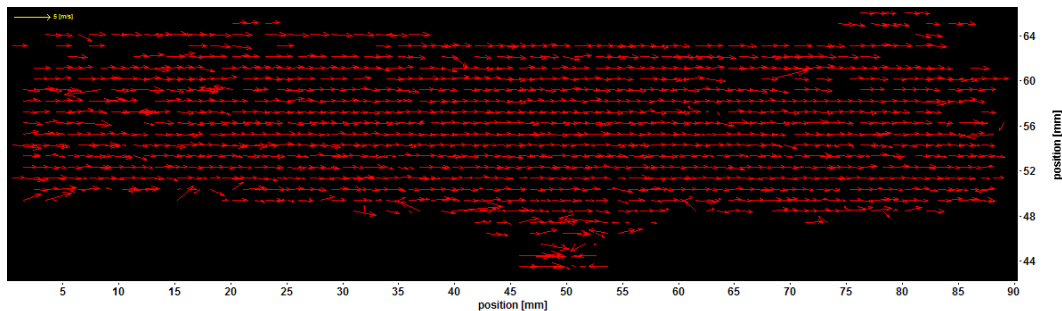


Figure 56 - Sample plot of time-averaged velocity vectors

In Figure 62, vectors appearing in the lower central portion of the image were determined to be clear spaces, rather than particles. These were removed in post-processing. Once the optical data was processed into numerical format, additional processing was required in order to gain useful information from it. The data sets were imported into Matlab and a series of processing steps were performed on them. They are outlined below.

1. Spurious vectors were removed. One problem location in all data sets occurred near the lower boundary of the shear layer, where the solids bed was too dense for individual particles to be resolved. Velocity vectors of up to 5 times the average magnitude were found at this location. As well, all negative and zero axial velocities were removed.
2. Plots of the data were created. To aid in understanding the velocity spread, separate histograms were created for axial and vertical velocities. Next, chord-averaged velocities (20 chords/mm) were calculated across the available vertical range; these were plotted with respect to vertical position, in order to aid in identifying the manner in which the velocity changes across the shear interface layer. Finally, the spatial distribution of the particles was plotted in two dimensions.

Plots are presented below, with discussions to follow. Eight plots are provided for each of 30, 40, and 50 Hz pump speeds. The first is a histogram showing the axial velocity spread of resolved particles. In each case the spread appears to be roughly Gaussian, as expected. The next plot shows vertical velocity spread, which again appears to be Gaussian. The third plot shows the distribution of particles within the pipe. The plot agrees with theory in that particles are densely congregated near the lower surface, while the concentration profile tapers off in the upper regions of the pipe. The shortcoming of this plot is that particle locations are shown for the entire test run. Hence, a single particle appears at multiple locations on the plot. This is seen clearly in the upper portion of Figure 59. However, this repetition occurs for every particle, and therefore the particle distribution profile retains consistency. The fourth plot shows particle distribution with respect to height in the pipe. This plot reveals a major shortcoming of the PTV method for slurry applications: regardless of efforts during pre-processing, large bubbles and voids are perceived as particles by the algorithm. This is clearly seen in the manner in which the “particle” count increases linearly to a point, and then decreases linearly at the same rate immediately beyond that point. While this is obviously not an accurate method of measuring particle count with height, it does demonstrate that particle distribution appears to decrease linearly with height. The fifth plot shows the axial velocity profile across the shear layer. Results appear to agree in principle with the modified two-layer slurry model: velocity increases linearly with height in the pipe. The sixth plot shows variation in axial velocity as a function of height within the pipe. This was calculated by finding the standard deviation of particle velocities at a specific height within the pipe. The seventh plot shows the distribution of the vertical velocity component across the pipe. The eighth plot shows the variation (standard deviation) in vertical velocity across the pipe. Red lines have been added to highlight linear trends and to define the shear layer boundaries.

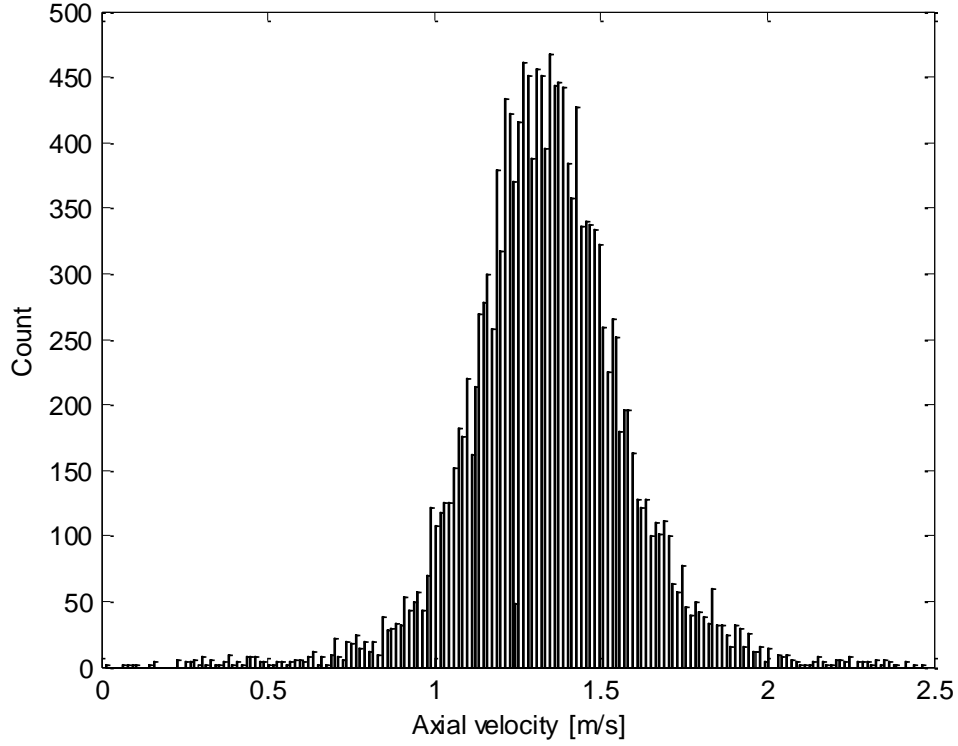


Figure 57 - Axial velocity histogram, 30 Hz pump speed

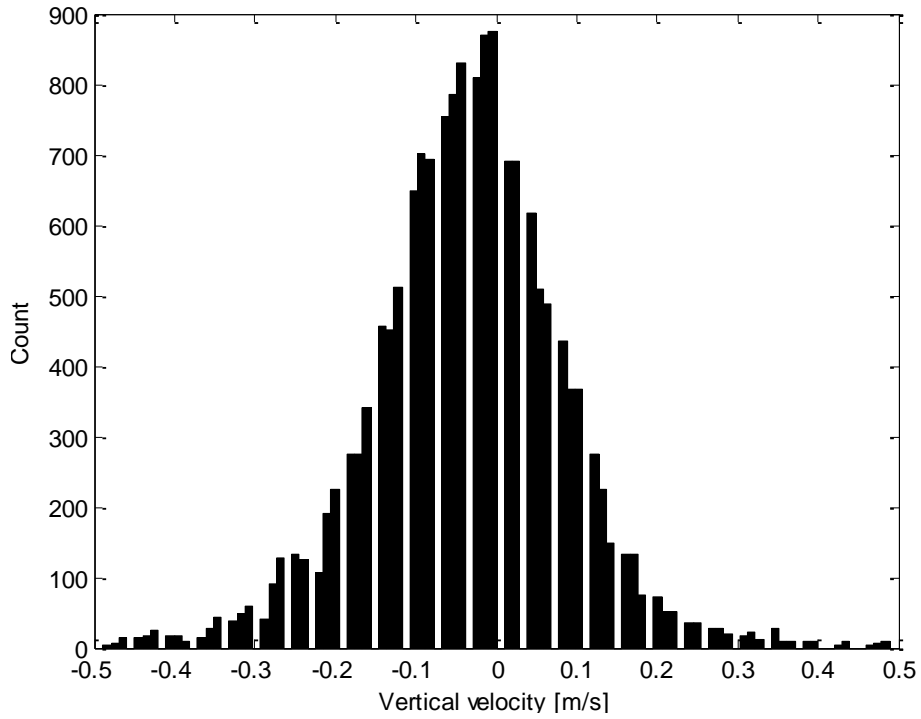


Figure 58 - Vertical velocity histogram, 30 Hz pump speed

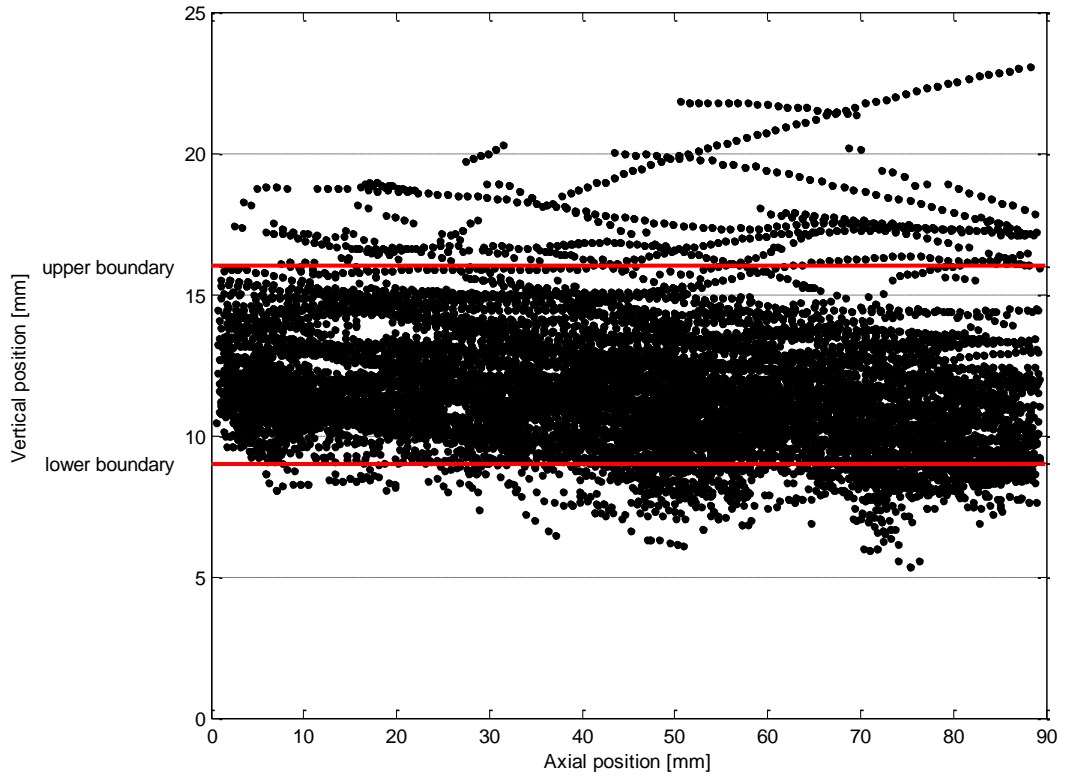


Figure 59 - Spatial distribution of particles, 30 Hz pump speed

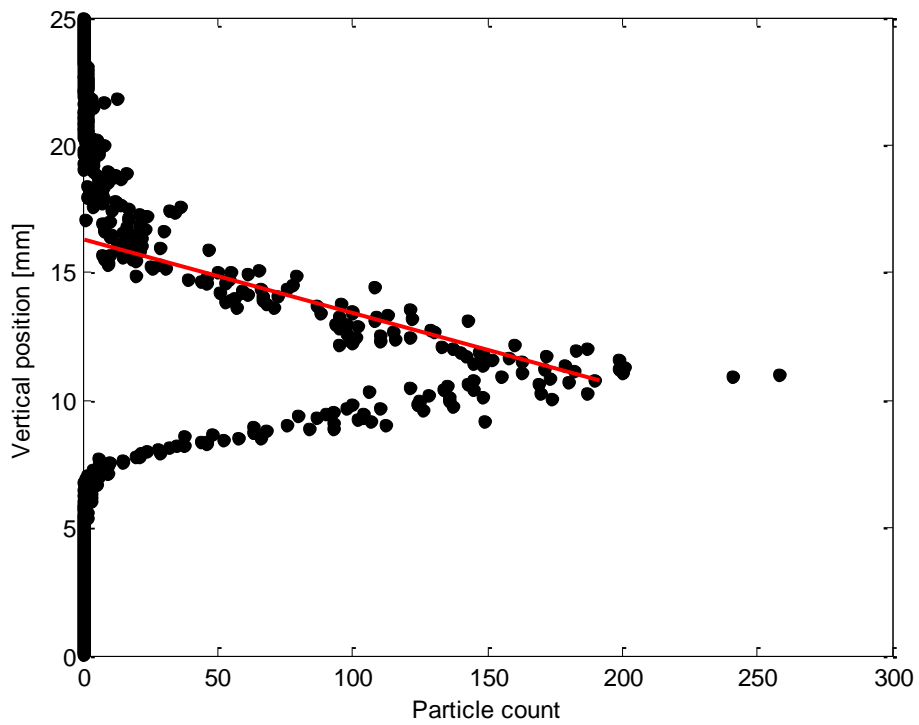


Figure 60 - Particle count with height, 30 Hz pump speed

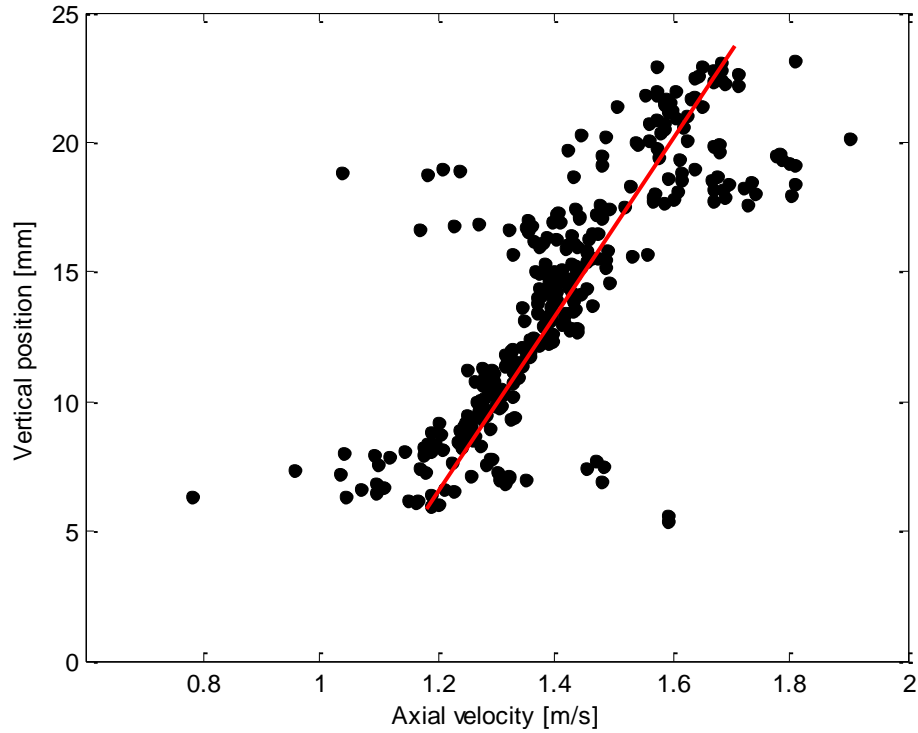


Figure 61 - Axial velocity distribution, 30 Hz pump speed

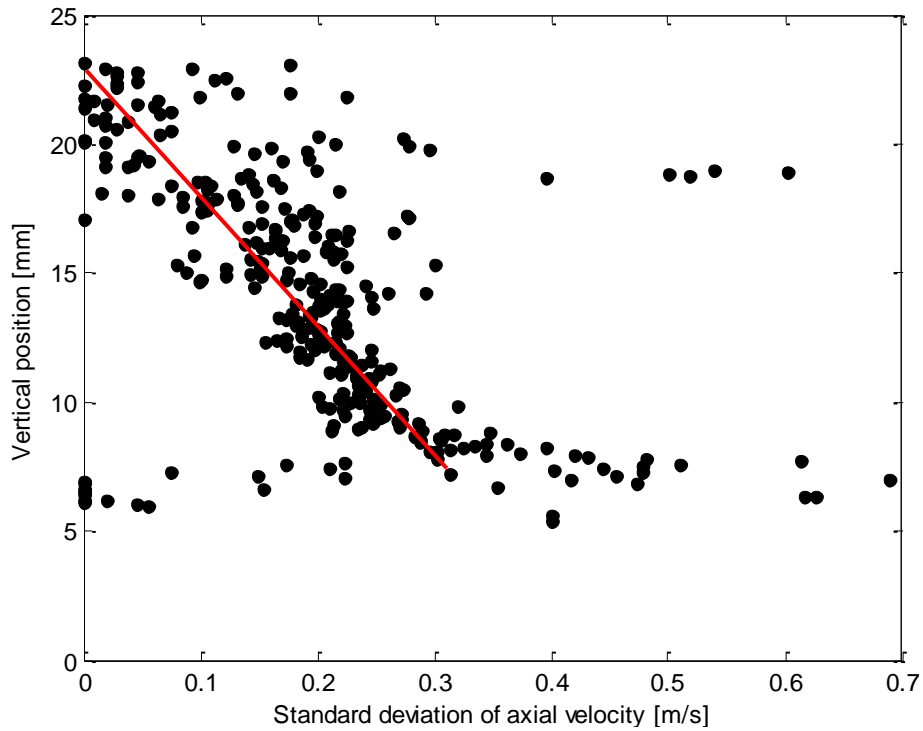


Figure 62 - Variation in axial velocity with height, 30 Hz pump speed

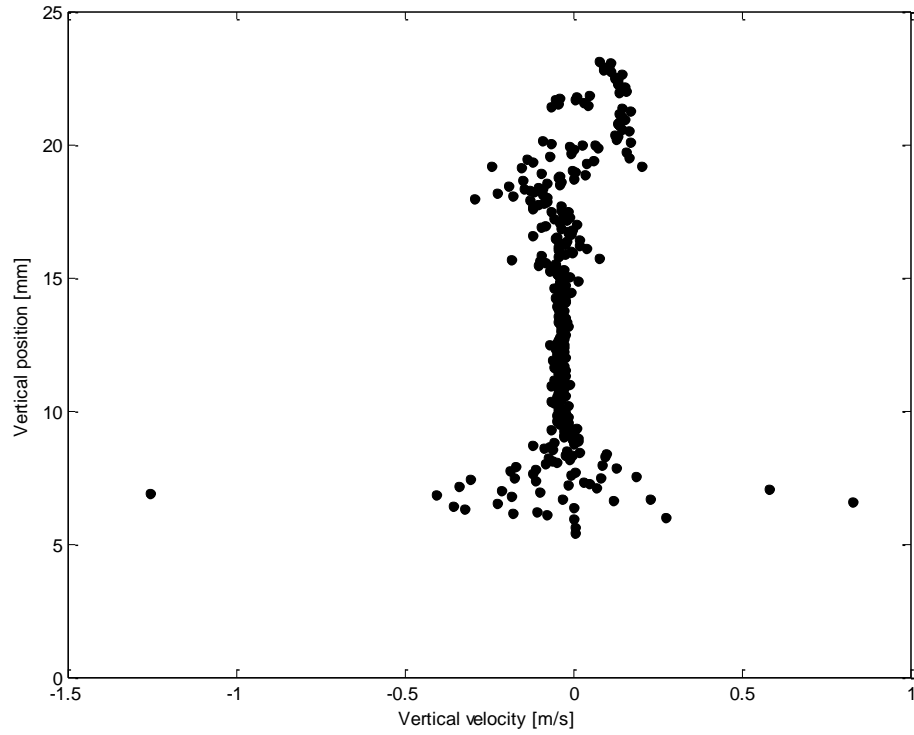


Figure 63 - Vertical velocity distribution, 30 Hz pump speed

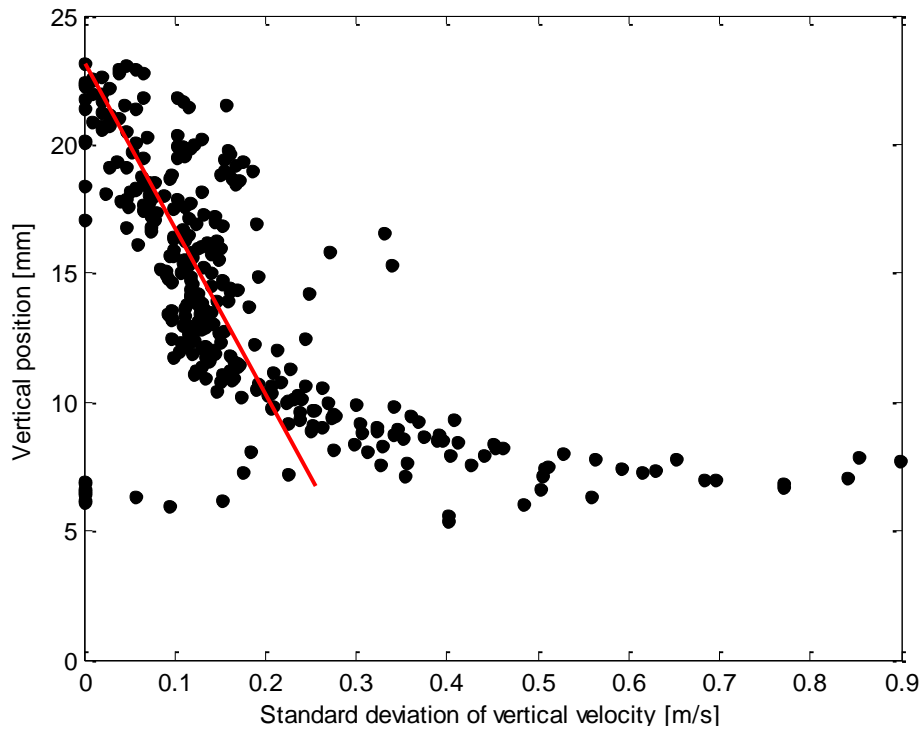


Figure 64 - Variation in vertical velocity with height, 30 Hz pump speed

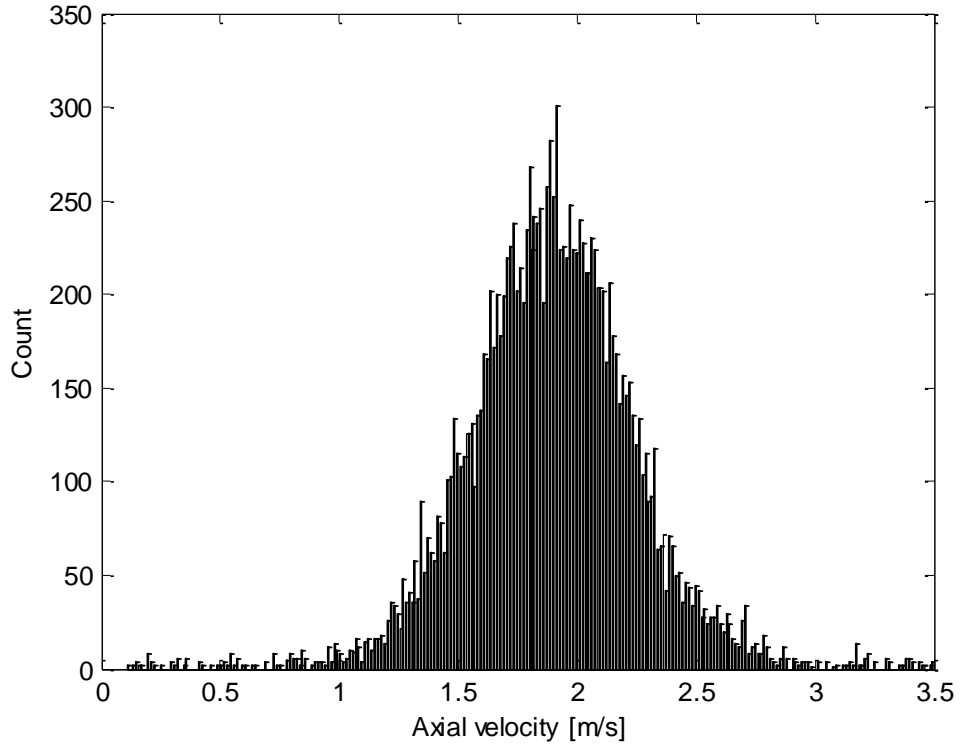


Figure 65 - Axial velocity histogram, 40 Hz pump speed

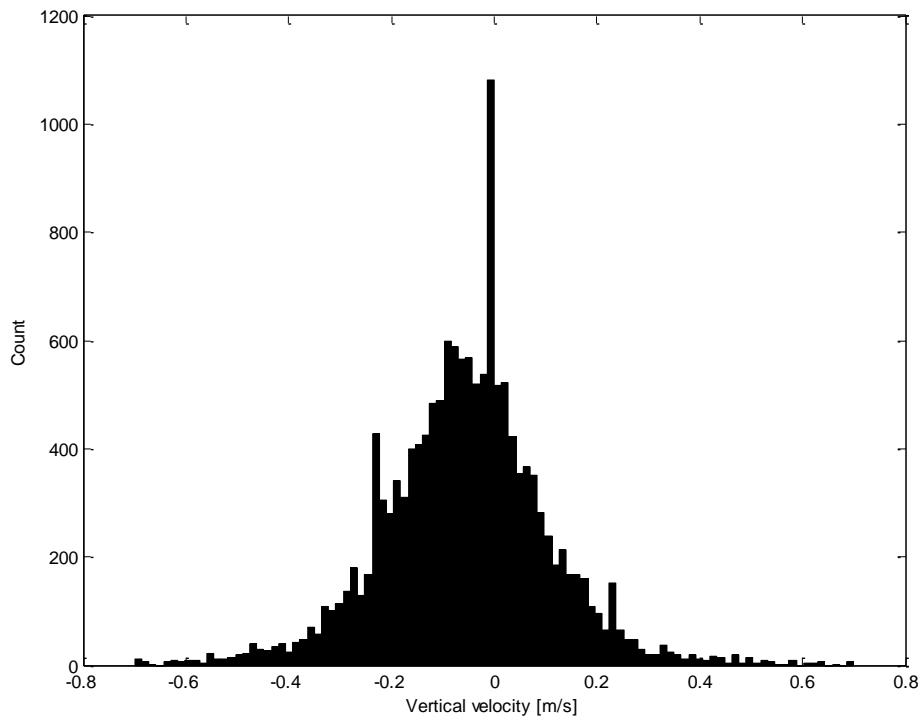


Figure 66 - Vertical velocity histogram, 40 Hz pump speed

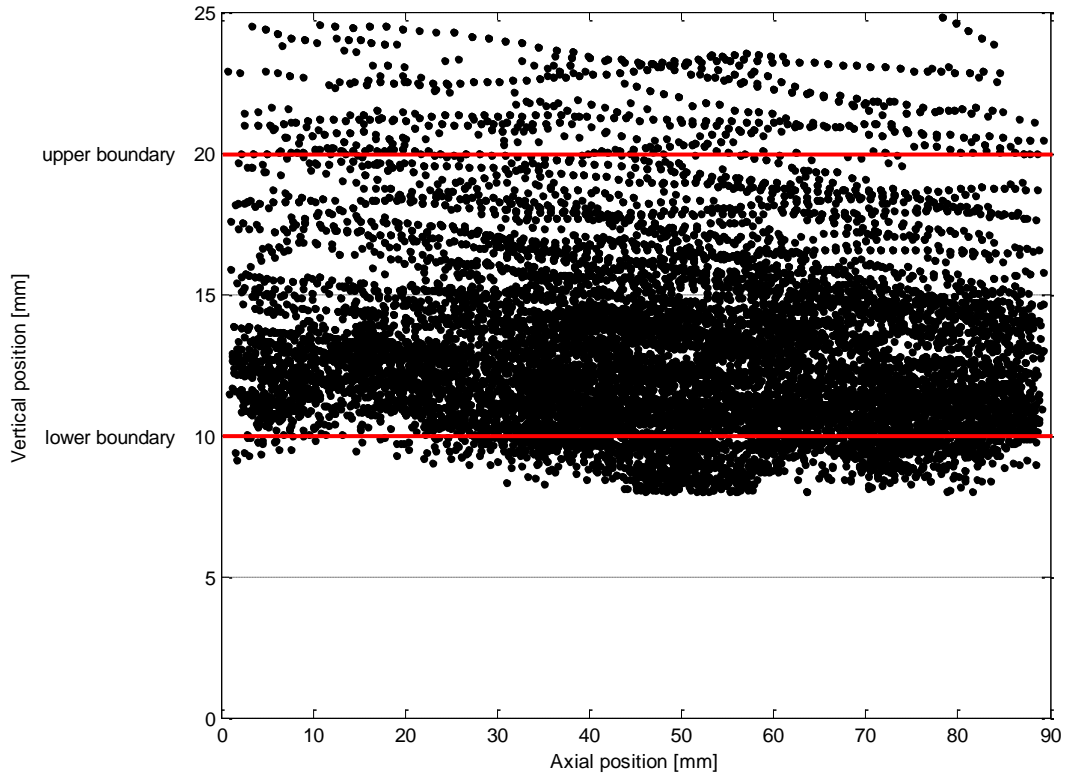


Figure 67 - Spatial distribution of particles, 40 Hz pump speed

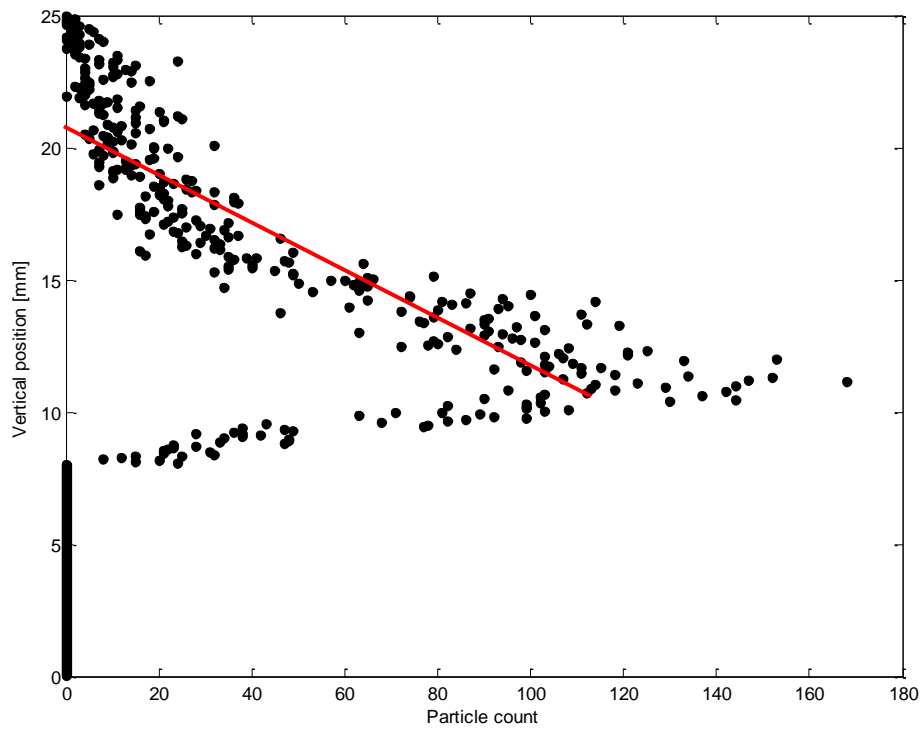


Figure 68 - Particle count with height, 40 Hz pump speed

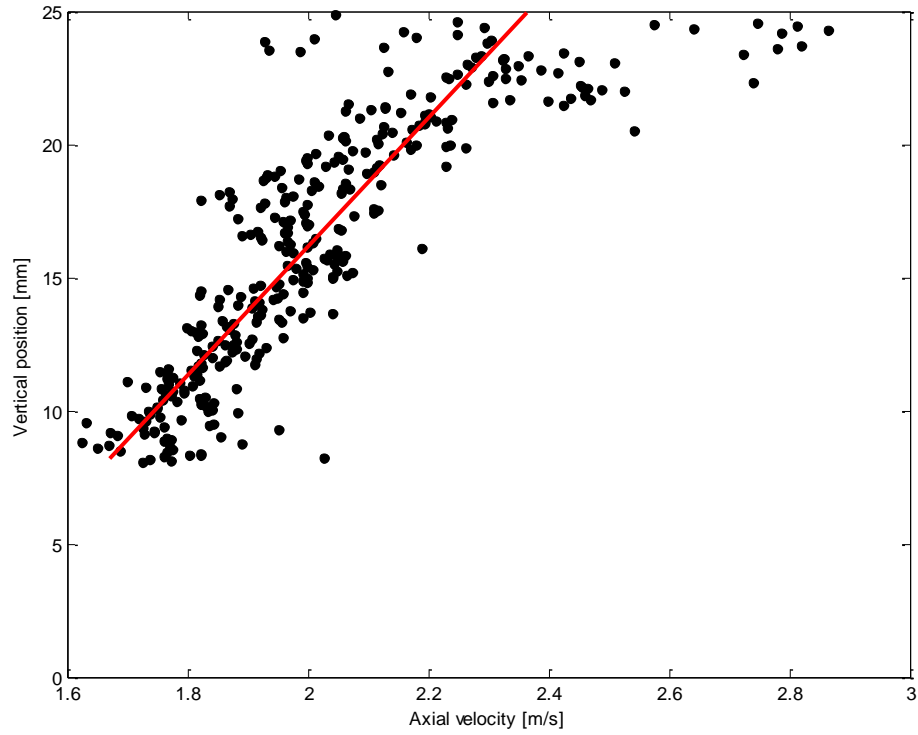


Figure 69 - Axial velocity distribution, 40 Hz pump speed

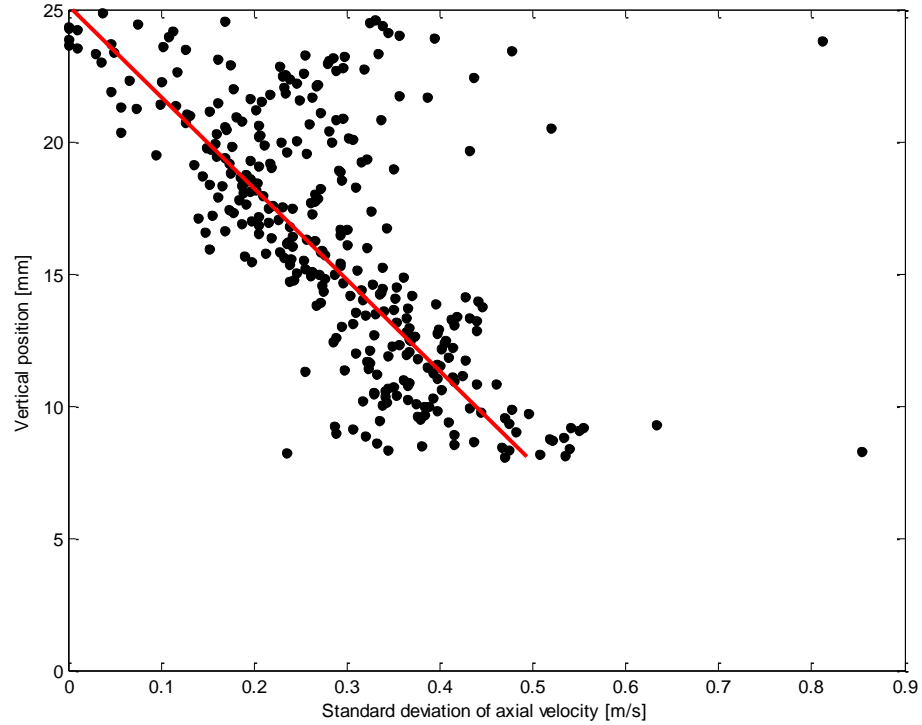


Figure 70 - Variation in axial velocity with height, 40 Hz pump speed

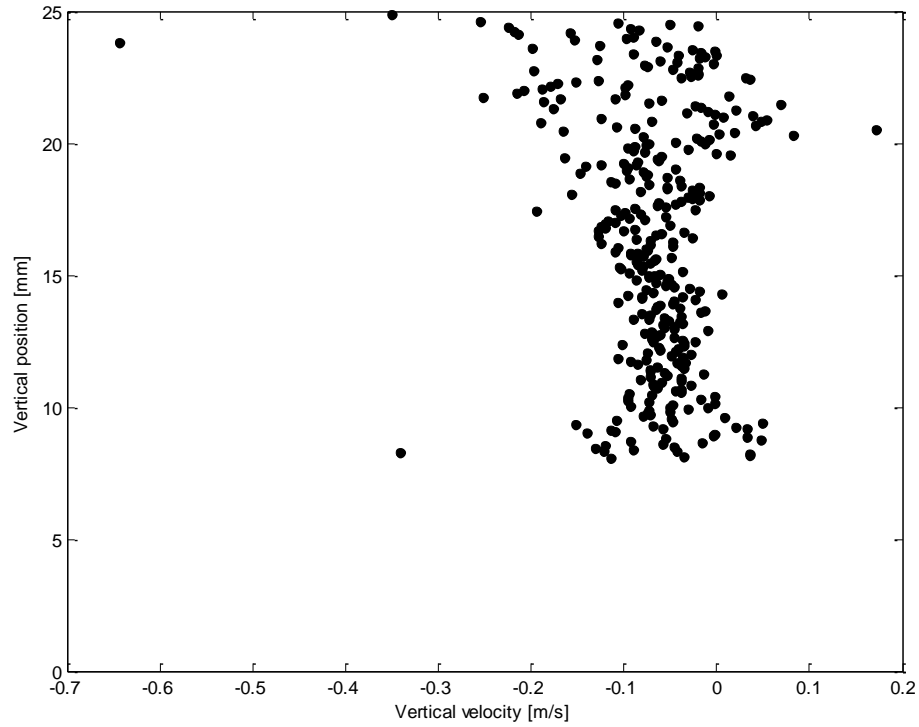


Figure 71 - Vertical velocity with height, 40 Hz pump speed

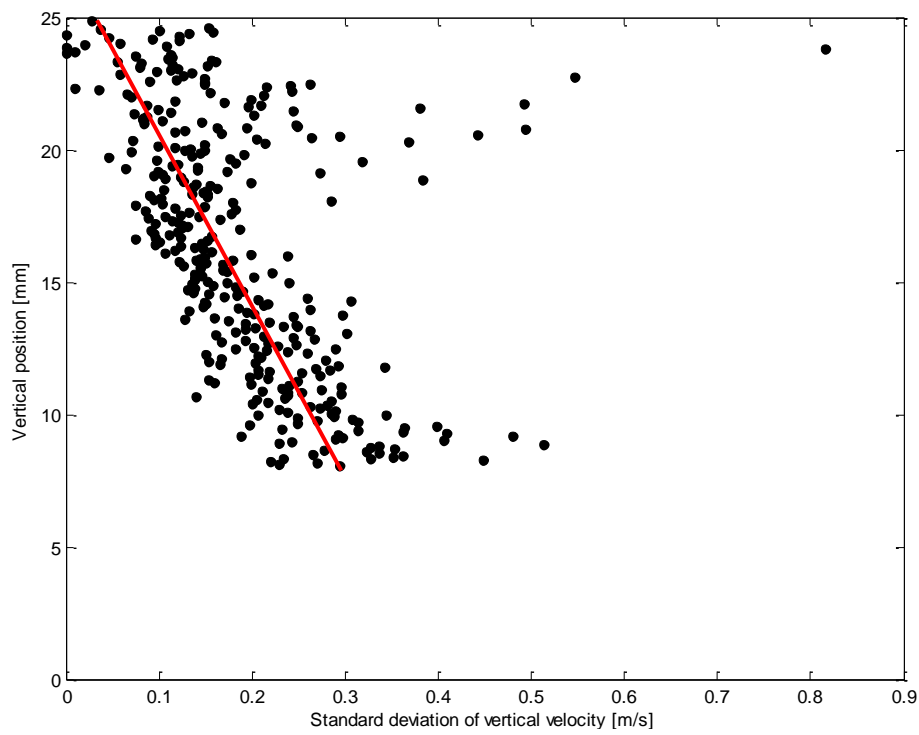


Figure 72 - Variation in vertical velocity with height, 40 Hz pump speed

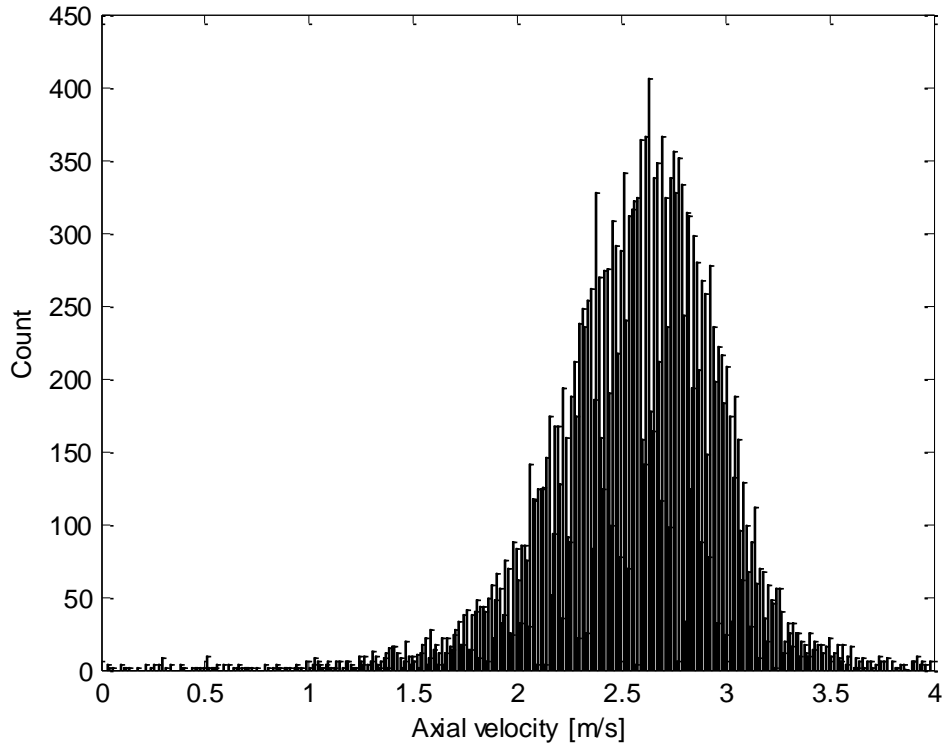


Figure 73 - Axial velocity histogram, 50 Hz pump speed

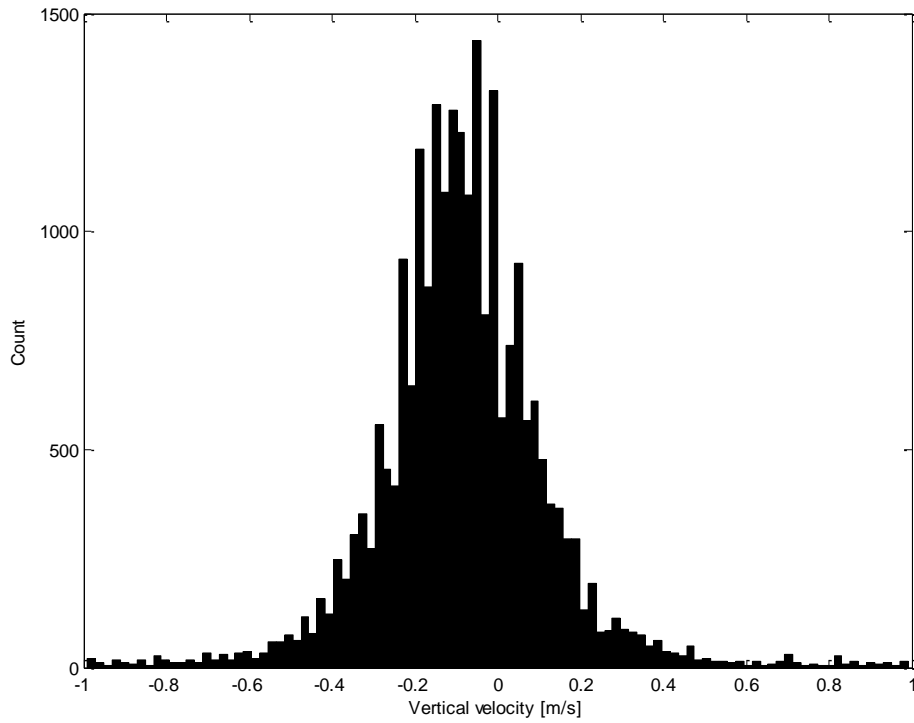


Figure 74 - Vertical velocity histogram, 50 Hz pump speed

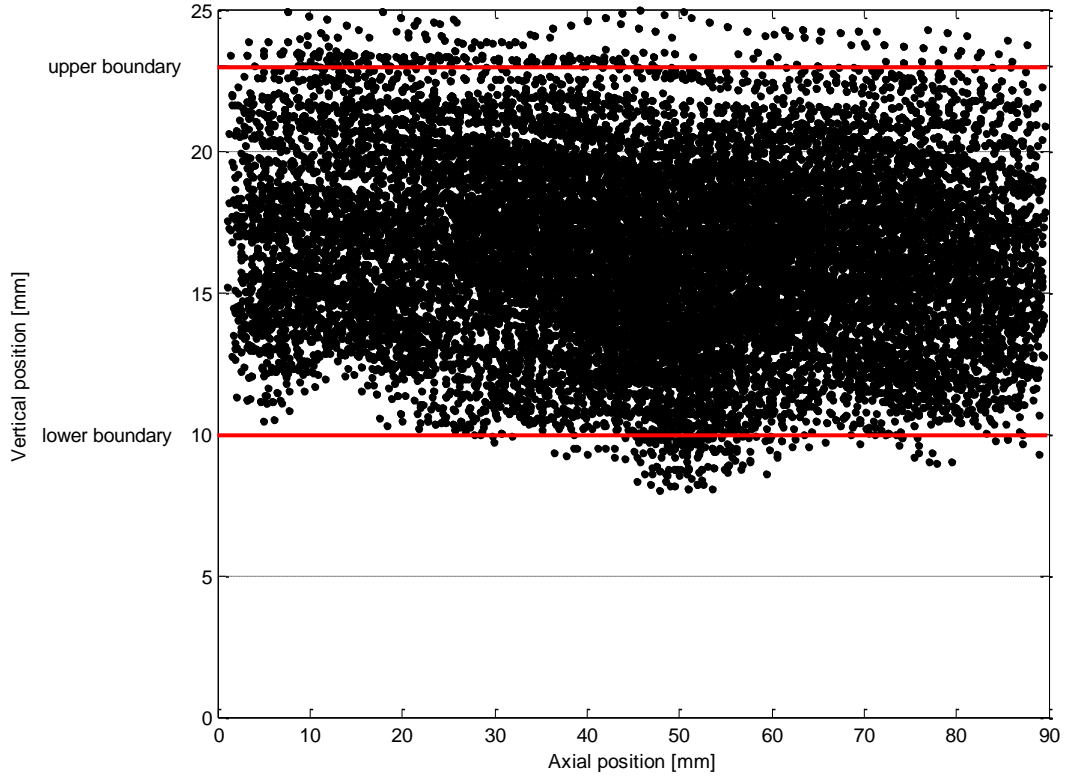


Figure 75 - Spatial distribution of particles, 50 Hz pump speed

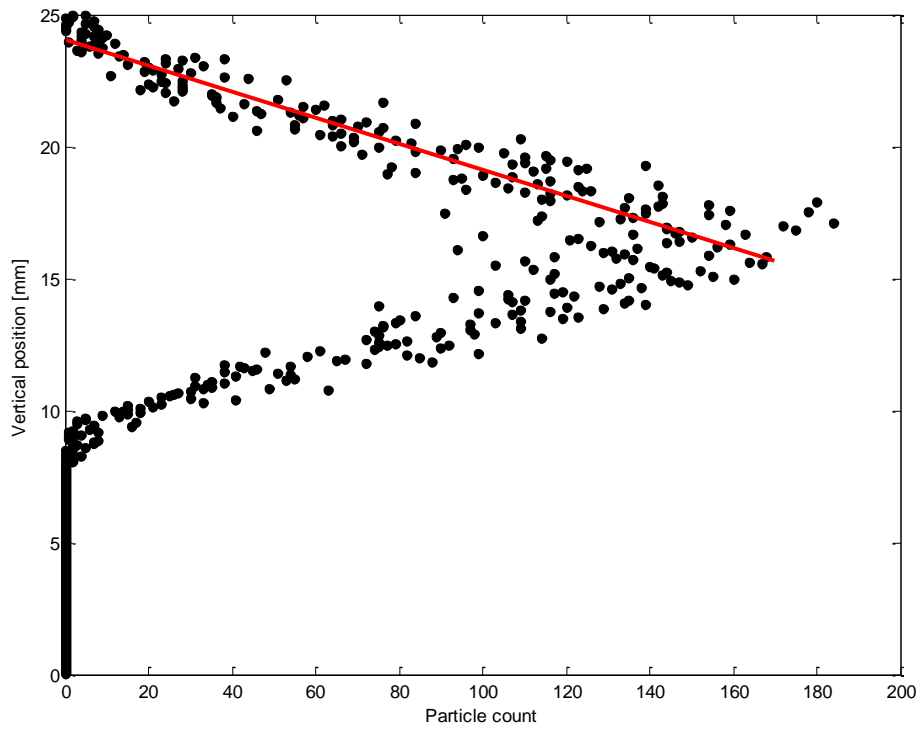


Figure 76 - Particle count with height, 50 Hz pump speed

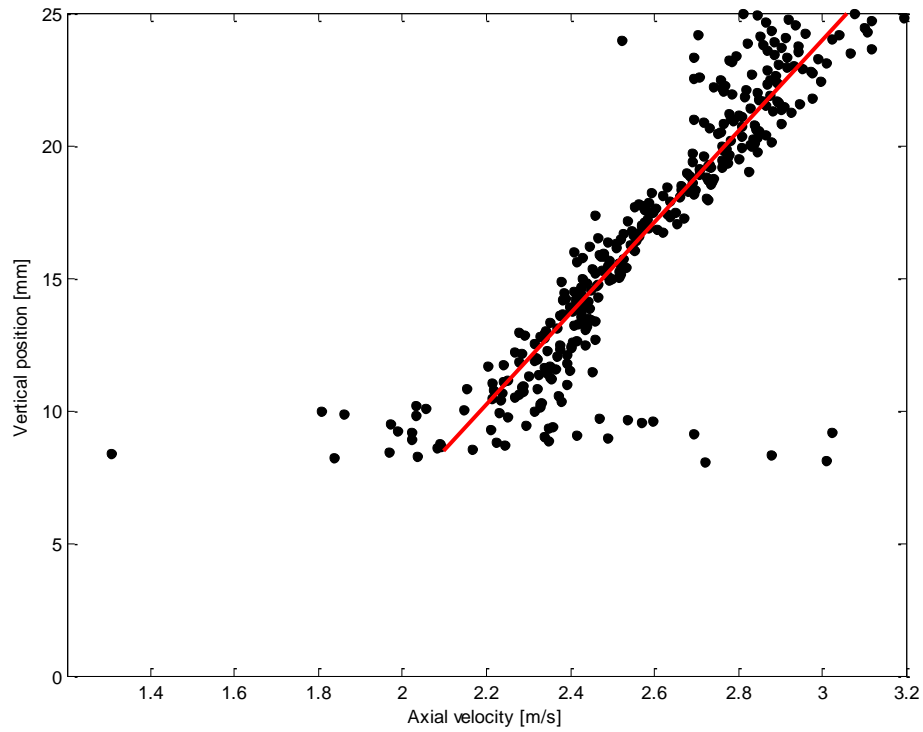


Figure 77 - Axial velocity distribution, 50 Hz pump speed

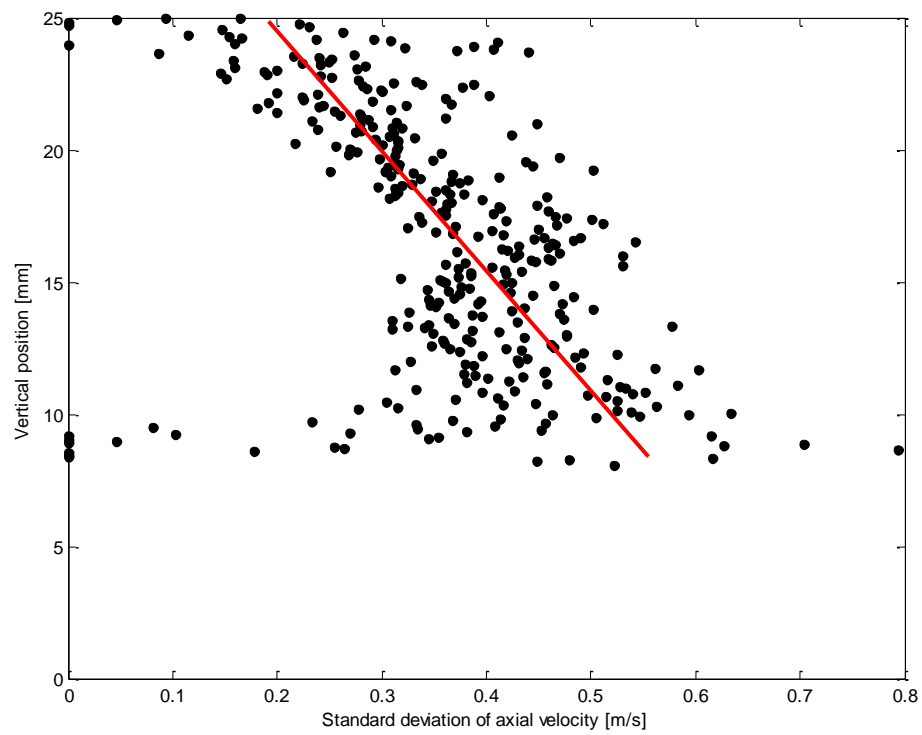


Figure 78 - Variation of axial velocity with height, 50 Hz pump speed

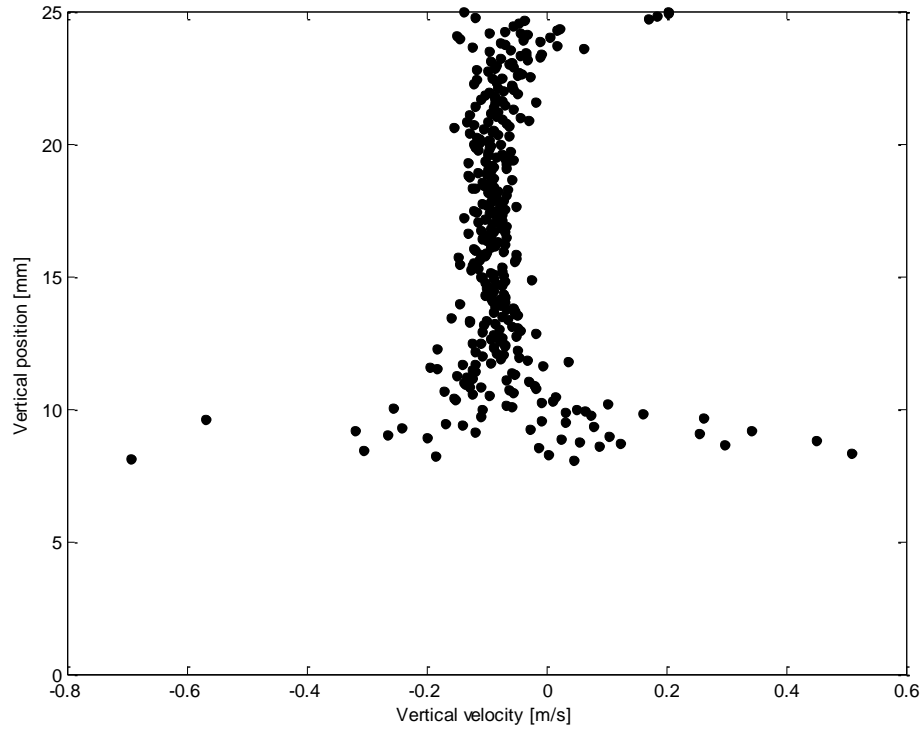


Figure 79 - Vertical velocity distribution, 50 Hz pump speed

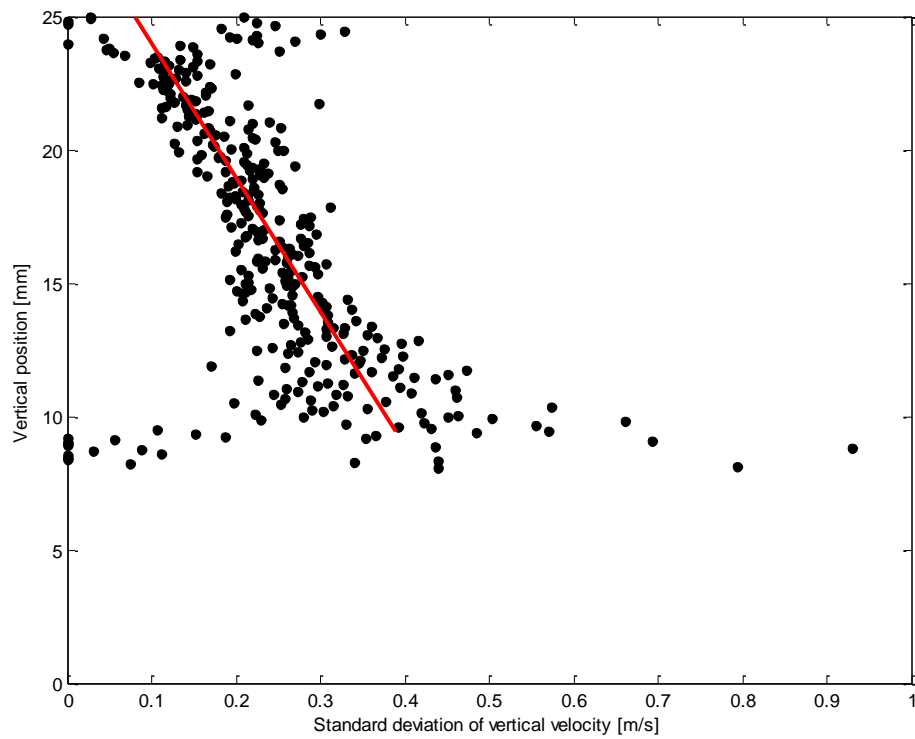


Figure 80 - Variation of vertical velocity with height, 50 Hz pump speed

From the above plots, several points may be noted regarding the shear interface layer:

- Upper and lower boundaries for the layer have been selected based on the following two assumptions:
 - The moving bed is too dense to allow individual particles to be resolved. Hence, the lower boundary is set at the point at which particles may be observed.
 - The upper layer exhibits a roughly uniform particle concentration. Thus, the upper boundary is located at the point at which the concentration gradient disappears.
- Velocities shown here are not those of the carrier fluid, but of the particles. Naturally, it is expected that the velocity of the carrier fluid will be greater than that of the particles.
- Behaviour within the layer matches the model assumptions very closely. Firstly, the layer exhibits a definite thickness, between 7-13 mm in these cases. This thickness appears to increase with velocity (Figure 59, Figure 67, Figure 75), although the rate of increase is difficult to determine visually. In principle this agrees with observations made by Nnadi & Wilson (1992), that shear-layer depth increases with bed shear stress. Secondly, both axial and vertical velocity distributions appear to be Gaussian. Vertical and axial turbulence values follow each other closely. Thirdly, the axial velocity exhibits a linear increase with vertical position across the layer. Finally, the variation (standard deviation) in vertical and axial velocities changes linearly with height. As expected, this variation increases with pump speed. However, the standard deviation of both vertical and axial velocities shows a decreasing trend with height. This contradicts what was originally expected when developing the modified two-layer model. It was expected that both velocity and turbulence would increase with height in the pipe. Note, though, that only particle motion is represented in these plots. It may be possible that the apparently higher levels of “turbulence” observed near the lower level of the shear layer may in fact be due to particle-particle interactions rather than fluid-particle interactions. Additional testing would be required to verify this. Regardless, larger variations in particle motion are seen near the bottom of the shear layer. This opens the possibility of a stronger impingement wear component near the bottom of the interface layer, which would agree with the industrial results of Schaan *et al.* (2007).

- The vertical velocity distribution is centred about a mean which is always slightly less than zero. This behaviour is to be expected in dense, settling slurries, particularly when using solid particles of a high specific gravity. Interestingly, the mean vertical velocity is fairly constant with height, though the variation is not. This may be an indication of saltation occurring (i.e. particles exhibiting a “bouncing” motion) in the upper flow region.
- The concentration profile (shown here as particle count) is linear with height. In Figure 60, Figure 68, and Figure 76, it appears that as height increases, the concentration increases to a point, and then suddenly decreases. It must be remembered that the optical algorithm relies on contrast from the background to determine what it deems to be particles. Because of this, a “particle” may be a bubble, a gap in the solids bed, or an actual particle. In the lower flow region, solid particles are packed closely together, implying that the lower (increasing concentration) leg of the plot actually shows the concentration of gaps in the bed. Thus, the local concentration of particles is linearly decreasing in this region.
- The actual layer thickness may vary significantly from the values determined here. Due to the density of the moving bed formation, the lower boundary may be located somewhat lower than anticipated. A more accurate characterization of the layer would require advanced measurement techniques, such as gamma-ray absorption.
- Due to camera placement and the design of the visualization spool, it was impossible to observe particle motion across the entire pipe diameter. However, plots indicate that the viewing window was sufficiently large to allow full observation of the shear interface layer.
- The PTV technique has demonstrated its usefulness here for obtaining velocities in two dimensions (vertical and axial). Because of the stratified nature of the slurry flow, it is difficult to obtain information on the third dimension (normal to the camera). Even if the camera were positioned directly above the flow, it would be impossible to gain this information because of the opaque bed of solids. One possibility may be to employ the stereo PTV technique. In this technique, both cameras would be located to the side of the visualization spool, but aimed at an angle to the spool. In this fashion, the third component of velocity is obtained. The probability of success from using this technique is not high, but it may be useful for obtaining near-wall particle velocities, provided that sufficient

lighting is available to illuminate the particles. An alternative possibility would be to employ a boroscope which is capable of vertically traversing the pipe cross-section.

7 Modeling and Simulation Results

7.1 Modified Two-Layer Flow Model Results

This section presents a side-by-side comparison of results obtained from the SRC Two-Layer model and the modified version developed in Chapter 3. The parameters of primary interest here are the layer velocities, wall shear stresses, and layer cross-sectional areas. Both models were used to solve for conditions over a range of bulk velocities.

For all calculations, the following parameters were kept constant:

- Pipe diameter: 2 inches, schedule 40
- Fluid temperature: 25°C
- Volume fraction of solids: 13.5%
- Solid density: 3992 kg/m³ (garnet)
- Average particle size: 1.5 mm

These parameters are used during wear tests in the laboratory pipe loop. The models are solved using the MathCAD worksheet provided in the Appendix.

In developing the modified two-layer model, care was taken to maintain consistency with the layer-specific velocities of the SRC model. Upper and lower layer velocities are calculated from the original SRC model. In addition, modified velocities are introduced for the upper and lower layers. The underlying reason for this addition is that the SRC model does not account for pseudo-homogeneous flow at elevated velocities. To model this phenomenon, modified velocities are introduced for the upper and lower layers. These are calculated by interpolating between the SRC layer velocity values and the average velocity values over the heterogeneous flow range. At the point of pseudo-homogeneous flow, these velocities converge, as would be expected in reality. These modified velocities are used to calculate local velocity and sand concentration across the shear layer. In Figure 81, the calculated velocities of the upper and lower layers increase with bulk velocity. As expected, the calculated average shear layer velocity falls between the upper and lower velocities. Shear and lower layer velocities increase at a slightly higher rate than the upper layer.

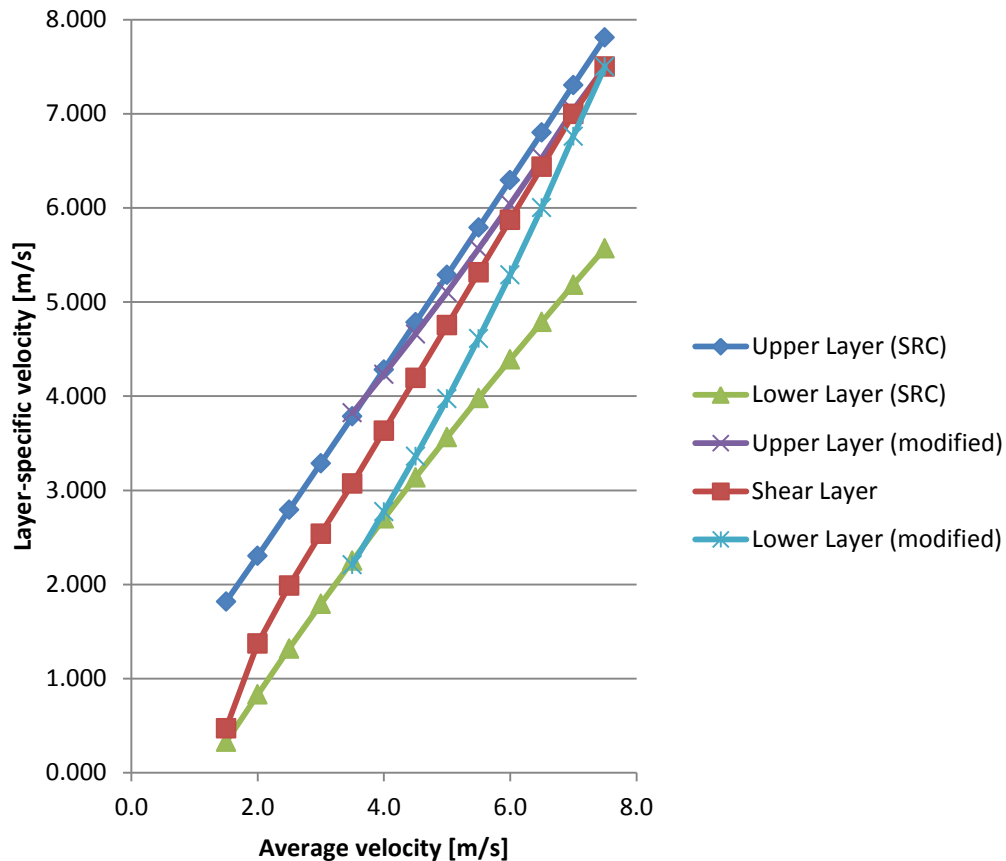


Figure 81 - Comparison of layer-specific velocities

Figure 82 compares the changes in cross-sectional area of each layer. The area increase of the shear layer is driven by a transfer of solids from the lower layer as bulk velocity increases. Above the deposition velocity (approximately 3.7 m/s here), the solids bed is assumed to disappear; solids are fully-suspended and distributed heterogeneously. With increasing velocity, turbulence and near-wall lifting forces increase, causing additional solids to migrate upwards. At approximately 8 m/s, solids are distributed pseudo-homogeneously across the pipe. At this point, the upper and lower layers disappear. Only the shear “layer” remains, with a velocity profile assumed to be flat.

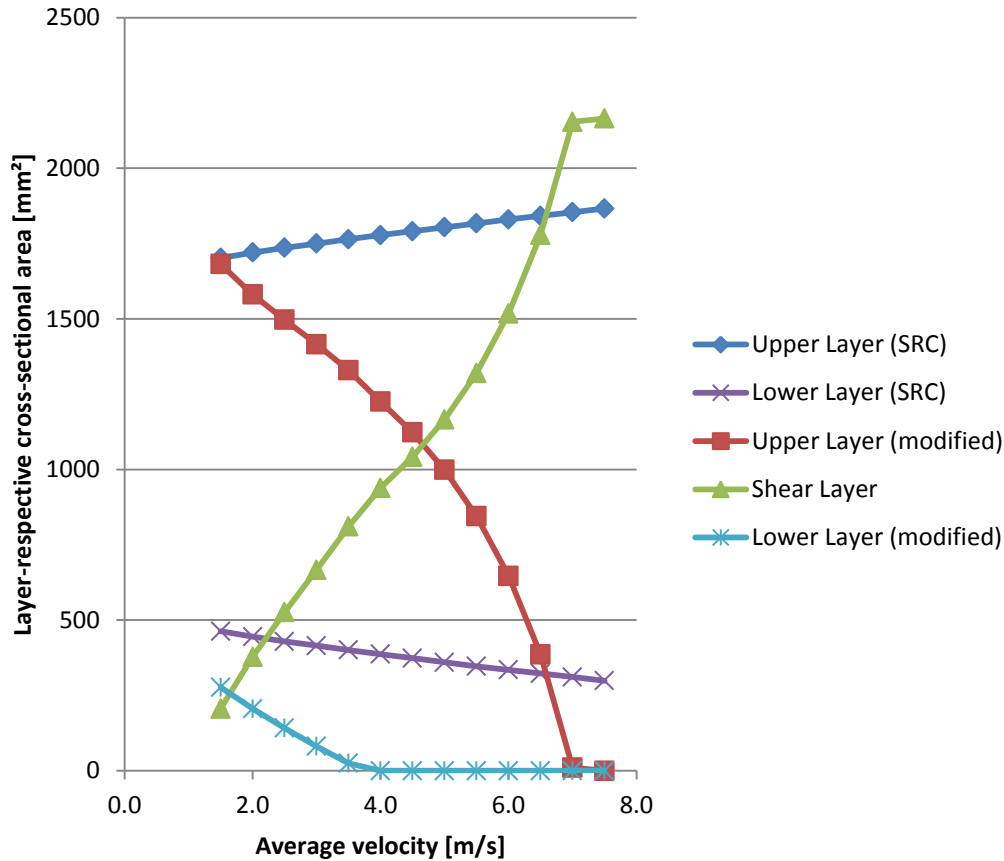


Figure 82 - Comparison of layer-specific cross-sectional areas

Model results have not yet been experimentally verified at the time of this writing. To do so would require sophisticated techniques such as gamma-ray imaging, which has been successfully used by SRC researchers in the past.

7.2 Impingement Wear Simulation Results

The wear testing conducted for this research was not conducive to observing impingement wear, mainly because of the use of garnet sand. Garnet sand, having a specific gravity of 4.0, tends to settle quickly to form a moving bed. Compared with another solid such as silica sand (with a specific gravity of 2.65), significant turbulent forces are required to not only suspend the particles, but to cause them to impinge against the pipe walls. Consequently, wear results for garnet will be skewed greatly in favour of sliding-abrasion rather than

impingement. To rectify this issue, the industrial observations of Schaan *et al.* (2007) are used here in lieu of experimental results, to aid with impingement wear modeling.

Based on the results obtained from the PTV experiments, minor corrections must be made to certain equations developed earlier in Chapter 3. In particular, it was found that the standard deviation of both axial and vertical velocity decreases with height in the shear interface layer. It appears that near the top of the moving bed, the turbulent motion of particles is quite high. Turbulent particle motion tapers off dramatically in the upper layer. These observations are contrary to what was expected, and the turbulence vector equations must be corrected to reflect this behaviour. It was noted that the velocity variation was similar for axial and vertical velocities, and thus the assumption of equal variation will remain unaltered for the present. The corrected equation is given below:

$$\tilde{v}_s(y) = \tilde{v}_1 \left(1 - \frac{y}{h_s} \right) \quad (121)$$

Several simulations were performed using the following parameters, which were selected to approximate the field conditions described by Schaan *et al.*

- Particle density: 2593 kg/m³ (silica sand)
- Average particle size: 150 microns (Schaan *et al.*)
- Lower layer velocity: 0 m/s (stationary bed conditions, as suggested by Schaan *et al.*)
- Upper layer velocity: 6.7 m/s (calculated from the modified two-layer model, based on a bulk velocity of 4.1 m/s given by Schaan *et al.*)
- Height of stationary bed: 0.18 m (calculated from the modified two-layer model)
- Thickness of shear interface layer: 0.23 m (calculated from the modified two-layer model)
- Lower-layer solids concentration: 46.6% by volume (calculated from the modified two-layer model)
- Upper-layer solids concentration: 17.5% by volume (calculated from the modified two-layer model)
- Minimum turbulence intensity: 5% of upper layer velocity (from optical tests)

- Maximum turbulence intensity: 20% of upper layer velocity (from optical tests)
- Threshold velocity for damage to occur to steel: 66.8 cm/s (provided by Bitter, 1962)
- Vickers hardness number for steel: 55

Using the flow conditions given above, several runs were executed; their numerical results are given below in Table 4. The given wear rates are average values for the entire circumference of the pipe, over an axial length of 1 mm. These wear rates were calculated by dividing the simulated wear quantities by the respective time duration to obtain the wear rates per second; these values were then scaled to obtain the given values. Longer simulated durations provide a larger pool of events, and are therefore expected to produce more accurate predictions. This may explain the manner in which the wear rates appear to approach an asymptotic value, as shown below in Figure 83. It must be emphasized that the manner in which the results adjust with simulated duration are a simulation artifact.

Table 4 - Impingement wear simulation results

Duration [s]	Wear rate [mm³/1000 hrs]
10	30.12
60	27.86
120	27.61

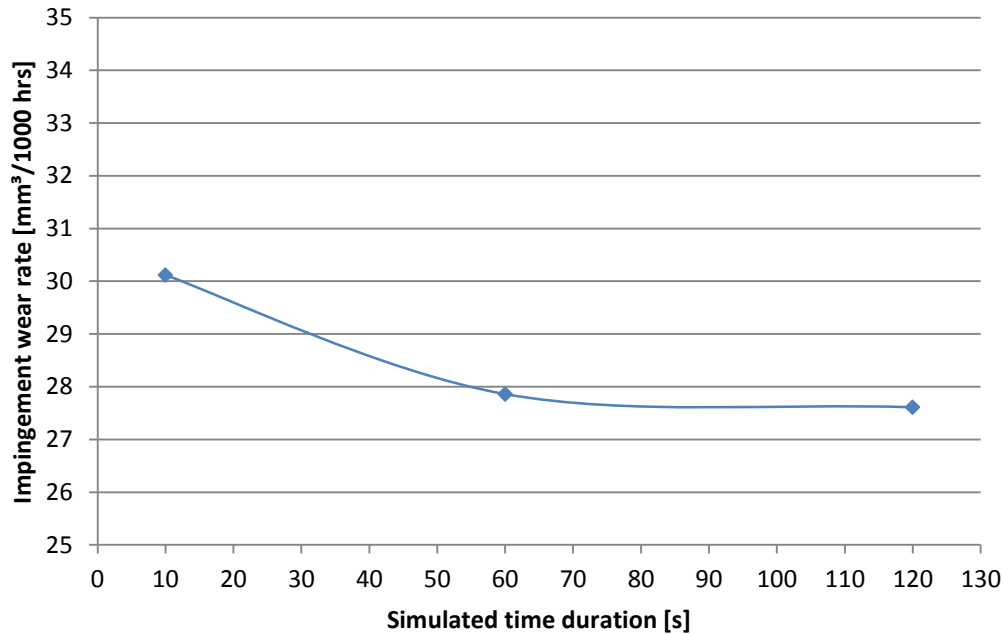


Figure 83 - Impingement wear rates predicted by Monte Carlo simulation

Plots of the simulated wear profiles are provided below in Figure 85, Figure 86, and Figure 87. One plot is provided for each simulation time. To provide consistency with the plots of Schaan *et al.*, the zero point on the x-axis represents the upper vertex of the inner pipe surface. Locations are measured circumferentially in degrees. It may be observed that even though the total wear (plot amplitude) increased with simulation time, there was little effect on the general shape of the wear profile. Two distinct peaks exist at the edges of the stationary bed, with rapidly diminishing wear occurring in the immediate vicinity of these points. Virtually no wear occurs across the upper layer (note that the motion of upper-layer particles was not included in this simulation). Noticeable wear is seen in the region beneath the stationary bed, however. This can be explained by the fact that particle-particle interactions were neglected in this simulation.

The reader will immediately note that the shape of the wear profiles differs from that of Schaan *et al.* in that the simulated profile features sharp peaks, rather than rounded ones. Likely, this is simply because the results of Schaan *et al.* utilize splines to connect data points. For comparison's sake, the wear profile observed by Schaan *et al.* in coarse tailings lines is provided below:

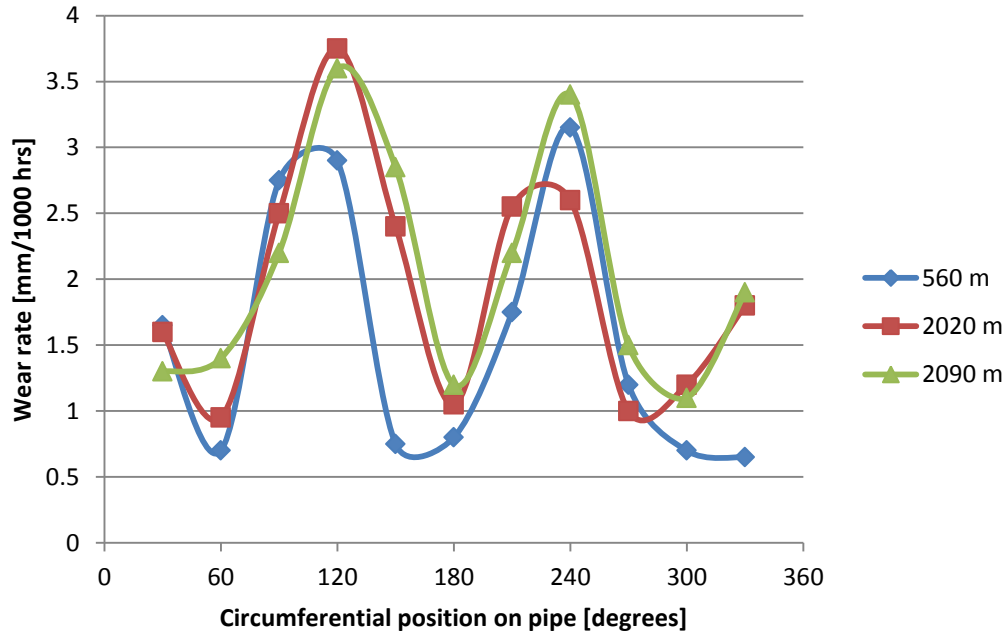


Figure 84 - Wear profiles observed in coarse tailings lines (points connected with splines) (replotted from Schaan *et al.*, 2007)

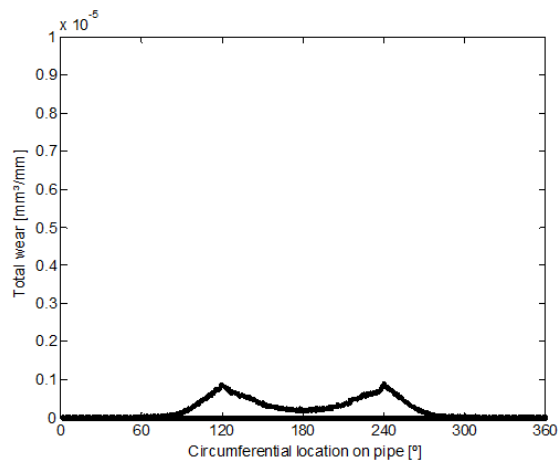


Figure 85 - Simulated wear profile (10 second duration)

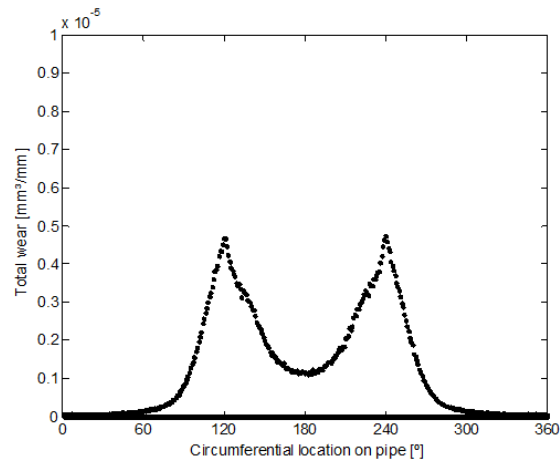


Figure 86 - Simulated wear profile (60 second duration)

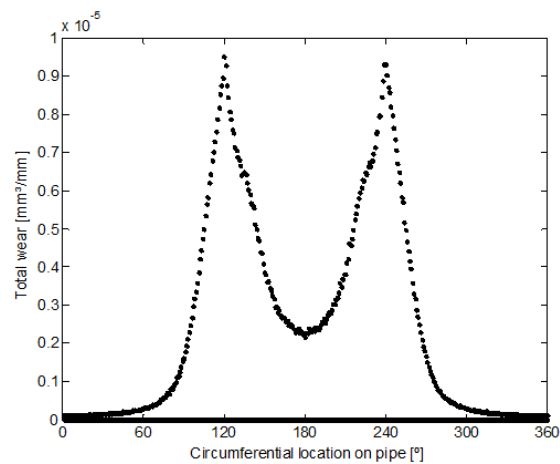


Figure 87 - Simulated wear profile (120 second duration)

One issue with this method is that Schaan *et al.* measured wear in mm of depth, while – due to the use of the Oka equations – this model gives results in mm^3/mm (mm^3 of material removal per mm of axial pipe length). However, from a visual comparison of the Schaan *et al.* results with those shown in Table 4, the model results appear to be within reason.

To demonstrate the usefulness of this method, additional runs were completed with varying flow parameters. All flow conditions were identical to those given above, except that particle size and concentration were varied. Varying these parameters resulted in adjustments to velocities and layer thicknesses as well. Conditions are given in Table 5.

Table 5 - Flow conditions for simulation, phase 2

Run #	Particle size [μm]	Concentration [vol%]	Upper-layer Velocity [m/s]	Bed height [m]	Shear layer Height [m]	Duration [s]
original	150	27.2	6.68	0.18	0.23	10
1	150	20.0	6.93	0.15	0.24	10
2	250	30.0	7.51	0.23	0.19	10
3	250	40.0	7.28	0.29	0.17	10

Results of the simulated flows are given in Table 6.

Table 6 - Simulation results, phase 2

Run #	Wear rate [mm ³ /1000 hrs]
1	33.43
2	39.45
3	33.25

Plots of the simulated wear profiles for each run are given below in Figure 88, Figure 89, and Figure 90. The wear profile varies in a similar fashion to what would be expected in an industrial scenario. From observation, several features are immediately apparent. Firstly, as the thickness of the stationary bed increases, so does the distance between the points of maximum wear. Secondly, as the thickness of the shear interface layer increases, so does the width of each maximum wear peak. Thirdly, as particle size increases, so does the height of each maximum wear peak (this observation is not expected to hold for very large particle sizes, due to a higher settling velocity). An increase in solids concentration – when accompanied by an increase in velocity – results in an increase in wear. However, when it is accompanied by a decrease in velocity (i.e. keeping particle size constant), the wear actually decreases. It is worth noting that the upper-layer velocity is a function of – among other parameters – bulk velocity, bulk solids concentration, and particle size. Even from this limited set of simulations, it is easily apparent that bulk velocity and bulk solids concentration play a key role in determining not only the wear rate, but also the wear profile.

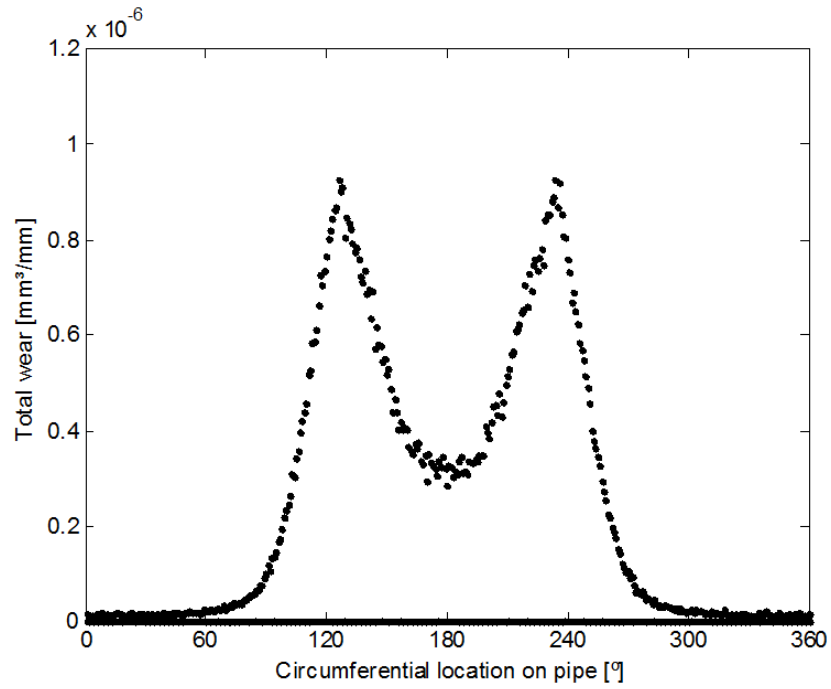


Figure 88 - Simulated wear profile - condition set #1

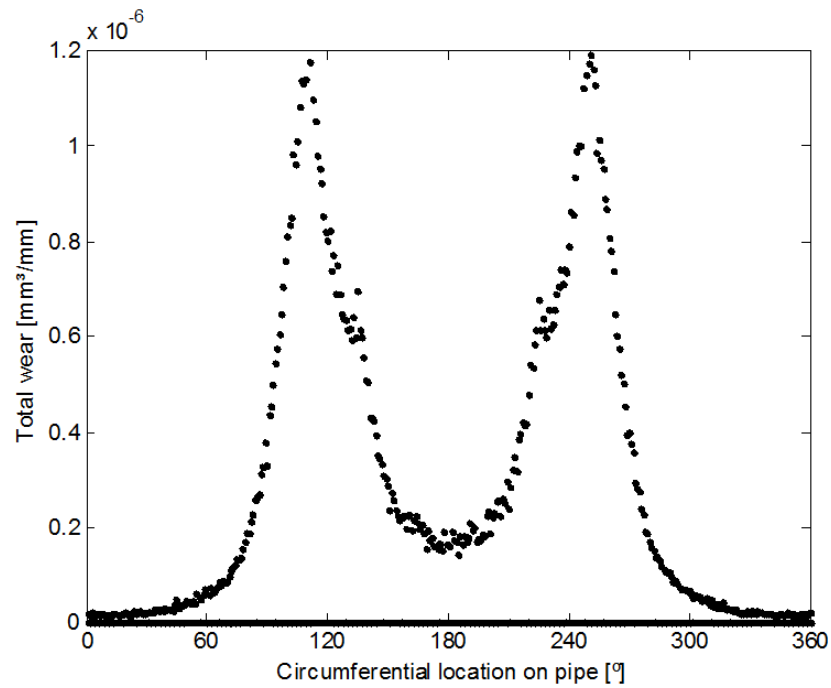


Figure 89 - Simulated wear profile - condition set #2

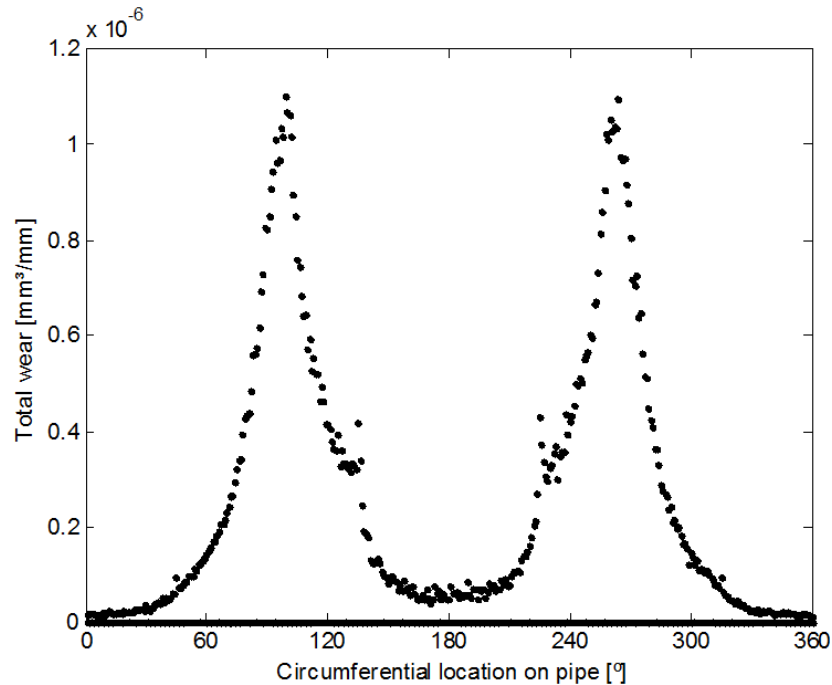


Figure 90 - Simulated wear profile - condition set #3

7.3 Sliding Abrasive Wear Modeling

Modified two-layer model equations were applied to the previously-obtained wear data to generate an abrasive wear model. The following form of equation was developed earlier, to be applied to damage modeling due to bed-flow abrasion:

$$\dot{D} = \varphi V_2 (\tau_2 - \tau_0)$$

Prior to determining the empirical constant, wear test data was inspected for linearity with respect to the model parameters. Plots were created to show the observed wear rate with respect to the predicted velocity and shear stress. These are given below in Figure 91 and Figure 92. Velocities and shear stresses were calculated using the modified two-layer slurry flow model. A review of the model equations will reveal that the majority of its parameters rely to some extent on the density and/or viscosity of water. Hence, in an effort to improve accuracy, water density and viscosity were calculated using the average temperature value measured during each respective experimental run. Note

that while data fit is strongly linear with respect to shear stress, the relationship with velocity may be fit either linearly or as a power-law function.

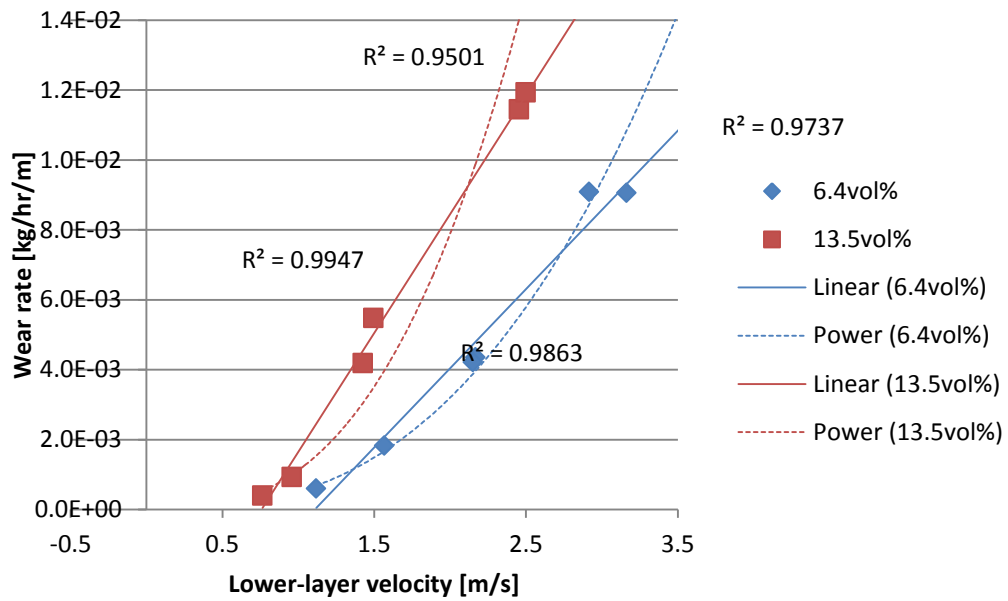


Figure 91 - Wear rate with respect to velocity

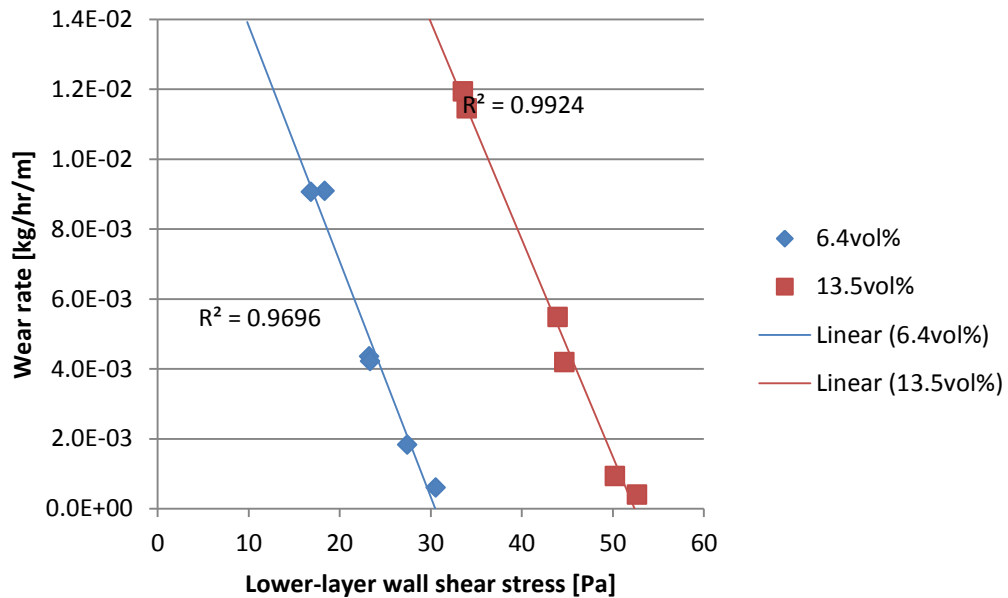


Figure 92 - Wear rate with respect to shear stress

In both Figure 91 and Figure 92, the plotted data appears to be grouped by solids concentration value. Note from a comparison of both figures that shear stress due to Coulombic friction decreases with velocity, as expected from the Two Layer model. Coulombic friction is calculated as the product of a coefficient of friction and the normal force exerted by the solids bed on the pipe wall. As velocity increases, near-wall lift forces increase, and an increasing number of particles are suspended by the carrier fluid turbulence. The size of the moving bed decreases, resulting in a decrease in Coulombic friction.

To further test the validity of the selected wear rate equation, observed wear rates were plotted against the product of velocity and shear stress. The result is shown below in Figure 93. The data may be fit either linearly or using a power-law function; as before, the data appears to be grouped by concentration, though not as tightly as in the individual velocity and shear plots.

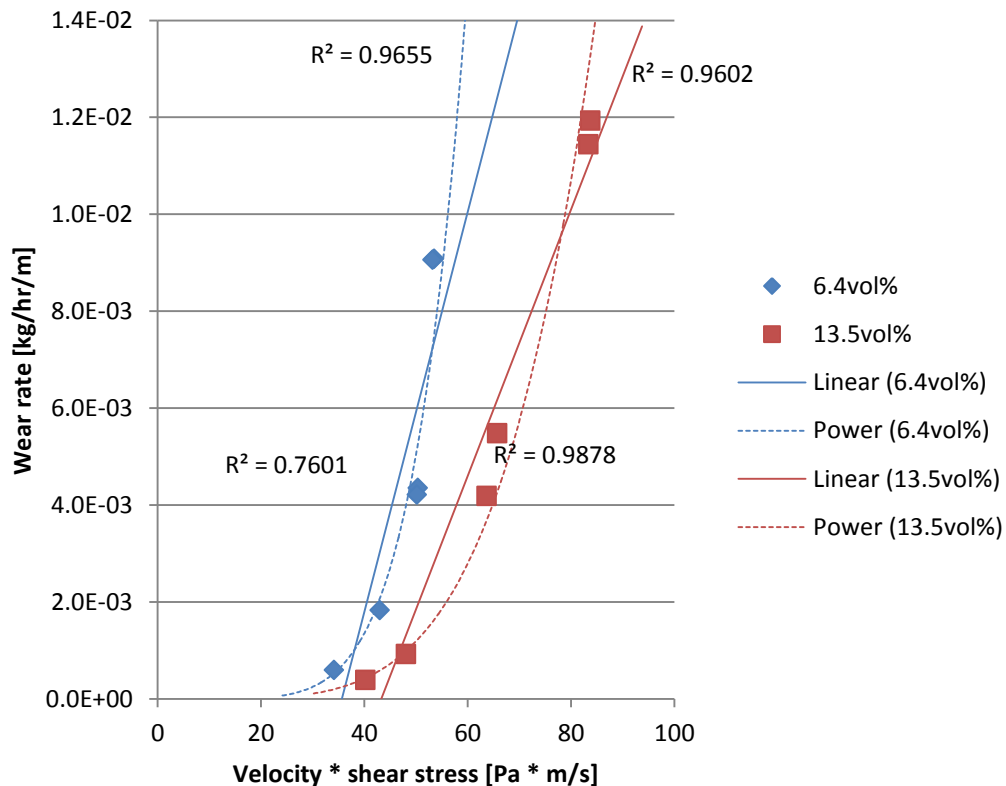


Figure 93 - Wear rate with respect to shear stress * velocity

To test the role of concentration in determining the wear rate, the velocity and shear stress were multiplied by the solids concentration value. A plot of wear rate as a function of this product shows that including a concentration factor appears to provide no extra value, as shown below in Figure 94. Other methods were evaluated, including the square, the cube, and the square root of the concentration value; none of these caused the data to align into a single, coherent set of linear results. Rather, including this concentration factor appears to have had the opposite effect.

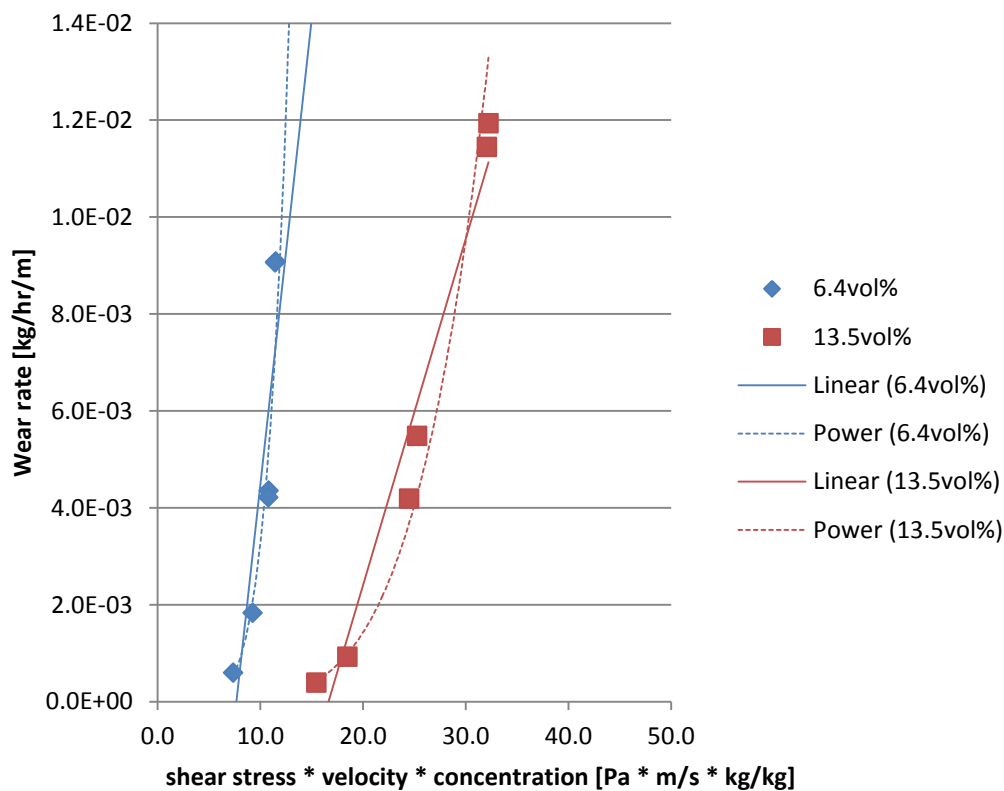


Figure 94 - Wear rate with respect to shear stress * velocity * concentration

The concept of a concentration factor was abandoned. Earlier it was discussed that solid particle erosion wear often follows a power-law function of particle velocity [Kosel, 1992]. The wear equation was re-formulated to include a power-law velocity relationship. Using a power-law least-squares, an exponent of 1.55 was found to provide excellent fit to the data.

The linear fit constants were calculated using the following format:

$$\dot{D} = \varphi V_2^{1.55} (\tau_2 + \tau_0) + \delta$$

Using a least-squares estimation, holding τ_0 zero, the values of φ and δ were found to be

$$\varphi = 9.753 \cdot 10^{-5}$$

$$\delta = -1.208 \cdot 10^{-3}$$

The linear intercept constant δ is unexpectedly large. It is on the same order of magnitude as the observed wear rates themselves, and the significance of this fact is of great interest. There are several possible explanations for this constant, given below.

- The intercept constant may be an artifact of the small sample size.
- Elevated flow rates tend to produce higher process temperatures due to increased friction and energy input from the pump. There is a possibility that at these elevated temperatures the urethane coating may begin to soften, causing the wear to accelerate. However, an investigation of thermal wear effects is beyond the scope of this research.
- As discussed earlier, there is the possibility that the Coriolis meter is out of calibration as a result of extensive solid slurry testing. The linear intercept constant may reflect data discrepancies.
- The constant confirms the existence of a threshold shear stress required for damage to occur. The intercept constant may – wholly or partially – represent this threshold stress. However, the urethane material which was used to coat the inner surfaces of the wear specimens is very soft (Shore D hardness of 68); a scratch from a human finger nail easily produces visible scarring. Thus, there is the alternative possibility that the threshold shear stress is very low and may be difficult to resolve with the current measuring techniques.

It is anticipated that the intercept constant represents the threshold shear stress of the wall material. Whether this representation is in whole or in part is unknown, but for lack of information let us assume that the representation is in whole. A tentative value for the threshold shear stress τ_0 was determined by iterating until δ approached zero, yielding $\tau_0 = 21.29$ Pa. This value caused the linear regression constants to adjust to the following values:

$$\varphi = 1.601 \cdot 10^{-4}$$

$$\delta = 1.590 \cdot 10^{-10}$$

Since the linear intercept constant is 6-7 orders of magnitude less than the wear rate values themselves, it was neglected. The final empirical wear equation is then:

$$\dot{D} = \phi V_2^{1.55} (\tau_2 - \tau_0)$$

Using this equation, wear rates were predicted for observed experimental flow conditions – specifically, those data points not used in building the model. As shown in Figure 95, the linear fit with the data appears to be good.

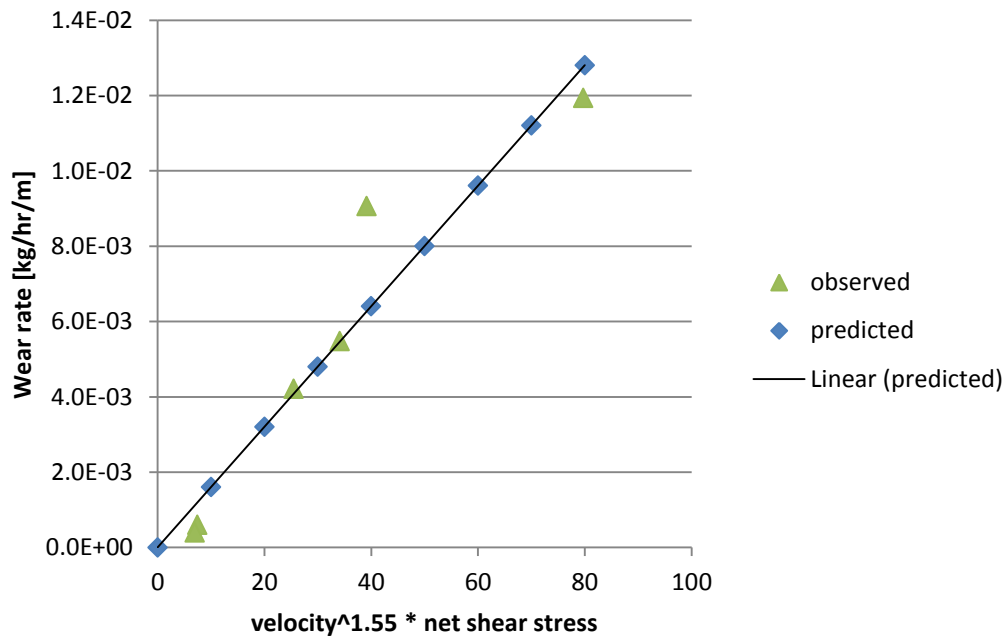


Figure 95 - Wear data corrected for threshold shear stress and concentration

It is worthwhile to reflect on how these results relate to theory. The sliding-erosive wear model developed here relies only on calculated layer-specific velocity and shear stress. The original objective was to develop a wear model which is a function of both flow rate and solids concentration. Outwardly it may appear that the effects of quantities such as concentration, particle size, and geometry are ignored. However, an examination of the Two-Layer model (both SRC and modified versions) reveals that velocity and shear stress of the lower layer are calculated using all of these quantities, in varying degrees. The

empirically-determined exponent 1.55 and constant φ reflect on the materials chosen, as well as any flow conditions not described by the SRC model. For instance, at dilute particle concentrations, turbulence and velocity profile may lead to a rolling, bouncing particle motion against the pipe wall. This may in turn result in a measure of impingement wear occurring simultaneously with sliding erosion.

As mentioned earlier, the data obtained from the Coriolis meter were known to be erroneous. From observations, the readings were incorrect, yet repeatable. Hence, this error was deemed to be a bias rather than an inaccuracy. The extent of this error has been quantified for the case of clean water, but is unknown for slurry flow measurements. In order to increase confidence in the predictive ability of this abrasion model, a sensitivity analysis was conducted on the model results. Mass flow rate was selected as the varying parameter, being the quantity whose integrity is in question, as well as being the dominant quantity (both velocity and shear stress are calculated from it). Nominal (as-read) mass flow values were varied by $\pm 10\%$, and these values were then used to calculate velocities and shear stresses for each experimental run. The value of 10% was chosen because it was nearly double the observed error between recorded and actual density values. The new velocities and shear stresses required that new values for the exponent n , φ , and τ_0 be determined. The model parameters for all cases are given in Table 7 below. Model predictions for each case were plotted next to the actual measured wear rates for comparison; see Figure 96.

Table 7 - Sensitivity analysis results

	Mass flow – 10%	Mass flow nominal	Mass flow + 10%
n	1.30	1.55	1.75
φ	$2.226 \cdot 10^{-4}$	$1.601 \cdot 10^{-4}$	$1.146 \cdot 10^{-4}$
τ_0	22.18	21.29	20.49

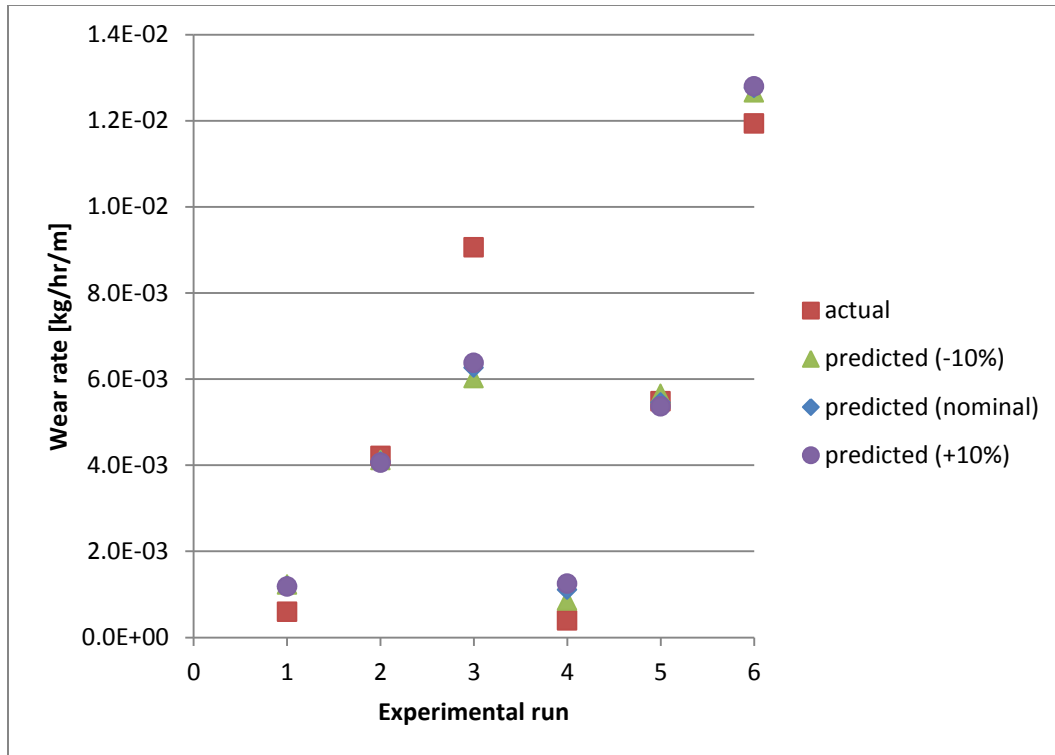


Figure 96 - Predicted and actual wear rates

Data for the experimental trials described above is provided in Table 8 below.

Table 8 - Experimental run properties

Trial	Concentration [vol%]	Pump speed [Hz]
1	6.4%	40
2	6.4%	40
3	6.4%	50
4	6.4%	50
5	6.4%	60
6	6.4%	60
7	13.5%	40
8	13.5%	40
9	13.5%	50
10	13.5%	50
11	13.5%	60
12	13.5%	60

Table 9 - Predictive error of the model

	Mass flow – 10%	Mass flow nominal	Mass flow + 10%
Mean error	32.63%	42.19%	47.65%
Error standard deviation	57.14%	74.26%	85.47%

From the data and the results discussed above, several conclusions can be drawn.

A total of six flow conditions (3 flow rates x 2 concentrations) have been used in the development of this model. To demonstrate repeatability, these conditions have been repeated twice. The “repeatability” data set has been used here to validate the model parameters. However, in order to reduce the predictive error so that confidence may be established in the model’s predictive reliability, a significantly greater pool of data is needed. For instance, it would be useful to more fully examine the role of particle concentration by running wear tests in increments of, say, 2.5vol% over a range of 0-35vol%. Similarly, the role of velocity may be more fully examined by running tests using pump speed increments of 5 Hz over the range of 0-60 Hz. It would also be worthwhile to further expand the data pool by examining the effects of several varieties of solid constituent (e.g. silica, oilsand, and crushed mineral ores) and pipe wall coating. Particle hardness, angularity, and size would be of primary interest.

The given threshold shear stress values rely on the assumption that τ_0 for the urethane coating is wholly represented by the linear intercept constant. As this model is only loosely based on wear physics, it is not expected that this assumption is true in reality. In practice, the true value for τ_0 should be determined through standardized abrasion tests. Additional slurry wear testing (perhaps using a variety of alternate solids) may be conducted to determine the cause of the linear intercept constant.

Predictive error is somewhat high for all three cases of the sensitivity analysis. It can readily be seen that on average, the model tends to over-predict wear rates. Practically speaking, this provides a margin of safety for scheduling pipe maintenance. However, a more precise prediction is preferable, as this would allow operators to make more informed decisions regarding the desired margin of safety. Additional experimental data is required to improve confidence in the predictive reliability of this model.

Mass flow rates provide an excellent starting point for calculating bulk velocities and layer-specific velocities, provided that the data is good. The Coriolis meter was used to provide flow rate data for these tests, and the reported values are adversely affected by the presence of bed flow through the device. In the future, it would be worthwhile to reconfigure the pipe rig so that the Coriolis meter is mounted in a section of vertical flow. This would prevent a solids bed from forming within the Coriolis meter and allow for more accurate measurements.

This model is designed to predict only the total mass loss, without providing any information regarding the wear location. At best, it can only predict a mean wear rate over the section of pipe wall which supports the slurry bed. In an industrial setting it would be much more useful to be able to predict localized mass loss, and in particular the localized wear depth. To make the link between this model and a localized wear model, surface profiling would be required. This may be accomplished by ultrasonic scanning (non-destructive), a surface probe (requires cutting the tube axially), or a coordinate-measuring machine (CMM) to scan the surface. Due to the non-homogeneous walls of the wear specimens, ultrasonic scanning of the wall thickness is not feasible at this time.

It should be stressed here that the objective of this research work was not only to build a formulation for a predictive wear model, but to link the wear rate data to flow rate and solids concentration, and to develop an apparatus for running slurry experiments. These objectives have been met. The existence of a shear interface layer has been demonstrated, and a formulation has been developed to describe its behaviour. The properties of this layer have been linked to sliding-abrasive and impingement wear models. This allows wear to be described as a function of flow parameters such as flow rate and solids concentration. Regarding the sliding-abrasive wear model, the proportionality assumption has been demonstrated to be valid with respect to shear stress and a power function of velocity.

8 Conclusions and Recommendations for Future Work

8.1 Conclusions

8.1.1 Experimental Apparatus Development

A pipe loop was built and commissioned in order to provide a platform for tests involving various types of slurries. This pipe loop may be effectively employed in the study of numerous aspects of slurry flow. These include:

- Pipe wear due to sliding abrasion and particle impingement
- Stresses and strains experienced at the pipe wall due to slurry flows
- Particle velocities at the vicinity of the pipe wall

Capabilities of the pipe loop are:

- Enabling observation of laboratory-scale stratified flows of coarse, settling slurries through hydrotransport pipelines and tailings pipelines, using a supplied pump head of up to 11 m.
- Measuring fluid pressure at several fixed locations along the loop, over a range of 0-200 kPa. These measurements enable calculation of the average pressure drop, as well as observation of pressure fluctuations at each location.
- Measuring process and ambient temperatures over a range of 0-100°C.
- Measuring the mass flow rate of the mixture through the loop, over a range of 0-10 kg/s.
- Measuring the density of the slurry mixture over a range of 500-1500 kg/m³.
- A modular design which allows for a variety of slurry testing to be undertaken.

A software application was developed using the National Instruments LabWindows/CVI 2010 platform for operation of the pipe loop as well as managing the sensor data. The software is capable of

- Controlling the motor speeds of the slurry pump and the mixer.
- Reading sensor data from the loop in real time, applying calibration constants, and logging the raw and calibrated data to a file.
- Selective sensor logging at varying sample rates.
- Displaying sensor data graphically on the user interface.
- Running experiments on “auto pilot” mode, in which the pump speed and duration of operation are provided in a text file.

Several calibration and commissioning experiments were run to ensure the integrity of the acquired data, as well as to verify that all equipment was functioning as intended. These are described below.

- Pressure transducers were calibrated using a factory-calibrated static air pressure regulator. Transducers were individually mounted to the device, and the pressure was raised in discrete increments of 10 kPa between 0 and 200 kPa. Calibration was completed using an Omega DPI610 pressure calibrator.
- RTDs were calibrated using a factory-calibrated water bath device. All sensors were suspended together in the bath while the fluid temperature was raised in increments of 5°C between 20°C and 40°C. At the time of calibration, preliminary testing had indicated that process temperatures would not exceed 40°C; however, temperatures of over 55°C were observed during later experiments. It was noted, however, that the sensor response showed excellent linearity over the range of calibration. Since process temperature was not integral to this testing, it was not felt that this would compromise the test results in any way.
- The Coriolis meter was calibrated by pumping a pre-determined volume of clean water through the pipe loop at a steady pump speed. Flow rates were determined by dividing the volume by the length of time required to pump it. These in turn were compared against the readings provided by the Coriolis meter.
- The instrumented strain spool was calibrated by resting a known weight axially on the spool and obtaining the gauge readings. The axial force was applied in increments of 5 kg (49.05 N) over the range of 0-15 kg (0-147.15 N).
- Slurries consisting of 5% and 10% silica sand by weight were pumped through the pipe loop in order to illuminate any potential issues with the

equipment or sensors. At this time several issues were noted with the slurry pump, the pipe routing, and the materials to be employed during wear tests. These issues were immediately rectified.

8.1.2 Summary of Experimental Results

Slurry pipe wear tests were conducted under varying conditions of solids concentration and pump speed. Test results are summarized below.

- Wear incurred by garnet sand slurries was primarily bed-flow abrasion over the lower surfaces of the wear specimens. No impingement wear was visible in the wear specimens. In order to create conditions conducive for the observation of impingement wear, it is advisable to utilize a solid component of either reduced density or reduced size. The results of Schaan *et al.* (2007) suggest that it may also be necessary to pump the mixture at a decreased velocity and/or increased solids concentration, such that a stationary solids bed is formed.
- Material loss in the wear specimens was dependent on velocity, wall shear stress, and bulk concentration. This dependence was determined to be proportional to the product of lower-layer velocity raised to a power of 1.55, and the lower-wall net shear stress. The net shear stress here is defined as the difference between the Coulombic friction shear stress and a threshold stress value beyond which wear may occur.

Pipe wall strain tests were performed using flow conditions identical to those used in the wear tests. The objective of these tests was to determine whether the pipe wall shear stresses induced by slurry flow may be measured from the exterior or the pipe. Results are described below.

- Circumferential strains showed close agreement with theoretical calculations for pressure-induced strain.
- Measured axial strains did not agree with theory. It is expected that this disparity is largely due to the wall shear stresses induced by the slurry solids sliding over the interior pipe surface.

- Strong disparities were noted between the readings of individual gauges. This may be at least partly attributed to irregularities in wall thickness.
- The acrylic spool exhibited viscoelastic behaviour under stress. This non-linear, time-dependent behaviour is undesirable, as it creates difficulties with obtaining accurate measurements. If this method of measuring strain is to be used in future studies, it is recommended that an alternative material be selected for construction of the spool.
- Due to unrepairable damage to the spool, further strain testing was not completed. It had been hoped that information on hysteresis behaviour of the spool could be obtained, but this may need to be reserved for a future project.
- Large variations in temperature were observed during experimental runs. While thermal effects on wear were neglected in this study, it is advisable to install a chiller / heat exchanger system for future studies, in order to regulate process temperature.

Particle tracking velocimetry (PTV) experiments were conducted using high-speed imaging through an optically clear section of pipe. In spite of the inherent difficulties created by conditions of low visibility and high solid density, it was expected to be able to observe the motions of particles in the vicinity of the pipe walls. Results are described below.

- The use of strong back-illumination created good optical contrast between the dark particles and the bright background.
- The ability of this method to resolve individual particles was improved by reducing the solids concentration values, and by keeping pump speed between 30-50 Hz.
- Particle detection was hampered by murkiness of the carrier fluid caused by solid fines entrained in the flow. Performance of the method was also reduced by motion blur at pump speeds in excess of 50 Hz.
- Test results confirmed several assumptions made earlier in the development of a wear model:
 - In a given slurry flow through a circular pipe, there exists a shear interface layer between the upper and lower flow layers.
 - Axial velocity shows a linear increase with height across the shear layer.
 - Turbulent particle motion shows a linear change with height across the shear layer. Contrary to what was originally expected,

- however, this change is a decrease with height, rather than an increase.
- Local solids concentration shows a linear increase with height across the shear layer.
 - The magnitude of turbulent particle motion may be described by a random, normal distribution.
 - The thickness of the shear layer appears to increase linearly with respect to the bulk flow rate.
 - As expected, the PTV method was unable to resolve motion in the bed flow region.

8.1.3 Modeling of Slurry Flow and Pipe Wear

A modified version of the SRC Two-Layer model [Gillies *et al.*, 1991, 2000, 2004] [Wilson *et al.*, 2009] was developed. The primary difference between the two models is the presence of a shear interface layer located between the upper and lower flow layers. Pipe wear in the vicinity of this layer is dominated by impingement, while wear at the lower layer is due only to sliding abrasion. A full set of equations was developed to describe the properties and behaviour of this layer. To compare the flow predictions of this model with those of the SRC model, a set of simulations were run. Holding all other parameters constant, the bulk velocity was increased in steps of 0.5 m/s, and the predicted velocities, shear stresses, and cross-sectional areas of each flow layer were recorded. The overall result was that the modified two-layer model performed comparably with the SRC Two-Layer model. Notable exceptions were:

- The cross-sectional layer areas of the modified two-layer model change rapidly with respect to increasing bulk velocity. This is a deliberate alteration, as it is felt to reflect the manner in which the upper and lower layers change in the presence of the shear interface layer.
- Modified upper and lower velocities were introduced, to allow the model to predict pseudo-homogeneous flow at elevated flow rates.

To model pipe wear, two separate predictive models were created: one to describe sliding abrasion wear, and the other to describe impingement wear.

Both models rely on the Modified Two-Layer flow model for their inputs (velocity, shear stress, layer thickness, etc.). The sliding abrasion model was developed on the results of the wear testing. It predicts wear as a function of lower-layer velocity, lower-layer wall shear stress, and a threshold shear stress above which wear occurs. The final empirical equation for garnet slurry erosion of cast urethane is

$$\dot{D} = \varphi V_2^{1.55} (\tau_2 - \tau_0)$$

Where

\dot{D} : material removal rate, given in [kg/hr/m]

φ : proportionality constant, found to be $1.601 \cdot 10^{-4}$ for Repro Light castable urethane

V_2 : lower-layer velocity, as predicted by the two-layer model

τ_2 : lower-layer wall shear stress, as predicted by the two-layer model

τ_0 : threshold shear stress, determined to be 21.29 Pa for Repro Light castable urethane

The impingement model employs a Monte Carlo simulation approach to determine the wear around the pipe circumference. Since the wear testing did not yield any visible impingement wear, the industrial results of Schaan *et al.* (2007) were used as a comparative base for the model results.

The model considers the turbulent particle motion to be entirely responsible for impingement wear. This motion is described by a random, normal distribution with a mean of zero. The standard deviation of this motion is highest at the base of the shear interface layer, and decreases linearly with height across the layer.

Using the flow conditions described in Schaan *et al.* (2007) for coarse tailings pipelines, results of the impingement model showed excellent agreement with the wear profile described in the literature. The authors measured wear in mm of depth, while – due to the use of the Oka equations – this model gives results in mm³/mm (mm³ of material removal per mm of axial pipe length). Additionally, the predictive model requires significant time to solve – over half a

minute for every second of simulated flow time. This makes a comparison of numerical results fairly difficult, but the predicted values appear to be within reason. In the future, large increases in calculation speed may be obtained by porting the model code from Matlab to C or C++.

Castable urethane (as opposed to steel) was used in the wear testing, as opposed to the steel pipe in Schaan *et al.* Once wear testing has been conducted on steel pipe (or impingement wear has been conducted on a urethane pipe coating), it will be possible to develop a unified pipe wear model.

8.2 Recommendations for Future Work

To expand on the knowledge gained from this study, it is suggested that the following projects be conducted by anyone wishing to continue this research.

- Conduct sliding abrasive wear testing on steel wear specimens. This is viewed as the step which will bridge the gap towards the completion of a unified pipe wear model. Since higher shear stresses are required to wear steel, such testing would require pumping dense slurry through larger-diameter pipe wear specimens. For this, the Large-Scale Fluids lab at the University of Alberta may be inadequate, and the use of alternate facilities may be required, such as the Alberta Innovates laboratory, the Syncrude test facility, or the SRC slurry flow lab.
- Expand the wear model to include other physical/chemical effects. It has been found here that mass flow rate and solids concentration play a large role in determining the rate of pipe wear. However, this study has purposely ignored the effects of several parameters in the interest of building a model formulation for mechanical wear. Specifically, the following are seen as potentially important contributing parameters:
 - Particle size and density
 - Particle angularity
 - Solid material (i.e. crushed mineral ores, oilsand)
 - Solid fines
 - Carrier fluid pH
 - Process temperature

- Conduct sliding abrasive wear tests under stationary (or near-stationary) bed conditions. This may provide insights into the mechanism of impingement wear.
- Refine the design of the floating-element sensor developed by El-Sayed (2010) as a method of measuring pipe wall shear stress. Currently it is prone to plugging by sand particles, but once this issue is remedied, the device could add great value to the study of pipe wear.
- Rather than focussing on the mechanism of pipe wear, concentrate on developing on-line methods for detecting pipe wear in real time. Examples of such techniques include acoustic emission and ultrasonic-B scanning.
- Develop alternative optical methods for observation of slurry flow through pipes. It may be possible to employ the stereo PIV technique, using glass or fused silica particles. If successful, this technique would provide information on three-dimensional particle motion, including particle motion in bed flow. Another possibility would be to develop a boroscope-type device which is capable of traversing the pipe diameter and observing flow patterns.
- Refine the impingement simulation to include particle-particle effects. There is no doubt that these effects play a role in defining the wear zones on the pipe walls. The inclusion of these effects will likely improve accuracy. Interaction between suspended particles would be very difficult to model, but interaction between suspended particles and the solids bed is straightforward to model. One approach would be to include a conditional statement such that if a given particle's projected point of impact lies below the upper boundary of the solids bed, that particle is neglected.
- The instrumented spool was redesigned for future use, taking safety of operation into account. The new changes are:
 - Utilize a shatter-resistant polymer, such as polycarbonate or PVC. PVC was eventually chosen due to manufacturing tolerances. Creep may still be an issue due to the viscoelastic nature of many polymers.
 - Use a thinned wall thickness of 1.5 mm. Avoid stress concentrations by introducing a 3 mm radius of curvature where the wall thickness changes.
 - Minimize variations in wall thickness by mounting the tube to the lathe, using the inner surface rather than the outer surface. This

will allow for uniform wall thinning which will also cause the strain gauges to read more accurately.

- Introduce a soft rubber gasket seal in each of the supporting flanges. These will absorb some of the clamping force, and reduce the overall amount of force needed to prevent leaks.
- Re-commission (i.e. clean and re-calibrate) the Coriolis meter and mount it vertically rather than horizontally on the pipe rig. This configuration will allow for more accurate density and flow rate measurements, especially at lower flow rates.

In the completion of the work described in this document, my personal contributions were the following:

- Final working design of the pipe loop, including sensor installation, management of repairs to the pump, design and installation of a flush-water system for the pump seal, re-routing of select piping sections, and installation of VFD Ethernet control modules
- Design and mounting of strain gauges on the instrumented strain spool
- Commissioning of the pipe loop components, and wiring and calibration of all sensors
- Designing and building (minus the machining) an instrumented spool for measuring pipe wall shear strains
- Design and development of a software application for controlling the pipe loop system and managing the data acquired from it
- Designing and executing experiments for determining wear rates (the final set of wear tests were run by Mr. Derek Russell and Mr. Shantanu Diwakar in my absence)
- Processing and analysis of all acquired data (with the exception of pre-processing of the optical PTV data, which was completed by Mr. Debjyoti Sen)
- Development of equations to modify the two-layer slurry flow model
- Development of a Matlab script to run a Monte Carlo-style impingement wear simulation

In these concluding remarks, it is worth recalling that the purpose of this work was to lay a foundation for a simple, robust model which may be applied in an industrial setting, as a means of predicting the useful life of a section of pipe. Through this work, strides have been made towards that goal; however, this predictive model remains simplistic at best. Significant development work is

required before this model may be applied successfully in a setting as demanding as an oilsands mine. Hopefully this work will inspire others to continue the research in order to eventually make this model a reality.

Bibliography

- Abulnaga, B. E. (2002). *Slurry Systems Handbook*. New York: McGraw-Hill.
- Alberta Environment and Water. *Water usage*.
<http://oilsands.alberta.ca/water.html>. Accessed May 19, 2012.
- Bagnold, R. A. (1956). *The Flow of Cohesionless Grains in Fluids*. Philosophical Transactions of the Royal Society London, Series A, Vol. 249 (pg. 235-297).
- BHRA Fluid Engineering (1980). *Wear in Slurry Pipelines*. BHRA Information Series, No. 1. Edited by Gittins, L. Cotswold Press Ltd., Oxford, U.K.
- Bhushan, V. (2011). Assessment of hyperspectral features and damage modeling of bitumen flotation process. Master of Science thesis, University of Alberta.
- Bitter, J. G. A. (1962). *A Study of Erosion Phenomena, Part 1*. *Wear*, Vol. 6 (pg. 5-21).
- Budynas, R. G. & Nesbitt, J. K. (2008). *Shigley's Mechanical Engineering Design*, 8th Edition. McGraw-Hill Science/Engineering/Math, Boston.
- Churchill, S. W. (1977). *Friction factor equation spans all fluid-flow ranges*. *Chemical Engineering*, Vol. 84, No. 24 (pg. 91-92).
- Colwell, J. M. & Shook, C. A. (1988). *The Entry Length for Slurries in Horizontal Pipeline Flow*. *The Canadian Journal of Chemical Engineering*, Vol. 66, October 1988 (pg. 714-720).
- Durand, R. (1952). *Basic Relationships of the Transportation of Solids in Pipes – Experimental Research*. Proceedings of the Minnesota International Hydraulics Convention, September 1953 (pg. 89-103).
- El-Sayed, S. (2010). *Measuring Wall Forces in a Slurry Pipeline*. Master of Science thesis, University of Alberta.
- El-Sayed, S. & Lipsett, M. G. (2009). *Monitoring Wear in Slurry Pipelines*. Sixth International Conference on Condition Monitoring 2009, Edinburgh.
- Evans, M. (2012). *Development of an Experimental Apparatus for Studying the Effects of Acoustic Excitation on Viscosity*. Master of Science thesis, University of Alberta.
- Finnie, I. (1960). *Erosion of Surfaces by Solid Particles*. *Wear*, Vol. 3 (pg. 87-103).

- Gillies, R. G., Shook, C. A., Wilson, K. C. (1991). *An improved two-layer model for horizontal slurry pipeline flow*. The Canadian Journal of Chemical Engineering, Vol. 69, February 1991 (pg. 173-178).
- Gillies, R. G. & Shook, C. A. (2000). *Modelling High Concentration Settling Slurry Flows*. The Canadian Journal of Chemical Engineering, Vol. 78, August 2000 (pg. 709-716).
- Gillies, R. G., Shook, C. A., Xu, J. (2004). *Modelling Heterogeneous Slurry Flows at High Velocities*. The Canadian Journal of Chemical Engineering, Vol. 82, October 2004 (pg. 1060-1065).
- Gysling, D. L. (2004). *Application of Sonar-Based, Clamp-on Flow Meter in Oilsand Processing*. ISA 2004 Exhibit and Conference – Edmonton Section.
- Hein, F. J. (2005). *Historical Overview of the Fort McMurray Area and Oil Sands Industry in Northeast Alberta*. Alberta Geological Survey.
- Hibbeler, R. C. (2005). *Mechanics of Materials*, 6th Ed. Upper Saddle River, New Jersey: Pearson Prentice Hall.
- Kosel, T. (1992). *Solid Particle Erosion*. ASM Handbook, Vol. 18: Friction, Lubrication, and Wear Technology (pg. 199-213).
- Lipsett, M. G. (2009). *Modeling wear damage accumulation in slurry pipeline systems*. COMADEM 2009.
- Lipsett, M. G. (2012). *Using Parametric Dynamical Models to Determine Observability Requirements for Condition Monitoring Systems*. Proc. 2nd Int'l Conf. Cond. Mon. in Non-Steady Ops, Tunisia, March 2012 (pg. 99-109).
- MATWEB – “Overview of materials for Cast Acrylic”.
<http://matweb.com/search/DataSheet.aspx?MatGUID=a5e93a1f1fff43bcbac5b6ca51b8981f>. Accessed 6 April 2013.
- Mochinaga, H. et al (2006). *Properties of Oil Sands and Bitumen in Athabasca*. CSPG – CSEG – CWLS Joint Convention 2006 (pg. 39-44).
- Nasr-El-Din, H., Shook, C. A. & Colwell, J. (1986). *Determination of Solids Concentration in Slurries*. Hydraulic Transport of Solids in Pipes, BHRA Fluid Engineering (pg. 191-198).
- Neville, A. & Reza, F. (2007). *Erosion-Corrosion of Cast White Irons For Application in the Oilsands Industry*. NACE Corrosion 2007 Conference & Expo. Paper #07678.

Nnadi, F. N. & Wilson, K. C. (1992). *Motion of Contact-Load Particles at High Shear Stress*. Journal of Hydraulic Engineering, Vol. 118, No. 12, December 1992 (pg. 1670-1684).

Nnadi, F. N. & Wilson, K. C. (1995). *Bed-Load Motion at High Shear Stress: Dune Washout and Plane-Bed Flow*. Journal of Hydraulic Engineering, Vol. 121, No. 3, March 1995 (pg. 267-273).

Oilsands Information Portal (2011). *Talk About Oilsands*. <http://oilsands.alberta.ca/>. Accessed May 17, 2012.

Oilsands Information Portal (2012). *Facts About Alberta's Oilsands: The Resource*. <http://oilsands.alberta.ca/>. Accessed May 17, 2012.

Oilsands Information Portal (2012). *Reclamation*. <http://oilsands.alberta.ca/>. Accessed August 10, 2012.

Oilsands Information Portal (2012). *Talk About Upgrading and Refining*. <http://energy.alberta.ca/>. Accessed May 17, 2012.

Oka, Y. I., Okamura, K., Yoshida, T. (2004). *Practical estimation of erosion damage caused by solid particle impact, Part 1: Effects of Impact Parameters on a Predictive Equation*. Wear 259, 2005 (pg. 95-101).

Oka, Y. I. & Yoshida, T. (2004). *Practical estimation of erosion damage caused by solid particle impact, Part 2: Mechanical Properties of Materials Directly Associated with Erosion Damage*. Wear 259, 2005 (pg. 102-109).

Plaseied, A. & Fatemi, A. (2009). *Tensile Creep and Deformation Modeling of Vinyl Ester Polymer and Its Nanocomposite*. Journal of Reinforced Plastics and Composites, Vol. 28, No. 14/2009 (pg. 1775-1788).

Pugh, F. J. & Wilson, K. C. (1999). *Role of the interface in stratified slurry flow*. Powder Technology 104 (pg. 221-226).

Roco, M. C. & Addie, G. R. (1987). *Erosion Wear in Slurry Pumps and Pipes*. Powder Technology 52 (pg. 35-46).

Roco, M. C. & Shook, C. A. (1983). *Modeling Slurry Flow: The Effect of Particle Size*. The Canadian Journal of Chemical Engineering, Vol. 61, August 1983 (pg. 494-503).

Schaan, J. A., Cook, N. A., & Sanders, R. S. (2007). *On-line wear measurements for commercial-scale, coarse-particle slurry pipelines*. The 17th International Conference on the Hydraulic Transport of Solids, May 2007 (pg. 291-300).

- Schaan, J. & Shook, C. A. (2000). *Anomalous Friction in Slurry Flows*. The Canadian Journal of Chemical Engineering, Vol. 78, August 2000 (pg. 726-730).
- Schaan, J., Sumner, R. J., Gillies, R. G., & Shook, C. A. (2000). *The Effect of Particle Shape on Pipeline Friction for Newtonian Slurries of Fine Particles*. The Canadian Journal of Chemical Engineering, Vol. 78, August 2000 (pg. 717-725).
- Shook, C. A., Gillies, R., Haas, D. B., Husband, W. H. W., & Small, M. (1982). *Flow of Coarse and Fine Sand Slurries in Pipelines*. Journal of Pipelines, Vol. 3, No. 1 (pg. 13-21).
- Wilson, K. C. (1987). *Analysis of Bed-Load Motion at High Shear Stress*. Journal of Hydraulic Engineering, Vol. 113, No. 1, January 1987 (pg. 97-103).
- Wilson, K. C. (2005). *Rapid Increase in Suspended Load at High Bed Shear*. Journal of Hydraulic Engineering, January 2005 (pg. 46-51).
- Wilson, K. C. & Addie, G. R. (1997). *Coarse-Particle Pipeline Transport: Effect of Particle Degradation on Friction*. Powder Technology 94 (1997) (pg. 235-238).
- Wilson, K. C. & Pugh, F. J. (1988). *Dispersive Force Basis for Concentration Profiles*. Journal of Hydraulic Engineering, Vol. 114, No. 7, July 1988 (pg. 806-810).
- Wilson, K. C., Sanders, R. S., Gillies, R. G. & Shook, C. A. (2009). *Verification of the near-wall model for slurry flow*. Powder Technology 197, October 2010 (pg. 247-253).
- Wilson, K. C. & Sellgren, A. (2003). *Interaction of Particles and Near-Wall Lift in Slurry Pipelines*. Journal of Hydraulic Engineering, Vol. 129, No. 1, January 2003 (pg. 73-76).

Appendices

Appendix A - Pipe Loop Software Code

```

#include "toolbox.h"
#include <ansi_c.h>
#include <analysis.h>
#include <utility.h>
#include <formatio.h>
#include <cvirte.h>
#include <userint.h>
#include <stdlib.h>
#include <math.h>
#include <NIDAQmx.h>
#include <DAQmxIOctrl.h>
#include <stdio.h>
#include <tcpsupp.h>
#include <string.h>
#include "client.h"
#include "DataLogger.h"

#define DAQmxErrChk(functionCall) if( DAQmxFailed(error=(functionCall)) ) goto Error; else
#define tcpChk(f) if( (g_TCPError=(f)) < 0 ) { ReportTCPError(); goto Done; } else

static int          panelHandle;

static TaskHandle   gTaskHandle = 0;
static float64      *gData = NULL;
static uInt32       gNumChannels;
static uInt32       sampsPerChan;

// 4-20 mA (=0-10 kg/s) mass flowrate from Coriolis meter
// 4-20 mA (=0-100°C) fluid temperature from Coriolis meter
// 4-20 mA (=500-1500 kg/m³) density from Coriolis meter
// 4-20 mA (=0-200 kPa gauge) pressure (pump outlet)
// 4-20 mA (=0-200 kPa gauge) pressure
// 4-20 mA (=0-200 kPa gauge) pressure
// 4-20 mA (=0-200 kPa gauge) pressure
// 4-20 mA (=0-200 kPa gauge) pressure (pump inlet)
// 100 Ohm (=0°C) RTD (ambient)
// 100 Ohm (=0°C) RTD (ambient/extra)
// 100 Ohm (=0°C) RTD (pump outlet)
// 100 Ohm (=0°C) RTD (pump inlet)

static int          logdata;
static CVIAbsoluteTime timestamp;
static double       timedouble;
static char         logfile[300];
static char         runfile[300];

unsigned char       errcode = 0;
FILE               *autoFile = NULL;
static int          numChecked = 0;
static int          runMode = 0;
static int          readParam = 0;

int Is_Log = 0;

static double       starttime;

double             autoStartTime, autoCurrTime;

typedef enum { Pump = 0, Mixer = 1 } motorType;
typedef enum { False = 0, True = 1 } bool;
typedef enum { current = 0, resistance = 1, strain = 2 } readoutType;
typedef struct
{
    motorType type;           // motor or pump
    bool started;           // the "run" signal has been sent (may or may not be physically turning)
    bool running;          // physically running or not
    bool connected;        // TCP connection is active
    unsigned int setpoint;  // speed in [Hz * 10]
    const char addr[15];    // IP address of device controller
    int CVICALLBACK (*TCP)( unsigned tcp, int event, int error, void *callbackData ); // pointer to TCP handler function
    unsigned int tcp;      // TCP handle for each device
    int Control;          // start/stop button control ID
    int Speed;           // set speed button control ID
    int Recon;          // reconnect button control ID
} motor;

typedef struct
{
    readoutType read;      // differentiate between 4-20 mA, 100 ohm, and strain
    float64 *raw;         // array of raw data (current/resistance)
    float64 *val;        // array of real data
    float64 raw_avg;     // 1-second average raw value
    float64 val_avg;     // 1-second average real value
    const char raw_unit[4]; // units used for raw data
    const char val_unit[6]; // units used for real data
    const char name[15];  // channel name
    const char channel[15]; // channel access string
    int chkbox;          // check box associated with this data value
    bool open;          // True = use, False = ignore
    int gauge;          // panel chart associated with this data value
    float64 cal[2];     // array of linear operations for calibration y = ax + b ([0] = a, [1] = b)
} dataPoint;

```

```

double timeVal = 60.0, pSpeed = 250.0, mSpeed = 200.0;
bool readFlag = False;

bool runbyFile = False;

bool sendData( motorType m, unsigned int parameter, unsigned int value );
bool readData( motorType m, unsigned int parameter, unsigned int *value );
void setRunning( motorType m, bool status );
int CVICALLBACK PumpTCP( unsigned ptcp, int event, int error, void *callbackData );
int CVICALLBACK MixerTCP( unsigned mtcp, int event, int error, void *callbackData );
int32 CVICALLBACK EveryNCallback( TaskHandle taskHandle, int32 everyNsamplesEventType, uInt32 nSamples, void *callbackData );
int32 CVICALLBACK DoneCallback( TaskHandle taskHandle, int32 status, void *callbackData );
bool Connect( motorType m );
bool initDAQ( void );

void LogFileHeader( void ); // Saves a header to the log file
void LogFile( void ); // Saves a header to the log file
void setSpeed( motorType m, unsigned int value );
bool startMotor( motorType m );
bool stopMotor( motorType m );
void handleChk( int index );

motor controller[2] = { { Pump, False, False, False, 250, "192.168.124.2", &PumpTCP, 0, PANEL_PUMP_START, PANEL_SETPUMPSPEED,
PANEL_PUMPRECON },
{ Mixer, False, False, False, 200, "192.168.124.3", &MixerTCP, 0, PANEL_MIXER_START, PANEL_SETMIXSPEED,
PANEL_MIXRECON } };

dataPoint data[28] = { { current, NULL, NULL, 0.0, 0.0, "mA", "kg/s", "Mass flowrate", "cDAQ1Mod8/ai0", PANEL_CHK1, True, PANE
L_MASSFLOW, {625.0, -2.5} },
{ current, NULL, NULL, 0.0, 0.0, "mA", "kg/m³", "Density", "cDAQ1Mod8/ai1", PANEL_CHK2, True, PANEL_DEN
SITY, {93750.0, 125.0} },
{ current, NULL, NULL, 0.0, 0.0, "mA", "°C", "Temperature", "cDAQ1Mod8/ai2", PANEL_CHK3, True, PANEL_TE
MPCOR, {6250.0, -25.0} },
{ current, NULL, NULL, 0.0, 0.0, "mA", "kPa", "Pressure 1", "cDAQ1Mod8/ai3", PANEL_CHK4, True, PANEL_PR
ESS1, {12456.5931866798, -50.3370216080576} },
{ current, NULL, NULL, 0.0, 0.0, "mA", "kPa", "Pressure 2", "cDAQ1Mod8/ai4", PANEL_CHK5, True, PANEL_PR
ESS2, {12465.7100452766, -50.8915434061953} },
{ current, NULL, NULL, 0.0, 0.0, "mA", "kPa", "Pressure 3", "cDAQ1Mod8/ai5", PANEL_CHK6, True, PANEL_PR
ESS3, {12439.0383864834, -50.1864616707234} },
{ current, NULL, NULL, 0.0, 0.0, "mA", "kPa", "Pressure 4", "cDAQ1Mod8/ai6", PANEL_CHK7, True, PANEL_PR
ESS4, {12429.4304348174, -50.0295584389912} },
{ current, NULL, NULL, 0.0, 0.0, "mA", "kPa", "Pressure 5", "cDAQ1Mod8/ai7", PANEL_CHK8, True, PANEL_PR
ESS5, {12429.8375165576, -49.6590910300129} },
{ resistance, NULL, NULL, 0.0, 0.0, "°C", "°C", "Temperature 1", "cDAQ1Mod7/ai0", PANEL_CHK9, True, PAN
EL_THERMO1, {0.759243321720842, 5.24412743683666} },
{ resistance, NULL, NULL, 0.0, 0.0, "°C", "°C", "Temperature 2", "cDAQ1Mod7/ai1", PANEL_CHK10, True, PA
NEL_THERMO2, {0.758723105171627, 5.23407906469192} },
{ resistance, NULL, NULL, 0.0, 0.0, "°C", "°C", "Temperature 3", "cDAQ1Mod7/ai2", PANEL_CHK11, True, PA
NEL_THERMO3, {0.75580746506743, 5.40211000403676} },
{ resistance, NULL, NULL, 0.0, 0.0, "°C", "°C", "Temperature 4", "cDAQ1Mod7/ai3", PANEL_CHK12, True, PA
NEL_THERMO4, {0.755612372917383, 5.40323047555604} },
{ strain, NULL, NULL, 0.0, 0.0, "%", "%", "Strain theta-1", "cDAQ1Mod5/ai0", PANEL_CHK13, True, PANEL_S
TRAIN1, {1.0, 0.0} },
{ strain, NULL, NULL, 0.0, 0.0, "%", "%", "Strain theta-2", "cDAQ1Mod5/ai1", PANEL_CHK14, True, PANEL_S
TRAIN2, {1.0, 0.0} },
{ strain, NULL, NULL, 0.0, 0.0, "%", "%", "Strain theta-3", "cDAQ1Mod5/ai2", PANEL_CHK15, True, PANEL_S
TRAIN3, {1.0, 0.0} },
{ strain, NULL, NULL, 0.0, 0.0, "%", "%", "Strain theta-4", "cDAQ1Mod5/ai3", PANEL_CHK16, True, PANEL_S
TRAIN4, {1.0, 0.0} },
{ strain, NULL, NULL, 0.0, 0.0, "%", "%", "Strain theta-5", "cDAQ1Mod5/ai4", PANEL_CHK17, True, PANEL_S
TRAIN5, {1.0, 0.0} },
{ strain, NULL, NULL, 0.0, 0.0, "%", "%", "Strain theta-6", "cDAQ1Mod5/ai5", PANEL_CHK18, True, PANEL_S
TRAIN6, {1.0, 0.0} },
{ strain, NULL, NULL, 0.0, 0.0, "%", "%", "Strain theta-7", "cDAQ1Mod5/ai6", PANEL_CHK19, True, PANEL_S
TRAIN7, {1.0, 0.0} },
{ strain, NULL, NULL, 0.0, 0.0, "%", "%", "Strain theta-8", "cDAQ1Mod5/ai7", PANEL_CHK20, True, PANEL_S
TRAIN8, {1.0, 0.0} },
{ strain, NULL, NULL, 0.0, 0.0, "%", "%", "Strain z-1", "cDAQ1Mod6/ai0", PANEL_CHK21, True, PANEL_STRAI
NZ1, {1.0, 0.0} },
{ strain, NULL, NULL, 0.0, 0.0, "%", "%", "Strain z-2", "cDAQ1Mod6/ai1", PANEL_CHK22, True, PANEL_STRAI
NZ2, {1.0, 0.0} },
{ strain, NULL, NULL, 0.0, 0.0, "%", "%", "Strain z-3", "cDAQ1Mod6/ai2", PANEL_CHK23, True, PANEL_STRAI
NZ3, {1.0, 0.0} },
{ strain, NULL, NULL, 0.0, 0.0, "%", "%", "Strain z-4", "cDAQ1Mod6/ai3", PANEL_CHK24, True, PANEL_STRAI
NZ4, {1.0, 0.0} },
{ strain, NULL, NULL, 0.0, 0.0, "%", "%", "Strain z-5", "cDAQ1Mod6/ai4", PANEL_CHK25, True, PANEL_STRAI
NZ5, {1.0, 0.0} },
{ strain, NULL, NULL, 0.0, 0.0, "%", "%", "Strain z-6", "cDAQ1Mod6/ai5", PANEL_CHK26, True, PANEL_STRAI
NZ6, {1.0, 0.0} },
{ strain, NULL, NULL, 0.0, 0.0, "%", "%", "Strain z-7", "cDAQ1Mod6/ai6", PANEL_CHK27, True, PANEL_STRAI
NZ7, {1.0, 0.0} },
{ strain, NULL, NULL, 0.0, 0.0, "%", "%", "Strain z-8", "cDAQ1Mod6/ai7", PANEL_CHK28, True, PANEL_STRAI
NZ8, {1.0, 0.0} } };

int main( int argc, char *argv[] )
{
char *errmsg = 0;

if( InitCVIRTE( 0, argv, 0 ) == 0 )
return( -1 ); /* out of memory */
if( (panelHandle = LoadPanel( 0, "DataLogger.uir", PANEL )) < 0 )
return( -1 );
}

```

```

DisableBreakOnLibraryErrors();

SetWaitCursor( 1 );

Connect( Pump );
Connect( Mixer );

switch( (errcode & 0x03) ) // check lower 2 bits of error byte
{
    case 1:
        errmsg = StrDup( "Unable to connect to pump controller." );
        break;
    case 2:
        errmsg = StrDup( "Unable to connect to mixer controller." );
        break;
    case 3:
        errmsg = StrDup( "Unable to connect to pump and mixer controllers." );
        break;
}

SetWaitCursor( 0 );

DisplayPanel( panelHandle );

if( ((errcode & 0x04) >> 2) == 1 )
    MessagePopup( "Warning!", "Unable to connect to DAQ." );
if( errmsg )
    MessagePopup( "Warning!", errmsg );

// set default speeds for pump and mixer
if( (errcode & 0x01) == 0 )
{
    stopMotor( Pump );
    //Delay( 0.5 );
    sendData( Pump, 61, controller[Pump].setpoint );
}
if( ((errcode & 0x02) >> 1) == 0 )
{
    stopMotor( Mixer );
    //Delay( 0.5 );
    sendData( Mixer, 61, controller[Mixer].setpoint );
}

if( errmsg )
    free( errmsg );

numChecked = 28;

// all clear, get the show on the road

RunUserInterface();

// finished working, clean up memory and exit

DisconnectFromTCPserver( controller[Pump].tcp );
DisconnectFromTCPserver( controller[Mixer].tcp );

if( gTaskHandle )
    DAQmxClearTask( gTaskHandle );
CloseCVIRTE();

DiscardPanel( panelHandle );
MainPanelCB( 0, EVENT_CLOSE, 0, 0, 0 );
return( 0 );
}

bool initDAQ( void )
{
    int i = 0;
    int32 error = 0;
    float64 rate = 0.0;
    int size = 0;

    switch( runMode )
    {
        case 0:
            sampsPerChan = 50;
            rate = 50.0;
            size = 1;
            break;
        case 1:
            sampsPerChan = 50;
            rate = 50.0;
            size = 50;
            break;
        case 2:
            sampsPerChan = 500;
            rate = 500.0;
            size = 500;
            break;
    }
}

```

```

// initialize the DAQ
DAQmxErrChk( DAQmxCreateTask( "", &gTaskHandle ) );

// setup DAQ channels and allocate memory
for( i = 0; i < 28; i++ )
{
    if( data[i].open )
    {
        switch( data[i].read )
        {
            case current:
                DAQmxErrChk( DAQmxCreateAICurrentChan( gTaskHandle, data[i].channel, data[i].name, DAQmx_Val_Cfg_Default,
0.004, 0.020, DAQmx_Val_Amps, DAQmx_Val_Internal, 85.0, "" ) );
                break;
            case resistance:
                DAQmxErrChk( DAQmxCreateAIRTDCChan( gTaskHandle, data[i].channel, data[i].name, 5.0, 40.0, DAQmx_Val_DegC,
DAQmx_Val_Pt3851, DAQmx_Val_3Wire, DAQmx_Val_Internal, 0.001, 100.0 ) );
                break;
            case strain:
                DAQmxErrChk( DAQmxCreateAISTrainGageChan( gTaskHandle, data[i].channel, data[i].name, -0.01, 0.01, DAQmx_Val_
al_Strain, DAQmx_Val_QuarterBridgeI, DAQmx_Val_Internal, 3.3, 2.14, 0.0, 350.0, 0.30, 0.0, "" ) );
                break;
        }

        if( (data[i].raw = malloc( sampsPerChan * sizeof( float64 ) )) == NULL )
            goto Error;
        if( (data[i].val = malloc( size * sizeof( float64 ) )) == NULL )
            goto Error;
    }
}

DAQmxErrChk( DAQmxCfgSampClkTiming( gTaskHandle, "", rate, DAQmx_Val_Rising, DAQmx_Val_ContSamps, sampsPerChan ) );
DAQmxErrChk( DAQmxGetTaskAttribute( gTaskHandle, DAQmx_Task_NumChans, &gNumChannels ) );
DAQmxErrChk( DAQmxRegisterEveryNSamplesEvent( gTaskHandle, DAQmx_Val_Acquired_Into_Buffer, sampsPerChan, 0, EveryNCallback
, NULL ) );
DAQmxErrChk( DAQmxRegisterDoneEvent( gTaskHandle, 0, DoneCallback, NULL ) );

DAQmxErrChk( DAQmxPerformBridgeOffsetNullingCalEx( gTaskHandle, "", 1 ) );

DAQmxErrChk( DAQmxStartTask( gTaskHandle ) );

// allocate memory for DAQ intermediate storage buffer
if( (gData = malloc( gNumChannels * sampsPerChan * sizeof( float64 ) )) == NULL )
    goto Error;

return( True );

Error:
MessagePopup( "Error", "Not enough memory" );
SetWaitCursor( 0 );
if( DAQmxFailed( error ) )
{
    if( gData )
    {
        free( gData );
        gData = NULL;
    }
    for( i = 0; i < 28; i++ )
    {
        if( data[i].raw )
        {
            free( data[i].raw );
            data[i].raw = NULL;
        }
        if( data[i].val )
        {
            free( data[i].val );
            data[i].val = NULL;
        }
    }
    errcode |= 0x04;
}
return( False );
}

int CVICALLBACK PanelCallback( int panel, int event, void *callbackData, int eventData1, int eventData2 )
{
    int i;
    if( event == EVENT_CLOSE )
    {
        DAQmxStopTask( gTaskHandle );
        DAQmxClearTask( gTaskHandle );
        gTaskHandle = 0;

        if( gData )
        {
            free( gData );
            gData = NULL;
        }
        for( i = 0; i < 28; i++ )
        {

```

```

        if( data[i].raw )
        {
            free( data[i].raw );
            data[i].raw = NULL;
        }
        if( data[i].val )
        {
            free( data[i].val );
            data[i].val = NULL;
        }
    }

    QuitUserInterface( 0 );
}
return( 0 );
}

int CVICALLBACK RangeCallback( int panel, int control, int event, void *callbackData, int eventData1, int eventData2 )
{
    if( event == EVENT_COMMIT )
    {
        // nothing
    }
    return( 0 );
}

int CVICALLBACK StartCallback( int panel, int control, int event, void *callbackData, int eventData1, int eventData2 )
{
    if( event == EVENT_COMMIT )
    {
        logdata = 1;

        SetCtrlAttribute( panel, PANEL_START, ATTR_DIMMED, 1 );
        SetCtrlAttribute( panel, PANEL_STOP, ATTR_DIMMED, 0 );
        SetCtrlAttribute( panel, PANEL_LOGFILE, ATTR_DIMMED, 1 );

        GetCurrentCVIAbsoluteTime( &timestamp );
        CVIAbsoluteTimeToCVIUILTime( timestamp, &starttime );
    }
    return( 0 );
}

int CVICALLBACK StopCallback( int panel, int control, int event, void *callbackData, int eventData1, int eventData2 )
{
    if( event == EVENT_COMMIT )
    {
        logdata = 0;
        SetCtrlAttribute( panel, PANEL_START, ATTR_DIMMED, 0 );
        SetCtrlAttribute( panel, PANEL_CHK1, ATTR_DIMMED, 0 );
        SetCtrlAttribute( panel, PANEL_CHK2, ATTR_DIMMED, 0 );
        SetCtrlAttribute( panel, PANEL_CHK3, ATTR_DIMMED, 0 );
        SetCtrlAttribute( panel, PANEL_CHK4, ATTR_DIMMED, 0 );
        SetCtrlAttribute( panel, PANEL_CHK5, ATTR_DIMMED, 0 );
        SetCtrlAttribute( panel, PANEL_CHK6, ATTR_DIMMED, 0 );
        SetCtrlAttribute( panel, PANEL_CHK7, ATTR_DIMMED, 0 );
        SetCtrlAttribute( panel, PANEL_CHK8, ATTR_DIMMED, 0 );
        SetCtrlAttribute( panel, PANEL_CHK9, ATTR_DIMMED, 0 );
        SetCtrlAttribute( panel, PANEL_CHK10, ATTR_DIMMED, 0 );
        SetCtrlAttribute( panel, PANEL_CHK11, ATTR_DIMMED, 0 );
        SetCtrlAttribute( panel, PANEL_CHK12, ATTR_DIMMED, 0 );
        SetCtrlAttribute( panel, PANEL_CHK13, ATTR_DIMMED, 0 );
        SetCtrlAttribute( panel, PANEL_CHK14, ATTR_DIMMED, 0 );
        SetCtrlAttribute( panel, PANEL_CHK15, ATTR_DIMMED, 0 );
        SetCtrlAttribute( panel, PANEL_CHK16, ATTR_DIMMED, 0 );
        SetCtrlAttribute( panel, PANEL_CHK17, ATTR_DIMMED, 0 );
        SetCtrlAttribute( panel, PANEL_CHK18, ATTR_DIMMED, 0 );
        SetCtrlAttribute( panel, PANEL_CHK19, ATTR_DIMMED, 0 );
        SetCtrlAttribute( panel, PANEL_CHK20, ATTR_DIMMED, 0 );
        SetCtrlAttribute( panel, PANEL_CHK21, ATTR_DIMMED, 0 );
        SetCtrlAttribute( panel, PANEL_CHK22, ATTR_DIMMED, 0 );
        SetCtrlAttribute( panel, PANEL_CHK23, ATTR_DIMMED, 0 );
        SetCtrlAttribute( panel, PANEL_CHK24, ATTR_DIMMED, 0 );
        SetCtrlAttribute( panel, PANEL_CHK25, ATTR_DIMMED, 0 );
        SetCtrlAttribute( panel, PANEL_CHK26, ATTR_DIMMED, 0 );
        SetCtrlAttribute( panel, PANEL_CHK27, ATTR_DIMMED, 0 );
        SetCtrlAttribute( panel, PANEL_CHK28, ATTR_DIMMED, 0 );

        SetCtrlAttribute( panel, PANEL_START, ATTR_DIMMED, 1 );
        SetCtrlAttribute( panel, PANEL_STOP, ATTR_DIMMED, 1 );
        SetCtrlAttribute( panel, PANEL_LOGFILE, ATTR_DIMMED, 0 );
    }
    return( 0 );
}

int32 CVICALLBACK EveryNCallback( TaskHandle taskHandle, int32 everyNsamplesEventType, uInt32 nSamples, void *callbackData )
{
    int32 error = 0;
    char errBuff[2048] = { 0 };
    int numRead, index = 0, i;

    DAQmxErrChk( DAQmxReadAnalogF64( taskHandle, nSamples, 10.0, DAQmx_Val_GroupByChannel, gData, (nSamples * gNumChannels), &
numRead, NULL ) );
}

```

```

for( i = 0; i < 28; i++ )
{
    if( data[i].open )
    {
        Subset1D( gData, (sampsPerChan * gNumChannels), (sampsPerChan * index), sampsPerChan, data[i].raw );
        Sum1D( data[i].raw, sampsPerChan, &(data[i].raw_avg) );
        data[i].raw_avg /= sampsPerChan;

        // use calibration data to obtain real values
        data[i].val_avg = (data[i].raw_avg * data[i].cal[0]) + data[i].cal[1];

        if( runMode > 0 )
            LinEvlD( data[i].raw, sampsPerChan, data[i].cal[0], data[i].cal[1], data[i].val );

        // send data to gauges
        SetCtrlVal( panelHandle, data[i].gauge, data[i].val_avg );
        index++;
    }
}

```

```

GetCurrentCVIAbsoluteTime( &timestamp );
CVIAbsoluteTimeToCVIUILTime( timestamp, &timedouble );

```

```

if( numRead > 0 )
{
    if( logdata == 1 )
    {
        LogFile();
        SetCtrlVal( panelHandle, PANEL_RUNTIME, timedouble - starttime );
    }
    else
        SetCtrlVal( panelHandle, PANEL_RUNTIME, 0.0 );
}

```

```

Error:
if( DAQmxFailed( error ) )
{
    DAQmxGetExtendedErrorInfo( errBuff, 2048 );
    DAQmxStopTask( taskHandle );
    DAQmxClearTask( taskHandle );
    gTaskHandle = 0;
    if( gData )
    {
        free( gData );
        gData = NULL;
    }
    for( i = 0; i < 28; i++ )
    {
        if( data[i].raw )
        {
            free( data[i].raw );
            data[i].raw = NULL;
        }
        if( data[i].val )
        {
            free( data[i].val );
            data[i].val = NULL;
        }
    }
    MessagePopup( "DAQmx Error", errBuff );
    SetCtrlAttribute( panelHandle, PANEL_START, ATTR_DIMMED, 0 );
}
return( 0 );
}

```

```

int32 CVICALLBACK DoneCallback( TaskHandle taskHandle, int32 status, void *callbackData )
{
    int32 error = 0;
    char errBuff[2048] = { 0 };

    taskHandle = 0;
    // Check to see if an error stopped the task.
    DAQmxErrChk( status );
}

```

```

Error:
DAQmxGetExtendedErrorInfo( errBuff, 2048 );
DAQmxClearTask( taskHandle );
if( DAQmxFailed( error ) )
    MessagePopup( "DAQmx Error", errBuff );
SetCtrlAttribute( panelHandle, PANEL_START, ATTR_DIMMED, 0 );
return( 0 );
}

```

```

/*-----*/
/* Respond to the UI and clear the receive screen for the user. */
/*-----*/
int CVICALLBACK ClearScreenCB( int panel, int control, int event, void *callbackData, int eventData1, int eventData2 )
{
    if( event == EVENT_COMMIT )
    {
        return( 0 );
    }
}

```



```

}
/*-----*/
/* Respond to the panel closure to quit the UI loop. */
/*-----*/
int CVICALLBACK MainPanelCB( int panel, int event, void *callbackData, int eventData1, int eventData2 )
{
    if( event == EVENT_CLOSE )
        QuitUserInterface( 0 );
    return( 0 );
}

void LogFileHeader( void )
{
    FILE *fp;
    char *date, *time;
    int choice, i;

    choice = FileSelectPopup( "", "*.log", "", "Enter the name of the log file", VAL_SAVE_BUTTON, 0, 0, 1, 0, logFile );
    while( choice == VAL_EXISTING_FILE_SELECTED )
    {
        MessagePopup( "Error!", "Please select a new file name!" );
        choice = FileSelectPopup( "", "*.log", "", "Enter the name of the log file", VAL_SAVE_BUTTON, 0, 0, 1, 0, logFile );
    }

    if( choice == VAL_NO_FILE_SELECTED )
        return;

    SetCtrlAttribute( panelHandle, PANEL_START, ATTR_DIMMED, 0 );
    SetCtrlAttribute( panelHandle, PANEL_STOP, ATTR_DIMMED, 1 );
    SetCtrlAttribute( panelHandle, PANEL_CHK1, ATTR_DIMMED, 1 );
    SetCtrlAttribute( panelHandle, PANEL_CHK2, ATTR_DIMMED, 1 );
    SetCtrlAttribute( panelHandle, PANEL_CHK3, ATTR_DIMMED, 1 );
    SetCtrlAttribute( panelHandle, PANEL_CHK4, ATTR_DIMMED, 1 );
    SetCtrlAttribute( panelHandle, PANEL_CHK5, ATTR_DIMMED, 1 );
    SetCtrlAttribute( panelHandle, PANEL_CHK6, ATTR_DIMMED, 1 );
    SetCtrlAttribute( panelHandle, PANEL_CHK7, ATTR_DIMMED, 1 );
    SetCtrlAttribute( panelHandle, PANEL_CHK8, ATTR_DIMMED, 1 );
    SetCtrlAttribute( panelHandle, PANEL_CHK9, ATTR_DIMMED, 1 );
    SetCtrlAttribute( panelHandle, PANEL_CHK10, ATTR_DIMMED, 1 );
    SetCtrlAttribute( panelHandle, PANEL_CHK11, ATTR_DIMMED, 1 );
    SetCtrlAttribute( panelHandle, PANEL_CHK12, ATTR_DIMMED, 1 );
    SetCtrlAttribute( panelHandle, PANEL_CHK13, ATTR_DIMMED, 1 );
    SetCtrlAttribute( panelHandle, PANEL_CHK14, ATTR_DIMMED, 1 );
    SetCtrlAttribute( panelHandle, PANEL_CHK15, ATTR_DIMMED, 1 );
    SetCtrlAttribute( panelHandle, PANEL_CHK16, ATTR_DIMMED, 1 );
    SetCtrlAttribute( panelHandle, PANEL_CHK17, ATTR_DIMMED, 1 );
    SetCtrlAttribute( panelHandle, PANEL_CHK18, ATTR_DIMMED, 1 );
    SetCtrlAttribute( panelHandle, PANEL_CHK19, ATTR_DIMMED, 1 );
    SetCtrlAttribute( panelHandle, PANEL_CHK20, ATTR_DIMMED, 1 );
    SetCtrlAttribute( panelHandle, PANEL_CHK21, ATTR_DIMMED, 1 );
    SetCtrlAttribute( panelHandle, PANEL_CHK22, ATTR_DIMMED, 1 );
    SetCtrlAttribute( panelHandle, PANEL_CHK23, ATTR_DIMMED, 1 );
    SetCtrlAttribute( panelHandle, PANEL_CHK24, ATTR_DIMMED, 1 );
    SetCtrlAttribute( panelHandle, PANEL_CHK25, ATTR_DIMMED, 1 );
    SetCtrlAttribute( panelHandle, PANEL_CHK26, ATTR_DIMMED, 1 );
    SetCtrlAttribute( panelHandle, PANEL_CHK27, ATTR_DIMMED, 1 );
    SetCtrlAttribute( panelHandle, PANEL_CHK28, ATTR_DIMMED, 1 );

    fp = fopen( logFile, "w" );

    date = DateStr();
    time = TimeStr();
    fprintf( fp, "Slurry Loop Log File\nDate\t%s\tTime\t%s\n", date, time );

    fprintf( fp, "Time (s)\t" );
    fprintf( fp, "Pump speed [Hz]\t" );
    fprintf( fp, "Mixer speed [Hz]\t" );

    for( i = 0; i < 28; i++ )
        if( data[i].open )
            fprintf( fp, "%-14s [%s]\t%-14s [%s]\t", data[i].name, data[i].val_unit, data[i].name, data[i].raw_unit );

    fprintf( fp, "\n" );
    fclose( fp );
}

void LogFile( void )
{
    FILE *fp;
    int i, j, max = 0;

    if( FileExists( logFile, 0 ) )
        fp = fopen( logFile, "a" );
    else
    {
        LogFileHeader();
        fp = fopen( logFile, "a" );
    }

    switch( runMode )
    {
        case 0:

```

```
fprintf( fp, "%08.2f\t", (timedouble - starttime) );
fprintf( fp, "%02.1f\t\t", (float)(controller[Pump].running * controller[Pump].setpoint) / 10.0 );
fprintf( fp, "%02.1f\t\t\t", (float)(controller[Mixer].running * controller[Mixer].setpoint) / 10.0 );
```

```
for( j = 0; j < 28; j++ )
    if( data[j].open )
        fprintf( fp, "%f\t\t%f\t\t", data[j].val_avg, data[j].raw_avg );
fprintf( fp, "\n" );
break;
```

```
case 1:
```

```
case 2:
```

```
max = (runMode == 1) ? 50 : 500;
```

```
for( i = 0; i < max; i++ )
```

```
{
    fprintf( fp, "%08.2f\t", ((timedouble - starttime) + (float)(i * (1 / max))) );
    fprintf( fp, "%02.1f\t\t", (float)(controller[Pump].running * controller[Pump].setpoint) / 10.0 );
    fprintf( fp, "%02.1f\t\t\t", (float)(controller[Mixer].running * controller[Mixer].setpoint) / 10.0 );
```

```
for( j = 0; j < 28; j++ )
```

```
    if( data[j].open )
```

```
        fprintf( fp, "%f\t\t%f\t\t", data[j].val[i], data[j].raw[i] );
```

```
    fprintf( fp, "\n" );
```

```
}
```

```
break;
```

```
}
```

```
fclose( fp );
```

```
return;
```

```
}
```

```
int CVICALLBACK LOGFILE( int panel, int control, int event, void *callbackData, int eventDatal, int eventData2 )
```

```
{
```

```
    switch( event )
```

```
    {
```

```
        case EVENT_COMMIT:
```

```
            LogFileHeader();
```

```
            break;
```

```
        case EVENT_RIGHT_CLICK:
```

```
            break;
```

```
    }
```

```
    return( 0 );
```

```
}
```

```
int CVICALLBACK StartDAQ( int panel, int control, int event, void *callbackData, int eventDatal, int eventData2 )
```

```
{
```

```
    switch( event )
```

```
    {
```

```
        case EVENT_COMMIT:
```

```
            if( initDAQ() )
```

```
            {
```

```
                SetCtrlAttribute( panelHandle, PANEL_LOGFILE, ATTR_DIMMED, 0 );
```

```
                SetCtrlAttribute( panelHandle, PANEL_START, ATTR_DIMMED, 0 );
```

```
                SetCtrlAttribute( panelHandle, PANEL_STOP, ATTR_DIMMED, 1 );
```

```
                SetCtrlAttribute( panelHandle, PANEL_RUNTIME, ATTR_DIMMED, 0 );
```

```
                SetCtrlAttribute( panelHandle, PANEL_CHK1, ATTR_DIMMED, 1 );
```

```
                SetCtrlAttribute( panelHandle, PANEL_CHK2, ATTR_DIMMED, 1 );
```

```
                SetCtrlAttribute( panelHandle, PANEL_CHK3, ATTR_DIMMED, 1 );
```

```
                SetCtrlAttribute( panelHandle, PANEL_CHK4, ATTR_DIMMED, 1 );
```

```
                SetCtrlAttribute( panelHandle, PANEL_CHK5, ATTR_DIMMED, 1 );
```

```
                SetCtrlAttribute( panelHandle, PANEL_CHK6, ATTR_DIMMED, 1 );
```

```
                SetCtrlAttribute( panelHandle, PANEL_CHK7, ATTR_DIMMED, 1 );
```

```
                SetCtrlAttribute( panelHandle, PANEL_CHK8, ATTR_DIMMED, 1 );
```

```
                SetCtrlAttribute( panelHandle, PANEL_CHK9, ATTR_DIMMED, 1 );
```

```
                SetCtrlAttribute( panelHandle, PANEL_CHK10, ATTR_DIMMED, 1 );
```

```
                SetCtrlAttribute( panelHandle, PANEL_CHK11, ATTR_DIMMED, 1 );
```

```
                SetCtrlAttribute( panelHandle, PANEL_CHK12, ATTR_DIMMED, 1 );
```

```
                SetCtrlAttribute( panelHandle, PANEL_CHK13, ATTR_DIMMED, 1 );
```

```
                SetCtrlAttribute( panelHandle, PANEL_CHK14, ATTR_DIMMED, 1 );
```

```
                SetCtrlAttribute( panelHandle, PANEL_CHK15, ATTR_DIMMED, 1 );
```

```
                SetCtrlAttribute( panelHandle, PANEL_CHK16, ATTR_DIMMED, 1 );
```

```
                SetCtrlAttribute( panelHandle, PANEL_CHK17, ATTR_DIMMED, 1 );
```

```
                SetCtrlAttribute( panelHandle, PANEL_CHK18, ATTR_DIMMED, 1 );
```

```
                SetCtrlAttribute( panelHandle, PANEL_CHK19, ATTR_DIMMED, 1 );
```

```
                SetCtrlAttribute( panelHandle, PANEL_CHK20, ATTR_DIMMED, 1 );
```

```
                SetCtrlAttribute( panelHandle, PANEL_CHK21, ATTR_DIMMED, 1 );
```

```
                SetCtrlAttribute( panelHandle, PANEL_CHK22, ATTR_DIMMED, 1 );
```

```
                SetCtrlAttribute( panelHandle, PANEL_CHK23, ATTR_DIMMED, 1 );
```

```
                SetCtrlAttribute( panelHandle, PANEL_CHK24, ATTR_DIMMED, 1 );
```

```
                SetCtrlAttribute( panelHandle, PANEL_CHK25, ATTR_DIMMED, 1 );
```

```
                SetCtrlAttribute( panelHandle, PANEL_CHK26, ATTR_DIMMED, 1 );
```

```
                SetCtrlAttribute( panelHandle, PANEL_CHK27, ATTR_DIMMED, 1 );
```

```
                SetCtrlAttribute( panelHandle, PANEL_CHK28, ATTR_DIMMED, 1 );
```

```
                SetCtrlAttribute( panelHandle, PANEL_INITDAQ, ATTR_DIMMED, 1 );
```

```
                SetCtrlAttribute( panelHandle, PANEL_REINITDAQ, ATTR_DIMMED, 1 );
```

```
                SetCtrlAttribute( panelHandle, PANEL_MODE, ATTR_DIMMED, 1 );
```

```
            }
```

```
            break;
```

```
    }
```

```

}
return( 0 );
}

int CVICALLBACK ReInitDAQ( int panel, int control, int event, void *callbackData, int eventData1, int eventData2 )
{
switch( event )
{
case EVENT_COMMIT:
if( initDAQ() )
{
SetCtrlAttribute( panelHandle, PANEL_LOGFILE, ATTR_DIMMED, 0 );
SetCtrlAttribute( panelHandle, PANEL_START, ATTR_DIMMED, 0 );
SetCtrlAttribute( panelHandle, PANEL_STOP, ATTR_DIMMED, 1 );
SetCtrlAttribute( panelHandle, PANEL_REINITDAQ, ATTR_DIMMED, 1 );
SetCtrlAttribute( panelHandle, PANEL_RUNTIME, ATTR_DIMMED, 0 );
SetCtrlAttribute( panelHandle, PANEL_CHK1, ATTR_DIMMED, 1 );
SetCtrlAttribute( panelHandle, PANEL_CHK2, ATTR_DIMMED, 1 );
SetCtrlAttribute( panelHandle, PANEL_CHK3, ATTR_DIMMED, 1 );
SetCtrlAttribute( panelHandle, PANEL_CHK4, ATTR_DIMMED, 1 );
SetCtrlAttribute( panelHandle, PANEL_CHK5, ATTR_DIMMED, 1 );
SetCtrlAttribute( panelHandle, PANEL_CHK6, ATTR_DIMMED, 1 );
SetCtrlAttribute( panelHandle, PANEL_CHK7, ATTR_DIMMED, 1 );
SetCtrlAttribute( panelHandle, PANEL_CHK8, ATTR_DIMMED, 1 );
SetCtrlAttribute( panelHandle, PANEL_CHK9, ATTR_DIMMED, 1 );
SetCtrlAttribute( panelHandle, PANEL_CHK10, ATTR_DIMMED, 1 );
SetCtrlAttribute( panelHandle, PANEL_CHK11, ATTR_DIMMED, 1 );
SetCtrlAttribute( panelHandle, PANEL_CHK12, ATTR_DIMMED, 1 );
SetCtrlAttribute( panelHandle, PANEL_CHK13, ATTR_DIMMED, 1 );
SetCtrlAttribute( panelHandle, PANEL_CHK14, ATTR_DIMMED, 1 );
SetCtrlAttribute( panelHandle, PANEL_CHK15, ATTR_DIMMED, 1 );
SetCtrlAttribute( panelHandle, PANEL_CHK16, ATTR_DIMMED, 1 );
SetCtrlAttribute( panelHandle, PANEL_CHK17, ATTR_DIMMED, 1 );
SetCtrlAttribute( panelHandle, PANEL_CHK18, ATTR_DIMMED, 1 );
SetCtrlAttribute( panelHandle, PANEL_CHK19, ATTR_DIMMED, 1 );
SetCtrlAttribute( panelHandle, PANEL_CHK20, ATTR_DIMMED, 1 );
SetCtrlAttribute( panelHandle, PANEL_CHK21, ATTR_DIMMED, 1 );
SetCtrlAttribute( panelHandle, PANEL_CHK22, ATTR_DIMMED, 1 );
SetCtrlAttribute( panelHandle, PANEL_CHK23, ATTR_DIMMED, 1 );
SetCtrlAttribute( panelHandle, PANEL_CHK24, ATTR_DIMMED, 1 );
SetCtrlAttribute( panelHandle, PANEL_CHK25, ATTR_DIMMED, 1 );
SetCtrlAttribute( panelHandle, PANEL_CHK26, ATTR_DIMMED, 1 );
SetCtrlAttribute( panelHandle, PANEL_CHK27, ATTR_DIMMED, 1 );
SetCtrlAttribute( panelHandle, PANEL_CHK28, ATTR_DIMMED, 1 );
SetCtrlAttribute( panelHandle, PANEL_INITDAQ, ATTR_DIMMED, 1 );
SetCtrlAttribute( panelHandle, PANEL_MODE, ATTR_DIMMED, 1 );
}
break;
}
return( 0 );
}

int CVICALLBACK LoadRunFile( int panel, int control, int event, void *callbackData, int eventData1, int eventData2 )
{
int choice = 0;

switch( event )
{
case EVENT_COMMIT:
choice = FileSelectPopup( "", "*.run", "", "Enter the name of the run file", VAL_LOAD_BUTTON, 0, 0, 1, 0, runFile );

if( choice == VAL_NO_FILE_SELECTED )
return( 1 );

GetCurrentCUIAbsoluteTime( &timestamp );
CUIAbsoluteTimeToCUIUITime( timestamp, &autoStartTime );

autoFile = fopen( runFile, "r" );
fscanf( autoFile, "%lf %lf %lf", &timeVal, &pSpeed, &mSpeed );

SetCtrlAttribute( panelHandle, PANEL_LOADRUNFILE, ATTR_DIMMED, 1 );
SetCtrlAttribute( panelHandle, PANEL_PAUSERESUME, ATTR_DIMMED, 0 );
SetCtrlAttribute( panelHandle, PANEL_STOPAUTORUN, ATTR_DIMMED, 0 );
SetCtrlAttribute( panelHandle, PANEL_PUMPSPEED, ATTR_CTRL_MODE, VAL_INDICATOR );
SetCtrlAttribute( panelHandle, PANEL_MIXERSPEED, ATTR_CTRL_MODE, VAL_INDICATOR );
SetCtrlAttribute( panelHandle, controller[Pump].Control, ATTR_DIMMED, 1 );
SetCtrlAttribute( panelHandle, controller[Pump].Speed, ATTR_DIMMED, 1 );
SetCtrlAttribute( panelHandle, controller[Mixer].Control, ATTR_DIMMED, 1 );
SetCtrlAttribute( panelHandle, controller[Mixer].Speed, ATTR_DIMMED, 1 );
SetCtrlVal( panelHandle, PANEL_AUTORUN, 1 );

setSpeed( Pump, (unsigned int)(pSpeed * 10) );
setSpeed( Mixer, (unsigned int)(mSpeed * 10) );
Delay( 0.5 );
startMotor( Pump );
startMotor( Mixer );

runbyFile = True;
SetCtrlAttribute( panelHandle, PANEL_TIMER, ATTR_INTERVAL, 10.0 );
ResetTimer( panelHandle, PANEL_TIMER );
break;
}
return( 0 );
}

```

```

int CVICALLBACK PauseResume( int panel, int control, int event, void *callbackData, int eventData1, int eventData2 )
{
    switch( event )
    {
        case EVENT_COMMIT:
            if( runbyFile )
            {
                runbyFile = False;
                SetCtrlAttribute( panelHandle, PANEL_PAUSERESUME, ATTR_LABEL_TEXT, "Resume Autorun" );
                SetCtrlAttribute( panelHandle, PANEL_PUMPSPEED, ATTR_CTRL_MODE, VAL_NORMAL );
                SetCtrlAttribute( panelHandle, PANEL_MIXERSPEED, ATTR_CTRL_MODE, VAL_NORMAL );
                SetCtrlAttribute( panelHandle, controller[Pump].Control, ATTR_DIMMED, 0 );
                SetCtrlAttribute( panelHandle, controller[Pump].Speed, ATTR_DIMMED, 0 );
                SetCtrlAttribute( panelHandle, controller[Mixer].Control, ATTR_DIMMED, 0 );
                SetCtrlAttribute( panelHandle, controller[Mixer].Speed, ATTR_DIMMED, 0 );
                SetCtrlVal( panelHandle, PANEL_AUTORUN, 0 );
            }
            else
            {
                runbyFile = True;
                SetCtrlAttribute( panelHandle, PANEL_PAUSERESUME, ATTR_LABEL_TEXT, "Pause Autorun" );
                SetCtrlAttribute( panelHandle, PANEL_PUMPSPEED, ATTR_CTRL_MODE, VAL_INDICATOR );
                SetCtrlAttribute( panelHandle, PANEL_MIXERSPEED, ATTR_CTRL_MODE, VAL_INDICATOR );
                SetCtrlAttribute( panelHandle, controller[Pump].Control, ATTR_DIMMED, 1 );
                SetCtrlAttribute( panelHandle, controller[Pump].Speed, ATTR_DIMMED, 1 );
                SetCtrlAttribute( panelHandle, controller[Mixer].Control, ATTR_DIMMED, 1 );
                SetCtrlAttribute( panelHandle, controller[Mixer].Speed, ATTR_DIMMED, 1 );
                SetCtrlVal( panelHandle, PANEL_AUTORUN, 1 );
            }
            break;
    }
    return( 0 );
}

```

```

int CVICALLBACK StopAutoRun( int panel, int control, int event, void *callbackData, int eventData1, int eventData2 )
{
    switch( event )
    {
        case EVENT_COMMIT:
            runbyFile = False;
            fclose( autoFile );
            SetCtrlAttribute( panelHandle, PANEL_LOADRUNFILE, ATTR_DIMMED, 0 );
            SetCtrlAttribute( panelHandle, PANEL_PAUSERESUME, ATTR_DIMMED, 1 );
            SetCtrlAttribute( panelHandle, PANEL_STOPAUTORUN, ATTR_DIMMED, 1 );
            SetCtrlAttribute( panelHandle, PANEL_PUMPSPEED, ATTR_CTRL_MODE, VAL_NORMAL );
            SetCtrlAttribute( panelHandle, PANEL_MIXERSPEED, ATTR_CTRL_MODE, VAL_NORMAL );
            SetCtrlAttribute( panelHandle, controller[Pump].Control, ATTR_DIMMED, 0 );
            SetCtrlAttribute( panelHandle, controller[Pump].Speed, ATTR_DIMMED, 0 );
            SetCtrlAttribute( panelHandle, controller[Mixer].Control, ATTR_DIMMED, 0 );
            SetCtrlAttribute( panelHandle, controller[Mixer].Speed, ATTR_DIMMED, 0 );
            SetCtrlVal( panelHandle, PANEL_AUTORUN, 0 );
            break;
    }
    return( 0 );
}

```

```

int CVICALLBACK TimerAutoRun( int panel, int control, int event, void *callbackData, int eventData1, int eventData2 )
{
    SetCtrlAttribute( panelHandle, PANEL_TIMER, ATTR_ENABLED, 0 );
    switch( event )
    {
        case EVENT_TIMER_TICK:
            if( runbyFile )
            {
                GetCurrentCVIAbsoluteTime( &timestamp );
                CVIAbsoluteTimeToCVIUILTime( timestamp, &autoCurrTime );

                if( (autoCurrTime - autoStartTime) >= (timeVal * 60.0) )
                {
                    GetCurrentCVIAbsoluteTime( &timestamp );
                    CVIAbsoluteTimeToCVIUILTime( timestamp, &autoStartTime );
                    fscanf( autoFile, "%lf %lf %lf", &timeVal, &pSpeed, &mSpeed );
                    if( feof( autoFile ) != 0 )
                    {
                        runbyFile = False;
                        SetCtrlAttribute( panelHandle, PANEL_PUMPSPEED, ATTR_CTRL_MODE, VAL_NORMAL );
                        SetCtrlAttribute( panelHandle, PANEL_MIXERSPEED, ATTR_CTRL_MODE, VAL_NORMAL );
                        SetCtrlAttribute( panelHandle, controller[Pump].Control, ATTR_DIMMED, 0 );
                        SetCtrlAttribute( panelHandle, controller[Pump].Speed, ATTR_DIMMED, 0 );
                        SetCtrlAttribute( panelHandle, controller[Mixer].Control, ATTR_DIMMED, 0 );
                        SetCtrlAttribute( panelHandle, controller[Mixer].Speed, ATTR_DIMMED, 0 );
                        SetCtrlAttribute( panelHandle, PANEL_LOADRUNFILE, ATTR_DIMMED, 0 );
                        SetCtrlAttribute( panelHandle, PANEL_PAUSERESUME, ATTR_DIMMED, 1 );
                        SetCtrlAttribute( panelHandle, PANEL_STOPAUTORUN, ATTR_DIMMED, 1 );
                        SetCtrlVal( panelHandle, PANEL_AUTORUN, 0 );
                        stopMotor( Pump );
                        stopMotor( Mixer );
                        return( 1 );
                    }
                    setSpeed( Pump, (unsigned int)(pSpeed * 10.0) );
                    setSpeed( Mixer, (unsigned int)(mSpeed * 10.0) );
                }
            }
    }
}

```

```

        Delay( 0.5 );
    }
    }
    break;
}
SetCtrlAttribute( panelHandle, PANEL_TIMER, ATTR_ENABLED, 1 );
return( 0 );
}

int CVICALLBACK PumpTCP( unsigned ptcp, int event, int error, void *callbackData )
{
    char receiveBuf[2048] = { 0 };
    int dataSize = sizeof( receiveBuf ) - 1;

    switch( event )
    {
        case TCP_DATAREADY:
            if( readFlag == False )
            {
                if( (dataSize = ClientTCPRead( ptcp, receiveBuf, dataSize, 0 )) < 0 )
                    MessagePopup( "Error", "Receive Error" );
                else
                    receiveBuf[dataSize] = '\0';
            }
            break;
        case TCP_DISCONNECT:
            Connect( Pump );
            break;
    }
    return( 0 );
}

int CVICALLBACK MixerTCP( unsigned mtcp, int event, int error, void *callbackData )
{
    char receiveBuf[2048] = { 0 };
    int dataSize = sizeof( receiveBuf ) - 1;

    switch( event )
    {
        case TCP_DATAREADY:
            if( (dataSize = ClientTCPRead( mtcp, receiveBuf, dataSize, 0 )) < 0 )
            {
                MessagePopup( "Error", "Receive Error" );
            }
            else
            {
                receiveBuf[dataSize] = '\0';
            }
            break;
        case TCP_DISCONNECT:
            Connect( Mixer );
            break;
    }
    return( 0 );
}

bool Connect( motorType m )
{
    if( ConnectToTCPSTerver( &(controller[m].tcp), 80, controller[m].addr, *(controller[m].TCP), NULL, 5000 ) < 0 )
    {
        errcode |= (m + 1);
        SetCtrlAttribute( panelHandle, controller[m].Control, ATTR_DIMMED, 1 );
        SetCtrlAttribute( panelHandle, controller[m].Speed, ATTR_DIMMED, 1 );
        SetCtrlAttribute( panelHandle, controller[m].Recon, ATTR_DIMMED, 0 );
        controller[m].connected = False;
    }
    else
    {
        errcode &= (255 - (m + 1));
        if( runbyFile == False )
        {
            SetCtrlAttribute( panelHandle, controller[m].Control, ATTR_DIMMED, 0 );
            SetCtrlAttribute( panelHandle, controller[m].Speed, ATTR_DIMMED, 0 );
            SetCtrlAttribute( panelHandle, controller[m].Recon, ATTR_DIMMED, 1 );
        }
        controller[m].connected = True;
    }
    return( controller[m].connected );
}

bool sendData( motorType m, unsigned int parameter, unsigned int value )
{
    char tempBuf[512] = { 0 };
    char transmitBuf[2048] = { 0 };
    bool success = False;

    SetWaitCursor( 1 );

    // add controls here
    // D900 = param number (i.e. 61, 65), D901 = param value
    // P61: speed [Hz x 10] (i.e. 300 = 30 Hz)
    // P65: 97 = start, 0 = stop

```

```

sprintf( tempBuf, "D900=%d&D901=%d&FGSP=Write", parameter, value );
sprintf( transmitBuf, "POST /GSP.htm HTTP/1.1\r\nAccept: image/gif, image/jpeg, image/pjpeg, image/pjpeg, application/x-shockwave-flash, application/xaml+xml, application/vnd.ms-xpsdocument, application/x-ms-xbap, application/x-ms-application, application/vnd.ms-excel, application/vnd.ms-powerpoint, application/msword, */*\r\nReferer: http://%s/GSP.htm\r\nAccept-Language: en-us\r\nUser-Agent: Mozilla/4.0 (compatible; MSIE 8.0; Windows NT 5.1; Trident/4.0; .NET CLR 2.0.50727; .NET CLR 3.0.04506.30; .NET CLR 1.1.4322; InfoPath.1; .NET CLR 3.0.04506.648; OfficeLiveConnector.1.3; OfficeLivePatch.0.0; .NET CLR 3.0.4506.2152; .NET CLR 3.5.30729)\r\nContent-Type: application/x-www-form-urlencoded\r\nAccept-Encoding: gzip, deflate\r\nHost: %s\r\nContent-Length: %d\r\nConnection: Keep-Alive\r\nCache-Control: no-cache\r\n\r\n%s", controller[m].addr, controller[m].addr, strlen( tempBuf ), tempBuf );

// dispatch the message to our controller
if( ClientTCPWrite( controller[m].tcp, transmitBuf, strlen( transmitBuf ), 0 ) < 0 )
    success = False;
else
    success = True;

SetWaitCursor( 0 );
strcpy( tempBuf, "\0" );
strcpy( transmitBuf, "\0" );

// say good-night Gracie

return( success );
}

bool readData( motorType m, unsigned int parameter, unsigned int *value )
{
    char tempBuf[512] = { 0 };
    char transmitBuf[2048] = { 0 };
    char receiveBuf[4096] = { 0 };
    bool success = False;
    int dataSize = sizeof( receiveBuf ) - 1, dataRead = 0, val = 0;
    char *location = NULL;

    SetWaitCursor( 1 );

    // add controls here
    // D900 = param number (i.e. 61, 65), D901 = param value

    // P506: voltage (read)
    // P507: load (read)
    // P508: current (read)
    // P509: torque (read)
    // P510: power draw (read)
    // P527: actual pump speed (read)

    sprintf( tempBuf, "D900=%d&D901=0&FGSP=Read", parameter );
    sprintf( transmitBuf, "POST /GSP.htm HTTP/1.1\r\nAccept: image/gif, image/jpeg, image/pjpeg, image/pjpeg, application/x-shockwave-flash, application/xaml+xml, application/vnd.ms-xpsdocument, application/x-ms-xbap, application/x-ms-application, application/vnd.ms-excel, application/vnd.ms-powerpoint, application/msword, */*\r\nReferer: http://%s/GSP.htm\r\nAccept-Language: en-us\r\nUser-Agent: Mozilla/4.0 (compatible; MSIE 8.0; Windows NT 5.1; Trident/4.0; .NET CLR 2.0.50727; .NET CLR 3.0.04506.30; .NET CLR 1.1.4322; InfoPath.1; .NET CLR 3.0.04506.648; OfficeLiveConnector.1.3; OfficeLivePatch.0.0; .NET CLR 3.0.4506.2152; .NET CLR 3.5.30729)\r\nContent-Type: application/x-www-form-urlencoded\r\nAccept-Encoding: gzip, deflate\r\nHost: %s\r\nContent-Length: %d\r\nConnection: Keep-Alive\r\nCache-Control: no-cache\r\n\r\n%s", controller[m].addr, controller[m].addr, strlen( tempBuf ), tempBuf );

    // dispatch the message to our controller
    if( ClientTCPWrite( controller[m].tcp, transmitBuf, strlen( transmitBuf ), 0 ) < 0 )
    {
        success = False;
        readFlag = True;
    }
    else
        success = True;

    // check receiveBuf

    strcpy( tempBuf, "<input name=\"D901\" type=\"text\" value=\"\" );

    while( (dataRead = ClientTCPRead( controller[m].tcp, receiveBuf, dataSize, 0 )) >= 0 )
    {
        receiveBuf[dataRead] = '\0';
        location = strstr( receiveBuf, tempBuf );
        if( location != NULL )
        {
            sscanf( location, "<input name=\"D901\" type=\"text\" value=\"%d\", &val );
            readFlag = False;
            break;
        }
    }

    *value = val;
    readFlag = False;

    SetWaitCursor( 0 );
    strcpy( tempBuf, "\0" );
    strcpy( transmitBuf, "\0" );

    // say good-night Gracie

    readFlag = False;

    // say good-night Gracie

```

```

return( success );
}

void setRunning( motorType m, bool status )
{
    controller[m].running = status;

    switch( m )
    {
        case Pump:
            SetCtrlVal( panelHandle, PANEL_RUNNING_PUMP, status );
            break;
        case Mixer:
            SetCtrlVal( panelHandle, PANEL_RUNNING_MIXER, status );
            break;
    }
}

int CVICALLBACK PumpStart( int panel, int control, int event, void *callbackData, int eventData1, int eventData2 )
{
    switch( event )
    {
        case EVENT_COMMIT:
            if( !(controller[Pump].started) ) // not running, so let's fire it up
                startMotor( Pump );
            else
                stopMotor( Pump );
            break;
    }
    return( 0 );
}

int CVICALLBACK MixerStart( int panel, int control, int event, void *callbackData, int eventData1, int eventData2 )
{
    switch( event )
    {
        case EVENT_COMMIT:
            if( !(controller[Mixer].started) ) // not running, so let's fire it up
                startMotor( Mixer );
            else
                stopMotor( Mixer );
            break;
    }
    return( 0 );
}

int CVICALLBACK SetPumpSpeed( int panel, int control, int event, void *callbackData, int eventData1, int eventData2 )
{
    double speed;
    GetCtrlVal( panelHandle, PANEL_PUMPSPEED, &speed );

    switch( event )
    {
        case EVENT_COMMIT:
            setSpeed( Pump, (unsigned int)(speed * 10) );
            break;
    }
    return( 0 );
}

int CVICALLBACK SetMixerSpeed( int panel, int control, int event, void *callbackData, int eventData1, int eventData2 )
{
    double speed;
    GetCtrlVal( panelHandle, PANEL_MIXERSPEED, &speed );

    switch( event )
    {
        case EVENT_COMMIT:
            setSpeed( Mixer, (unsigned int)(speed * 10) );
            break;
    }
    return( 0 );
}

int CVICALLBACK PumpReconnect( int panel, int control, int event, void *callbackData, int eventData1, int eventData2 )
{
    switch( event )
    {
        case EVENT_COMMIT:
            if( Connect( Pump ) == False )
                MessagePopup( "Warning!", "Unable to connect to pump controller." );
            else
            {
                setSpeed( Pump, controller[Pump].setpoint );
                MessagePopup( "Success!", "Connected to pump controller." );
            }
            break;
    }
    return( 0 );
}

int CVICALLBACK MixReconnect( int panel, int control, int event, void *callbackData, int eventData1, int eventData2 )

```

```

switch( event )
{
    case EVENT_COMMIT:
        if( Connect( Mixer ) == False )
            MessagePopup( "Warning!", "Unable to connect to mixer controller." );
        else
        {
            setSpeed( Mixer, controller[Mixer].setpoint );
            MessagePopup( "Success!", "Connected to mixer controller." );
        }
        break;
}
return( 0 );
}

void setSpeed( motorType m, unsigned int value )
{
    sendData( m, 61, value );
    controller[m].setpoint = value;
    if( controller[m].started == True && controller[m].setpoint > 0 )
        setRunning( m, True );
    else
        setRunning( m, False );
    if( m == Pump )
        SetCtrlVal( panelHandle, PANEL_PUMPSPEED, (double)value / 10.0 );
    else
        SetCtrlVal( panelHandle, PANEL_MIXERSPEED, (double)value / 10.0 );
}

bool startMotor( motorType m )
{
    if( !(controller[m].connected) )
        Connect( m );
    if( !sendData( m, 65, 97 ) )           // if attempt to fire up the motor fails...
    {
        if( !Connect( m ) )               // attempt a TCP reconnect
        {
            controller[m].started = False;
            setRunning( m, False );
            if( m == Pump )
                MessagePopup( "Warning!", "Lost connection to pump controller." );
            else
                MessagePopup( "Warning!", "Lost connection to mixer controller." );
            return( False );              // all attempts have failed, return
        }
        sendData( m, 65, 97 );            // try again
    }
    if( m == Pump )
        SetCtrlAttribute( panelHandle, controller[m].Control, ATTR_LABEL_TEXT, "__Stop Pump" );
    else
        SetCtrlAttribute( panelHandle, controller[m].Control, ATTR_LABEL_TEXT, "__Stop Mixer" );
    controller[m].started = True;
    if( controller[m].setpoint > 0 )
        setRunning( m, True );
    return( True );
}

bool stopMotor( motorType m )
{
    if( !sendData( m, 65, 0 ) )           // if attempt to shut down the motor fails...
    {
        if( !Connect( m ) )               // attempt a re-connect
        {
            setRunning( m, False );
            MessagePopup( "Warning!", "Lost connection to Pump controller." );
            return( False );              // all attempts have failed, return
        }
        sendData( m, 65, 0 );            // try again
    }
    if( m == Pump )
        SetCtrlAttribute( panelHandle, controller[m].Control, ATTR_LABEL_TEXT, "__Start Pump" );
    else
        SetCtrlAttribute( panelHandle, controller[m].Control, ATTR_LABEL_TEXT, "__Start Mixer" );
    controller[m].started = False;
    setRunning( m, False );
    return( True );
}

int CVICALLBACK ModeSelect( int panel, int control, int event, void *callbackData, int eventData1, int eventData2 )
{
    int i;
    switch( event )
    {
        case EVENT_COMMIT:
            GetCtrlVal( panel, PANEL_MODE, &runMode );
            if( runMode == 2 )
            {
                if( numChecked > 1 )
                {
                    MessagePopup( "DataLogger", "Please ensure that only one input channel is selected." );

                    for( i = 0; i < 28; i++ )

```



```

        {
            data[i].open = False;
            SetCtrlVal( panelHandle, data[i].checkbox, False );
        }
        numChecked = 0;
    }
}
else
{
    for( i = 0; i < 28; i++ )
    {
        data[i].open = True;
        SetCtrlVal( panelHandle, data[i].checkbox, True );
    }
    numChecked = 28;
}
break;
}
return( 0 );
}
}

void handleChk( int index )
{
    int i = 0;
    index--; // convert "natural" index to array-style

    switch( runMode )
    {
        case 2: // 500 Hz single-channel sampling
            if( !data[index].open )
            {
                for( i = 0; i < 28; i++ )
                {
                    if( data[i].open )
                    {
                        SetCtrlVal( panelHandle, data[i].checkbox, (data[i].open = False) );
                        numChecked--;
                    }
                }
                data[index].open = True;
                numChecked++;
            }
            else
            {
                data[index].open = False;
                numChecked--;
            }
            break;
        default: // 50 Hz multi-channel sampling
            data[index].open = !data[index].open;
            if( data[index].open )
                numChecked++;
            else
                numChecked--;
            break;
    }
    SetCtrlVal( panelHandle, data[index].checkbox, data[index].open );
}

int CVICALLBACK Chk1( int panel, int control, int event, void *callbackData, int eventData1, int eventData2 )
{
    switch( event )
    {
        case EVENT_COMMIT:
            handleChk( 1 );
            break;
    }
    return( 0 );
}

int CVICALLBACK Chk2( int panel, int control, int event, void *callbackData, int eventData1, int eventData2 )
{
    switch( event )
    {
        case EVENT_COMMIT:
            handleChk( 2 );
            break;
    }
    return( 0 );
}

int CVICALLBACK Chk3( int panel, int control, int event, void *callbackData, int eventData1, int eventData2 )
{
    switch( event )
    {
        case EVENT_COMMIT:
            handleChk( 3 );
            break;
    }
    return( 0 );
}

int CVICALLBACK Chk4( int panel, int control, int event, void *callbackData, int eventData1, int eventData2 )
{
    switch( event )

```

```

    {
        case EVENT_COMMIT:
            handleChk( 4 );
            break;
    }
    return( 0 );
}

int CVICALLBACK Chk5( int panel, int control, int event, void *callbackData, int eventData1, int eventData2 )
{
    switch( event )
    {
        case EVENT_COMMIT:
            handleChk( 5 );
            break;
    }
    return( 0 );
}

int CVICALLBACK Chk6( int panel, int control, int event, void *callbackData, int eventData1, int eventData2 )
{
    switch( event )
    {
        case EVENT_COMMIT:
            handleChk( 6 );
            break;
    }
    return( 0 );
}

int CVICALLBACK Chk7( int panel, int control, int event, void *callbackData, int eventData1, int eventData2 )
{
    switch( event )
    {
        case EVENT_COMMIT:
            handleChk( 7 );
            break;
    }
    return( 0 );
}

int CVICALLBACK Chk8( int panel, int control, int event, void *callbackData, int eventData1, int eventData2 )
{
    switch( event )
    {
        case EVENT_COMMIT:
            handleChk( 8 );
            break;
    }
    return( 0 );
}

int CVICALLBACK Chk9( int panel, int control, int event, void *callbackData, int eventData1, int eventData2 )
{
    switch( event )
    {
        case EVENT_COMMIT:
            handleChk( 9 );
            break;
    }
    return( 0 );
}

int CVICALLBACK Chk10( int panel, int control, int event, void *callbackData, int eventData1, int eventData2 )
{
    switch( event )
    {
        case EVENT_COMMIT:
            handleChk( 10 );
            break;
    }
    return( 0 );
}

int CVICALLBACK Chk11( int panel, int control, int event, void *callbackData, int eventData1, int eventData2 )
{
    switch( event )
    {
        case EVENT_COMMIT:
            handleChk( 11 );
            break;
    }
    return( 0 );
}

int CVICALLBACK Chk12( int panel, int control, int event, void *callbackData, int eventData1, int eventData2 )
{
    switch( event )
    {
        case EVENT_COMMIT:
            handleChk( 12 );
            break;
    }
}

```

```

return( 0 );
}

int CVICALLBACK Chk13( int panel, int control, int event, void *callbackData, int eventData1, int eventData2 )
{
    switch( event )
    {
        case EVENT_COMMIT:
            handleChk( 13 );
            break;
    }
    return( 0 );
}

int CVICALLBACK Chk14( int panel, int control, int event, void *callbackData, int eventData1, int eventData2 )
{
    switch( event )
    {
        case EVENT_COMMIT:
            handleChk( 14 );
            break;
    }
    return( 0 );
}

int CVICALLBACK Chk15( int panel, int control, int event, void *callbackData, int eventData1, int eventData2 )
{
    switch( event )
    {
        case EVENT_COMMIT:
            handleChk( 15 );
            break;
    }
    return( 0 );
}

int CVICALLBACK Chk16( int panel, int control, int event, void *callbackData, int eventData1, int eventData2 )
{
    switch( event )
    {
        case EVENT_COMMIT:
            handleChk( 16 );
            break;
    }
    return( 0 );
}

int CVICALLBACK Chk17( int panel, int control, int event, void *callbackData, int eventData1, int eventData2 )
{
    switch( event )
    {
        case EVENT_COMMIT:
            handleChk( 17 );
            break;
    }
    return( 0 );
}

int CVICALLBACK Chk18( int panel, int control, int event, void *callbackData, int eventData1, int eventData2 )
{
    switch( event )
    {
        case EVENT_COMMIT:
            handleChk( 18 );
            break;
    }
    return( 0 );
}

int CVICALLBACK Chk19( int panel, int control, int event, void *callbackData, int eventData1, int eventData2 )
{
    switch( event )
    {
        case EVENT_COMMIT:
            handleChk( 19 );
            break;
    }
    return( 0 );
}

int CVICALLBACK Chk20( int panel, int control, int event, void *callbackData, int eventData1, int eventData2 )
{
    switch( event )
    {
        case EVENT_COMMIT:
            handleChk( 20 );
            break;
    }
    return( 0 );
}

int CVICALLBACK Chk21( int panel, int control, int event, void *callbackData, int eventData1, int eventData2 )
{

```

```

switch( event )
{
    case EVENT_COMMIT:
        handleChk( 21 );
        break;
}
return( 0 );
}

int CVICALLBACK Chk22( int panel, int control, int event, void *callbackData, int eventData1, int eventData2 )
{
    switch( event )
    {
        case EVENT_COMMIT:
            handleChk( 22 );
            break;
    }
    return( 0 );
}

int CVICALLBACK Chk23( int panel, int control, int event, void *callbackData, int eventData1, int eventData2 )
{
    switch( event )
    {
        case EVENT_COMMIT:
            handleChk( 23 );
            break;
    }
    return( 0 );
}

int CVICALLBACK Chk24( int panel, int control, int event, void *callbackData, int eventData1, int eventData2 )
{
    switch( event )
    {
        case EVENT_COMMIT:
            handleChk( 24 );
            break;
    }
    return( 0 );
}

int CVICALLBACK Chk25( int panel, int control, int event, void *callbackData, int eventData1, int eventData2 )
{
    switch( event )
    {
        case EVENT_COMMIT:
            handleChk( 25 );
            break;
    }
    return( 0 );
}

int CVICALLBACK Chk26( int panel, int control, int event, void *callbackData, int eventData1, int eventData2 )
{
    switch( event )
    {
        case EVENT_COMMIT:
            handleChk( 26 );
            break;
    }
    return( 0 );
}

int CVICALLBACK Chk27( int panel, int control, int event, void *callbackData, int eventData1, int eventData2 )
{
    switch( event )
    {
        case EVENT_COMMIT:
            handleChk( 27 );
            break;
    }
    return( 0 );
}

int CVICALLBACK Chk28( int panel, int control, int event, void *callbackData, int eventData1, int eventData2 )
{
    switch( event )
    {
        case EVENT_COMMIT:
            handleChk( 28 );
            break;
    }
    return( 0 );
}

int CVICALLBACK ManualRead( int panel, int control, int event, void *callbackData, int eventData1, int eventData2 )
{
    unsigned int param = 0, value;
    char tempBuf[11] = { 0 };

    switch( event )
    {

```

```

// P506: voltage (read)
// P507: load (read)
// P508: current (read)
// P509: torque (read)
// P510: power draw (read)
// P527: actual pump speed (read)
case EVENT_COMMIT:
    switch( readParam )
    {
        case 0:
            param = 506;
            break;
        case 1:
            param = 508;
            break;
        case 2:
            param = 507;
            break;
        case 3:
            param = 509;
            break;
        case 4:
            param = 510;
            break;
        case 5:
            default:
                param = 527;
                break;
    }
    readData( Pump, param, &value );
    sprintf( tempBuf, "%d", value );
    SetCtrlVal( panel, PANEL_PARAMVALUE, tempBuf );

    break;
}
return( 0 );
}

int CVICALLBACK ParamSelect( int panel, int control, int event, void *callbackData, int eventData1, int eventData2 )
{
    switch( event )
    {
        case EVENT_COMMIT:
            GetCtrlVal( panel, PANEL_READPARAM, &readParam );
            break;
    }
    return( 0 );
}

int CVICALLBACK CmdZeroGauges( int panel, int control, int event, void *callbackData, int eventData1, int eventData2 )
{
    int32 error = 0;
    switch( event )
    {
        case EVENT_COMMIT:
            DAQmxErrChk( DAQmxStopTask( gTaskHandle ) );
            DAQmxErrChk( DAQmxPerformBridgeOffsetNullingCalEx( gTaskHandle, "", 1 ) );
            DAQmxErrChk( DAQmxStartTask( gTaskHandle ) );
            break;
    }
    return( 0 );
}
Error:
MessagePopup( "Error!", "Gauges cannot be zeroed out at this time." );
return( 1 );
}

```

Appendix B - Impingement Wear Model Code

```

conc_l = 0.4657;
conc_h = 0.1747;
timestep = 1;
density = 2593; % density of impinging particles (silica in this case)
size_p = 250; % average particle size in Schaan, Cook, & Sanders (2007)
VN = 55; % Vickers hardness for mild steel

rad = 369; % pipe internal radius [mm] in Schaan, Cook, & Sanders (2007)
bedheight = 290;
delta_s = 170;
vel_l = 0; % velocity of lower layer [mm/s] (stationary bed in this case)
vel_h = 7280; % velocity of upper layer [mm/s]
vel_t = 668;

turb_l = 0.2 * vel_h;
turb_h = 0.05 * vel_h;
duration = 10; % simulated flow time [s]

circ = zeros( rad * 2 + 1, rad * 2 + 1, 3 );

for y = 1:1:(2*rad)+1
    for x = 1:1:(2*rad)+1
        if (((x-rad)^2) + ((y-rad)^2)) < (rad^2)
            if y <= bedheight
                circ(x,y,1) = conc_l;
                circ(x,y,2) = vel_l;
                circ(x,y,3) = turb_l;
            elseif y < (bedheight+delta_s) && y > bedheight
                circ(x,y,1) = conc_l + (conc_h - conc_l) * (y - bedheight)/delta_s;
                circ(x,y,2) = vel_l + (vel_h - vel_l) * (y - bedheight)/delta_s;
                circ(x,y,3) = turb_l + (turb_h - turb_l) * (y - bedheight)/delta_s;
            else
                circ(x,y,1) = conc_h;
                circ(x,y,2) = vel_h;
                circ(x,y,3) = turb_h;
            end
        end
    end
end

totaldamage = 0;
impact = zeros( round(2*pi*rad) );

for t = 0:1:duration
    for x = 1:1:(2*rad)+1
        x_r = x-rad;
        for y = (bedheight+1):1:(bedheight+delta_s)
            y_r = y-rad;
            if ((y_r^2) + (x_r^2)) < (rad^2)
                vn = normrnd( 0, circ(x,y,3) );
                vt = normrnd( 0, circ(x,y,3) );
                vz = normrnd( 0, circ(x,y,3) );
                [s yes] = isDamage( x_r, y_r, vn, vt, vel_t, timestep, rad );
                damage = yes * circ(x,y,1) * (density / 1000000000) * E( vn, vt, circ(x,
y,2) + vz, size_p, VN );
            end
        end
    end
end

```

```

        if damage > 0
            impact( s ) = impact( s ) + damage;
        end
        totaldamage = totaldamage + damage;
    end
end
end
end

damagerate = totaldamage / duration; % mm3/s
wear1000 = damagerate * 3600 * 1000 % mm3 per 1000 hrs

figure1 = figure( 'Color', [1 1 1] );
axes1 = axes( 'Parent', figure1 );
box( axes1, 'on' );
hold( axes1, 'all' );
plot( impact, 'MarkerFaceColor', [0 0 0], 'MarkerEdgeColor', [0 0 0], 'MarkerSize', 3,
'Marker', 'o', 'LineStyle', 'none', 'DisplayName', 'data 1' );
xlabel( { 'Circumferential location on pipe [mm]' } );
ylabel( { 'Total wear [mm3/mm]' } );

function [s yes] = isCollision( x,y,vn,vt,t,r )

    theta = atan2( y, x );
    vx = vn * cos(theta) + vt * sin(theta);
    vy = vn * sin(theta) + vt * cos(theta);
    m = vy/vx;
    b = y - (m * x);
    x1 = (-2*b*m+sqrt(4*((m^2)*(r^2)+(r^2)-(b^2))))/(2*((m^2)+1));
    x2 = (-2*b*m-sqrt(4*((m^2)*(r^2)+(r^2)-(b^2))))/(2*((m^2)+1));
    y1 = m*x1+b;
    y2 = m*x2+b;
    if sign(vy) == sign((y1-y))
        yp = y1;
        xp = x1;
    else
        yp = y2;
        xp = x2;
    end
    d = sqrt(((xp-x)^2) + ((yp-y)^2));
    s = round(r * (atan2( yp, xp )-(pi/2)));
    if s <= 0
        s = s + (2*pi*r);
    elseif s > 2*pi*r
        s = s - (2*pi*r);
    end
    s = round(s);

    if d <= (sqrt((vx^2)+(vy^2)) * t)
        yes = 1;
    else
        yes = 0;
    end
end

```


end

```
function [s yes] = isDamage(x,y,vn,vt,v_t,t,r)
```

```
if vn > v_t
```

```
    [s yes] = isCollision(x,y,vn,vt,t,r);
```

```
else
```

```
    s=0;
```

```
    yes=0;
```

```
end
```

```
function [ wear ] = E( vn,vt,vz,ps,Hv )
```

```
%UNTITLED6 Summary of this function goes here
```

```
% Detailed explanation goes here
```

```
k1 = -0.12;
```

```
k2 = 2.3 * (Hv^0.038);
```

```
k3 = 0.19;
```

```
K = 64;
```

```
E90 = K * (Hv^k1) * ((vn/104000)^k2) * ((ps/326)^k3);
```

```
wear = E90 * G( a( vn,vt,vz ), Hv );
```

```
end
```

```
function [ wear ] = G( theta, Hv )
```

```
%UNTITLED5 Summary of this function goes here
```

```
% Detailed explanation goes here
```

```
n1 = 0.71 * (Hv^0.14);
```

```
n2 = 2.4 * (Hv^-0.94);
```

```
wear = ((sin(theta))^n1)*((1+(Hv*(1-sin(theta))))^n2);
```

```
end
```

```
function [ theta ] = a( vn,vt,vz )
```

```
%UNTITLED7 Summary of this function goes here
```

```
% Detailed explanation goes here
```

```
theta = (pi/2) - atan2(vn,sqrt((vt^2)+(vz^2)));
```

```
end
```

Appendix C – Modified Two-Layer Model MathCAD Worksheet

Set up flow parameters

$$U := 6 \frac{m}{s} \quad m_{sand} := 33.3 \text{ kg} \quad T := (42.42 + 273.15) \text{ K} \quad D_i := 2.067 \text{ in}$$

$$r_i := \frac{D_i}{2} = 26.251 \text{ mm} \quad A := \frac{1}{4} \cdot \pi \cdot D_i^2 = (2.165 \cdot 10^3) \text{ mm}^2 \quad d_{50} := 1.5 \text{ mm}$$

$$\varepsilon := 0.109536 \text{ mm} \quad \alpha_{water} := 0.000207 \frac{1}{K} \quad g := 9.80665 \frac{m}{s^2}$$

$$\mu_{water} := (0.00002414 \text{ Pa} \cdot \text{s}) \cdot 10^{\frac{247.8 \text{ K}}{T - 140 \text{ K}}} = (6.225 \cdot 10^{-4}) \text{ Pa} \cdot \text{s}$$

$$\rho_{water} := \frac{998.2071 \frac{kg}{m^3}}{1 + \alpha_{water} \cdot (T - 293.15 \text{ K})} = 993.596 \frac{kg}{m^3}$$

$$\rho_{garnet} := 3992 \frac{kg}{m^3} \quad \rho_{silica} := 2645 \frac{kg}{m^3} \quad \rho_{sand} := \rho_{garnet}$$

$$V_{system} := 62 \text{ L} \quad V_{sand} := \frac{m_{sand}}{\rho_{sand}} = 8.342 \text{ L} \quad V_{water} := V_{system} - V_{sand} = 53.658 \text{ L}$$

$$m_{water} := V_{water} \cdot \rho_{water} = 53.315 \text{ kg}$$

$$C_w := \frac{m_{sand}}{\rho_{water} \cdot V_{water} + m_{sand}} = 0.384 \quad C_r := \frac{\frac{C_w}{\rho_{sand}}}{\frac{C_w}{\rho_{sand}} + \frac{(1 - C_w)}{\rho_{water}}} = 0.135$$

$$\rho_{slurry} := \frac{1}{\frac{C_w}{\rho_{sand}} + \frac{1 - C_w}{\rho_{water}}} = (1.397 \cdot 10^3) \frac{kg}{m^3} \quad SG_{slurry} := \frac{\rho_{slurry}}{\rho_{water}} = 1.406$$

$$\mu_{slurry} := \mu_{water} \cdot (1 + 2.5 \cdot C_r + 10 \cdot C_r^2 + 0.0019 \cdot e^{20 \cdot C_r}) = (9.62 \cdot 10^{-4}) \text{ Pa} \cdot \text{s}$$

$$Re_{slurry} := \frac{\rho_{slurry} \cdot U \cdot D_i}{\mu_{slurry}} = 4.575 \cdot 10^5 \quad Re_{water} := \frac{\rho_{water} \cdot U \cdot D_i}{\mu_{water}} = 5.028 \cdot 10^5$$

$$C_f := 0$$

$$C_t := C_r + C_f = 0.135$$

$$C_{max} := 0.6$$

$$\rho_f := \frac{\rho_{water} \cdot (1 - C_t) + \rho_{sand} \cdot C_f}{1 - C_t + C_f} = 993.596 \frac{kg}{m^3}$$

$$\mu_f := \mu_{water}$$

$$Re_p := \frac{\rho_f \cdot d_{50} \cdot U}{\mu_f} = 1.437 \cdot 10^4$$

$$C_D := \frac{24}{Re_p} \cdot (1 + 0.15 \cdot Re_p^{0.687}) + \frac{0.42}{1 + \frac{42500}{Re_p^{1.16}}} = 0.438$$

$$U_{inf} := \sqrt{\frac{4 \cdot g \cdot d_{50} \cdot (\rho_{sand} - \rho_f)}{3 \cdot C_D \cdot \rho_f}} = 0.368 \frac{m}{s}$$

$$\lambda := \left(\left(\frac{C_{max}}{C_r} \right)^{\frac{1}{3}} - 1 \right)^{-1} = 1.548$$

$$f_f := \frac{1}{4 \cdot \left(\log \left(\frac{\frac{\varepsilon}{D_i}}{3.7} + \frac{5.74}{Re_{water}^{0.9}} \right) \right)^2} = 0.024$$

$$Ar := \frac{4 \cdot g \cdot d_{50}^3 \cdot \rho_{water} \cdot (\rho_{sand} - \rho_{water})}{3 \cdot \mu_{water}^2} = 3.393 \cdot 10^5$$

$$Fr := \min \left(\frac{U}{\sqrt{g \cdot D_i \cdot (SG_{slurry} - 1)}}, 3 \right) = 3$$

$$F_L := \frac{Fr}{\sqrt{2}} = 2.121$$

$$Re := \min \left(\frac{\rho_{slurry} \cdot U \cdot D_i}{\mu_f \cdot (1 + 0.21 \cdot \lambda^2)}, 120000 \right) = 1.2 \cdot 10^5$$

$$U_d := F_L \cdot \sqrt{2 \cdot g \cdot D_i \cdot \left(\frac{\rho_{sand}}{\rho_{water}} - 1 \right)} = 3.739 \frac{m}{s}$$

$$U_h := \sqrt[3]{1800 \cdot g \cdot D_i \cdot U_{inf}} = 6.985 \frac{m}{s}$$

$$C_c := C_r \cdot e^{-0.0097 \cdot \left(\frac{U}{U_{inf}}\right)^{0.864} \cdot Re^{0.193} \cdot Fr^{-0.292}} = 0.064$$

$$C_{lim} := C_{max} - (C_{max} - C_r) \cdot 0.074 \cdot \left(\frac{U}{U_{inf}}\right)^{0.44} \cdot (1 - C_r)^{0.189} = 0.485$$

$$C_1 := C_r - C_c = 0.071$$

$$\rho_1 := \rho_f \cdot (1 - C_1) + \rho_{sand} \cdot C_1 = (1.207 \cdot 10^3) \frac{kg}{m^3}$$

$$\rho_{2f} := \frac{\rho_f \cdot (1 - C_{lim}) + \rho_{sand} \cdot C_1}{1 - C_{lim} + C_1} = (1.357 \cdot 10^3) \frac{kg}{m^3}$$

$$C_2 := C_{lim} - C_1 = 0.414 \quad d_{plus} := \frac{d_{50} \cdot \rho_f \cdot U \cdot \sqrt{\frac{f_f}{8}}}{\mu_f} = 789.304$$

$$\delta := \frac{5 \cdot \mu_f}{\rho_f \cdot U \cdot \sqrt{\frac{f_f}{2}}} = (4.751 \cdot 10^{-6}) \text{ m} \quad \zeta := \min\left(1, 2 \cdot \frac{1 \text{ m} - \delta}{d_{50}}\right) = 1$$

$$\eta_{s0} := 0.5 \quad \eta_s := \zeta \cdot \eta_{s0} = 0.5 \quad f_{sl} := \lambda^{1.25} \cdot (0.00005 + 0.00033 \cdot e^{-0.1 \cdot d_{plus}}) = 8.633 \cdot 10^{-5}$$

$$Y := 5 + 1.86 \cdot \log\left(\frac{d_{50}}{D_i}\right) = 2.128$$

$$f_{12} := \frac{1 + 2 \cdot Y}{\left(4 \cdot \log\left(\frac{D_i}{d_{50}}\right) + 3.36\right)^2} = 0.058$$

$$F_f := 0$$

$$\mu_1 := \mu_{water} \cdot \left(1 + 2.5 \cdot C_1 + 10 \cdot C_1^2 + 0.0019 \cdot e^{20 \cdot C_1}\right) = (7.694 \cdot 10^{-4}) \text{ Pa} \cdot \text{s}$$

$$\mu_2 := \mu_{water} \cdot \left(1 + 2.5 \cdot C_{lim} + 10 \cdot C_{lim}^2 + 0.0019 \cdot e^{20 \cdot C_{lim}}\right) = 0.022 \text{ Pa} \cdot \text{s}$$

$$A_2 := A \cdot \frac{C_c}{C_2} = 331.736 \text{ mm}^2$$

$$\beta := \pi \cdot \frac{A_2}{A}$$

$$A_2 = r_i^2 \cdot (\beta - \sin(\beta) \cdot \cos(\beta))$$

$$\beta := \text{Find}(\beta) = 54.627 \text{ deg}$$

$$A_1 := A - A_2 = (1.833 \cdot 10^3) \text{ mm}^2$$

$$h_2 := r_i \cdot (1 - \cos(\beta)) = 11.054 \text{ mm}$$

$$h_1 := D_i - h_2 = 41.447 \text{ mm}$$

$$S_1 := 2 \cdot r_i \cdot (\pi - \beta) = 114.883 \text{ mm} \quad S_{12} := 2 \cdot r_i \cdot \sin(\beta) = 42.81 \text{ mm} \quad S_2 := 2 \cdot r_i \cdot \beta = 50.057 \text{ mm}$$

$$D_{h1} := \frac{4 \cdot A_1}{S_1 + S_{12}} = 46.5 \text{ mm}$$

$$D_{h2} := \frac{4 \cdot A_2}{S_2 + S_{12}} = 14.289 \text{ mm}$$

$$F_2 := \frac{1}{2} \cdot \eta_s \cdot D_i^2 \cdot g \cdot \frac{C_2 \cdot (1 - C_{lim})}{1 - C_2} \cdot (\rho_{sand} - \rho_{water}) \cdot (\sin(\beta) - \beta \cdot \cos(\beta)) = 1.944 \frac{\text{N}}{\text{m}}$$

$$U_1 := 1.0455 \cdot U = 6.273 \frac{\text{m}}{\text{s}}$$

$$U_2 := \frac{U \cdot A - U_1 \cdot A_1}{A_2} = 4.491 \frac{\text{m}}{\text{s}}$$

$$Re_1 := \frac{\rho_1 \cdot U_1 \cdot D_{h1}}{\mu_1} = 4.575 \cdot 10^5$$

$$Re_2 := \frac{\rho_{2f} \cdot U_2 \cdot D_{h2}}{\mu_2} = 3.9 \cdot 10^3$$

$$f_l(Re_l) := 2 \cdot \left(\left(\frac{8}{Re_l} \right)^{12} + \left(-2.457 \cdot \ln \left(\left(\frac{7}{Re_l} \right)^{0.9} + 0.27 \cdot \frac{\varepsilon}{D_i} \right) \right)^{16} + \left(\frac{37530}{Re_l} \right)^{16} \right)^{-1.5} \frac{1}{12}$$

$$\tau_1 := \frac{U_1 \cdot |U_1|}{2} \cdot (f_l(Re_1) \cdot \rho_1 + f_{sl} \cdot \rho_{sand}) = 150.307 \text{ Pa}$$

$$\tau_2 := \frac{U_2 \cdot |U_2|}{2} \cdot (f_l(Re_2) \cdot \rho_{2f} + f_{sl} \cdot \rho_{sand}) = 151.389 \text{ Pa}$$

$$\tau_{12} := \frac{1}{2} \cdot f_{12} \cdot (U_1 - U_2) \cdot |U_1 - U_2| \cdot \rho_1 = 110.672 \text{ Pa}$$

$$i_2 := \frac{\tau_2 \cdot S_2 + F_2 - \tau_{12} \cdot S_{12}}{\rho_{\text{water}} \cdot g \cdot A_2} = 1.48$$

$$i_1 := \frac{\tau_1 \cdot S_1 + \tau_{12} \cdot S_{12}}{\rho_{\text{water}} \cdot g \cdot A_1} = 1.232$$

$$i := \frac{i_1 + i_2}{2} = 1.356$$

Solve the model

$$A \cdot U = A_1 \cdot U_1 + A_2 \cdot U_2$$

$$Re_1 = \left| \frac{\rho_1 \cdot U_1 \cdot D_{h1}}{\mu_1} \right| \quad Re_2 = \left| \frac{\rho_{2f} \cdot U_2 \cdot D_{h2}}{\mu_2} \right| \quad U_1 > U_2 \quad U_2 \geq 0$$

$$\tau_1 = \frac{U_1 \cdot |U_1|}{2} \cdot (f_l(Re_1) \cdot \rho_1 + f_{sl} \cdot \rho_{\text{sand}}) \quad \tau_2 = \frac{U_2 \cdot |U_2|}{2} \cdot (f_l(Re_2) \cdot \rho_{2f} + f_{sl} \cdot \rho_{\text{sand}})$$

$$\tau_{12} = \frac{1}{2} \cdot f_{12} \cdot (U_1 - U_2) \cdot |U_1 - U_2| \cdot \rho_1$$

$$i \cdot \rho_{\text{water}} \cdot g = \frac{\tau_2 \cdot S_2 + F_2 - \tau_{12} \cdot S_{12}}{A_2}$$

$$i \cdot \rho_{\text{water}} \cdot g = \frac{\tau_1 \cdot S_1 + \tau_{12} \cdot S_{12}}{A_1}$$

$$\begin{bmatrix} U_1 \\ U_2 \\ \tau_1 \\ \tau_{12} \\ \tau_2 \\ Re_1 \\ Re_2 \\ i \end{bmatrix} := \text{Find}(U_1, U_2, \tau_1, \tau_{12}, \tau_2, Re_1, Re_2, i) = \begin{bmatrix} 6.287 \frac{\text{m}}{\text{s}} \\ 4.416 \frac{\text{m}}{\text{s}} \\ 150.953 \text{ Pa} \\ 121.951 \text{ Pa} \\ 147.023 \text{ Pa} \\ 4.585 \cdot 10^5 \\ 3.834 \cdot 10^3 \\ 1.263 \end{bmatrix}$$

MODIFIED TWO-LAYER CALCULATIONS

$$\mu_s := \frac{\mu_1 + \mu_2}{2} = 0.012 \text{ Pa}\cdot\text{s} \quad \rho_s := \frac{\rho_1 + \rho_{2f}}{2} = (1.282 \cdot 10^3) \frac{\text{kg}}{\text{m}^3}$$

$$A_{2mod} := \max\left(0, A \cdot \frac{C_c}{C_2} \cdot \left(1 - \frac{U}{U_d}\right)\right) = 0 \text{ mm}^2 \quad C_{avg} := \frac{U_1 \cdot C_1 \cdot A_1 + U_2 \cdot C_{lim} \cdot A_2}{A \cdot U} = 0.118$$

$$U_u(u) := U_1 + (u > U_d) \cdot \left(\frac{\min(u, U_h) - U_d}{U_h - U_d}\right) \cdot (U - U_1)$$

$$U_l(u) := U_2 + (u > U_d) \cdot \left(\frac{\min(u, U_h) - U_d}{U_h - U_d}\right) \cdot (U - U_2)$$

$$C_u(u) := C_1 + (u > U_d) \cdot \left(\frac{\min(u, U_h) - U_d}{U_h - U_d}\right) \cdot (C_{avg} - C_1)$$

$$C_l(u) := C_{lim} + (u > U_d) \cdot \left(\frac{\min(u, U_h) - U_d}{U_h - U_d}\right) \cdot (C_{avg} - C_{lim})$$

$$\beta_{mod} := \pi \cdot \frac{A_{2mod}}{A}$$

$$A_{2mod} = r_i^2 \cdot (\beta_{mod} - \sin(\beta_{mod}) \cdot \cos(\beta_{mod}))$$

$$\beta_{mod} := \text{Find}(\beta_{mod}) = 0 \text{ deg}$$

$$h_{2mod} := r_i \cdot (1 - \cos(\beta_{mod})) = 0 \text{ mm}$$

$$m_s := \left(\frac{\min(U, U_d)}{U_d}\right) \cdot A_2 \cdot U_2 \cdot C_{lim} + \left(\frac{\min(U, U_h)}{U_h}\right) \cdot A_1 \cdot U_1 \cdot C_1 = (1.414 \cdot 10^6) \frac{\text{mm}^3}{\text{s}}$$

$$h_s := D_i \cdot \frac{\min(U, U_h)}{U_h} = 45.099 \text{ mm}$$

$$h_s := D_i \cdot \frac{\min(U, U_h)}{U_h} \quad A_s := A_1 \quad A_{1mod} := A - (A_{2mod} + A_s) \quad U_s := \frac{U_1 + U_2}{2}$$

$$m_s = \langle U < U_h \rangle \cdot 2 \cdot \int_{h_{2mod}}^{h_{2mod} + h_s} \left(U_l(U) + \frac{y - h_{2mod}}{h_s} \cdot (U_u(U) - U_l(U)) \right) \cdot \left(C_l(U) + (C_u(U) - C_l(U)) \cdot \left(\frac{y - h_{2mod}}{h_s} \right) \right) \cdot \sqrt{r_i^2 - (r_i - y)^2} dy$$

$$A_s = 2 \cdot \int_{h_{2mod}}^{h_{2mod} + h_s} \sqrt{r_i^2 - (r_i - y)^2} dy$$

$$U_s = \frac{2}{A_s} \cdot \int_{h_{2mod}}^{h_{2mod} + h_s} \left(U_l(U) + \frac{y - h_{2mod}}{h_s} \cdot (U_u(U) - U_l(U)) \right) \cdot \sqrt{r_i^2 - (r_i - y)^2} dy$$

$$A \cdot U = A_s \cdot U_s + A_{1mod} \cdot U_1 + A_{2mod} \cdot U_2 \quad U_s \geq U_2$$

$$A = A_{1mod} + A_s + A_{2mod}$$

$$[h_s \ A_s \ A_{1mod} \ U_s] := \mathbf{Find}(h_s, A_s, A_{1mod}, U_s) = \left[0.035 \text{ m} \ 0.002 \text{ m}^2 \ (6.303 \cdot 10^{-4}) \text{ m}^2 \ 5.882 \frac{\text{m}}{\text{s}} \right]$$

$$\alpha := \max \left(\beta_{mod}, \left| \arccos \left(\cos(\beta_{mod}) - \frac{h_s}{r_i} \right) \right| \right) = 109.536 \text{ deg}$$

$$h_{1mod} := D_i - (h_{2mod} + h_s) = 17.473 \text{ mm}$$

$$S_{1mod} := 2 \cdot r_i \cdot (\pi - \alpha) = 64.568 \text{ mm}$$

$$S_{1s} := 2 \cdot r_i \cdot \sin(\alpha) = 49.479 \text{ mm}$$

$$S_s := r_i \cdot (\alpha - \beta_{mod}) = 50.186 \text{ mm}$$

$$S_{2s} := 2 \cdot r_i \cdot \sin(\beta_{mod}) = 0 \text{ mm}$$

$$S_{2mod} := 2 \cdot r_i \cdot \beta_{mod} = 0 \text{ mm}$$

$$D_{hs} := \frac{4 \cdot A_s}{S_{1s} + S_{2s} + 2 \cdot S_s} = 40.964 \text{ mm}$$

$$Re_s := \frac{\rho_s \cdot U_s \cdot D_{hs}}{\mu_s} = 2.674 \cdot 10^4$$

$$\tau_s := \frac{1}{2} \cdot U_s \cdot |U_s| \cdot (f_l(Re_s) \cdot \rho_s + f_{st} \cdot \rho_s) = 162.764 \text{ Pa}$$

$$\tau_{1s} := \frac{1}{2} \cdot f_{12} \cdot (U_1 - U_s) \cdot |U_1 - U_s| \cdot \rho_1 = 5.699 \text{ Pa}$$

$$\tau_{2s} := \frac{1}{2} \cdot f_{12} \cdot (U_s - U_2) \cdot |U_s - U_2| \cdot \rho_{2f} = 84.287 \text{ Pa}$$

LIST OF MODEL PARAMETERS

$$U = 6 \frac{m}{s}$$

$$U_u(U) = 6.087 \frac{m}{s}$$

$$U_l(U) = 5.519 \frac{m}{s}$$

$$U_1 = 6.287 \frac{m}{s}$$

$$U_2 = 4.416 \frac{m}{s}$$

$$U_s = 5.882 \frac{m}{s}$$

$$C_r = 0.135$$

$$C_l(U) = 0.229$$

$$C_u(U) = 0.104$$

$$F_2 = 1.944 \frac{N}{m}$$

$$\frac{F_2}{S_2} = 38.841 \text{ Pa}$$

$$h_1 = 41.447 \text{ mm}$$

$$h_2 = 11.054 \text{ mm}$$

$$i \cdot \rho_{water} \cdot g = 12.308 \frac{kPa}{m}$$

$$h_{1mod} = 17.473 \text{ mm}$$

$$h_{2mod} = 0 \text{ mm}$$

$$h_s = 35.029 \text{ mm}$$

$$\beta = 54.627 \text{ deg}$$

$$\beta_{mod} = 0 \text{ deg}$$

$$\alpha = 109.536 \text{ deg}$$

$$A_{1mod} = 630.302 \text{ mm}^2$$

$$A_{2mod} = 0 \text{ mm}^2$$

$$A_s = (1.535 \cdot 10^3) \text{ mm}^2$$

$$A_1 = (1.833 \cdot 10^3) \text{ mm}^2$$

$$A_2 = 331.736 \text{ mm}^2$$

$$A = (2.165 \cdot 10^3) \text{ mm}^2$$

$$\frac{A_{1mod}}{A} = 0.291$$

$$\frac{A_{2mod}}{A} = 0$$

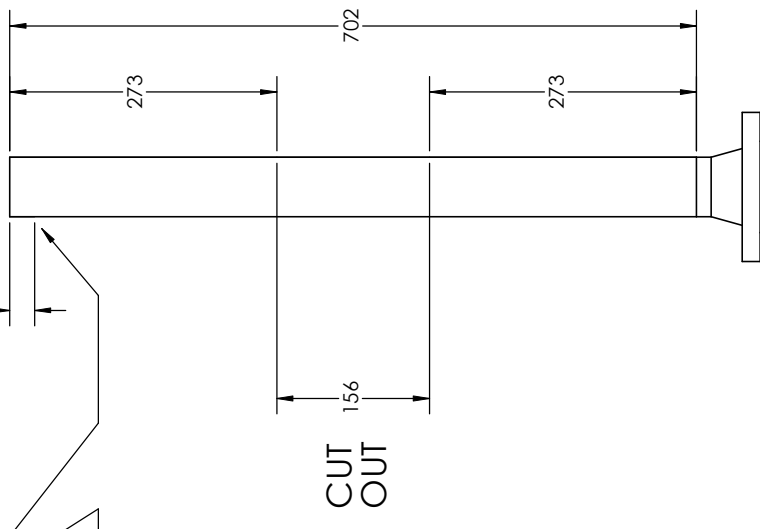
$$\frac{A_s}{A} = 0.709$$

Appendix D – Modified Piping Drawings

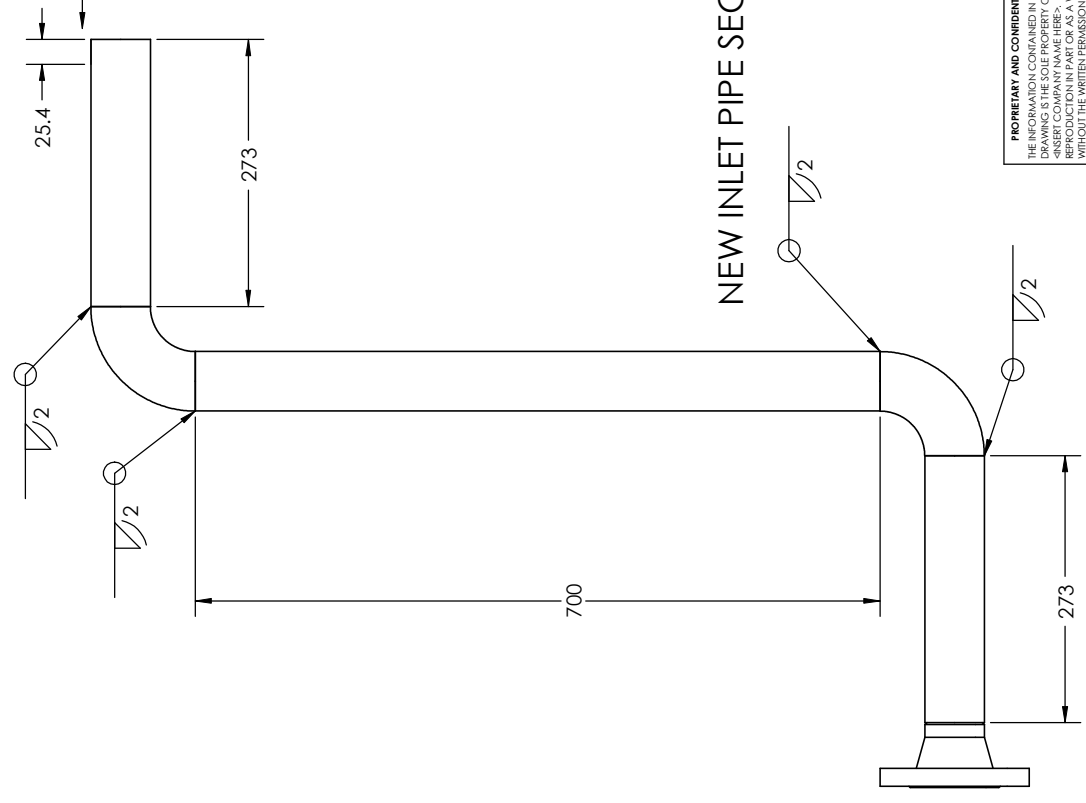
ITEM NO.	PART NUMBER	DESCRIPTION	QTY.
1	90 DEGREE ELBOW - STEEL, 2 INCH	SUPPLIED	2
3	MCMMASTER P/N 7750K196	2 INCH STEEL PIPE, 36 INCH LENGTH CUT TO 700 MM LENGTH	1

OLD INLET PIPE SECTION

PIPE THREAD



NEW INLET PIPE SECTION



UNLESS OTHERWISE SPECIFIED:	NAME	DATE
DIMENSIONS ARE IN INCHES		
TOLERANCES:	DRAWN	
FRACTIONAL: ±	CHECKED	
ANGULAR: MACH ±	ENG APPR:	
DECIMAL: ±	MFG APPR:	
THREE PLACE DECIMAL ±	Q. A.	
INTERPRET GEOMETRIC TOLERANCING PER:	COMMENTS:	
MATERIAL:		
FINISH:		
USED ON:		
APPLICATION:		
DO NOT SCALE DRAWING		

PROPRIETARY AND CONFIDENTIAL
 THE INFORMATION CONTAINED IN THIS DRAWING IS THE PROPERTY OF
 MCMMASTER-CARR. ANY REPRODUCTION OR
 REPRODUCTION IN PART OR AS A WHOLE
 WITHOUT THE WRITTEN PERMISSION OF
 MCMMASTER-CARR IS PROHIBITED.

SIZE DWG. NO. REV
Fixing tank inlet
 SCALE: 1:20 WEIGHT: SHEET 1 OF 1

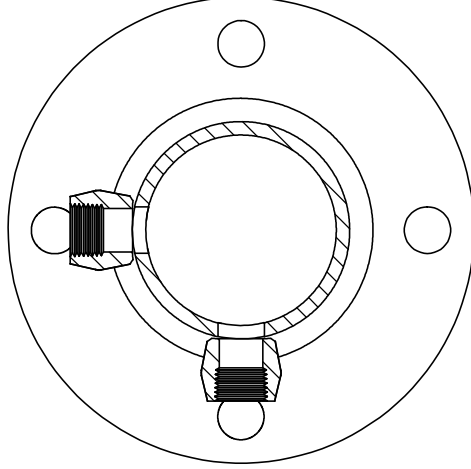
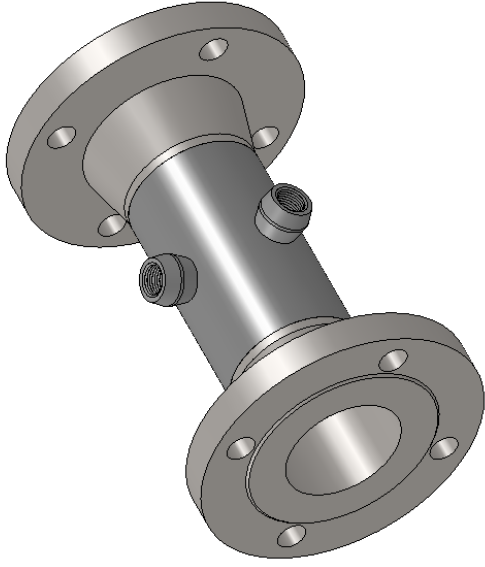
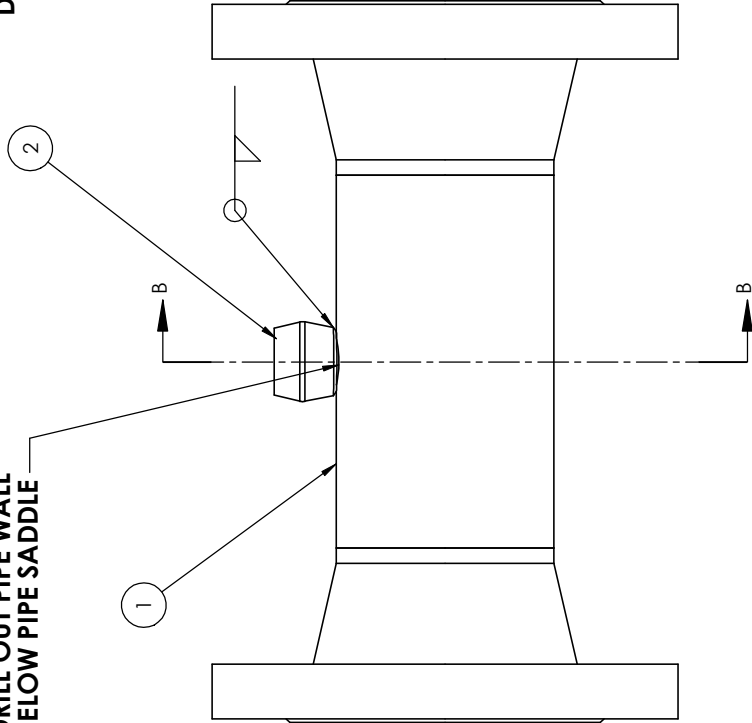
ITEM NO.	PART NUMBER	DESCRIPTION	QTY.
1	N/A	PUMP INTAKE SECTION	1
2	MCMaster P/N 4587K23	PIPE SADDLE - 2" PIPE TO 1/2" NPT	1

NOTE:

**JOB NUMBER: 10557
SPEED CODE: 58775
PLEASE RETURN FINISHED PART TO:
DEREK LOEWEN, MECE 2-22**

NOTE:

**DRILL OUT PIPE WALL
BELOW PIPE SADDLE**



SECTION B-B
SCALE 1 : 2

UNLESS OTHERWISE SPECIFIED:	NAME	DATE
DIMENSIONS ARE IN INCHES	DRAWN	
TOLERANCES:	CHECKED	
FRACTIONAL ±	ENG APPR.	
ANGULAR: MACH ±	MFG APPR.	
BEND ±	Q. A.	
THREE PLACE DECIMAL ±	COMMENTS:	
	INTERPRET GEOMETRIC TOLERANCING PER:	
	MATERIAL	
	FINISH	
	USED ON	
	APPLICATION	
	DO NOT SCALE DRAWING	

PROPRIETARY AND CONFIDENTIAL
THE INFORMATION CONTAINED IN THIS DRAWING IS THE PROPERTY OF PUNBp. ANY REPRODUCTION IN PART OR AS A WHOLE WITHOUT THE WRITTEN PERMISSION OF PUNBp IS PROHIBITED.

SIZE	DWG. NO.	REV
SCALE: 1:5	WEIGHT:	SHEET 1 OF 1

PunBp intake section 2

Appendix E - Material Data Sheets

Sil Blasting Sands

Features and Advantages

Sil Industrial Minerals Blasting Sands are sub-angular grain, crystalline silica sand with a hardness and uniformity superior to common or local river sands.

All *Sil Industrial Minerals Blasting Sands* are mined, washed, sized, dried and screened under our ISO 9002 Quality Assurance Program. Both feed stock and final products are processed through our modern Bruderheim Plant using the latest industrial sand processing technology. The result is chemical purity, minimal clay and adhesion impairing contaminants with a consistent uniform particle size distribution.

Using *Sil Industrial Minerals Blasting Sands* can minimize coating failures due to surface impingement or trace mineral contamination, and can significantly reduce fine particle dusting to improve worker production.

Sil Industrial Minerals Blasting Sands are used for the surface preparation for coatings of bridges, concrete, construction equipment, derricks, rigs, tanks, vessels and many other heavy equipment items.

Particle Size Analysis

	Mesh (ASTM E-11)	Sil 1 Fine	Sil 4 Medium	Sil 7 Coarse
Sieve Analysis	8			0.0
	16		0.0	5.5
(Typical mean %	20		0.3	8.5
Retained on	30	0.0	5.0	25.5
Individual Sieves)	40	0.4	51.1	40.0
	50	10.3	38.9	18.4
	60	28.1	3.6	1.5
	80	44.1	0.8	0.4
	100	10.6		
	140	5.8		
	200	0.1	0.3	0.2

Product Properties

Property	Test Method	Unit	Typical Values
Mineral	Petrographic	--	Quartz
Shape	Krumbein	--	Sub-Angular
Hardness		Moh	6.5
Specific Gravity	ASTM C-128	--	2.65
Bulk Density, aerated	ASTM C-29	Lbs/Ft ³	92-95
compactd	ASTM C-29	Lbs/Ft ³	98-100

Chemical Analysis

Mean Percent by Weight		Sil 1	Sil 4 & 7	ASTM Test Method
Silicon Dioxide	(SiO ₂)	92.53	92.30	
Iron Oxide	(Fe ₂ O ₃)	0.95	0.90	
Aluminum Oxide	(Al ₂ O ₃)	4.32	4.42	
Calcium Oxide	(CaO)	0.48	1.09	
Titanium Dioxide	(TiO ₂)	0.06	0.08	
Magnesium Oxide	(MgO)	0.08	0.24	
Potassium Oxide	(K ₂ O)	0.99	0.68	
Sodium Oxide	(Na ₂ O)	0.82	0.86	
Sulphur	(SO ₃)	0.06	0.07	
Manganese	(MnO)	0.01	0.02	
Phosphorous	(P ₂ O ₂)	0.03	0.08	ASTMC 114-15
Loss on Ignition	(L.O.I.)	0.24	0.54	LiBO ₃

Ordering Information

Shipping Point: Bruderheim, AB & Edmonton, AB

Packaging: *Sil Industrial Minerals Blasting Sands* are available in 22.7 kg (50 lb) and 40 kg (88 lb) multiwall paper bags, 1.725 tonne (3,800 lb) bulk bags and bulk in dedicated pneumatic truckloads.

Features and Advantages

Garnet is a chemically inert nonmetallic mineral that is quite common in the natural environment. It is found in trace amounts in most river and beach sands and is known for its hardness and durability. The high levels of harness and toughness make garnet ideal for many abrasive applications. Its high specific gravity as well as its chemical and abrasive resistance makes garnet ideal for many applications.

Applications

The environmentally friendly abrasive media, **Garnet** cleans a wide range of substrates from steel bridges, ships, tanks, aluminum and composites to cleaning turbines, generators, glass etching and the Aerospace industry.

Key markets are abrasive blast cleaning, water filtration, waterjet cutting and high temperature gravel pack for deep oil wells.

Particle Size Analysis

TYPICAL VALUES – Data shown is accurate and reliable, but not a specification.

ABRASIVE BLASTING SPECIFICATIONS (Percent Retained)

MM	Sieve (US Standard)	#8-12	#16	#25	#36	#30/40	#50	#60	#60/80	#80	#100	#150
2.38	8	0-10										
1.68	12	40-75	0-2	0-2								
1.41	14	20-40	5-40	10-30								
1.19	16	0-5	30-70	20-30								
1.00	18		20-40	5-20	10-20							
0.841	20		0-5	5-20	20-35							
0.594	30			5-20	40-60	0-5	0-5					
0.417	40			0-5	0-12	60-90	40-65	0-5	0-5	0-5		
0.297	50					5-35	30-50	60-80	30-60	0-50		
0.249	60						10-20	20-40	15-30	15-50		
0.208	70							0-5	10-20	10-55		
0.178	80								5-20	5-40	0-20	
0.150	100								0-5	0-15	30-45	
0.124	120										30-45	0-15
0.104	140										0-15	20-30
0.064	230											50-70
0.049	325											1-10

Continued next page...

Chemical Analysis

TYPICAL VALUES – Data shown is accurate and reliable, but not a specification.

Major elements

Silicon Dioxide	(SiO ₂)	37% (non-crystalline)
Ferric Oxide (Iron Oxide)	(Fe ₂ O ₃)	33%
Aluminum Oxide	(Al ₂ O ₃)	25%
Magnesium Oxide	(MgO)	3%
Calcium Oxide	(CaO)	1%
Manganese Oxide	(MnO)	1%

All abrasive blasting properties meet the following standards:

Specific Gravity	>4.0
Hardness	7.5 – 8.0 on Moh scale

Toxicity Characteristic Leaching Procedure

Element	TCLP Limit Mg/l	Actual Mg/l
Arsenic	5.0	<0.1
Barium	100	<0.1
Cadmium	1.0	<0.02
Chromium	5.0	<0.05
Lead	5.0	<0.5
Mercury	0.2	<0.001
Selenium	1.0	<0.10
Silver	5.0	<0.05

Ordering Information

Shipping Point:

Edmonton Distribution Centre

Packaging:

100 lb. multiwall paper bags

Edmonton Distribution Centre

305 – 116 Ave. N.W., Edmonton, AB T6S 1G5
Order Desk: (780) 467-2627
Fax: 467-2752
Toll Free: 1-800-661-6982

“Blasting Abrasive & Equipment Specialists”



REPRO[®] LIGHT

Description

Repro Light is a versatile castable urethane that is approximately 1/2 the weight of our other Repro products. This material, which is colored brown, can be used for lightweight tools, backfill applications, and as an adhesive for many urethane and epoxy tooling boards. It's hardness and color is an almost exact match to the popular tooling board RenShape 450. This material also offers low internal porosity compared to competitive products. Repro Light offers easy machinability and can be readily worked and carved with hand tools.

Special Note: Since Repro Light uses a lightweight filler, the material towards the top of the can may harden during shipment. This is normal and will mix easily with the liquid underneath when properly agitated.

Physical Properties

Color (when mixed)	Tan
Mix Ratio (by weight or volume)	1:1
Mixed Viscosity (cps)	1,500
Gel Time (min. @ 72°F.)	6-8
Hardness (Shore D)	68
Compressive Strength ^[1] (psi)	3,980
Flexural Strength ^[2] (psi)	2,620
Flexural Modulus ^[2] (psi)	347,000
Tensile Strength ^[3] (psi)	1,530
Tensile Modulus ^[3] (psi)	350,000
Izod Impact Strength ^[4] (ft-lbs./in.)	0.15
Specific Gravity	0.9
Linear Shrinkage ^[6] (in./in.*)	0.0014
Vol. Wt. Ratio (cu. in./ lb.)	30
Deflection Temperature @ 66 psi ^[7] (°F)	132°F
Demold Time (minutes)	90-120

*-Actual shrinkage dependent upon mass

ASTM Tests: [1]-D695, [2]-D790, [3]-D638, [4]-D256, [5]-D696-98, [6]-D2566, [7]-D648

Ordering Information

Item Number	Description	Net Wt.
053197	Repro Light Quart Kit	2.5 lbs
053198	Repro Light Gallon Kit	10 lbs
053199	Repro Light 5 Gallon Kit	50 lbs

Physical and mechanical properties of tooling plastics herein reported are typical after a full cure of seven (7) days at room temperature or equivalent. Designated mix ratios must be adhered to for desired results.

READ SAFETY DATA SHEETS AND PRODUCT LABELS BEFORE USING PRODUCT

Freeman Mfg.
& Supply Co.
1101 Moore Rd
Avon, OH 44011

Phone 800 321 8511
Fax 440 934 7200

www.freemansupply.com

www.freemanwax.com



REPRO USER INFORMATION

The following information, except when specifically noted, is common to the entire line of Repro Fast-Cast Urethanes. A separate instruction sheet is available for using Repro Surface Coat and Laminating Resin System.

Instructions For Use

Materials Needed

- Repro Fast-Cast Urethane A & B Components
- Plastic or Lined Paper Mixing Containers
- Jiffy, Plunge, Hula Girl, or Red Devil Mixer
- Freeman Wax Release, and Partall PVA Mold Release
- Plastic or Rubber Gloves
- Acetone or Alcohol Solvent
- Clean Cloth
- Mixing Paddles or Tongue Depressors

Preparation

- If bonding Repro to a surface, clean and abrade the surface to be bonded.
- If Repro is to be parted from a surface that it is poured against, follow proper sealing and release procedures to prevent bonding.
- Procedures for releasing Repro from metal, wood, plastic, wax, and plaster are available from **Customer Service 800-321-8511** or our website www.freemansupply.com.

Mixing and Pouring

- Plastic or rubber gloves **MUST** be worn when working with Repro (read Warning Information)
- Using an appropriate mixer, **THOROUGHLY** mix Parts A and B in their original containers. When using a drill driven mixer, it is preferable to use separate mixers for the A and B components. A single mixer may be used, but it essential to completely clean it with solvent before mixing the other component to avoid contamination.
- By weight or volume pour equal amounts of Part A and Part B into separate clean and dry containers. Replace the lids on both sides of the original Repro containers to prevent contamination.
- Pour the A side into the B side cup and mix well, approximately 30 seconds, using a tongue depressor or paint paddle. Be aware of the Pot Life for the particular Repro formulation that you are using to avoid the premature solidification of the material.
- When mixing is complete pour the liquid into a third container and mix briefly to ensure a complete mix.
- Pour the mixed Repro into your mold cavity. To help avoid air entrapment, hold the container well above the mold surface if possible, and pour in a thin stream.

Freeman Manufacturing & Supply Company
 Avon, Ohio 44011 USA
 1/09

Pot Life and Demold Times

Product	Pot Life (Min.)	Demold Time (Min)
Repro Fast	4-5	15-30
Repro 10	5-6	30-60
Repro 83	6-7	60-90
Repro NS - Non Settling	6-7	60-90
Repro One - Non Settling	6-7	60-90
Repro 95 - Aluminum Filled	6-7	60-90
Repro Light	6-8	90-120
Repro Ultra Light	10-11	120-180
Repro Slow	12-14	180-240

**Note: Demold times are greatly affected by poured mass and ambient temp.*

FOR INDUSTRIAL USE ONLY
KEEP OUT OF REACH OF CHILDREN

A-Side contains POLYOL

B-Side contains ISOCYANATE

WARNING

Direct contact may cause eye or skin irritation. Exposure to vapor or liquid might cause respiratory and skin sensitization, as well as eye irritation.

Avoid contact with eyes, skin, and clothing. **DO NOT TAKE INTERNALLY.** Avoid breathing of vapors. Use only with adequate ventilation. Wash thoroughly after handling.

FIRST AID - If inhaled, move person(s) to fresh air. If contact with eyes or skin, flush immediately with water for at least 15 minutes and get medical attention. Wash skin with soap and water. If swallowed seek medical attention immediately.

IN CASE OF FIRE: Extinguish fire with dry chemicals, carbon dioxide, foam, or water spray.

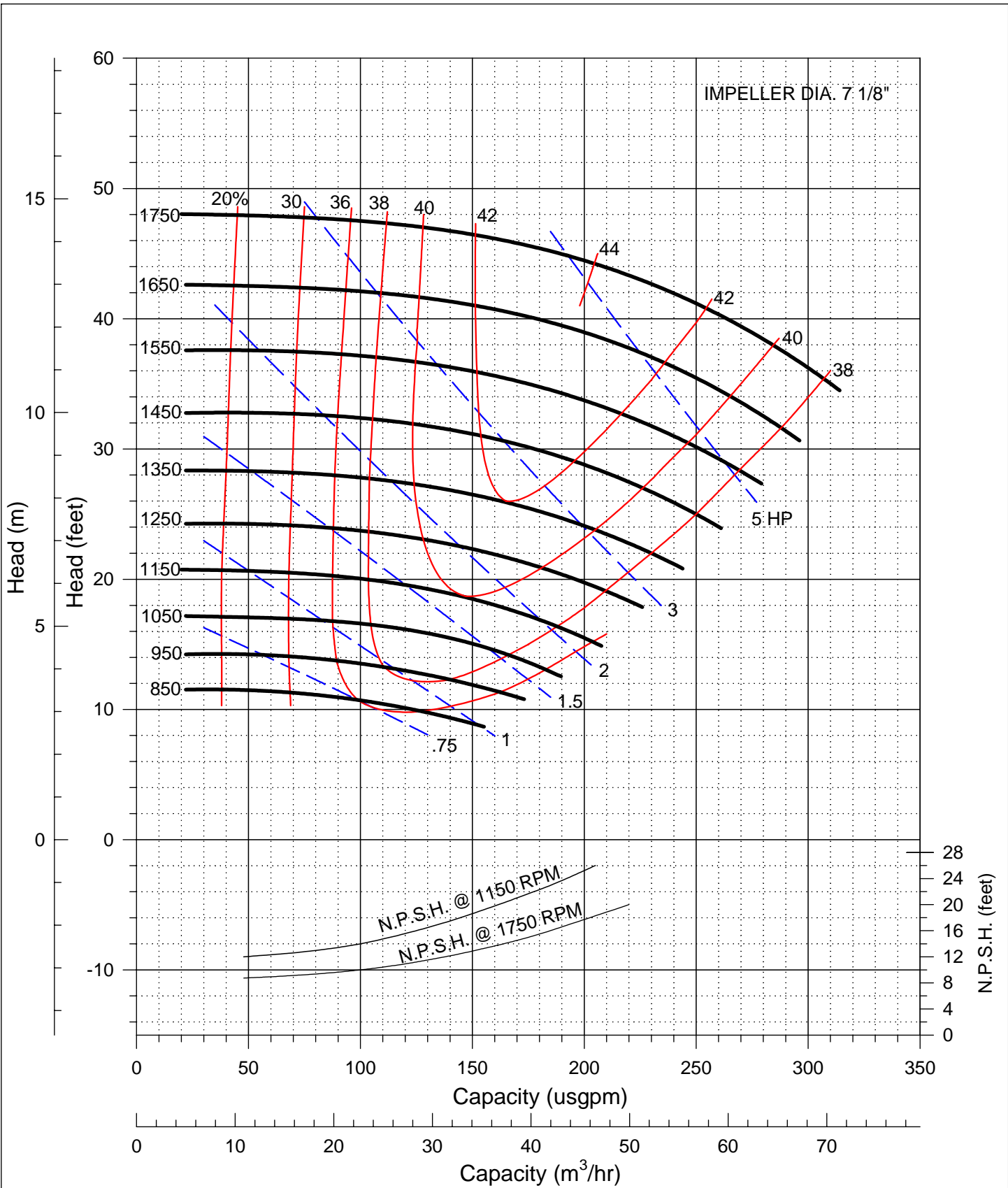
Moisture Sensitivity


IMPORTANT - Because all urethanes are sensitive to moisture, the user must keep Repro container lids closed when not in use. Repeated opening and closing of the container may introduce moisture and negatively affect performance of the product. We recommend that Freeman 302 Urethane Protectant be sprayed into the opened A and B container before resealing the unused material.

IMPORTANT NOTICE TO PURCHASER

Manufacturer/seller shall NOT be liable for any injury, loss, damage arising directly, consequentially from the proper/improper use of product, but shall be obligated to replace quantity of product proved defective for intended application. User shall determine suitability of the product for intended use and assumes all risk and liability whatsoever in connection therewith. The foregoing may not be altered except by express written consent by an officer of manufacturer/seller.

Appendix F – Pump Data Sheets



HAYWARD GORDON LTD.  Performance Curves TORUS Pumps	MODEL	SIZE	CURVE	REV.
	XR2(7)	2 x 3 x 7	095-10110	3
	DRN.DATE 04.03.96 REV.DATE 10.05.07	DRN. J.M. REV. LF	MAX SPHERE 2"	SPEED VARIABLE

Appendix G – Sensor Data Sheets

AST4000 *Industrial Grade*



Stainless Steel Media Isolated Pressure Sensor

Overview

Utilizing a one-piece stainless steel sensing element, the AST4000 covers a wide variety of applications that require rugged construction, high cycle life, as well as media compatibility to deliver outstanding and long-term performance. The AST4000 is offered with a variety of threads, pressure ranges, outputs and electrical connections in order to make system integration seamless.

Benefits

- ◆ High Strength Stainless Steel Construction
- ◆ No Oil, Welds or Internal O-rings
- ◆ Wide Operating Temperature Range
- ◆ Ranges up to 10,000 PSI
- ◆ Low Static and Thermal Errors
- ◆ Unparalleled Price and Performance
- ◆ Compatible with Wide Range of Liquids and gases
- ◆ EMI/RFI Protection
- ◆ UL/cUL 508 Approved

Applications

- ◆ Industrial OEM Equipment
- ◆ Water Management
- ◆ Pneumatics
- ◆ Hydrogen Storage
- ◆ Sub Sea Pressure
- ◆ HVAC/R Equipment
- ◆ Control Panels
- ◆ Hydraulic Systems
- ◆ Data Loggers



Performance @ 25°C (77°F)

Accuracy*	< ±0.5% BFSL
Stability (1 year)	±0.25% FS, typical
Over range Protection	2X Rated Pressure
Burst Pressure	5X or 20,000 PSI (whichever is less)
Pressure Cycles	> 100 Million

* Accuracy includes non-linearity, hysteresis & non-repeatability

Electrical Data

Output	4-20mA	1-5VDC, 1-6VDC	0-50mV (10mV/V)	0.5-4.5V Ratiometric
Excitation	10-28VDC	10-28VDC	5VDC, typical	5VDC, regulated
Output Impedance	>10k Ohms	<100 Ohms, Nominal	1100 Ohms, Nominal	<100 Ohms, Nominal
Current Consumption:	20mA, typical	<10mA	<5mA	<10mA
Bandwidth	(-3dB): DC to 250 Hz	(-3dB): DC to 1kHz	(-3dB): DC to 5kHz, min	(-3dB): DC to 1kHz
Output Noise:	-	<2mV RMS	-	<2mV RMS
Zero Offset:	<±1% of FS	<±1% of FS	< ±2% of FS	<±1% of FS
Span Tolerance:	<±2% of FS	<±1.5% of FS	< ±2% of FS	<±1.5% of FS
Output Load:	0-800 Ohms@10-28VDC	10k Ohms, min	>1M Ohms	10K Ohms, min
Reverse Polarity Protection	Yes	Yes	-	Yes

Environmental Data

Temperature	
Operating	-40 to 85°C (-40 to 185°F)
Storage	-40 to 100°C (-40 to 212°F)
Thermal Limits	
Compensated Range	0 to 55°C (30 to 130°F)
TC Zero	<±1.5% of FS
TC Span	<±1.5% of FS
Other	
Shock	100G, 11 msec, 1/2 sine
Vibration	10G peak, 20 to 2000 Hz.
EMI/RFI Protection:	Yes
Rating:	IP-66 (housing only)

Ordering Information

AST4000 A 00500 P 4 E 0 000

Series Type**Process Connection**

- A= 1/4" NPT Male
- B= 1/8" NPT Male**
- C= 1/4" BSPP Male
- F= 7/16" - 20 UNF Male**
- K= SAE4 Female
- (use option codes 006 or 143)
- P= 1/2" MNPT

Pressure Range: Insert 5-digit pressure range code**Pressure Unit**

- B= Bar
- K= kg/cm2
- P= PSI

Outputs

- 1= 0.5-4.5V ratiometric 6= 1-6V
- 3= 1-5V A= 10mV/V
- 4= 4-20mA (2 wire loop powered)

Electrical (Wiring information available at: <http://www.astsensors.com/mediacenter.php>)

- A= 2 ft. (0.6m)
- B= 4 ft. (1.2m)
- C= 6 ft. (1.8m)
- D= 10 ft. (3.0m)
- E= Mini DIN 43650
- F= Packard Metripack 150 3-Pin Conn.
- G= 4-pin Molex Conn. (No housing)
- I= DIN 43650A
- X= Special
- Y= M12 Eurofast
- Z= DT04 Deutsch

Wetted Material

- 0= 17-4PH
- 1= 316L
- 2= Inconel 718*

Options

- 000 = No Options
- 006= Schrader Depressor Pin+
- 009= Sealed Gauge Reference*
- 094= Impulse Subsea Connection & all 316L wetted material (use with X electrical connection and 1 for wetted materials)*
- 117= Internal Restrictor Plug*
- 143= Schrader Depressor Pin & Sealed Gauge References+
- 165= Internal Restrictor Plug & Sealed Gauge References*

*Consult factory on availability

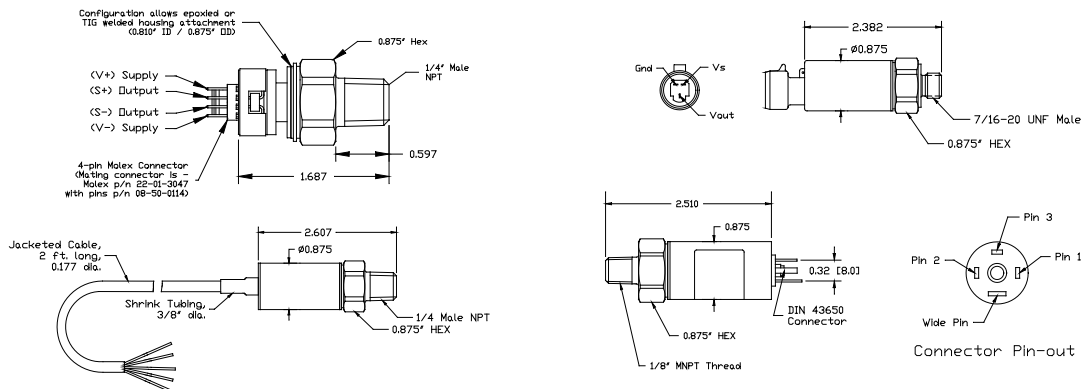
** Not available under 50PSI (1/8" NPT Male not available in 316L)
+Options only available with SAE4 Female Pressure Port option "K."

Pressure Ranges*

PSIG Measurement Range	Pressure Range Code	BARG Measurement Range	Pressure Range Code
-14.7 to 25**	V0025**	-1 to 2**	V0002**
0-25	00025	0-2	00002
0-50	00050	0-5	00005
0-100	00100	0-7	00007
0-150	00150	0-10	00010
0-200	00200	0-20	00020
0-250	00250	0-35	00035
0-500	00500	0-50	00050
0-1,000	01000	0-70	00070
0-2,500	02500	0-100	00100
0-5,000	05000	0-250	00250
0-7,500	07500	0-350	00350
0-10,000	10000	0-500	00500
		0-700	00700

*Typical ranges. All ranges between 0-25 PSI and 0-10,000 PSI available.
**Compound ranges up to -14.7 to 500 PSI available. Please consult factory.

Dimensional Data



Warranty

Workmanship - AST, Inc. pressure transmitters have a limited one-year warranty to the original purchaser. AST, Inc. will replace or repair, free of charge, any defective transmitter. This warranty does not apply to any units that have been modified; misused, neglected or installed where the application exceeds published ratings. AST's sensors are made with pride in New Jersey, USA. If in the area please feel free to stop by for a visit!

Installation/Applications - The purchaser is responsible for media compatibility, functional adequacy, and correct installation of the transmitter.

RTD SPECIFICATIONS

STANDARD RTD ELEMENT SPECIFICATIONS

ELEMENT MATERIAL*	RESISTANCE @ 0°C	TEMPERATURE COEFFICIENT	OPERATING RANGE†	AVAILABLE ACCURACIES @ 0°C
Platinum	100 Ohm	.00385	-200 to 850°C	± .5% ± .1% ± .06% ± .01%
Platinum	100 Ohm	.00391	-200 to 600°C	± .1% ± .06%
Copper	10 Ohm	.00427	-200 to 204°C	± .2% ± .5%
Nickel	120 Ohm	.00672	-200 to 204°C	± .3% ± .5%

* Sensing elements of other materials and temperature coefficients are available upon request.

† Stated operating ranges are typical values and are dependant upon the sensing element and the construction style of the sensor assembly. Assemblies to exceed the stated limits may be available upon request.

RTD Elements

Aircom can supply elements of several different materials, base resistances, temperature coefficients, accuracies and configurations for installation into RTD assemblies that meet customer supplied requirements. The most common element we use is Platinum with a base resistance of 100 ohms @ 0°C, accuracy of ± 0.5% and temperature coefficient of 0.00385 ohms/ohm/°C. The second most common element is a 392 curve (0.00392 ohms/ohm/°C) element found in most Japanese and a few American made assemblies. Our most common construction of these elements is a Platinum wound element enclosed in a ceramic housing. Process conditions may dictate use of other types of element construction such as Thin-Film, Glass Bulb, or Kapton insulated. The following standards dictate the specifications to which our elements are manufactured to:

For 0.00385 ohms/ohm/°C elements

- International Electromechanical Commission Standard IEC 751, 1995
- British Standards Institution BS 1904, 1984
- Deutsches Institut fur Normung (Germany) DIN 43760, 1987

For 0.00392 ohms/ohm/°C elements

- Scientific Apparatus Manufacturers Association SAMA RC21-4-196
- Japanese Standards Association JIS C 1604-1989

RESISTANCE/TEMPERATURE		
	Copper	Nickel
Base resistance:	10 Ω at 25°C	120 Ω at 0°C
TCR (Ω/Ω°C)	.00427	.00672
Sensitivity (Average Ω/°C)	0.039	0.806
Temperature (°C)	Resistance (ohms)	
-100	5.128	120.00
-80	5.923	66.60
-60	6.712	79.62
-40	7.490	92.76
-20	8.263	106.15
0	9.035	120.00
20	9.807	134.52
40	10.580	149.79
60	11.352	165.90
80	12.124	182.84
100	12.897	200.64
120	13.669	219.29
140	14.442	238.85
160	15.217	259.30
180	15.996	280.77
200	16.776	303.46
220	17.555	327.53
240	18.335	353.14
260	19.116	380.31

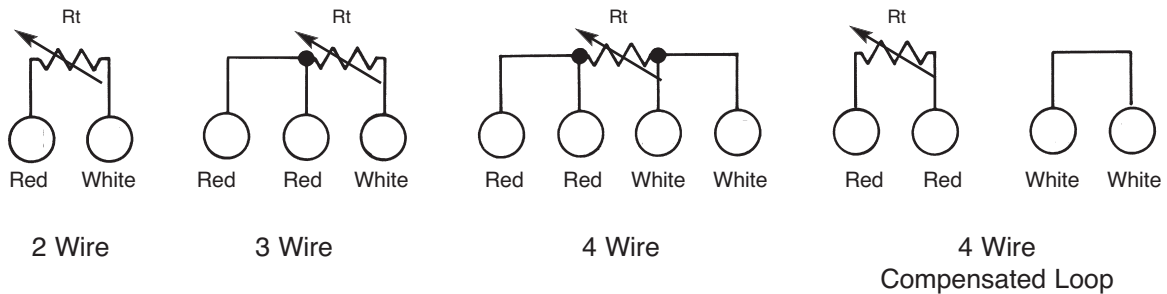
RESISTANCE/TEMPERATURE			
Platinum Elements			
Resistance at 0°C: TCR (Ω/Ω°C)	100 Ω .00392	100 Ω .00391	100 Ω .00385
Sensitivity (Average Ω/°C)	0.392	0.391	0.385
Temperature (°C)	Resistance (Ohms)		
-200	17.00	17.26	18.52
-180	25.72	25.97	27.10
-160	34.31	34.54	35.54
-140	42.80	43.01	43.88
-120	51.19	51.37	52.11
-100	59.49	59.64	60.25
-80	67.71	67.83	68.32
-60	75.87	75.96	76.33
-40	83.96	84.03	84.27
-20	92.01	92.04	92.16
0	100.00	100.00	100.00
20	107.95	107.92	107.79
40	115.85	115.78	115.54
60	123.70	123.60	123.24
80	131.50	131.38	130.90
100	139.26	139.11	138.51
120	146.97	146.79	146.07
140	154.64	154.42	153.58
160	162.25	162.01	161.05
180	169.82	169.55	168.48
200	177.35	177.04	175.86
220	184.82	184.49	183.19
240	192.25	191.89	190.47
260	199.64	199.24	197.71
280	206.97	206.55	204.90
300	214.26	213.81	212.05
320	221.50	221.02	219.15
340	228.70	228.19	226.21
360	235.85	235.31	233.21
380	242.95	242.38	240.18
400	250.00	249.41	247.09
420	257.01	256.39	253.96
440	263.97	263.32	260.78
460	270.88	270.21	267.56
480	277.75	277.04	274.29
500	284.57	283.84	280.98
520	291.34	290.58	287.62
540	298.06	297.28	294.21
560	304.74	303.93	300.75
580	311.37	310.54	307.25
600	317.96	317.09	313.71
620	324.49	323.60	320.12
640	330.98	330.07	326.48
660	337.43	336.49	332.79
680	343.82	342.86	339.06
700	350.17	349.18	345.28
720			351.46
740			357.59
760			363.67
780			369.71
800			375.70
820			381.65
840			387.54
850			390.48

RTD SPECIFICATIONS

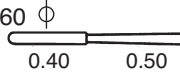
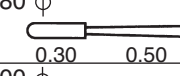
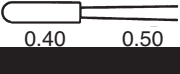
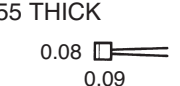
RTD INTERCHANGEABILITY			
Temperature °C	Platinum RTD		
	±0.06% at 0°C	±0.1% at 0°C	±0.5% at 0°C
-200	±0.55°C	±1.3°C	±2.1°C
-100	±0.35°C	±0.8°C	±1.7°C
0	±0.15°C	±0.3°C	±1.3°C
20	±0.19°C	±0.4°C	±1.6°C
100	±0.35°C	±0.8°C	±2.9°C
200	±0.55°C	±1.3°C	±4.4°C
260	±0.67°C	±1.6°C	±5.5°C
300	±0.75°C	±1.8°C	
400	±0.95°C	±2.3°C	
500	±1.15°C	±2.8°C	
600	±1.35°C	±3.3°C	
700		±3.8°C	
800		±4.3°C	
850		±4.6°C	

Temperature °C	Copper RTD		Nickel RTD	
	±0.02% at 25°C	±0.5% at 25°C	±0.3% at 0°C	±0.5% at 0°C
-100	±1.5°C	±2.2°C		
0	±0.7°C	±1.5°C	±0.5°C	±0.8°C
20	±0.5°C	±1.3°C	±0.8°C	±1.2°C
100	±1.5°C	±2.5°C	±1.8°C	±2.2°C
150	±2.2°C	±3.3°C	±2.5°C	±3.0°C
200	±2.8°C	±4.1°C	±3.1°C	±3.7°C
260	±3.6°C	±5.1°C	±3.4°C	±4.0°C

WIRING CONFIGURATIONS:



ELEMENT DIMENSIONS:

Dimensions in inches	R (0°C)	Temperature Range	Leads	63% response time Sec. in water, 0.4 m/s
550°C wire-wound elements				
0.060 ϕ 	100 Ω	-100 to 550°C	0.010" (0.25 mm) ϕ Platinum alloy	0.14
0.080 ϕ 	100 Ω	-100 to 550°C	0.010" (0.25 mm) ϕ Platinum alloy	0.18
0.100 ϕ 	100 Ω	-100 to 550°C	0.014" (0.35 mm) ϕ Platinum alloy	0.22
400°C and 600°C thin-film elements				
0.055 THICK 	100 Ω	-70 to 400°C	0.010" ϕ Ag 0.004 Ω /mm/lead	0.2
0.08 0.09 Lead Length: 0.4	100 Ω	-70 to 600°C	0.008" (0.20 mm) ϕ Pd 0.036 Ω /mm/lead	0.2

Appendix H - High-Speed Camera Data Sheet

///MotionPro™

High-Speed CMOS PCI Camera

The MotionPro high-speed CMOS PCI camera from Redlake MASD combines an advanced high-speed, mega-pixel resolution CMOS camera with the features you need for meaningful high-speed motion analysis on your PC. Designed as a peripheral for capturing high-speed digital images directly into the PC, the MotionPro system consists of a high-speed camera, full size single-slot PCI camera control and frame storage board (with up to 6 GB onboard memory), user interface, and easy to use analysis software. Up to four MotionPro systems can be operated in a single PC, providing multiple synchronous views of a high-speed event.

Video capture using MotionPro cameras may be initiated via software or a wide variety of external triggers including optical, acoustic, electrical, and motion-controlled devices, as well as simple hand-held switches. Flexible recording options offer several recording modes allowing the user to either use the memory as a circular buffer into which specified numbers of pre- and post-trigger frames may be recorded, or to divide the memory into a segmented buffer for multiple session operation.



S N A P S H O T

High-Speed High-Resolution CMOS Sensor

Full-frame resolution of 1280 x 1024 pixels and recording rates up to 10,000 frames per second with state-of-the-art CMOS sensor, available in color or monochrome.

Flexible Triggering and Recording Options

Enables record and capture of both controlled and intermittent events.

Intuitive Camera Control and Motion Analysis Software

Controls up to four MotionPro cameras and accurately analyzes high-speed motion events on Windows 2000 / WinNT- based software.

Motion analysis software completes the system functionality with many valuable features including angular, linear, velocity and rotational measurements as well as tracking multiple points over multiple frames. MotionPro also has a lens calculator tool that computes lens selection, depth of field, magnification factor and motion blur for any setup.



REDLAKE

1.800.462.4307

MotionPro™

PERFORMANCE SPECIFICATIONS

Sensor Array	Ten Channel 1280 x 1024 pixel CMOS Sensor
Image Resolution	Up to 1280 x 1024. Pixel depth is 8 bits (mono), 24 bits (color)
Sensitivity	User-accessible gain controls allow sensitivity and linearity control
Models	500 – up to 500 frames per second 2000 – up to 2,000 frames per second 10000 – up to 10,000 frames per second
Shutter	Global Electronic Shutter with exposure times from 2 μ seconds to 1/frame rate in increments of 2 μ seconds
Lens Mount	Standard C-mount, optional F-mount
Camera Head Size	4.15"W x 3.60"H x 1.67"D (105.4 x 91.44 x 42.42mm)
Controller Board	Full size PCI 2.2 board (occupies one slot)
Cable	5 meter length
Trigger	TTL (5V-tolerant) compatible signal User selects logical high, low, positive edge, negative edge or switch closure.
Electrical Properties	
Variable Positioning	The trigger position (i.e. the number of pre- and post-trigger frames) is selectable in 1% increments between 0 and the frame capacity -1
Frame Sync	Any number of cameras may be synchronized either to a "master" camera or to an external source Accuracy of synchronization between cameras is within 2 μ seconds
Exposure out	An exposure out signal is available for synchronizing a strobe or another device This signal remains high (3.3V) while the shutter is open
Recording Modes	
Circular Buffer	Records images into circular buffer until triggered, then user- selected number of post-trigger frames (from 0 to total number of frames in buffer -1) are recorded
Multiple Session	
Burst on Trigger	User-selected numbers of frames are recorded every time the camera receives a trigger until the memory is full
Record on Trigger	Records whenever the trigger signal is "true" until the memory is full
Frame Storage	
Standard	Up to 2 GB: 1635 full frames
Enhanced	Up to 4 GB: 3273 full frames
Maximum	Up to 6 GB: 4912 full frames
Playback Rates	User selectable variable playback
Multi-Camera Control	Up to four cameras may be operated on one PC
Operator Environment	Point & click environment for Windows 2000 and Windows NT 4.0 SP6
Reticle	Pixel coordinates of the reticle position are always displayed on screen
Analysis Features	Microsoft Excel compatible features including angular, linear, velocity and rotational measurements Track multiple points over multiple frames. Also has a lens calculator tool that computes lens selection, depth of field, magnification factor and motion blur.
File Formats	AVI, BMP, JPEG, TIFF
PC Minimum Platform	Minimum platform: Celeron 800 MHz, 1024 x 768 display resolution, 128 MB RAM, 10 GB Hard Drive, 64 MB video RAM, CD-R Drive, 3.3V PCI 2.2 compliant motherboard, at least one empty full-length PCI slot, Windows™ NT or Windows™ 2000.



REDLAKE

Redlake MASD, Inc.

tel: 800.462.4307

tel: 858.481.8182

fax: 858.792.3179

email: sales@redlake.com

www.redlake.com



Note: Specifications are typical and subject to change. M112-02

Appendix I – Sample Thermal Correction For Strain Readings

Thermal correction on strain readings is accomplished as follows:

Thermal strain is calculated from

$$\varepsilon_{\text{thermal}} = \alpha \Delta T$$

where α is the coefficient of thermal expansion, given to be 104 mm/mm/°C for acrylic [MATWEB, accessed April 6, 2013]

Strain gauge correction is calculated from the manufacturer-supplied equation

$$\Delta\varepsilon_{\text{gauge}} = a_0 + a_1T + a_2T^2 + a_3T^3 + a_4T^4$$

where

- $a_0 = -2.49 \cdot 10^1$
- $a_1 = 2.38 \cdot 10^0$
- $a_2 = -6.42 \cdot 10^{-2}$
- $a_3 = 3.77 \cdot 10^{-4}$
- $a_4 = -4.52 \cdot 10^{-7}$
- T is the temperature, given in degrees Celcius

Then, the final correction is given by

$$\varepsilon = \varepsilon_{\text{measured}} + \Delta\varepsilon_{\text{gauge}} - \varepsilon_{\text{thermal}}$$

Appendix J – Experimental Equipment Issues

J.1 Pump

The ceramic component of the mechanical seal was cracked into several pieces. Upon investigation, it was found that the lubrication chamber had not been filled with oil, and a flush-water system had not been installed at the mechanical seal. Both of these factors ultimately led to overheating and subsequent failure of the seal. These issues were immediately rectified and a replacement seal was installed.

It appeared that flush water was bypassing the mechanical seal into the pump volute. The manufacturer was consulted, and an engineer confirmed that this behaviour was normal for pump models utilizing a single mechanical seal. The option of fitting the pump with a double seal was explored, but the cost and effort required were prohibitive.

Unusual sounds were noted during operation, especially at elevated speeds. In an attempt to identify any underlying issues, inlet and outlet pressures were recorded while the pump was run through its entire speed range. Results are displayed below in Figure 97. During this test, the rig was filled only with water and flow was routed through the mixing tank. The mixing tank is open to atmospheric pressure (open-loop conditions) and gravity-feeds into the pump inlet – a fact which helps to explain the inlet pressure readings.

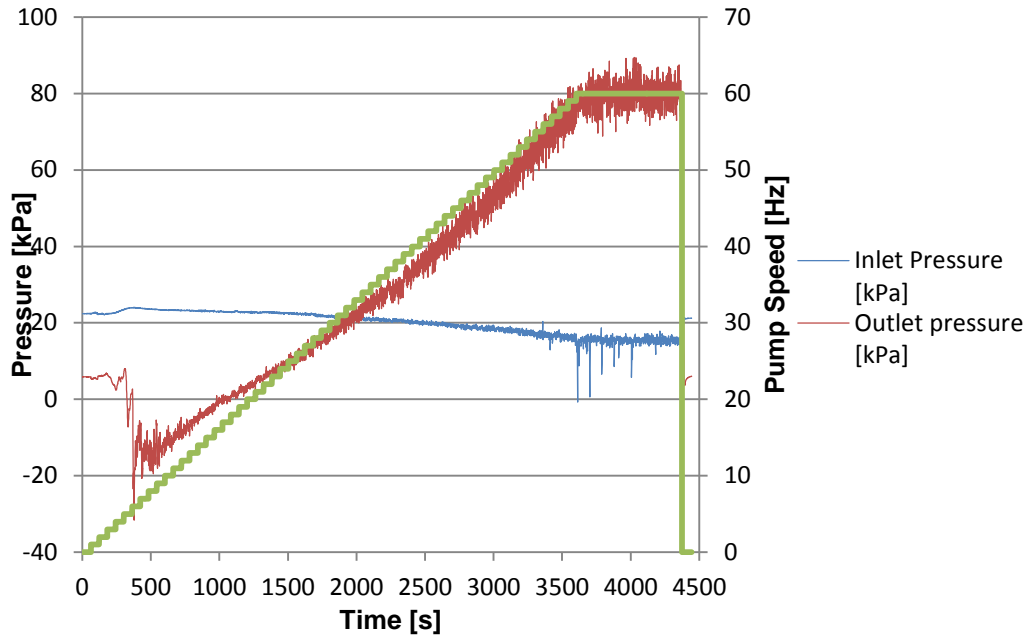


Figure 97 - Pump inlet/outlet pressure with respect to pump speed

Of interest (and concern) was the manner in which the outlet gauge pressure became negative over the range of pump speeds between 5-17 Hz. At speeds in excess of 35 Hz, unusual noises could be heard from the pump; the sound was similar to that which would be produced if gravel had been present in the pump. Beyond this speed, the inlet pressure began to fluctuate heavily, turning violent at elevated pump speeds. Cavitation was immediately suspected.

Before attempting to diagnose the issues, every attempt was made to ensure that the other rig components were functioning correctly. Pressure transducers were re-calibrated and their wiring was checked for issues. Disassembly of the pipe components revealed that the pipes were clear of blockage. No issues were discovered in the pipe rig components.

The observed pressure drop at low pump speed was not clearly understood. One possible explanation is that since the outlet pressure transducer is within such close proximity of the pump, it is likely that strongly turbulent developing flows exist at that location. Changes in pump speed could result in dramatic alterations of these flows. It is surmised that at a specific speed range, secondary flows are induced which result in localized drops in pressure. This phenomenon was deemed to be of little consequence to the slurry wear tests.

The symptoms occurring at higher speeds were attributed to cavitation arising from insufficient NPSH. This was deemed a more serious concern, as the potential exists for severe pump damage if this problem is left unchecked. A study of the model-specific pump literature revealed that the minimum required NPSH value for this pump was 13 feet. The allotted lab space did not allow for more than 7 feet. At this point several options were explored, such as replacing the pump, introducing a spiral diffuser at the inlet, or installing a booster pump. All of these options were considered either too costly or impractical, and were abandoned.

The solution was relatively simple, although perhaps not ideal. Once the flush-water system was installed for the pump's mechanical seal, the flush-water leakage across the seal was put to good use. When the loop was run in closed conditions (i.e. the mixing tank was isolated and flow was routed through a bypass line), it was discovered that opening the flush-water valve caused the system pressure to rise dramatically. This increase in pressure was directly affected by the degree to which the valve was opened. Naturally, this pressure increase brought about a sharp decrease in cavitation. Although cavitation may not have been completely eliminated, it was suppressed sufficiently that full-speed operation was considered "safe."

J.2 Coriolis Meter

As testing proceeded, it was noted that density readings began to deviate strongly from calculated values. Water yielded readings in the range of 1043-1045 kg/m³, well outside the ± 20 kg/m³ acceptable range. Although horizontal Coriolis meters are generally known to return erroneous density data for settling slurries under non-homogeneous flow conditions, single-phase density measurements are generally consistent. This indicated that the device was running incorrectly. Since Coriolis meters calculate density from mass flow, the mass flow readings were suspect as well. A simple bucket-and-stopwatch test at varying speeds confirmed this suspicion. The bucket-and-stopwatch test was completed twice to check repeatability of results. A comparison of flow data and Coriolis readings is shown below in Figure 98. A possible explanation for the erratic behaviour is that the device is simply out of calibration due to extensive service in an aggressive environment. This possibility has not been looked into.

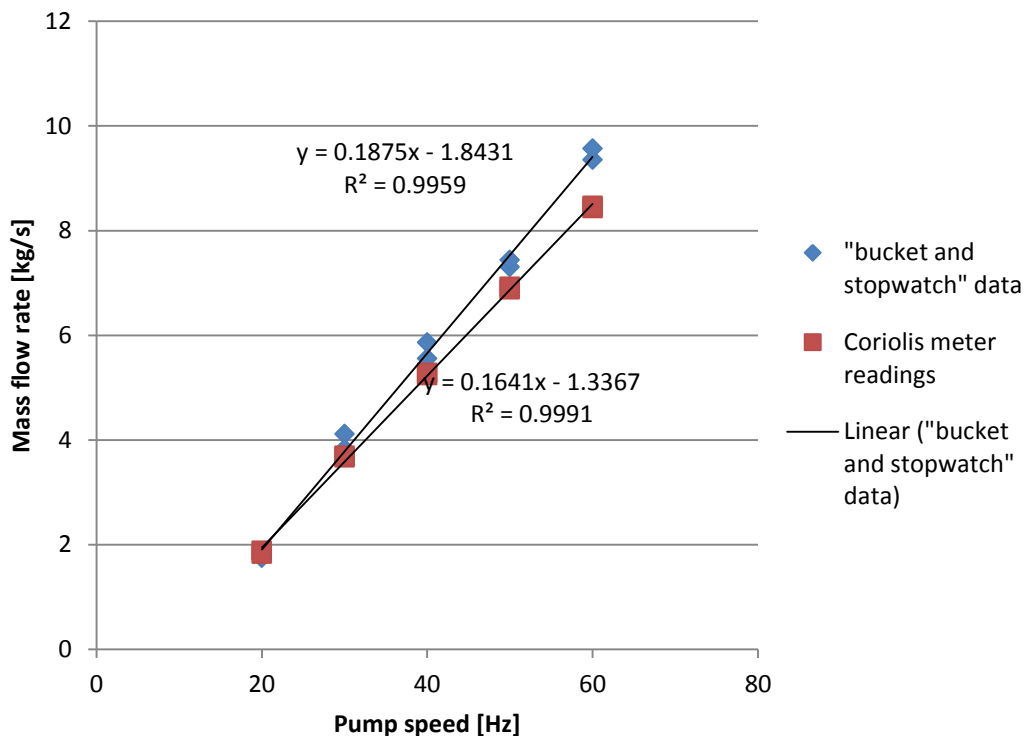


Figure 98 - Mass flow data proving for the Coriolis meter

During some experimental runs, it was observed that the density and mass flow readings rose slowly as the test progressed; this is seen dramatically in Figure 99 and Figure 100. Resetting the Coriolis meter usually fixed the issue. This behaviour was not observed until all testing was completed, and the cause is unknown. Unfortunately, it is difficult to know exactly when the Coriolis meter began returning inaccurate data, or how quickly the inaccuracies compounded. However, it is reassuring to observe that in most cases the reported data differs from real values in a proportional fashion. It is shown in a later section that the integrity of the flow rate data and of the modeling has suffered only minor losses as a result.

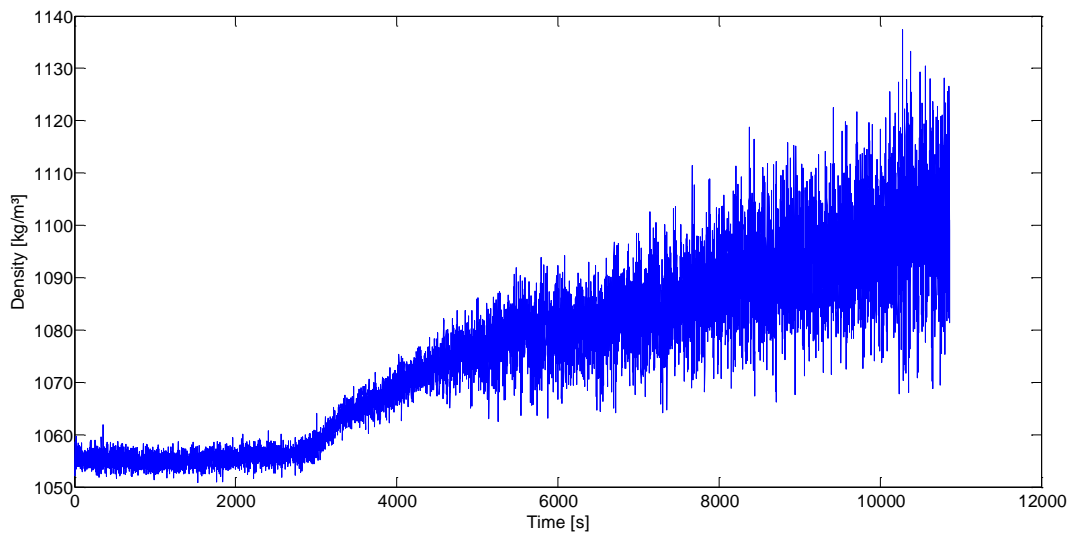
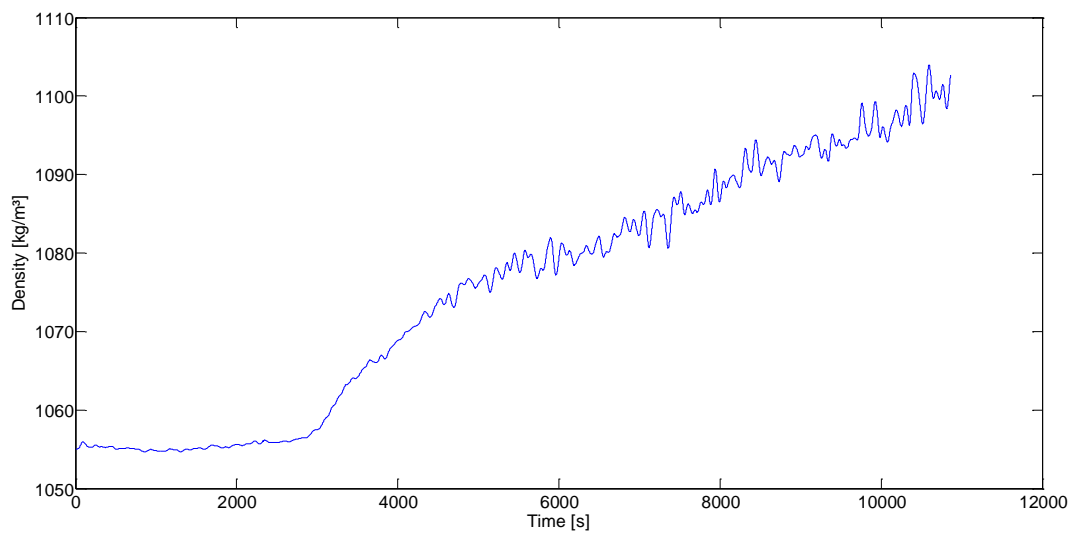


Figure 99 - Density at 60 Hz, 6.4vol% concentration (run #1)



**Figure 100 - Density at 60 Hz, 6.4vol% concentration (run #1),
filtered using 5th-order Butterworth lowpass filter (0.01 Hz)**